UNIVERSIDADE FEDERAL DE SÃO CARLOS
CENTRO DE CIÊNCIAS EXATAS E DE TECNOLOGIA
PROGRAMA DE PÓS-GRADUAÇÃO EM CIÊNCIA E ENGENHARIA DE MATERIAIS

SOLIDIFICATION MICROSTRUCTURES, MECHANICAL AND WEAR PROPERTIES OF Al-Cu-Sn ALLOYS WITH VARIOUS COMPOSITIONS

Sarah Maria de Albuquerque Sousa

São Carlos-SP
2025

UNIVERSIDADE FEDERAL DE SÃO CARLOS
CENTRO DE CIÊNCIAS EXATAS E DE TECNOLOGIA
PROGRAMA DE PÓS-GRADUAÇÃO EM CIÊNCIA E ENGENHARIA DE MATERIAIS

SOLIDIFICATION MICROSTRUCTURES, MECHANICAL AND WEAR PROPERTIES OF Al-Cu-Sn ALLOYS WITH VARIOUS COMPOSITIONS

Sarah Maria de Albuquerque Sousa

Tese apresentada ao Programa de Pós-Graduação em Ciência e Engenharia de Materiais como requisito parcial à obtenção do título de DOUTORA EM CIÊNCIA E ENGENHARIA DE MATERIAIS

Advisor: Dr. José Eduardo Spinelli
Co-advisor: Dr. Danielle Cristina Camilo Magalhães
Co-orientation advisor: Dr. Henri Nguyen-Thi
Co-orientation co-advisor: Dr. Guillaume Reinhart
Financing Agency: CNPq – Processo: 140498/2023-0, CAPES – Processo: 88887.823004/2023-00

São Carlos-SP
2025

UNIVERSIDADE FEDERAL DE SÃO CARLOS

Centro de Ciências Exatas e de Tecnologia
Programa de Pós-Graduação em Ciência e Engenharia de Materiais

Folha de Aprovação

Defesa de Tese de Doutorado da candidata Sarah Maria de Albuquerque Sousa, realizada em 02/12/2025.

Comissão Julgadora:

Prof. Dr. Reginaldo Teixeira Coelho (USP)

Prof. Dr. José Eduardo Spinelli (UFSCar)

Prof. Dr. Henri Nguyen-Thi (amU)

Prof. Dr. Guilherme Yuuki Koga (UFSCar)

Prof. Dr. Julien Zollinger (UL)

Profa. Dra. Myriam Dumont (ENSAM)

O Relatório de Defesa assinado pelos membros da Comissão Julgadora encontra-se arquivado junto ao Programa de Pós-Graduação em Ciência e Engenharia de Materiais.

ACKNOWLEDGMENTS

I would like to express my deep gratitude to my supervisors and co-supervisors, José E. Spinelli, Henri Nguyen-Thi, Danielle C. C. Magalhães, and Guillaume Reinhart, for assisting and guiding me through such a challenging task. I am thankful for all the knowledge shared and for being exemplary role models of dedicated researchers.

My sincere thanks to:

The Federal University of São Carlos, Graduate Program in Materials Science and Engineering.

CNPq – Conselho Nacional de Desenvolvimento Científico e Tecnológico, for the financial support provided for the completion of this work through a scholarship, process n° 140498/2023-0.

CAPES – Coordenação de Aperfeiçoamento de Pessoal de Nível Superior, for the financial support for carrying out this work through a scholarship, process n° 88887.823004/2023-00.

This study was financed in part by the Coordenação de Aperfeiçoamento de Pessoal de Nível Superior - Brasil (CAPES) - Finance Code 001.

Campus France, the French Embassy in Brazil, and the Institut Matériaux Microélectronique et Nanosciences de Provence (IM2NP – UMR CNRS 7334), for funding my research in France.

This thesis was carried out under a cotutelle agreement with the IM2NP laboratory, associated with Aix-Marseille Université (AMU). I would like to thank all the members of the Microstructures de Croissance Auto-organisées (MCA) team for their support during my stay in France, as well as my friends from the M2PS Laboratory at UFSCar (Guilherme, Jaderson, Rodrigo, Marcela, Mariana, Mila, Danusa, Felipe, Argos, Anderson T., Anderson D., Moises, Lorrany, and Denize) for their constant support and friendship throughout this journey.

Finally, I would like to express my gratitude to my family: my parents, José Francisco and Modina de Albuquerque Sousa, for always providing me with the tools, opportunities, and unconditional support to pursue my goals; my sister, Lara, whose perseverance and dedication inspired me to go beyond my own expectations; and my partner, Thiago Holanda, for his companionship, encouragement, and unwavering support throughout all these years.

RESUMO

MICROESTRUTURAS, PROPRIEDADES MECÂNICAS E DE DESGASTE DE LIGAS DE Al-Cu-Sn COM VÁRIAS COMPOSIÇÕES

Esta tese apresenta dois estudos complementares sobre ligas do sistema Al-Sn-Cu, que embora distintos em seus objetivos e abordagens, convergem para a compreensão dos mecanismos que controlam a formação microestrutural e o desempenho funcional desses materiais. No primeiro estudo, ligas modelo foram investigadas com o objetivo de aprofundar o entendimento dos fenômenos de separação da fase líquida e transformação monotética. No segundo, uma liga industrial autolubrificante (SAE 783) foi analisada visando correlacionar microestrutura, propriedades mecânicas e comportamento ao desgaste.

O sistema Al-Sn-Cu, com altos teores de Cu e Sn, apresenta elevada complexidade devido à separação da fase líquida. Nesse contexto, os caminhos de solidificação de três ligas Al-10Cu-xSn (x = 5, 10 e 20 % em massa) foram estudados por meio de uma abordagem integrada, combinando cálculos termodinâmicos pelo método CALPHAD, análises térmicas por DSC e observações *in-situ* por radiografia de raios-X. Os resultados demonstraram que o mecanismo de separação da fase líquida depende fortemente do teor de Sn: em ligas pobres em Sn, ocorre de forma progressiva, enquanto ligas ricas em Sn exibem um mecanismo de separação em duas etapas, não previsto pelos cálculos termodinâmicos.

A liga SAE 783 (Al-20%Sn-1%Cu) foi estudada sob condições de solidificação direcional transiente. A caracterização microestrutural incluiu a medição automatizada do espaçamento dendrítico, análises por microtomografia de raios-X e por MEV/EDS, permitindo avaliar a morfologia e a distribuição do Sn na matriz. Os resultados evidenciaram que a interface entre a fase β-Sn e a matriz α-Al é determinante para o aumento simultâneo da resistência mecânica e da ductilidade, além de exercer papel central no desempenho ao desgaste, contribuindo para uma melhor compreensão do compromisso entre propriedades mecânicas e resistência ao desgaste em ligas autolubrificantes à base de Al-Sn.

Palavras-chave: Solidificação; Al-Sn-Cu; Radiografia; Propriedades mecânicas; Desgaste

ABSTRACT

This thesis presents two complementary studies on alloys of the Al-Sn-Cu system which, although distinct in their objectives and approaches, converge toward a deeper understanding of the mechanisms governing microstructural formation and the functional performance of these materials. In the first study, model alloys were investigated to advance the fundamental understanding of liquid phase separation phenomena and monotectic transformation. In the second study, an industrial self-lubricating alloy (SAE 783) was analyzed with the aim of correlating microstructure with mechanical properties and wear behavior.

The Al-Sn-Cu system with high Cu and Sn contents exhibits pronounced complexity due to liquid phase separation during solidification. Within this context, the solidification paths of three Al-10Cu-xSn alloys (x = 5, 10, and 20wt.%) were examined using an integrated approach that combined thermodynamic calculations based on the CALPHAD method, thermal analysis by differential scanning calorimetry (DSC), and *in situ* observations by X-ray radiography. The results demonstrated that the mechanism of liquid phase separation strongly depends on the Sn content: in Sn-poor alloys, the process occurs progressively and culminates in a monotectic reaction, whereas Sn-rich alloys exhibit a two-step separation mechanism that is not predicted by thermodynamic calculations.

The SAE 783 alloy (Al-20wt.%Sn-1wt.%Cu) was studied under transient directional solidification conditions. Microstructural characterization included automated measurements of dendritic arm spacing, X-ray microtomography, and SEM/EDS analyses, enabling the evaluation of Sn morphology and distribution within the matrix. The results revealed that the interface between the β-Sn phase and the α-Al matrix is critical for the simultaneous enhancement of strength and ductility and plays a central role in wear performance, contributing to a better understanding of the trade-off between mechanical properties and wear resistance in Al-Sn based self-lubricating alloys.

Keywords: Solidification; Al-Sn-Cu; X-radiography; Mechanical properties; Wear

PUBLICATIONS

- S. De Albuquerque, G. Reinhart, D.C.C. Magalhães, J.E. Spinelli, H. Soltani, W. Boumechta, F. Bertelli, H. Nguyen-Thi, Solidification paths of Al-Cu-Sn alloys: Comparison of thermodynamic analyses and solidification experiments using *in situ* X-radiography, Mater. Today Commun. 40 (2024).

- S. De Albuquerque, G. Reinhart, H. Soltani, D.C.C. Magalhães, J.E. Spinelli, H. Nguyen-Thi, *In Situ* Observation by X-Ray Radioscopy of Liquid Decomposition During Directional Solidification of Al-Cu-Sn Alloys, Metals (Basel). 15 (2025).

- S. De Albuquerque, V. Leme, R. V Reyes, G. Reinhart, D.C.C. Magalhães, J.E. Spinelli, H. Nguyen-thi, Al-20Sn-1Cu self-lubricating alloy : Correlations between microstructure coarsening, mechanical, and application properties, Journal of Materials Research and Technology 36 (2025) 7284–7303.

CONTENTS

Page.

CHAPTER 1 - INTRODUCTION

This thesis is dedicated to the study of solidification phenomena, with a special emphasis on aluminum-based systems containing copper and tin. The motivation for this work stems from the crucial role that solidification microstructures play in determining the final properties of metallic materials. Characteristics such as mechanical strength, ductility, electrical conductivity, and wear resistance are intrinsically linked to the solidification path and the resulting morphology. Furthermore, the performance of alloys during subsequent processing steps, such as heat treatments, machining, and welding, is strongly influenced by their solidified microstructures [1]. Consequently, understanding and controlling microstructural evolution during solidification is essential both from a fundamental point of view and in terms of industrial applications.

This thesis was carried out as part of a joint doctoral program between the University of Aix-Marseille in France and the Federal University of São Carlos in Brazil, under a co-supervision agreement. The work was structured around two distinct lines of research, both involving fundamental and applied perspectives.

The first research axis, presented in Chapter 2, was developed in France at the IM2NP institute (Institut Matériaux Microélectronique Nanosciences de Provence). It was focused on the solidification of model alloys of the Al-10Cu-xSn system (with x = 5, 10, and 20wt.%), motivated by research into the solidification path in immiscible systems. A combination of thermodynamic calculations, thermal analyses, and *in-situ* experimental techniques was employed. Thermodynamic calculations based on the CALPHAD method provided predictions of solidification sequences and critical transformations. Differential scanning calorimetry (DSC) experiments provided experimental confirmation of phase transition during heating and cooling cycles. Most importantly, directional solidification experiments were performed using real-time X-ray radiography, a powerful technique capable of directly monitoring microstructural evolution throughout the process. This methodology allowed for a detailed investigation of monotectic reaction and liquid phase separation, phenomena of central importance in immiscible systems. Distinct behaviors were observed as a function of Sn content, offering new insights into the kinetics of liquid phase separation.

The second axis of research, presented in Chapter 3, was developed in Brazil at the M2PS (Microestruturas e Propriedades em Processos de Solidificação) laboratory. It was dedicated to the study of an industrially relevant material, the SAE 783 alloy (Al-20%Sn-1%Cu, % by weight), commonly used in plain bearings due to its self-lubricating properties. As part of the work carried out in Brazil, directional solidification experiments were performed under transient heat extraction conditions, generating a microstructural range. The resulting microstructures were analyzed in relation to the spacing of the dendritic arms and the morphology of Sn. These characteristics were subsequently correlated with the mechanical properties, determined by hardness and tensile tests, and with the tribological behavior, evaluated by wear experiments. The results demonstrated a complex interaction between the microstructural scale and performance: microstructural refinement was found to simultaneously improve tensile strength and ductility, while coarser microstructures provided superior wear resistance. This duality highlights the importance of adapting the solidification parameters to the intended service conditions of the alloy. Thanks to a combination of X-ray microtomography (XCT) analysis, and mechanical and wear tests, it was found that the strength and wear responses can be attributed to the morphology, fraction, and distribution of the β-Sn phase.

By integrating fundamental and applied approaches, this study contributes both to advancing scientific understanding of solidification phenomena in immiscible alloys and providing guidelines for optimizing self-lubricating materials used in demanding industrial contexts.

CHAPTER 2 – APPLICATION OF IN-SITU AND REAL-TIME X-RAY RADIOGRAPHY TO INVESTIGATE DIRECTIONAL SOLIDIFICATION OF AL-SN-CU ALLOYS

2.1 Introduction

The increasing importance of Al-Sn-Cu alloys for producing self-lubricating bearing materials in automotive industries requires the development of uniform microstructures with improved performance.

In this context, as-cast microstructures play a crucial role in defining the performance and processability of metallic alloys. They influence not only mechanical strength, ductility and electrical conductivity of the final product, but also govern the responses of the material to downstream processing steps such as heat treatment, machining and welding. For all these reasons, understanding the evolution of microstructures during solidification is essential for tailoring the properties of metallic alloys [1–3]. Among the key features that influence the final material properties is the morphology of the solid/liquid interface, which is strongly governed by thermal conditions such as the temperature gradient as well as the interface growth rate. These solidification variables play a decisive role in determining whether the solid/liquid interface remains planar or evolves into more complex cellular or dendritic structures [4].

In multicomponent alloy systems such as Al-Sn-Cu, the complexity of solidification increases dramatically due to phase transformations that occur beyond primary dendritic solidification. One particularly notable phenomenon is liquid phase separation, where immiscibility between the alloy components leads to the coexistence of two different liquids. Closely tied to this is the occurrence of the monotectic reaction, which contributes further to the complexity of resulting microstructure and so demands careful analysis [5].

Accordingly, this chapter explores the interplay between solidification conditions and interface morphology, the conditions that lead to liquid phase separation, and the characteristics of the monotectic reaction. The discussion follows the

solidification path for Al-Sn-Cu alloys; from controlled growth of primary dendrites, through the onset of liquid phase separation, to the monotectic reaction.

It is important to consider that solidification is an inherently dynamic process that evolves continuously over time. Although post-mortem analysis techniques, such as quenching during directional solidification [6,7] have significantly contributed to the understanding of the phenomenon, they are not able to capture the full sequence of events as they developed. This limitation becomes especially critical in the study of monotectic alloys, where inherent features are the liquid phase separation and the complex interaction between liquid droplets and the solidification front [8,9], which cannot be faithfully inferred from the final solidified structure alone.

Therefore, X-ray radiography has emerged as a powerful tool for the investigation of solidification, offering real-time and *in-situ* visualization of microstructures formation during the process. This technique relies on the different attenuation of X-rays as they pass through optically opaque materials, producing contrast that reflects local variation in density and composition [10–12]. While the development of highly brilliant synchrotron X-ray sources has dramatically enhanced the capabilities of radiographic techniques, the recent improvements of compact micro-focus X-ray source and sensitive detectors have opened new possibilities for laboratory-scale devices, allowing time-resolved and *in-situ* radiography with sufficient spatial and temporal resolution to resolve the evolving microstructures during aluminum alloy solidification [13,14].

Within the framework of this PhD, the main objective was to deepen the understanding of the solidification paths of Al-10wt.%Cu-x wt.% Sn (with x=0; 5; 10 and 20) alloys. These compositions were selected to assess the influence of Sn content on the Al-10wt.%Cu alloy, which has been previously studied in detail [15]. The high Cu content was maintained because it improves the quality of radiographs by generating high contrast between the growing solid and the surrounding liquid phase during solidification and promotes liquid phase separation in the Al-Sn system [5]. The alloys were produced by upward directional solidification in a study conducted by Bertelli *et al.* [16] and were donated for the development of the present research.

To attain this objective, their solidification paths were investigated by different complementary approaches. Firstly, the solidification paths were calculated by the

CALPHAD method. Secondly, experimental thermodynamic analyses were carried out by DSC (Differential Scanning Calorimetry) and thirdly, all alloys were directionally solidified and *in-situ* and real-time observation were achieved by using X-ray radiography.

2.2 Literature review

2.2.1 Solidification of dilute binary alloys

2.2.1.1 Non-faceted and faceted solid/liquid interface

Solidification is a phase transformation in which a material in a liquid state turns into solid when cooled below its freezing point, under constant pressure. For crystals bulks, this process is characterized by the transition from highly mobile atomic state in liquid phase to an organized atomic state in solid phase, with periodic structure and low mobility. Solidification occurs due to a search for a condition of lower Gibbs free energy in the system and can occurs either isothermally in the case of pure materials, or over a temperature range between the *liquidus* temperature (T_L) above which the material is completely liquid, and the *solidus* temperature (T_S), below which the material is completely solid, in the case of alloys. Solidification begins with the formation of a stable solid nucleus, and its growth depends on how easily atoms attach to the advancing solid-liquid interface. Due to the difference of atom distribution in solid and liquid phases, there is an increasing disorder across the interface and, in thermodynamic terms, both enthalpy (heat content) and entropy (degree of disorder) change across the interface. When the solid and liquid are in equilibrium, at the melting temperature (T_M), both phases have the same free energy. However, at the solidifying interface, the balance is slightly disturbed and the system naturally selects the structure that minimizes the system Gibbs free energy [4,17].

There are two possible types of atomic arrangement at the solid/liquid interface. One has a rough nature when the transition takes place over a several atomic layers. The other is an atomically flat close-packed interface, or faceted, where the transition from the liquid to solid happens over a very organized thin layer, about few atoms thick [17].

The most favorable atomic arrangement can be more or less predicted by using a parameter called the Jackson alpha factor (α), written in Equation 2..

$$\alpha = \frac{\eta}{Z}\frac{L}{k_B T_M} \qquad \textit{Equation 2.1}$$

Where, η is the number of nearest neighbor sites adjacent to an atom in the plane of the interface, *Z* the total number of nearest neighbors of an atom in the crystal, *L* the latent heat of fusion, k_B the Boltzmann's constant, and T_M the melting point of the material.

When α is less than 2, the surface tends to be rough, like in Figure 2.1(a), which is typical for most metals. On the other hand, materials like many semi-conductors (silicon, bismuth), minerals, some intermetallic compounds, and organic crystals (salol) tend to have higher α values, resulting in faceted interfaces, like in Figure 2.1(b) [18]. Experiments show that the free energy of rough interfaces does not change significantly with respect to the crystal orientation, whereas materials with faceted interfaces are strongly affected by crystallography and tend to grow with well defined, low-index facets [17].

(a)  (b) 

Figure 2.1: Examples of solid growth interfaces in transparent metal analog. (a) The crystal is growing dendritically. (b) The benzyl crystal is growing with well-developed facets at the solid-liquid interface [18].

2.2.1.2 Phase diagram for dilute binary alloy

Most metallic materials with industrial applications are alloys, which adds complexity to the description of the solidification step. In general, the solubility of solute in alloys differs between the liquid and the solid phases. This behavior is characterized by the solute partition coefficient (k), defined as the ratio between the solute concentration in the solid (C_S) and in the liquid (C_L) phases, at the solid/liquid interface (Equation 2.2).

$$k = \frac{C_S}{C_L} \qquad \textbf{\textit{Equation 2.2}}$$

By approximating the *liquidus* and *solidus* lines as straight segments in the phase diagram, this coefficient is assumed constant, as illustrated in Figure 2.2. This configuration is often used for its simplicity in theoretical models or numerical simulations. When the solute is less soluble in the solid than in the liquid, as the case in Figure 2.2, k is less than 1 and m_L is negative, which is the most common case. In the remainder of the manuscript, we will consider the case $k < 1$ and m_L negative, unless otherwise specified.

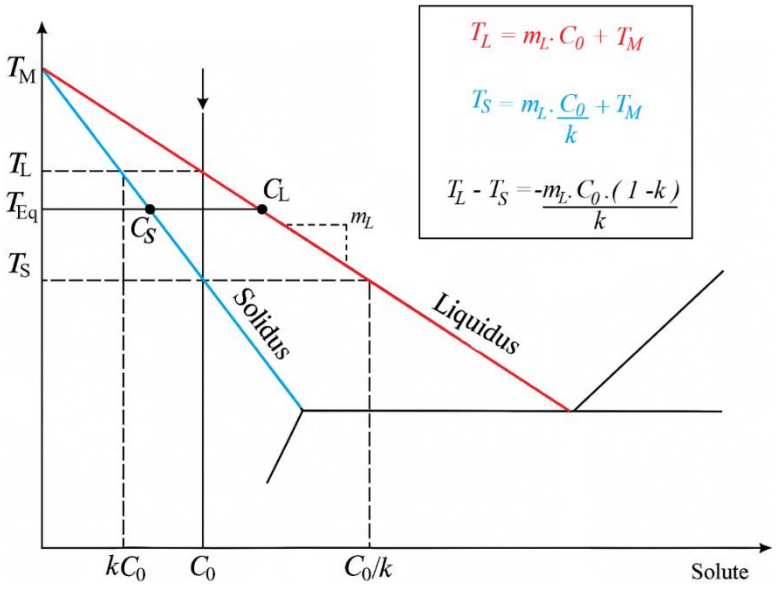

Figure 2.2: Schematic representation of a binary phase diagram for $k < 1$ and the linear equations that characterize the *liquidus* line and the *solidus* line. (T_M: Melting temperature of the pure solvent, T_L: *liquidus* temperature, T_{Eq}: equilibrium temperature, T_S: so*lidus* temperature, C_0 nominal concentration). Adapted from [17].

2.2.1.3 Morphological solid/liquid interface instability

In a first step we will consider the cooling of a liquid with a nominal composition C_0, in a constant temperature gradient G, which is moved at a constant pulling velocity V. This type of conditions corresponds to a typical experiment of directional solidification of a binary alloy. When the melt temperature reaches the *liquidus* line at T = T_L, the first solid to form will have a lower solute concentration than the nominal composition, equal to kC_0.

As solidification proceeds, the composition of the formed solid increases gradually up to C_0 at the *solidus* temperature. Meanwhile, the composition of the liquid in contact with the solid/liquid interface increases from C_0 to C_0/k, due to the continuous solute rejection at the solid/liquid interface (Figure 2.2). During this initial transient, a solute-enriched boundary layer develops ahead of the solid/liquid interface and eventually reaches a stationary profile. In diffusive conditions, the stationary concentration profile exponentially decreases with distance z into the liquid, as written in Equation 2.3 and drawn in Figure 2.3(a).

The characteristic length of the solute exponential profile is given by $l_S = D/V$, with D the solute diffusivity coefficient in the liquid and V the growth rate.

$$C_L(z) = C_0\left[1 + \left(\frac{1-k}{k}\right) exp\left(-\frac{V}{D_L}z\right)\right] \qquad \textbf{\textit{Equation 2.3}}$$

As a result of the varying solute concentration in the liquid ahead of the solidification front, there is a corresponding variation of the local equilibrium temperature (i.e., the *liquidus* temperature T_L), which decreases with increasing solute content, as written in Equation 2.4 and drawn in Figure 2.3(b).

$$T_L(z) = T_M + m_L C_L(z) = T_L + m_L(C_L(z) - C_0) \qquad \textbf{\textit{Equation 2.4}}$$

In Figure 2.3, two different cases are represented:

- If $T_R(z) = T_M + m_L C_0/k + G.z$, the real temperature of the liquid ahead of the interface, lies above the *liquidus* temperature profile T_L, the liquid ahead of the solid/liquid interface is thermodynamically stable. It is thus assumed that the planar solid/liquid interface is also stable and then remains planar [1,17].
- In contrast, if T_R, the real temperature of the liquid ahead of the interface, lies under the *liquidus* temperature profile, as illustrated by T_R (straight line in black) and T_L (red curve) in Figure 2.3(b), the liquid ahead of the solid/liquid interface is thermodynamically undercooled (region with red dots). The planar solid/liquid interface is then unstable and will destabilize. As the undercooling is driven by constitutional effects, it is known as constitutional undercooling.

The existence of this undercooled liquid ahead of the solid/liquid interface depends on the values of the temperature gradients of the real temperature and the *liquidus* temperature at the interface. Therefore, there is a critical temperature gradient for the liquid above which the planar solidification interface remains stable [1,17].

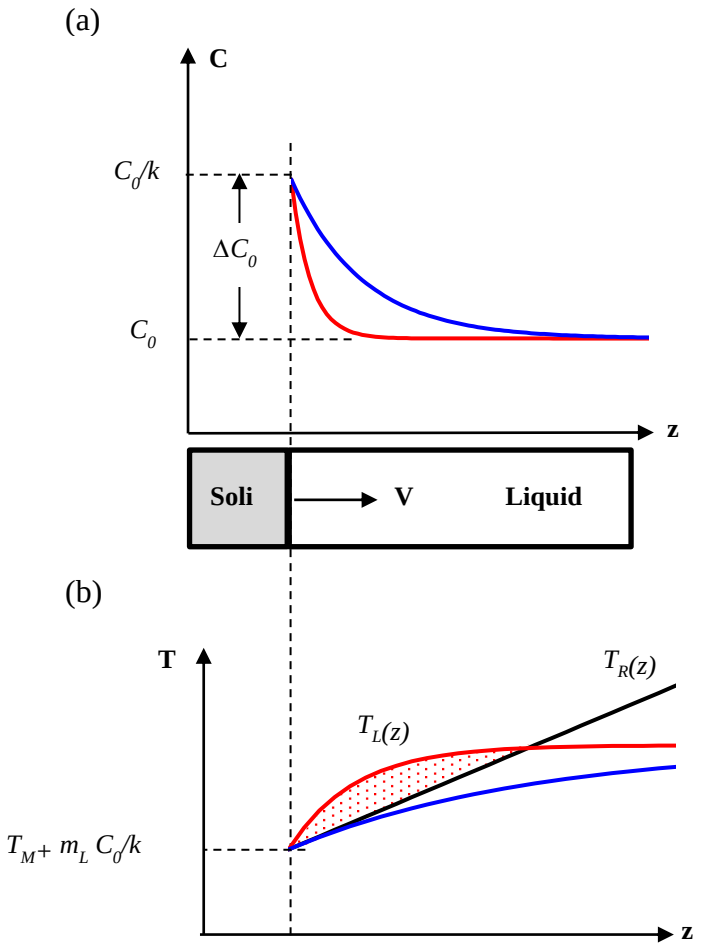

Figure 2.3: Origin of constitutional undercooling ahead of a planar solidification front. (a) Solute concentration profile in the liquid for a steady state solidification ($V < V_c$, blue graph) and unsteady state solidification ($V > V_c$, red graph) of a binary alloy with z the distance from the interface. (b) Temperature of the liquid ahead of the solidification front follows line T_R. Constitutional supercooling arises when T_R lies under the *liquidus* temperature T_L (red curve).

Mathematically, the planar solidification interface stability condition can be obtained by comparing the temperature gradients of the two curves at the origin:

$$\left(\frac{dT_R}{dx}\right)_{x=0} \geq \left(\frac{dT_L}{dx}\right)_{x=0} \qquad \textit{Equation 2.5}$$

Assuming a steady state with no diffusion in the solid and only diffusion-driven mixing in the liquid (no convection in the liquid phase), the criterion for avoiding constitutional undercooling can be written as [1]:

$$V < \frac{GDk}{m_L C_0 (k-1)} \qquad \textbf{\textit{Equation 2.6}}$$

Where, m_L is the slope of the *liquidus* line, V is the solidification front velocity and D is the solute diffusivity in the liquid. From this relation, it is possible to identify key factors that reduce the right-hand side of the inequality term (the critical velocity V_C) and therefore promote constitutional undercooling [1]:

- For experimental parameters: low thermal gradient G in the liquid, and high solid/liquid interface velocity V.
- For the alloy phase diagram: high solute concentration C_0, large *liquidus* slope m_L, and low partition coefficient k.
- Alloy property: low solute diffusivity D.

If Equation 2.6 is not satisfied, the planar solid/liquid interface is said unstable, which means that any small fluctuations (bumps or protrusions) will be amplified rather than smothered out. Physically, the primary instability of the planar front results from a "point effect". If we assume that the planar front presents a minor perturbation by an outgrowth (Figure 2.4(b)), the isothermal lines will be locally tightened, increasing the concentration gradient locally. At this point, the solute flux will be more important, favoring the growth of the protuberance as drawn in Figure 2.4(c and d). The perturbation at this point will be amplified. The temperature gradient, for its part, opposes this growth and tries to melt back the bump.

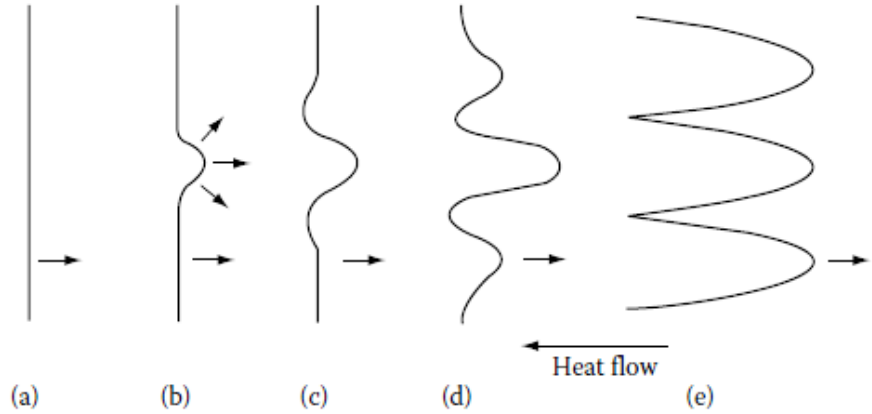

Figure 2.4: The breakdown of an initially planar solidification front into cells [6].

Rough interfaces, typical of metals, are especially prone to such morphological instabilities, particularity under strong solute gradients or undercooling. In contrast, faceted interfaces, are more resistant to such instabilities due to their crystallographic constraints. In essence, once constitutionally undercooling sets stage, interface perturbations are not only inevitable but also evolve rapidly under favorable conditions. This phenomenon shapes the final microstructure of solidified materials [1,4,17].

2.2.1.4 Solidification microstructures: cells and dendrites

The cellular morphology is characterized by solute being rejected both ahead and to the sides of the interface, resulting in a higher solute concentration along the cell walls than at the center. In addition, the solidification of each protuberance releases latent heat at the interface, which locally reduces undercooling and delays the formation of new protrusions in neighboring regions. As a result, an alternative pattern of projections is established, as illustrated in Figure 2.5(a). However, cellular structures are only stable within a limited range of solidification conditions. If the growth velocity is increased, the solid/liquid interface becomes more unstable and a change of the interface morphology is required to maintain balance. In that case, the cells evolve into dendrites, which are characterized by secondary arms and growth directions governed by crystallographic preferences (Figure 2.5(b)). Figure 2.5 illustrates the morphological differences between the smooth cells and the branches dendrites [1,17].

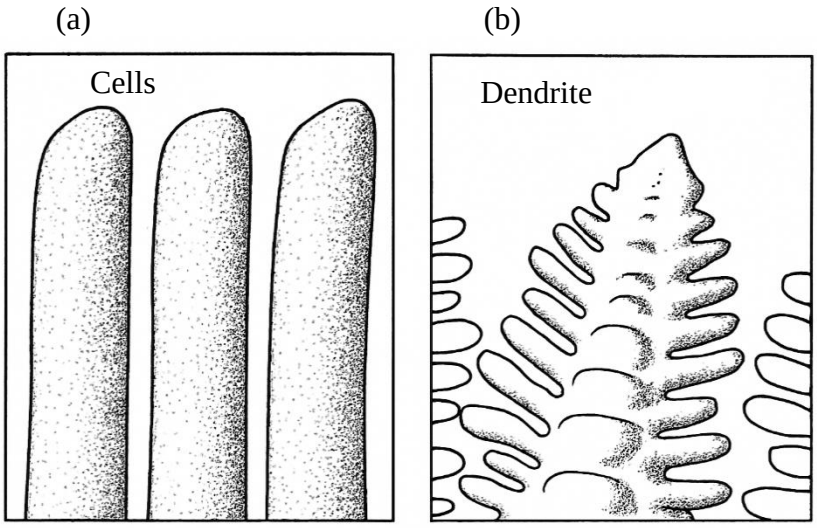

Figure 2.5: Illustrations of typical (a) cellular and (b) dendritic morphology [4].

Dendritic growth is the most commonly encountered microstructure in casting. In ingot solidification, heat extraction occurs in the opposite direction of dendrite growth. Thus, dendrites grow perpendicular to the mold wall toward the thermal gradient at a speed controlled by the rate of advance of the isotherms. In equiaxial solidification, heat dissipates from the crystal to the liquid in all directions and growth occurs freely, normally at the center of the melt and is limited only by the available undercooling. Dendrites grow radially, and their tips stop advancing once they encounter the diffusion fields of neighboring branches. At this point, they begin to coarsen and thicken [4,17].

In directional growth, dendrites are mostly aligned along the temperature gradient direction, and several characteristic dendrite spacings can be identified: primary spacing between the mean trunks, and secondary or tertiary spacings between the secondary or tertiary breaches, respectively. The quantification of this parameters is imperative since they directly influence the mechanical and functional properties of the alloys [19–22]. Several theoretical models of dendritic growth have been developed to describe the evolution of the spacings. These include the models by Hunt, 1979, Kurz and Fisher, 1981, Feurer, 1977, and e Kirkaldy, 1995, among others [1]. Nevertheless, experimental data remain essential for validating and adjusting these predictions [23,24].

2.2.1.5 Solidification microstrucutre selection map

As previously discussed, the stability of a planar solidification front for a binary alloy of composition C_0 depends on both the thermal gradient G and the interface velocity V. Typically, these parameters cannot be controlled independently throughout most of the solidification process, as they are inherently linked to the rate at which heat is extracted from the solidifying alloy, accordingly to the relationship $R = G.V$. However, when the interaction between G and V is well understood, it becomes possible to tailor the resulting microstructure to achieve improved or even optimal properties [25].

Kurz and Fisher [4] summarize this in a graph (Figure 2.6), which illustrates how the morphologies of the solid-liquid interface vary depending on the balance between G and V. In this diagram:

- The downward-sloping lines at a -45° angle represent conditions where the cooling rate ($R = G.V$) remains constant and the microstructure becomes finer as the cooling rate increases. This demonstrates that the cooling rate magnitude is directly proportional to the degree of refinement, even when morphology remains the same.
- On the other hand, the upward-slopping gray bands at 45° angle correspond to constant values of the G/V ratio. When this ratio remains constant, the type of microstructure tends to stay the same. As the G/V ratio decreases, the interface becomes progressively more unstable, leading to a sequence of morphologies (from top to bottom): dendritic structure, then cellular and finally by planar front (when the velocity is below the critical value).
- In casting, characteristics generally change according to the indicated right-to-left arrow.
- In directional solidification experiments, the temperature gradient is constant so that solid/liquid interface morphologies change according to indicated the straight line.

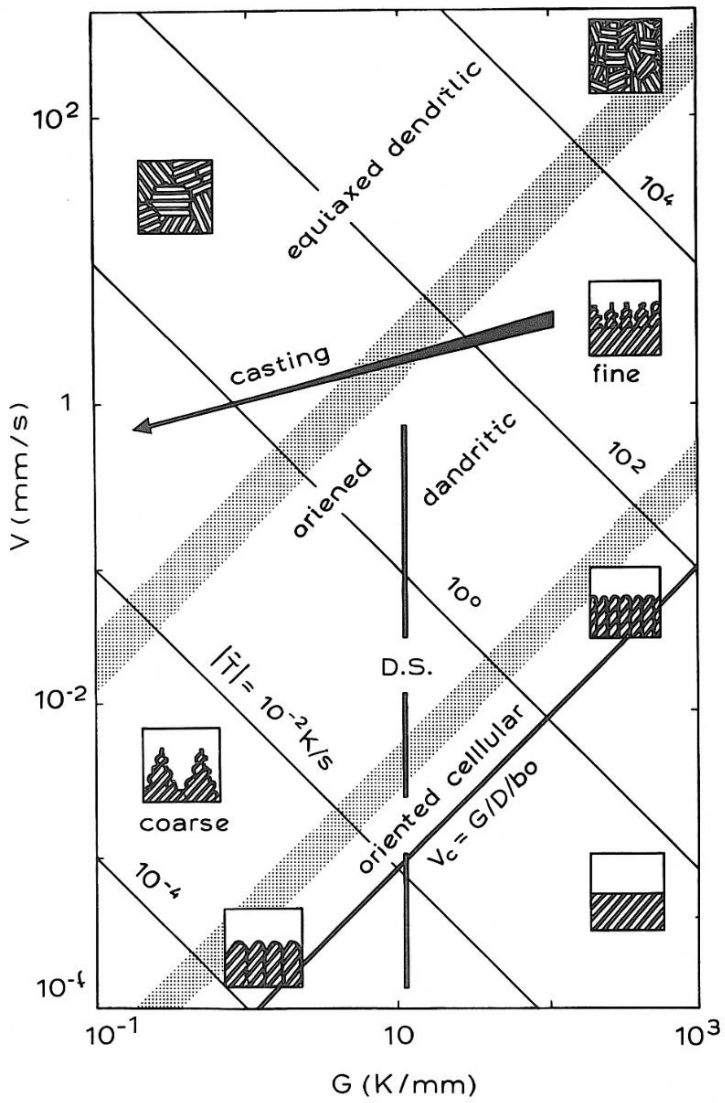

Figure 2.6: Qualitative correlations between solidification thermal parameters, microstructural refinement and interface morphologies for a generic alloy [4].

2.2.2 A more complex solidification case: the monotectic solidification

2.2.2.1 Phase diagram with a monotectic reaction

The phase diagram is a crucial part of metallurgy as it shows the equilibrium states of a mixture, so that it is possible to calculate which phases will be formed, and in what quantities at any given temperature and composition. In the previous section, some important generalities about the directional solidification of ideal dilute binary alloys have been described. In that case, the phase diagram is only limited to two straight lines (*solidus* and *liquidus*). However, much more complex types of binary phase diagrams

exist, with the existence of eutectic, peritectic, and monotectic among others. For instance:

- An eutectic reaction is a three-phase reaction, by which, on cooling, a liquid is transformed into two solid phases at the same time [26]. The eutectic reaction is:

$$\text{Liquid} \rightarrow \text{solid-}\alpha + \text{solid-}\beta$$

- A peritectic reaction is a three-phase reaction by which, on cooling, two phases (one of them liquid) react to give a single new solid phase [27]. The peritectic reaction is:

$$\text{Liquid} + \text{solid-}\alpha \rightarrow \text{solid-}\beta$$

- A monotectic reaction is a phase transition from one liquid phase to another liquid phase and solid phase [28]. The monotectic reaction is:

$$L_1 \rightarrow \text{solid-}\alpha + L_2$$

The phase diagram shown in Figure 2.7 gives the terminology for this type of system: monotectic point, monotectic reaction isotherm, hypo-monotectic, and hyper-monotectic. The phase diagram shows a dome-shaped region within which the two liquids coexist. The maximum temperature of this dome, *Tc*, is called the critical temperature.

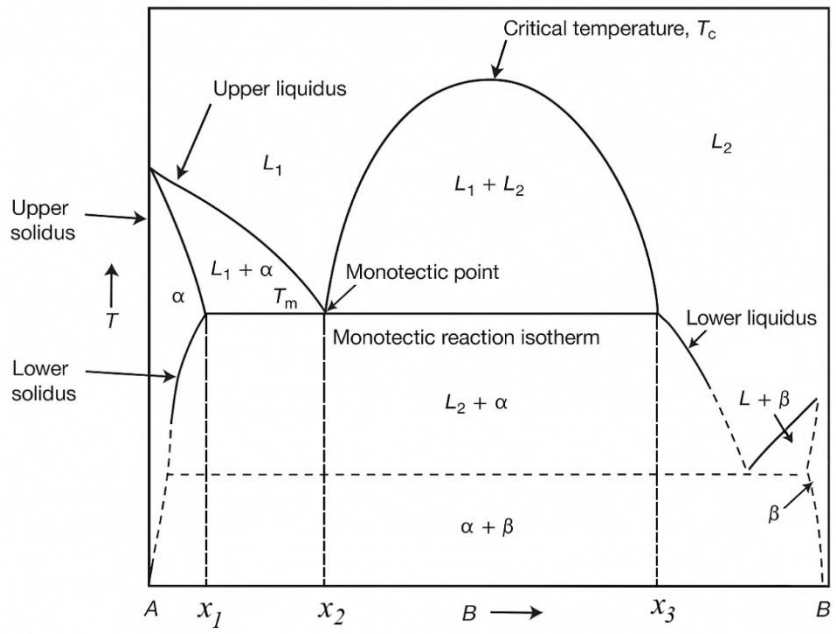

Figure 2.7: Phase diagram showing the monotectic point at concentration x_2, the monotectic isotherm (from x_1, to x_3) and the miscibility gap [28]**.**

2.2.2.2 Monotectic reaction

As mentioned above, monotectic reactions are a distinct class of invariant phase transformation. Phase diagrams that exhibit this type of reaction are characterized by a horizontal line indicating the monotectic temperature, along with a dome-shaped region where the two immiscible liquid phases coexist. Figure 2.7 illustrates a schematic binary phase diagram of such a monotectic system.

Alloys with exact monotectic composition solidify at the monotectic temperature by decomposition into a solid and a liquid phase. Alloys with hyper-monotectic composition have to pass the liquid miscibility gap and thus a large region ahead of the monotectic reaction front is thermodynamically in a two-phase liquid state. In this section, some key elements will be presented about a phase diagram with a liquid miscibility gap, which is the case for the Al-Sn-Cu alloys that will be studied in the framework of this PhD. The solidification of alloys with a liquid miscibility gap, often called hyper-monotectic alloys, remains puzzling since decades especially compared to eutectic solidification to which they seem very similar.

Above the critical temperature *Tc*, both components are miscible with each other for any composition. The x_2 is the monotectic point, with hypo-monotectic compositions

to its left, between x_1 and x_2, and hyper-monotectic compositions to its right, between x_2 and x_3. Inside the dome, there is a liquid miscibility gap, as discussed previously, where the original liquid separates into two liquids, L_1 and L_2, where the L_2 is rich in B and L_1 is rich in A. When the temperature decreases and reaches the isotherm T_m, the liquid L_1 becomes unstable and undergoes the monotectic reaction, which is described by $L_1 \rightarrow L_2 + \alpha$. For this example, continued cooling will cause L_2 to solidify into β phase through the eutectic reaction on the dashed line, described as $L_2 \rightarrow \alpha + \beta$ [28,29].

As Garcia [1] has observed, the majority of monotectic phase diagrams indicate that a greater quantity of solid phase than liquid is produced in the reaction. This observation suggests that, in the majority of these systems, the microstructure consists of a continuous matrix, with the immiscible secondary phase distributed in isolation within it. For this reason, monotectic reactions have attracted considerable attention in recent decades, as they bring the possibility of combining phases with different characteristics in a same material [9,30–32]. However, despite their promising range of applications, monotectic alloys present significant challenges in controlling the microstructure network.

For instance, near the monotectic temperature, during the cooling, the liquid adjacent to the solid/liquid interface is enriched by solute rejection and becomes super-saturated compared to the parent liquid (L_1). In order to relieve this saturation, droplets of L_2 nucleate, simultaneously with the growth of the solid (α). Nevertheless, the nucleation site and the interaction between the liquids and the solid are governed by the relative magnitudes of interfacial surface tensions. Garcia [1] and Chadwick [33] describe the three possible interactions between the phases as follow:

- If the interfacial energies satisfy the condition $\gamma_{\alpha/L2} > \gamma_{\alpha/L1} + \gamma_{L1/L2}$, then the L_2 phase will not nucleate at the solid/liquid interface. Instead, L_2 droplets will form as isolated droplets in the middle of L_1 liquid, where it will be free to move in the melt according to its density and the moving solid/liquid interface. This is illustrated in Figure 2.8(a).
- Alternatively, if the interfacial tension satisfies $\gamma_{\alpha/L2} = \gamma_{\alpha/L1} - \gamma_{L1/L2}\cos\theta$, where θ is the wetting angle and varies between 0° and 180°, as in Figure 2.8(b), L_2 nucleates at the solid interface, can grow under steady-state conditions,

similar to eutectic solidification, and may be trapped in the solid in the form of fibers.

- Finally, if the resulting surface tension is given by $\gamma_{\alpha/L1} > \gamma_{\alpha/L2} + \gamma_{L1/L2}$, the L_2 droplet may solidify and spread entirely across the solid substrate, as depicted Figure 2.8(c).

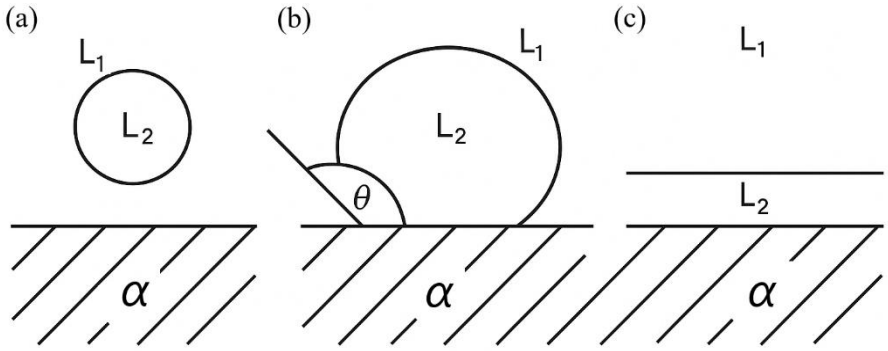

Figure 2.8: Solid-liquid interface morphologies for different interfacial energy conditions: (a) $\gamma\alpha/L_2 > \gamma\alpha/L_1 + \gamma L_1/L_2$, b) $\gamma\alpha/L_2 = \gamma\alpha/L_1 - \gamma L_1/L_2 \cos\theta$, c) $\gamma\alpha/L_1 > \gamma\alpha/L_2 + \gamma L_1/L_2$ [23] modified.

As examples, Bi often exhibits a granular morphology dispersed throughout the Al matrix, reflecting the high surface tension between these elements [22], suggesting that it follows the Figure 2.8(a) case. In contrast, Sn is typically observed with a retiform morphology [34], which indicates a slightly lower surface tension and the potential for nucleation to occur in the Al substrate, resembling Figure 2.8(c). It is clear, however, that these are not fixed conditions depending only upon the material. The final microstructure of L_2 may change as a function of temperature gradient ahead of the solidification front and the solidification velocity [35] or changes in the alloy composition [36].

2.2.2.3 Liquid phase separation

Liquid phase separation, which occurs inside the miscibility gap, is an intrinsic characteristic of hyper-monotectic alloys that can be expressed in terms of Gibbs free energy. The free energy is a thermodynamic potential that measures the feasibility of the reactions occurring at given temperature and pressure. In any spontaneous reaction,

there is a decrease in the free energy of the system. In the case of alloys, the change takes into account the Gibbs free energy of the pure elements and the change due to the mixing of them, called the Gibbs free energy of mixture ΔG_{mix}, which, for a given temperature *T*, is given by Equation 2.7 [17,28,29].

$$\Delta G_{mix} = \Delta H_{mix} - T.\Delta S_{mix} \qquad \textbf{\textit{Equation 2.7}}$$

Where ΔH_{mix} is the enthalpy of the mixture and represents the difference in internal energy before and after mixing. Its sign is really important in determining the concavity of the Gibbs free energy curve and thus the stability of the phases, as the ΔS_{mix}, which is the entropy of the mixture and is the difference in entropy after mixing, is always positive [17,29,37].

Immiscible alloys are generally characterized by a positive ΔH_{mix}, which means that for a sufficiently low temperature, the Gibbs free energy versus composition curve has a shape as shown in Figure 2.9(a), with negative curvature and increasing free energy value according to the mixture of elements [9]. As a result, the system forms two immiscible liquid phases for minimizing its total energy from G_0 to G_1, corresponding to the points ‘a’ and ‘b’ in Figure 2.9(a).

Additional characteristic features are the binodal and spinodal curves shown in Figure 2.9(b), which represent different levels of instability in such an immiscible system, these curves are derived from the Gibbs free energy as function of composition graph. The binodal curve defines the miscibility gap, which is the limit where two distinct phases can coexist, varying between ‘a’ and ‘b’ in Figure 2.9(a). On the other hand, the spinodal curve marks the region where the mixture becomes unstable and is linked to the inflexion in the Gibbs free energy curve: it is defined by the points where the second derivative of the Gibbs free energy is equal to zero with respect to composition [9,29].

The liquid outside the miscibility gap is stable, forming a homogeneous solution and is limited by a critical temperature, T_C. Within the spinodal line, the liquid becomes thermodynamically unstable because even very small variation in composition, as slight increases in A-rich or B-rich regions, lead to a spontaneous decrease in free energy, driving the system to separate into two phases without any energy barrier. This is called the liquid-state spinodal decomposition [9,38,39]. The region between the binodal and

spinodal lines is metastable. In this zone, the liquid is stable against infinitesimal compositions changes, but larger fluctuations, on the other hand, may lead to a phase separation into two liquids by nucleation and growth. Therefore, it requires the system to overcome an energy barrier [9,29].

In general, liquid phase separation begins with droplets of the minority phase. This is followed by spatial separation. Then, the droplets can grow by diffusion or coalescence, and can either settle or rise due to the difference in density between the two liquids under the action of gravity (Stokes motion) and temperature or concentration gradient (Marangoni effect) [40–42]. This liquid demixing can have significant effects on the final microstructure of the solidified material [43,44]. Upon cooling, the spatial separation of the two liquids may lead to macrosegregation, complex morphologies, and heterogenous properties. This phenomenon can be detrimental to certain applications; however, in some specific cases, as in bearing alloys [31,36,45] or natural composites [32,40] this behavior can be intentionally used to tailor certain desirable features. This aspect has led to its extensive research.

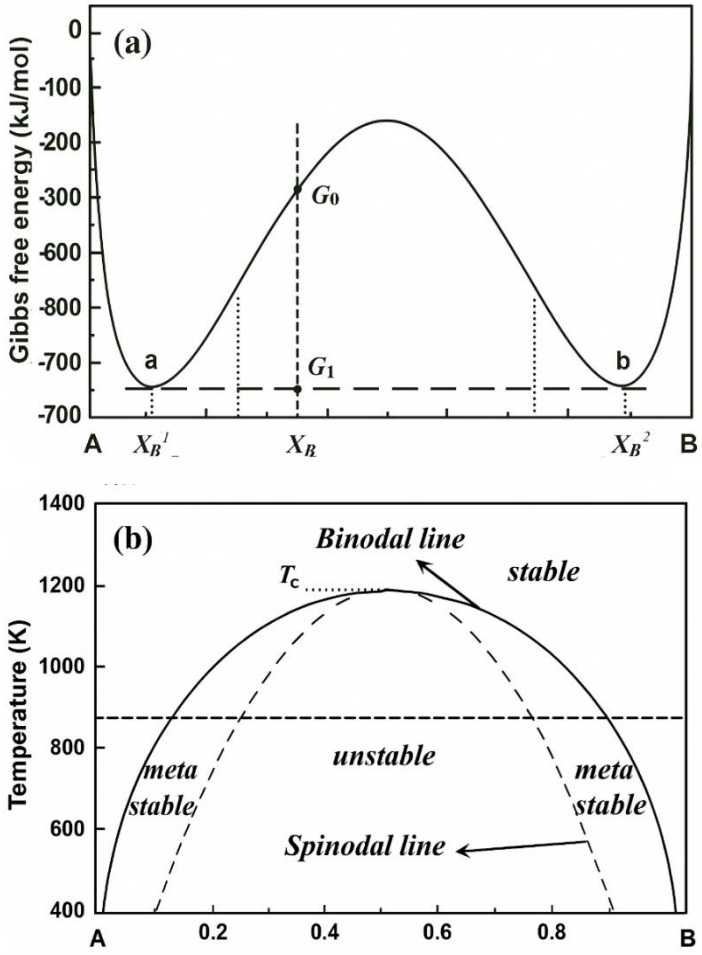

Figure 2.9: (a) Gibbs free energy variation as a function of composition for a generic immiscible alloy. (b) Phase diagram showing the miscibility gap and the spinodal line in a regular solution system [9].

Numerous studies have been conducted to explore microstructural evolution in immiscible alloys using the phase-field method [9]. These models enable the simulation of phase morphologies and their evolution over time, accounting for composition variation, fluid motion, and phase interactions. For instance, Nestler *et al.* [46] introduced two phase-field models designed to describe the solidification behavior of a generic immiscible alloy. The numerical simulations demonstrated that the proposed models effectively capture the key features such as droplets coarsening and the interaction with the monotectic front. However, the models present certain limitation, particularly its applicability being confined to a narrow temperature range near the monotectic temperature.

Further contributions were made by Wang *et al*. [47] and Oliveira *et al.* [38], who developed phase-field models to investigate liquid phase separation withing the miscibility gap of real alloy system, such as Fe-Sn and Bi-Zn, respectively. Their simulations revealed that the phase separation process evolves continuously, with specific decompositions patterns depending on composition and temperature.

Oliveira *et al.* [38] conducted a phase-field simulation to investigate the liquid demixing withing the miscibility gap of the Bi-Zn system across a range of temperatures and for two distinct compositions. Their studies revealed a variety of equilibrium microstructures depending on the specific location withing the Bi-Zn phase diagram, as shown in Figure 2.10. The model proposed by the authors indicated that the resulting microstructure is highly sensitive to both temperature and alloy composition. Specifically, when the Zn content deviates from the critical composition (horizontal dashed line). Furthermore, the morphological analysis with respect to temperature indicated that this interconnected network of the minority phase gradually transforms into a droplets-like, spherical morphology, as the temperature approaches the upper boundary of the miscibility gap (vertical dashed line).

Although these models provide valuable insights, they also present significant limitations typical of simulations studies and must be validated through comparison with experimental data. Furthermore, there is a need to extend these understandings to more complex systems, such as ternary alloys, and to scenarios where the liquid phase separation occurs within a primary solid phase.

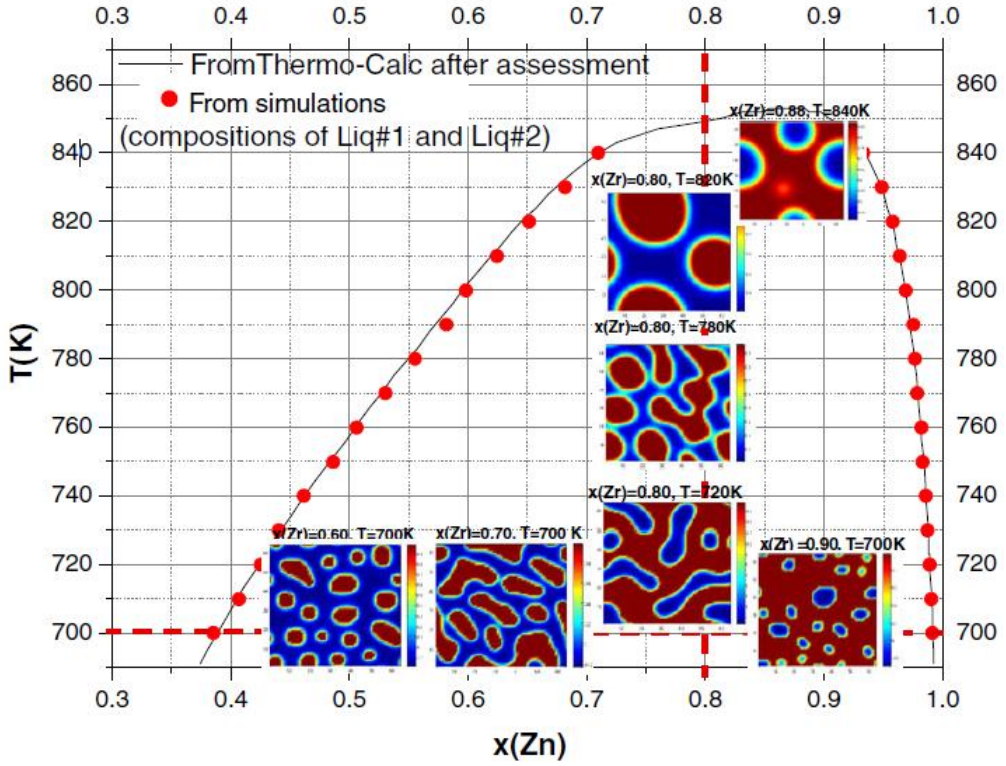

Figure 2.10: Miscibility gap occurring in the liquid region of Bi–Zn system. Simulation pictures present the variations of the stable morphology at different temperatures and compositions [38].

2.2.2.4 Generalities on the Al-Sn-Cu system solidification path

Al-Sn-Cu alloys represents a category of monotectic ternary systems that have attracted considerable attention in various engineering application. The appeal of these stems from a unique combination of mechanical and tribological properties, which often surpass those achievable with their binary base alloys [16,48–51].

Let's consider in a first step the binary Al-Sn system (Figure 2.11), where two phases are present. During the solidification, α-Al grains nucleate and grow first, rejecting Sn at the growth interface. As a result, the Sn content in the remaining liquid increases rapidly until it reaches the eutectic temperature, at which point it solidifies as practically pure Sn. This process leads to a microstructure characterized by an Al-rich dendritic matrix with Sn pockets located in the interdendritic regions. The morphology

is typically retiform, and the distribution and spacing of the Sn pockets are closely related to the fineness of the dendritic spacing [34,52].

The ability to have more than two components in an alloy opens up possibilities to improve material properties beyond the limits of binary alloys. The addition of copper to the Al-Sn binary system has the potential to increase mechanical strength through the formation of an Al_2Cu intermetallic phase. Moreover, depending on the composition balance, Cu can promote liquid phase separation lead by a quaternary monotectic reaction. For instance, when the Cu content exceeds 3 wt.% in the Al-20wt.%Sn alloy, liquid demixing occurs, extending the range of expected microstructures [53]. In fact, studies on Al-Sn-Cu alloys with Cu additions of up to 10% are extensive, however, most focus on post-mortem microstructure analysis [16,41,43,49–51,53,54]. Among them, Zhai *et al.* [5] conducted one of the most comprehensive investigations into the microstructure features and solidification path in the Al-Sn-Cu system. Although their work relies solely on differential scanning calorimetry (DSC) and post-mortem micrographs, it provides valuable insight into the complexity of this system and will be described below.

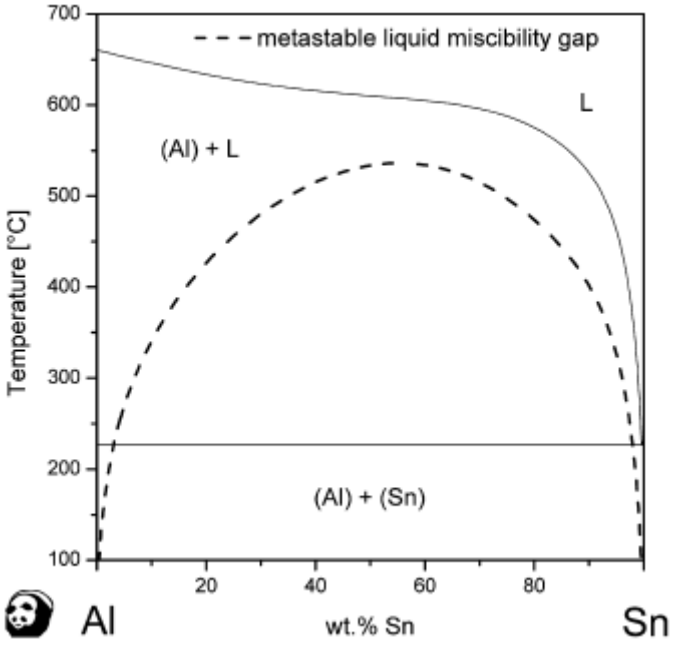

Figure 2.11: Calculated binary system Al–Sn with metastable miscibility gap [43].

Figure 2.12 presents the pseudo-binary phase diagram of the Al-10wt.%Cu-xwt.% Sn system (where x% ranges from 3 to 75 wt.%), experimentally determined via differential scanning calorimetry (DSC). It can be observed that the liquidus line can be divided into two distinct regimes according to the solidification path. For Sn contents below 47%, solidification begins with the formation of primary α-Al phase. While, for Sn contents above 47%, the first reaction is the separation of the liquid phase into Al-rich L_1 and Sn-rich L_2. As a result, five different solidification paths (indicated by vertical dashed lines) and different liquid separation patterns are possible.

The diagram also shows a monotectic monovariant reaction occurring at 801K (528°C), classified as a decomposition-type E3 [43,54]. This reaction involves the transformation of a single liquid phase into three phases: $L_1 \rightarrow L_2 + \alpha\text{-Al} + \theta\text{-}Al_2Cu$. Additionally, a eutectic reaction is observed at 501K (228°C), where $L_2 \rightarrow \alpha\text{-Al} + \theta\text{-}Al_2Cu + \beta\text{-Sn}$.

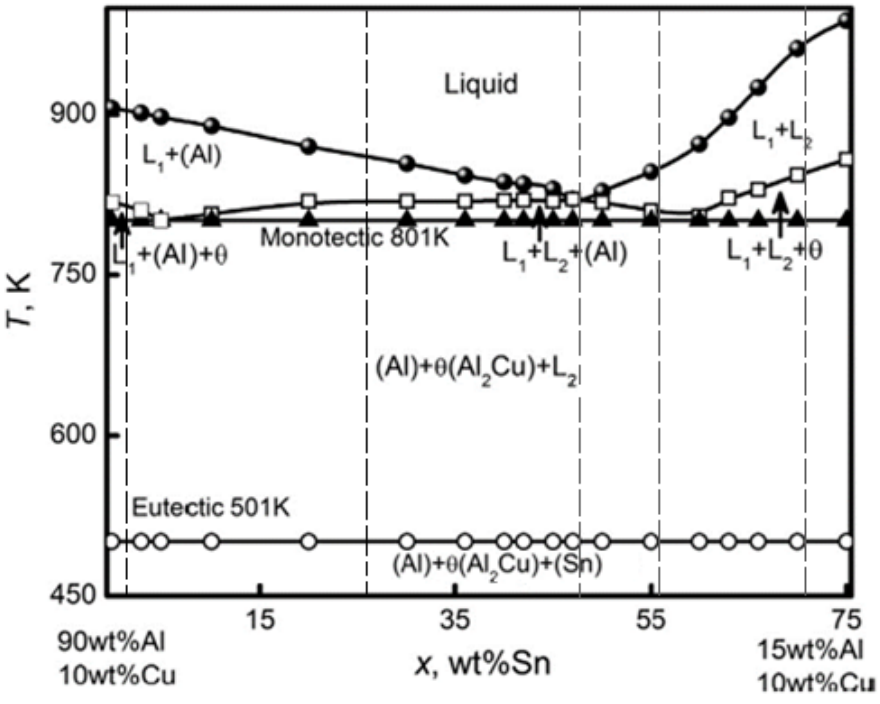

Figure 2.12: Diagram of ternary Al-Cu-x%Sn alloys at constant 10%Cu determined by DSC method. Adapted from [5].

In alloys with Sn content between 0% and 5%, a significant amount of the primary phase α-Al develops from the liquid alloy, $Liquid \rightarrow L_1$ + α-Al and as cooling progress, the θ-Al_2Cu phase and additionally α-Al precipitate via: $L_1 \rightarrow$ α-Al + θ-Al_2Cu. Figure 2.13 shows the microstructure of an Al-10wt.%Cu-3%wt.%Sn alloy solidified at 0.08 K/s. Coarse α-Al dendrites are observed, surrounded by the θ-Al_2Cu phase, along with a small amount of β-Sn phase. The presence of β-Sn is associated with the monotectic reaction (as isolated) and its subsequent solidification during eutectic reaction, according to: $L_2 \rightarrow$ α-Al + θ-Al_2Cu + β-Sn.

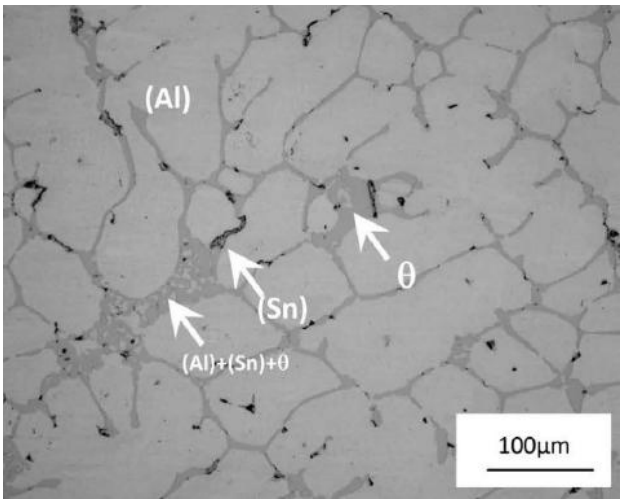

Figure 2.13: Microstructure of Al-10%Cu-3%Sn alloy at 0.08K/s [5].

When the Sn content ranges between 10 and 47%, the α-Al phase also precipitates from the liquid through the reaction: $Liquid \rightarrow L_1$ + α-Al. However, in sequence, the L_2 phase begins to separate from the initial liquid simultaneously with the continued formation of α-Al, both occurring at the expense of $_{L1}$, according to: $L_1 \rightarrow L_2$ + α-Al, which is the liquid phase separation. Subsequently, the L_1 phase is consumed in the monotectic four-phase reaction described above, and then the liquid L2 phase finally solidifies as β-Sn phase via the eutectic four-phase transformation, same as for the Al-10%Cu-3%Sn alloy.

Within Sn composition range of 10% to 47%, although the solidification path remains the same, the pattern of liquid phase separation varies significantly. As

illustrated in Figure 2.12, the volume fraction of the primary α-Al phase decreases progressively with increasing Sn content. When the amount of Sn is less than 40%, the microstructure patterns are characterized by the presence of small L_2 droplets distributed homogeneously in the matrix. This occurs because, during the liquid phase separation process, movement and coalescence of L_2 droplets are hindered by the presence of large α-Al dendrites, which restrict their movement.

Conversely, in the Sn range of 40% to 47% Sn, the amount of α-Al formed is minimal due to the short interval available for its nucleation and growth before liquid demixing occurs. As a result, there is a decrease in the volume fraction of primary α-Al dendrites and an increase of the interdendritic liquid areas, which facilitates the sedimentation and coagulation of small L_2 droplets. Figure 2.14 and Figure 2.15 illustrate these differences. On the same scale, Figure 2.14(a) shows the Al-10%Cu-30%Sn alloy and the Al-10%Cu-45%Sn alloy Figure 2.14(b). Comparing, the Sn-richer alloy shows a reduction in the volume fraction of the primary α-Al dendrites, resulting in the coalescence of the L_2 droplets into several large blocks that sink to the bottom of the sample, as indicated in full view in Figure 2.15.

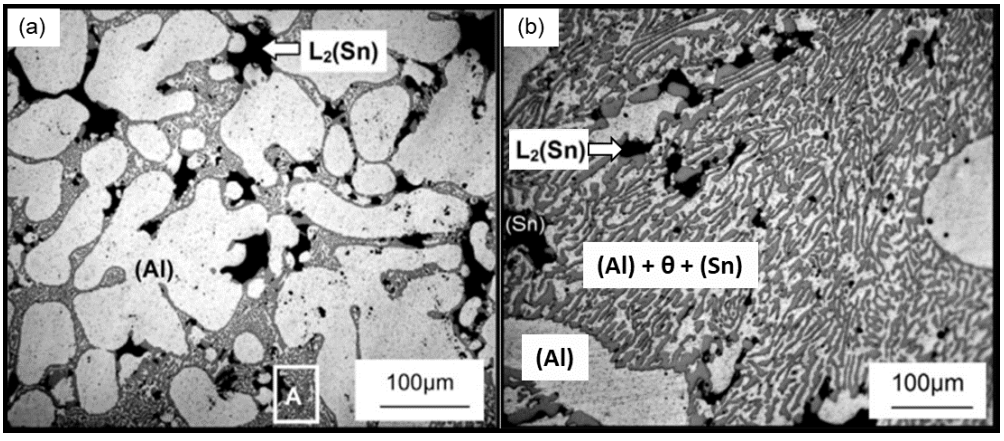

Figure 2.14: Solidification microstructure at 0.08 K/s, at the same scale. Growth morphology of primary (Al) phase and distribution characteristic of L_2 phase of (a) Al-10%Cu-30%Sn alloy and (b) Al-10%Cu-45%Sn alloy [5].

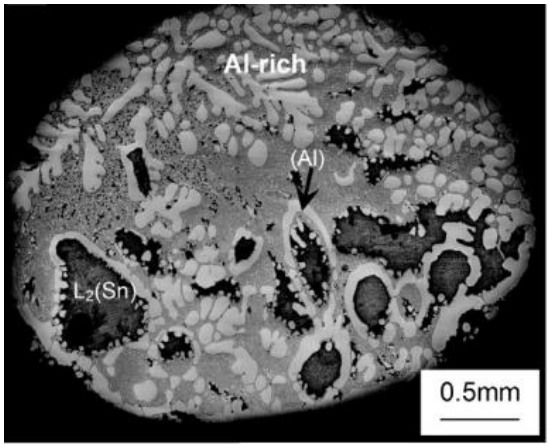

Figure 2.15: Structural morphologies of Al-10%Cu-45%Sn alloy full view [5].

Upon reaching a concentration of 47% Sn, the *liquidus* line intersects with the L_1+L_2+α-Al zone, resulting in the liquid phase separation simultaneously with the solidification of the α-Al phase accordingly $Liquid \rightarrow L_1 + L_2$ + α-Al. In this instance, the movement of the $L2$ droplets is more pronounced, and the segregation of the liquid phases becomes more pronounced as well. If the Sn content increases continuously, severe macro-segregation patterns will occur, leading to the formation of a layered structure in which the lower-density L_1 phase floats to the top, while the higher-density L_2 phase sinks to the bottom. Illustrated in Figure 2.16 for Al-10%Cu-70%Sn.

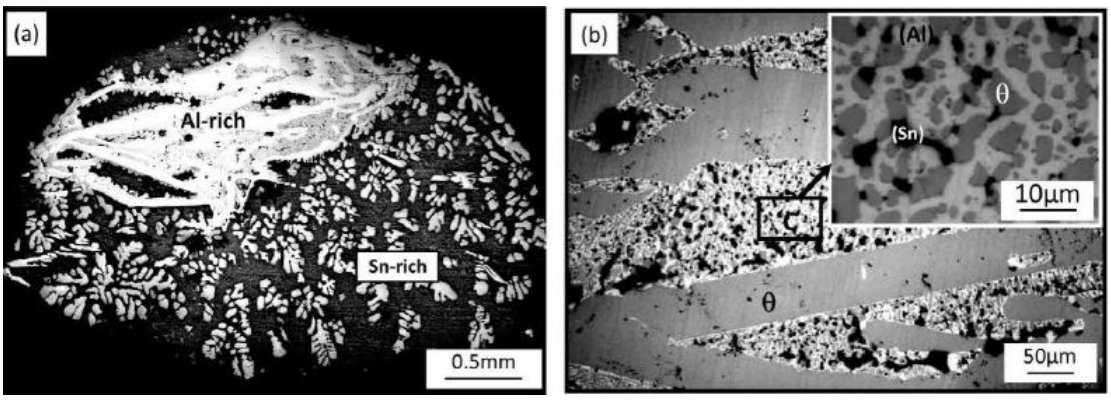

Figure 2.16: Solidification morphology of Al-10%Cu-70%Sn alloy cooled at 0.08K/s: (a) full view of sample; (b) enlarged view of Al-rich zone. The inset presents the ternary (Al)+θ-Al_2Cu+(β-Sn) structure [5].

The morphological variations presented in this section indicate that the formation of the primary phase α-Al prior to liquid demixing and its volume fraction are important in determining the final microstructural pattern, as well as illustrate why for Al-Sn-Cu systems that exhibit liquid phase separation, it is appropriate to choose relatively low Sn contents.

The main research themes surrounding these alloys focus on optimizing mechanical properties, such as strength, ductility and fatigue resistance, as well as tribological behavior, including wear resistance and self-lubrication. These improvements are typically pursued through the addition of alloying elements and by analyzing or modifying solidification conditions. However, investigation of processes like liquid phase separation and monotectic reaction on metal alloys still has lacks, considering that it is more difficult compared to systems with solid-solid immiscibility and requires more dynamic analysis techniques, such as in-situ radiography as performed in the framework of the present PhD.

2.2.3 *In-situ* characterization of alloy solidification by X-ray radiography

2.2.3.1 A brief history of X-ray radiography applied to solidification studies

Due to the inherent opacity of metals, early experimental efforts to study the dynamics of solidification often relied on transparent analogs to investigate phenomena such as the planar-to-dendritic transition and the evolution of the solid-liquid interface morphology [55]. However, comparison with metallic systems is fundamentally limited, as these organic compounds differ significantly in thermal behavior from metals. Additionally, transparent alloys have no direct industrial relevance when compared to their metallic counterparts. Thus, X-ray radiography has emerged as a powerful alternative, enabling real-time visualization of internal structures during solidification [56].

One of the first X-ray radiography setups for the study of solidification was developed in 1967 by Forsten and Miekkoja [57], aiming to investigate solute distribution and boundary layer propagation. Following this initial attempt, Miller and Beech (1972) [58] used a device with a significantly improved spatial resolution and

conducted continuous recording of the solidification in bulk specimens of Al-Cu and Al-Sn alloys using microradiography.

In their study, the samples were melted by passing a large electric current through the crucible, capable of generating sufficient resistive heating. Then, controlled solidification was achieved by gradually reducing the power input, during which a series of radiographs were taken. Figure 2.17 presents a sequence of these radiographs in the case of the Al-Cu alloy. Although no distinct solute diffusion profile could be observed around the growing solid, there was an increase in X-ray absorption in the liquid region as solidification progresses. This effect was visible despite the inherent artefacts of the X-ray sensitive films.

The observed increase in absorption is due to the rejection of copper by the growing α-Al phase, resulting in an enrichment of the liquid toward the eutectic composition. This result was achieved without quenching artifacts and provided one of the first direct demonstration of the capability of X-ray radiography to simultaneously visualize growth morphology and solute redistribution during metallic alloy solidification, marking a significant milestone in the development of *in-situ* X-ray based techniques for solidification research.

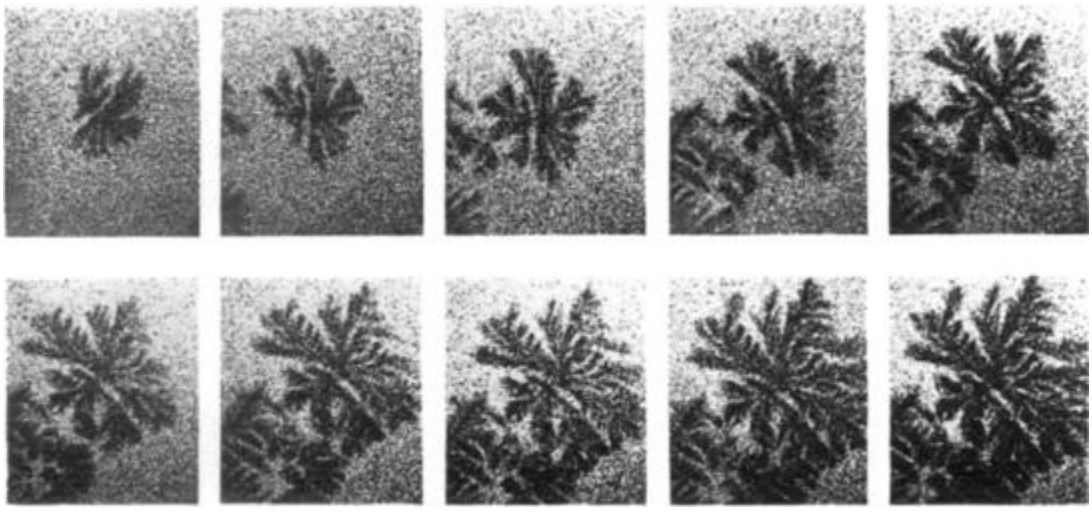

Figure 2.17: Growth sequence showing the development of equiaxed dendrites in the Al-30%Cu alloy, 20x magnification [58].

A significant advancement in real-time X-ray observation of solidification dynamics came in 1994, when Kaukler and Rosenberger introduced a novel X-ray

transmission microscope designed to monitor morphological features at the solid-liquid interface [59]. Their study focused on the Al-Pb system, aiming to investigate the complex interaction between droplets and the advancing solid interface. Their set up incorporated a micro-scale X-ray source and a CCD camera. This innovative approach enabled a spatial resolution of approximately 70 μm through projection, and more importantly, allowed real-time image capture during solidification.

In 1997, Less and Hunt combined real-time microfocus X-ray radiography with precise control of the thermal gradient during solidification to investigate the formation of porosities in Al-Cu alloys [60]. They also applied image processing techniques to enhance image quality. Figure 2.18 displays two pair of four frames, before and after image processing. In Figure 2.18(a), the raw images reveal that the *solidus*/*liquidus* front remain stationary relative to the camera as the sample is moved down into the cooler regions. In Figure 2.18(b), the same frames are shown after background subtraction and contrast enhancement, making easier to identify the pores. One of these pores is marked with the letter "p", illustrating its downward movement along the sample and its growth over time. This work demonstrates the potential of real-time X-ray radiography to advance the understanding of solidification features.

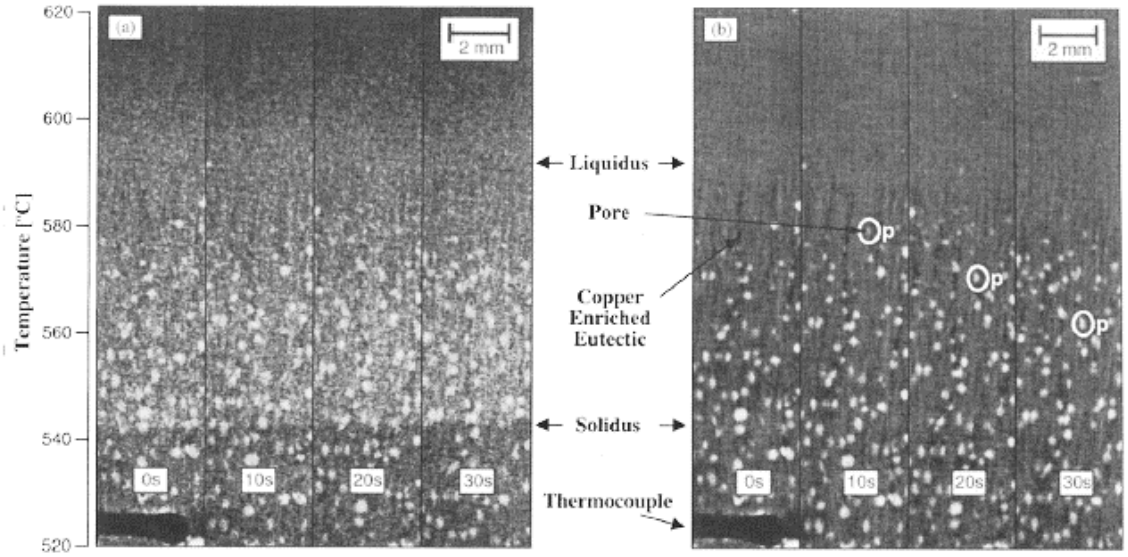

Figure 2.18: Observation by Less and Hunt on their work about combing in-situ observation whit thermal gradient control. Four frames at 0, 10, 20 and 30 s for Al-

20wt.%Cu with V = 0.15 mm/s and G = 57°C. (a) Before and (b) after image processing [60].

Synchrotron light sources have revolutionized in-situ imaging by providing exceptionally high brilliance, which significantly reduces exposure time during experiments. Additionally, the selection of specific photon energies through monochromatization is possible, allowing an optimized balance between transmission and contrast. Furthermore, the natural collimation of synchrotron beams results in a high degree of transverse coherence in the incident wave front, which can be exploited for phase-contrast imaging [61]. These unique properties have greatly expanded the ability to investigate several important phenomena associated with the solidification of metal alloys.

For instance, in 2005, Reinhart *et al.* [62] utilized a synchrotron X-ray source to study the columnar-to-equiaxed transition (CET) during solidification of aluminum alloys, as shown in Figure 2.19. This research enabled direct measurements of key CET parameters, such as the evolution of the undercooling at the advancing columnar front, nucleation undercooling, and the density of active nuclei. These findings provided critical insights for modeling CET and equiaxed growth mechanism, phenomena with significant implications for alloy design and process optimization in the metallurgical industry.

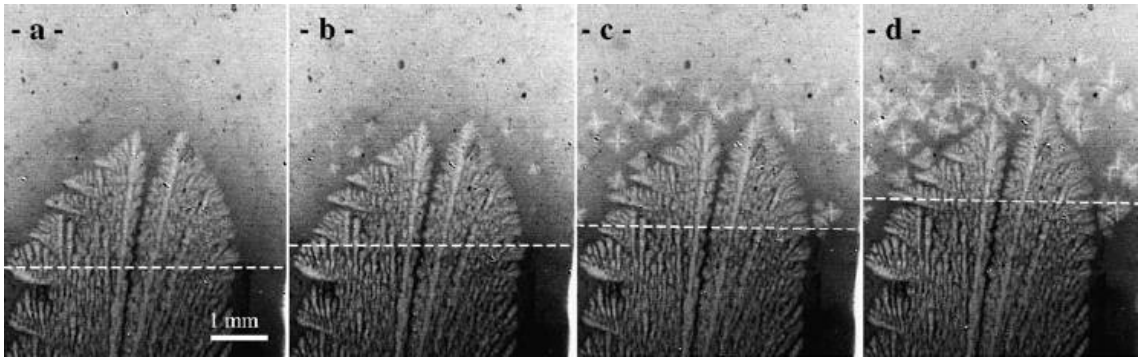

Figure 2.19: Sequence of four images of refined Al-3.5wt.% Ni solidification, recorded during the CET induced by a sharp pulling rate jump from 1.5 to 15 μm/s by synchrotron X-ray radiography, G = 20 K/cm. The dash line underlines the eutectic front position [62].

Subsequently, in 2008, Nguyen-Thi *et al*. [11] employed real-time synchrotron X-ray radiography to investigate the Temperature Gradient Zone Melting (TGZM) phenomenon in aluminum alloys. The study focused on the microstructural evolution of Al-Ni and Al-Si systems during directional solidification, capturing dynamic processes such as the migration of liquid droplets and the detachment of secondary dendrite arms under an imposed thermal gradient. This imaging technique has also substantially advanced the understanding of equiaxed grain growth and dendrite interaction. For example, Bogno *et al.*[63], in 2013, identified two distinct growth regimes from dendrite arms: an initial accelerated phase characterized by free growth, followed by a decelerated phase resulting from solute field interactions as neighboring dendrites approach each other. These observations provided critical insights into the grain self-poisoning phenomenon during which solute accumulation impedes further growth, thus influencing the final microstructural morphology.

Dendrite arm fragmentation is a complex phenomenon to understand, since it occurs during the interaction of the solid and liquid phases. Several studies have investigated this process, including the work of Abou-Khalil *et al*. [64] (2022), who utilized synchrotron radiation to examine its underlying mechanisms as shown in Figure 2.20(a). Their study focused on the directional solidification of an Al-Sn alloy, aiming to assess how increasing growth velocity influences dendrite fragmentation dynamics.

The results demonstrated that higher growth velocities lead to a greater number of detachments, mainly due to localized solute accumulation and the release of latent heat at the solidification front. The study also showed that fragmentation significantly impacts the final grain structure by inducing local misorientations and altering grain morphology under transient solidification conditions. Notably, the authors observed that, under specific thermal and solute conditions, the detached fragments can trigger a columnar-to-equiaxed transitions (CET), as illustrated in Figure 2.20(b).

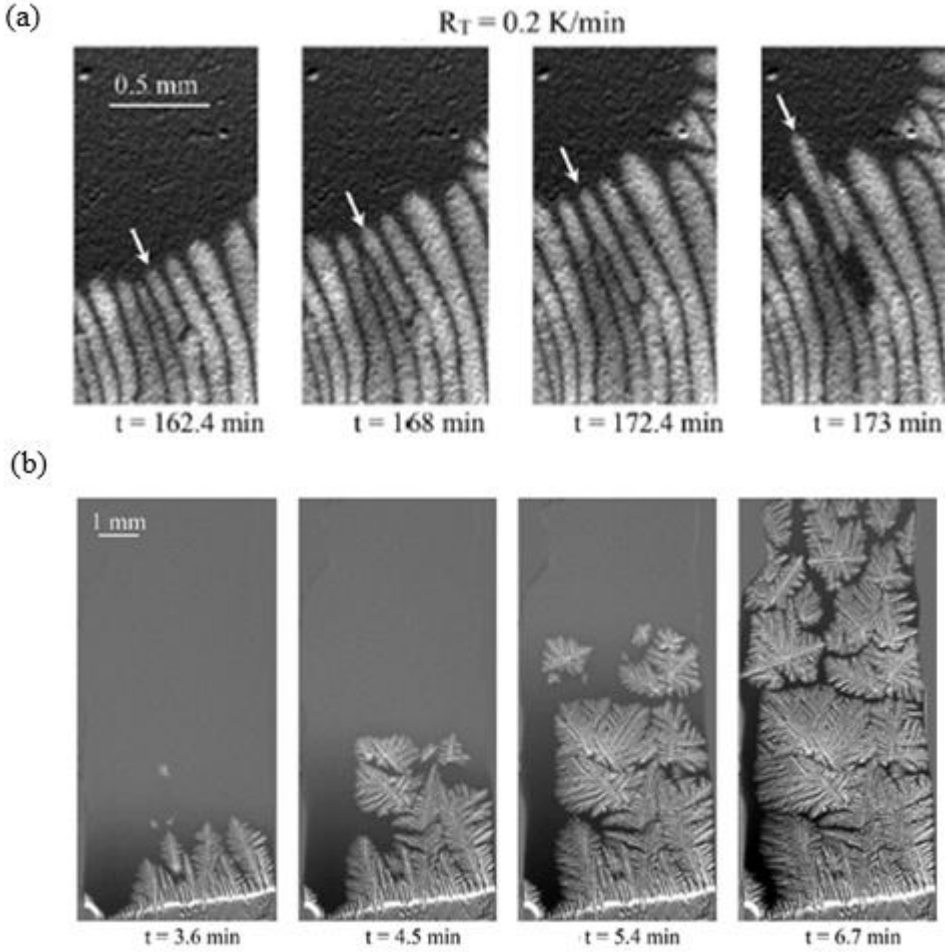

Figure 2.20: Sequence of radiographs, taken from the experiments solidified (a) showing the evolution of cell neck shape and size before its detachment. (b) showing the Equiaxed-to-Columnar Transition [64].

2.2.3.2 Application of X-ray radiography to the study of monotectic alloys

In the case of monotectic alloys, one of the earliest studies involving radiographic analysis was conducted by Kaukler and Rosenberger [59] in 1994, focusing on the Al–Pb system. However, at that time, both spatial and temporal resolutions were limited. Over the following decades, research in this field advanced considerably, with hyper-monotectic Al–Bi alloys becoming a focal point of numerous studies involving both melting [65] and solidification processes.

Among the key contributors in this area, Schaffer, Mathiesen and Amberg extensively investigated the solidification of hyper-monotectic Al–Bi alloys using

synchrotron X-ray radiography. In a 2008 study [66], Schaffer *et al.* explored spinodal decomposition and the subsequent dynamics of liquid–liquid phase separation, observing that a significant undercooling, when approaching the monotectic reaction temperature, was required to initiate the separation of Bi-rich (L_2) droplets from the Al-rich (L_1) matrix. These L_2 droplets displayed complex, size-dependent motion within the melt.

In a subsequent 2010 investigation [8], Schaffer *et al*. investigated the motion and spatial distribution of L_2 droplets during solidification, revealing that their behavior results from a complex interplay of forces, including temperature-gradient-driven hydrodynamics, sedimentation, and short-range interactions such as diffusion-field coupling and droplet coagulation (Figure 2.21). Notably, thermocapillary (Marangoni) forces induced by thermal gradients were found to oppose gravitational settling of the dense Bi-rich phase, thereby enhancing the potential for producing more homogeneous microstructures in hyper-monotectic castings.

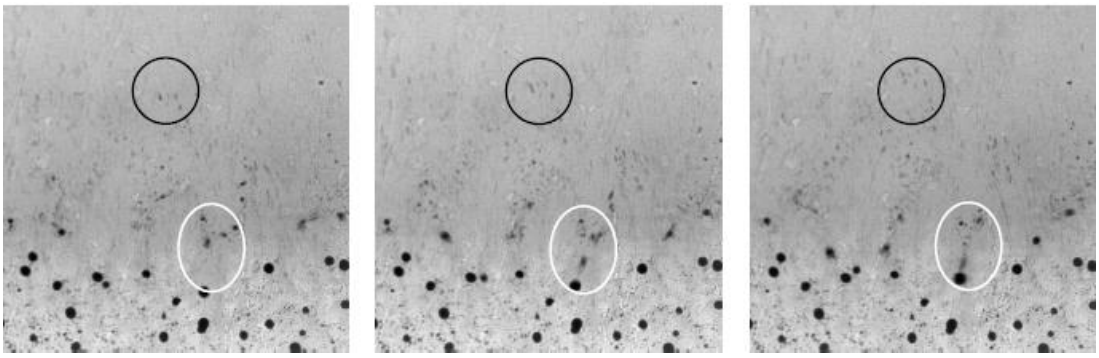

Figure 2.21: Image sequence of Al-6%Bi alloy solidified. Small droplets are transported parallel the thermal gradient Marangoni motion (black circles) whereas large droplets settle due to gravity (white circles) [8].

Further insights came from directional solidification experiments performed in 2009 [67], in which Schaffer et al. examined the interaction between Bi droplets and the advancing solidification front. The study showed that larger droplets were frequently pushed ahead of the front, whereas smaller ones were engulfed, contradicting classical models for solid particle–front interaction. This behavior was attributed to droplet–droplet interactions and local solute gradients. It was also observed that L_2 droplets nucleate at the monotectic interface, and engulfment occurs when the front velocity

closely matches the droplet growth rate. Larger droplets, in turn, are set in motion by solutal Marangoni effects or repulsive diffusion-field coupling, which prevent their incorporation into the solid phase.

All these experiments demonstrated the great interest of using synchrotron X-ray radiography to perform in-situ and real-time investigations of metal alloy solidification. However, the major constraint in using a synchrotron source is the difficult access to such a facility as well as the high cost of the beam time.

2.2.3.3 New generation of laboratory X-ray devices

In addition to large-scale synchrotron facilities, significant advancements have also been made in the development of laboratory-scale devices, driven by the emergence of compact micro-focus X-ray sources and highly sensitive detectors. These technological improvements have made in-situ and time-resolved investigations of solidification dynamics more accessible and widely applicable [13].

As a result, a growing number of studies are being conducted in laboratory settings with sufficient spatial and temporal resolution to resolve key microstructural features. These include investigations exploring the influence of sample orientation relative to gravity [68], dynamic of the grain structure formation in refined alloys [69], as well as experiments performed under microgravity conditions using specialized platforms [10].

For example, the XRMON facility (In-situ X-ray Monitoring of Advanced Metallurgical Processes under Microgravity and Terrestrial Conditions) was developed to enable high-resolution in-situ radiographic studies aboard microgravity platforms. The primary objectives of these studies were to confirm the predominance of fragmentation as a key CET mechanism and to enhance the understanding of its underlying processes, particularly the influence of gravity at each stage of the transition as illustrated in Figure 2.22 [10].

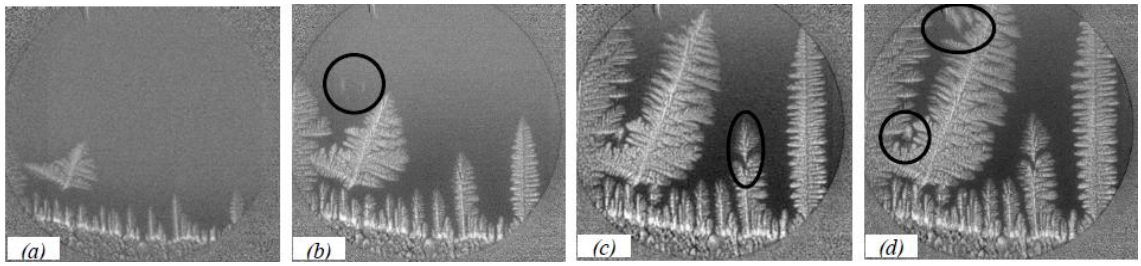

Figure 2.22: Sequence of radiographies during columnar growth of Al-20wt% Cu, taken at XRMON device, showing several dendrite fragmentations [10].

The XRMON device has also enabled comparative studies on the influence of gravity on columnar grain growth, as illustrated in Figure 2.23 [70]. Each row presents a time-resolved sequence acquired during the solidification of an Al-20 wt.% Cu alloy: the first row corresponds to experiments conducted under microgravity conditions, while the second and third rows show reference experiments performed under normal gravity.

This setup allowed for direct observation of microstructural differences arising from the presence or absence of gravity-driven convection. In microgravity, the suppression of buoyancy-induced fluid flow significantly affects both nucleation and solid growth mechanisms, resulting in distinct morphological patterns compared to those observed under terrestrial conditions [70].

Laboratory-based experiments conducted under terrestrial conditions have also yielded valuable insights. For instance, Xavier et al. [71] investigated the formation and growth of α-Al solid and Bi droplets during the monotectic reaction under varying cooling rates. The study revealed that high cooling rates result in more homogeneous microstructures with uniformly distributed Bi droplets. In contrast, lower cooling rates promote morphological transitions of α-Al from dendritic to cellular structures, driven by local Bi depletion due to droplet formation (Figure 2.24).

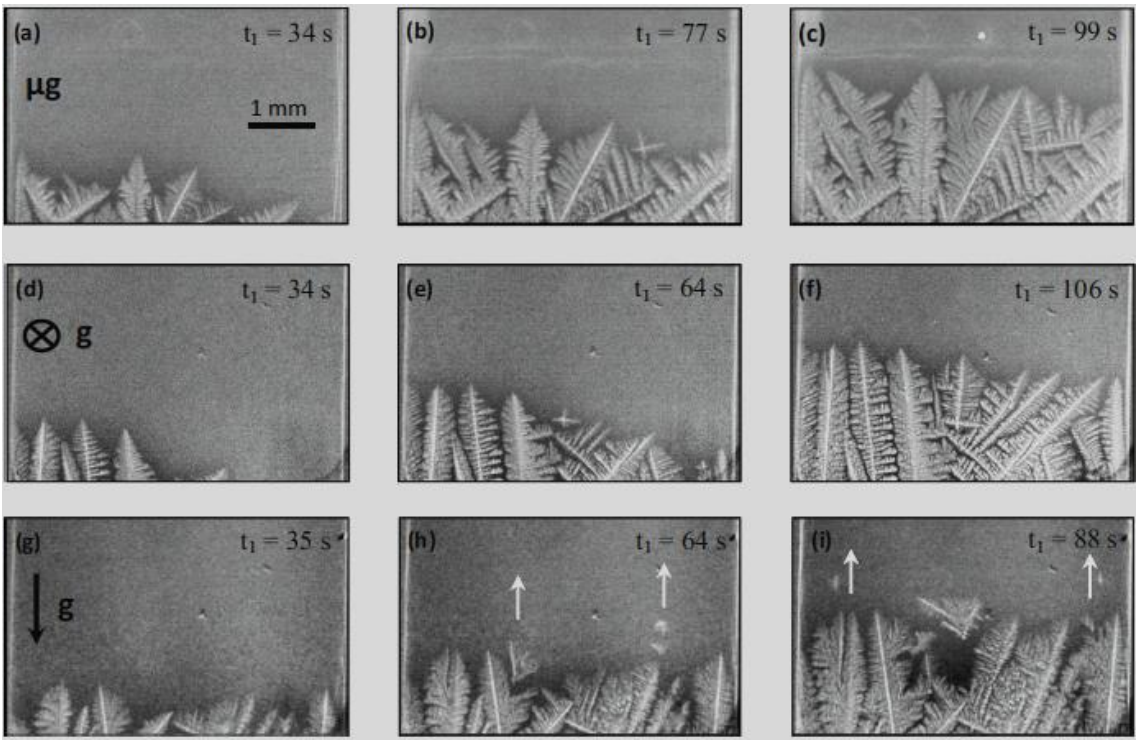

Figure 2.23: Image sequence of columnar solidification of Al-20wt%Cu: (a)-(c) In microgravity conditions, (d)-(f) Sample in horizontal position in gravity conditions, and (g)-(h) Sample in vertical position in gravity condition [70].

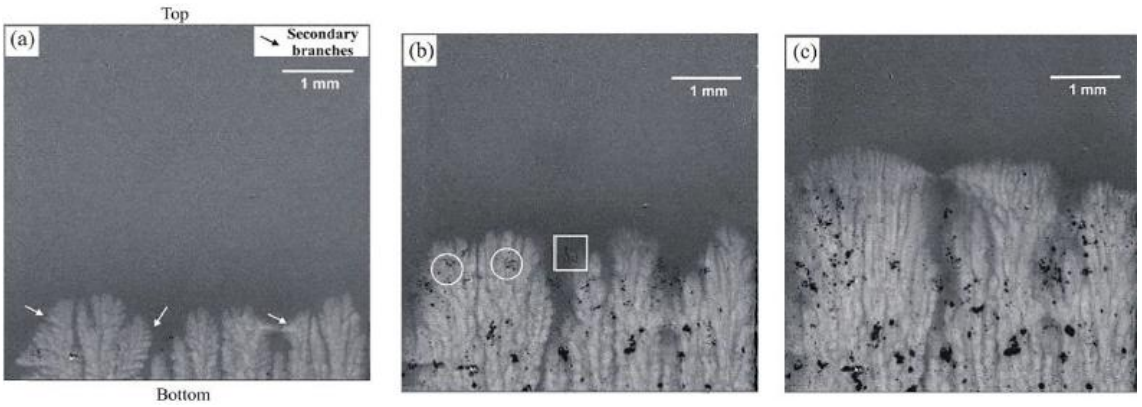

Figure 2.24: Sequence of radiographs recorded during directional solidification of the Al-3.2wt.%Bi-3.0wt.%Cu alloy showing the occurrence of a dendritic-to-cellular transition: (a) dendritic microstructure, (b) transition step, and (c) cellular microstructure [71].

2.2.3.4 Principles of X-ray radiography

The fundamental principle of X-ray radiography involves placing a sample between a radiation source and a detector. An incident X-ray beam with initial intensity I_0 and energy E passes through the sample of thickness x. As the beam crosses the material, variation in density, composition and thicknesses cause a different absorption, leading to variations in the transmitted intensity I_T, which is captured by the detector positioned at distance d_{SD} from the sample, like illustrated in Figure 2.25. When a CCD camera is used, the transmitted X-rays are transformed into visible light by a scintillator [15,61].

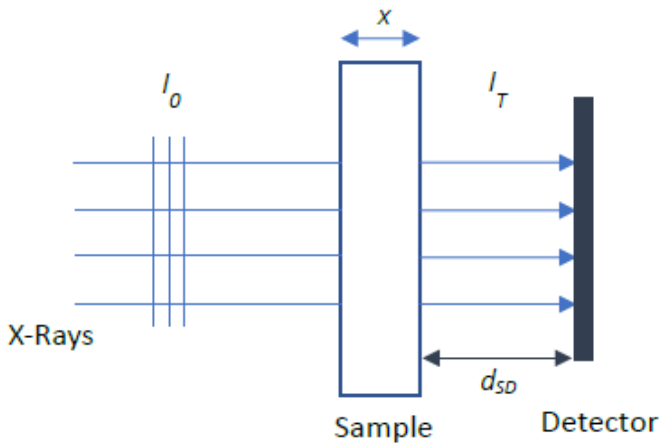

Figure 2.25: X-ray radiography principle.

The Beer-Lambert law relates the transmitted X-ray intensity I_T to the initial intensity I_0 according to Equation 2.:

$$I_T = I_0 \exp\left(\mu_{lin}(T, C) \cdot x\right) \qquad \textbf{Equation 2.8}$$

The transmitted intensity I_T decreases proportionally to I_0, following an exponential decay governed by the thickness x and the linear absorption coefficient μ_{lin}, which depends on the chemical composition C of the crossed material and the temperature T. This transmitted intensity can be rewritten as follow:

$$I_T = I_0 \exp\left(\mu' \cdot \rho(T, C) \cdot x\right) \qquad \textbf{Equation 2.9}$$

Here ρ (*T,C*) is the density of material, which is a function of temperature and chemical composition. The parameter μ' denotes the mass absorption coefficient, which only depends on the material composition. This coefficient decreases as the atomic number of the constituent elements increases, as well as with the energy of the incident beam. For materials composed of multiple elements, such as metallic alloys, the overall mass absorption coefficient $\mu'(C)$ can be written as a linear combination of the mass absorption coefficients $\mu'j$ of the different elements weighted by their concentration *Cj* [15,61].

$$\mu' = \sum_j \mu'_j C_j = \sum_j \frac{\mu_j}{\rho_j} C_j \qquad \textbf{Equation 2.10}$$

2.2.3.5 Transmission and contrast calculations

X-ray transmission is a key parameter that provides insight into the degree to which X-ray can penetrate a material. This parameter is quantitatively described by the transmission coefficient *T*, which derived from the Beer-Lambert law, as shown in *Equation 2.*.

$$T = \frac{I_T}{I_0} = \exp\left(-\mu' \rho(T, C) \cdot x\right) \qquad \textbf{Equation 2.11}$$

Figure 2.26, along with *Equation 2.*, illustrates the impact of several factors on X-ray transmission in the case of a binary Al-Cu alloy. Analysis of the graph reveals that transmission decreases as the sample thickness increases (Figure 2.26(a)). Additionally, transmission is inversely proportional to the atomic number of the alloying element, for instance, copper (Z=29) attenuates X-rays more effectively than aluminum (Z=13), leading to lower transmission in heavier elements (Figure 2.26(b)).

Another observation is the slight variation in transmission between the solid and the liquid states of the material, which may be attributed to minor density changes upon melting, Figure 2.26(c). Lastly, increasing the concentration of solute (copper) in the alloy results in a reduction of the transmission coefficient as shown in Figure 2.26(d). In summary, X-ray transmission decreases with increasing sample thickness, higher atomic number, and greater alloy concentration [15,61].

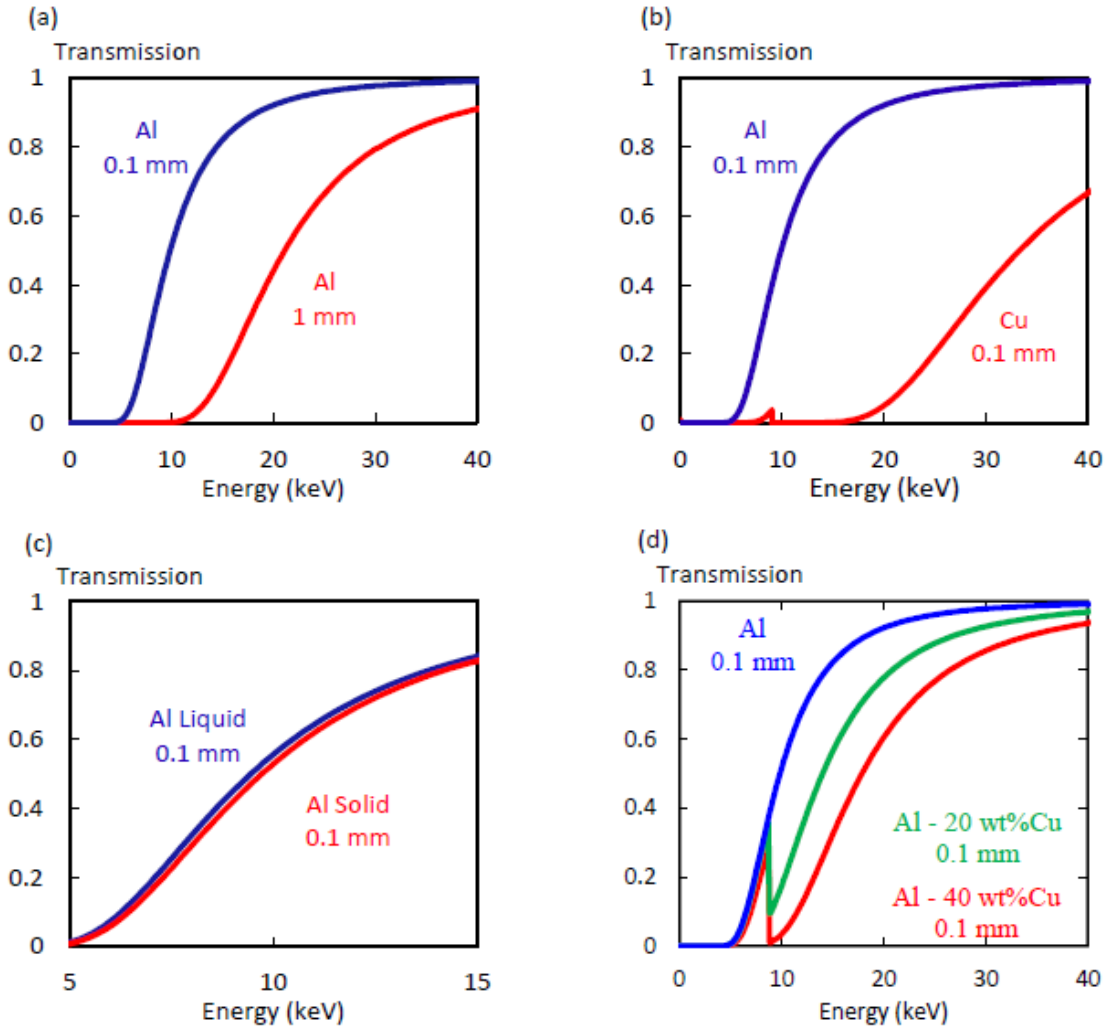

Figure 2.26: Variation of X-ray transmission as a function of (a) thickness, (b) material (pure Al and pure Cu), (c) solid or liquid phase, (d) composition [61].

To achieve high-quality absorption radiographs with an adequate signal-to-noise ratio and reasonable exposure time, a sufficient number of photons must be transmitted

through the sample. This typically requires increasing the incident beam energy. However, higher energy also reduces the contrast between different components, according to *Equation 2.*.

$$Cont = \frac{I_{T1} - I_{T2}}{I_{T1}} \qquad \textbf{\textit{Equation 2.12}}$$

An optimal energy must therefore be found to balance transmission and contrast. A practical criterion is to select the energy corresponding to the intersection of the transmission and contrast curves, as displayed in Figure 2.27. In experiments at synchrotron sources, it is possible to accurately choose this energy. However, in laboratory equipment, the intensity of the X-ray peaks depends on the anode material used in the X-ray source, commonly copper, tungsten, or molybdenum. For investigations involving the solidification of aluminum-based alloys, molybdenum is typically preferred. This is due to its characteristic emission peaks at 17.4 keV and 19.6 keV, which have been demonstrated to provide optimal energy levels for achieving high-quality radiographic images of Al-Cu alloys [15,61].

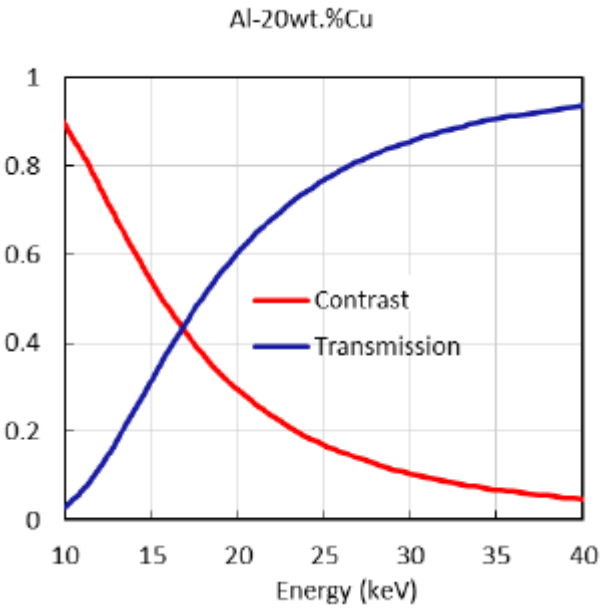

Figure 2.27: Transmission and contrast of Al-20wt.%Cu (the thickness used for calculations is 0.2 mm [61].

2.3 Materials and Methods

2.3.1 The SFINX apparatus

2.3.1.1 Development

The device named SFINX, an acronym for “Solidification Furnace with In-situ X-ray radiography”, is a laboratory-scale equipment developed by the MCA (Microstructures de Croissance Auto-organisées) team at IM2NP institute in collaboration with the Swedish Space Corporation (SSC). It is a replica of devices previously developed by SSC as part of the ESA-MAP XRMON project (In-situ X-Ray MONitoring of Advanced metallurgical processes under microgravity and terrestrial conditions), which focused on directional solidification experiments.

Figure 2.28 shows the laboratory layout of the SFINX apparatus, which consists of two parts: an experimental rack and a control system. The SFINX control system includes computers that are responsible for regulating temperature, controlling the X-ray source, and the images acquisition. The experimental rack houses a Bridgman-type furnace, an X-ray microfocus source, and a CCD camera. It is worth noticing that the experimental rack is capable of carrying out solidification experiments with the sample in vertical or horizontal orientations, which is useful for experiments in which the effects of gravity are investigated in relation to the solidification direction [68]. All the elements of the setup will be described in detail subsequently.

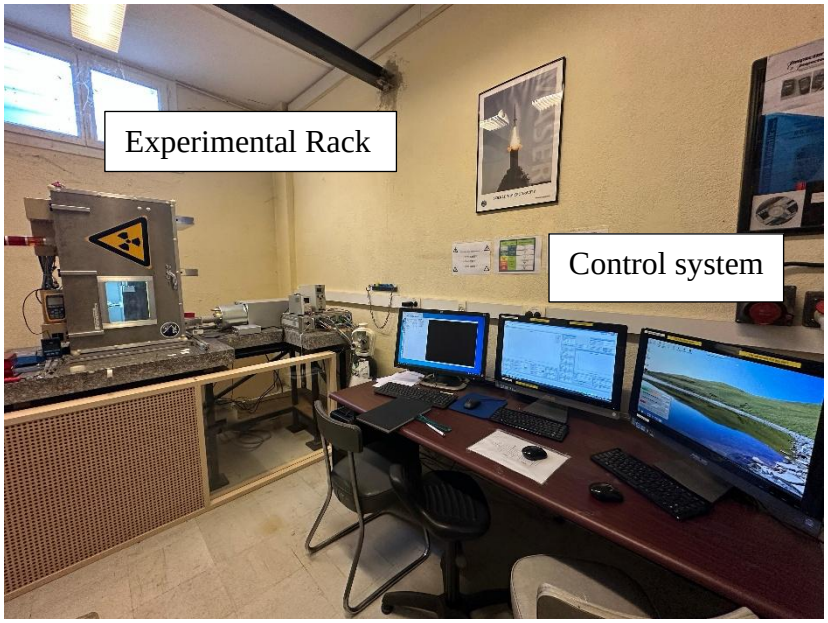

Figure 2.28: SFINX laboratory layout, where lead box encloses the experimental rack next to the control computers system

2.3.1.2 X-ray radiography device

The core of the SFINX apparatus is the experimental rack, which contains a Bridgman-type furnace, an X-ray microfocus source, and a CCD camera, as illustrated in Figure 2.29.

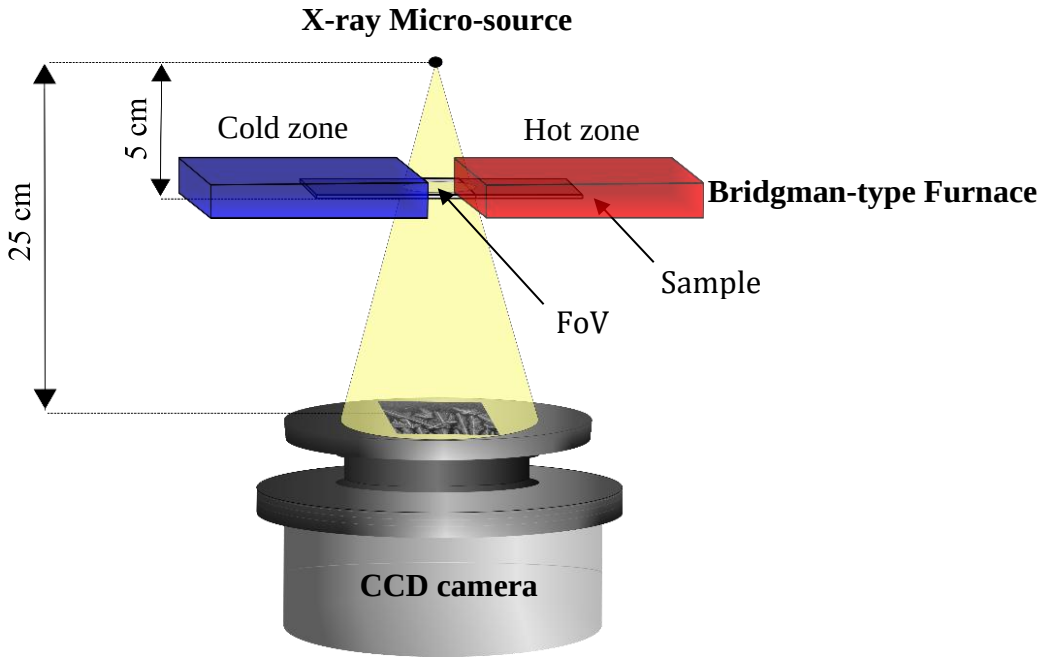

Figure 2.29: Overview of the SFINX device with the furnace in horizontal position.

The X-ray source of the SFINX device is a microfocus X-ray tube from FineTec FineFocus Technologies GmbH, featuring a 3 µm focal spot and a 170° beam angle. The tube incorporates a 5 µm molybdenum transmission target whose characteristic emission lines (Kα= 17.4 KeV and Kβ= 19.6KeV) are well-suited for radiographic analysis of Al-high Cu content alloys, as this energy spectrum allows to distinguish pure aluminum from solute-rich liquid Al-Cu.

Given that the laboratory microfocus source emits a cone-beam, as illustrated in Figure 2.29, there is an image magnification depending on the ratio of the distance between the source, the sample, and the camera. In the example illustrated in Figure 2.30, the nominal magnification is calculated by the ratio between the camera - X-ray source distance (25 mm) and the sample - X-ray source (5 mm) distance, resulting in a magnification equal to M = 5. However, due to manual positioning of the furnace along a graduated rail, spatial uncertainty of ± 1 mm must be considered. On the present study, the sample width was used as the calibration standard and for each experiment a calibration according to the sample dimensions had to be made. For example, in Figure 2.31, the 5 mm sample width corresponds to 1200 pixels, giving an effective pixel size

of 4.16 µm and a field of view of 5.5 mm x 8.4 mm. This indicates a magnification of 4.3, implying a 0.8 mm deviation from the intended furnace position.

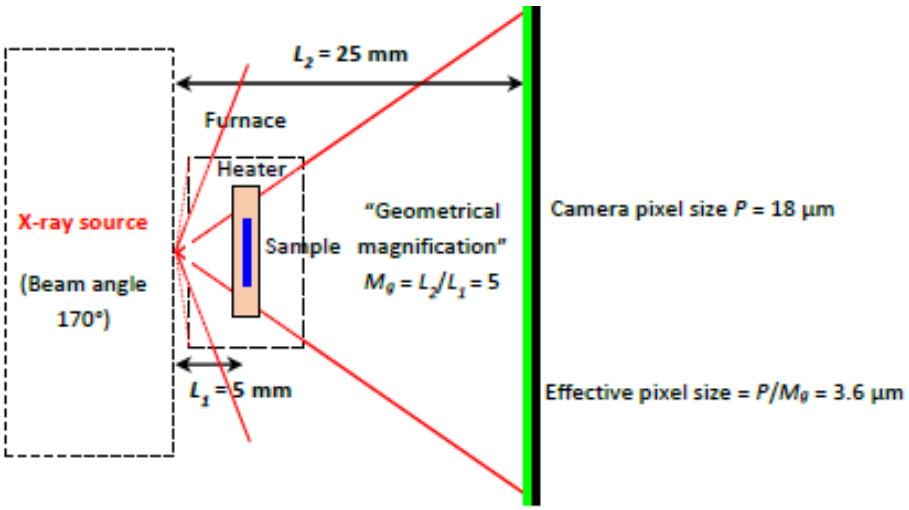

Figure 2.30: Scheme of the imaging system showing the distances L_1 and L_2 used to determine the geometric magnification factor [15].

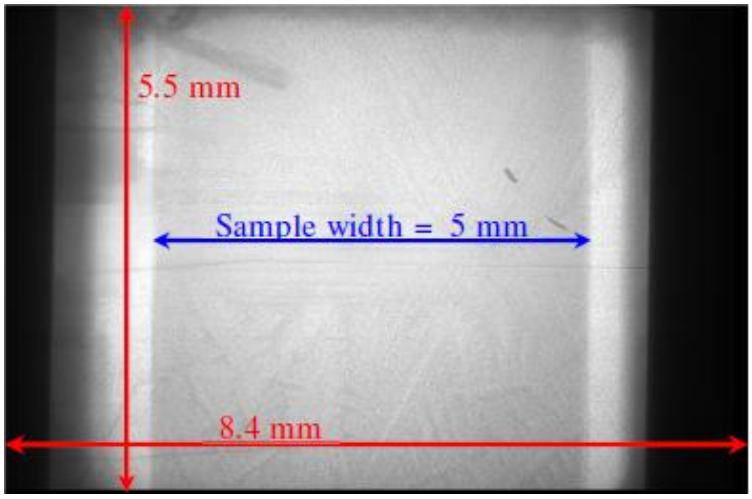

Figure 2.31: Example of a raw image of a sample inside the furnace before the solidification experiment. The sample width is used as reference size for magnification calculation and for effective pixel size [15].

The camera system used to capture the images uses a Vosskuhler 11000 digital camera with a 24 mm x 36 mm CCD sensor and 18 µm/pixels. A scintillator, which converts incoming X-rays into visible light, is placed inside the camera, in front of the

optical fibers. The camera then captures this light and converts it into electrical signals to form images. A Peltier cooler and a fan help maintain low temperatures and prevent image degradation during high-temperature solidification experiments.

The camera and image recording are controlled by an acquisition system that captures uncompressed 16-bit images at a resolution of 2012 x 1340 pixels (2.7 million pixels). For solidification experiments, exposure time for X-ray imaging recording is optimized to obtain a sufficient photon transmission and to avoid contrast loss and detector saturation.

2.3.1.3 Bridgman-type furnace

The melting and solidification experiments are conducted in a Bridgman-type gradient furnace, which has two identical heating elements, one for the hot zone and one for the cold zone. Each heater is composed of two boron nitride parts joined together and wrapped with platinum-rhodium 10% coil, ensuring uniform temperature distribution across both halves. The assembly includes an aperture that allows X-rays to pass through the sample as indicated in Figure 2.32(b).

To minimize heat loss and thermal expansion, the heating elements are enclosed in a stainless-steel case with a tungsten cover, Figure 2.32(c). To enable X-ray transmission through the sample there is a 5 mm diameter hole sealed with glassy carbon as cover. To prevent oxidation of graphite parts in the furnace system when the temperature reaches values above 500°C, the experiments are conducted in a pressurized nitrogen environment to keep the oxygen level in the furnace box below 5%.

Two K-type thermocouples, spaced 13.5 mm apart and positioned at the extremities of the FoV are used to monitor and control the temperature of each heater, as illustrated in Figure 2.32(a). These sensors help manage the applied thermal gradient, although the actual gradient in the sample differs slightly due to heat losses. The heaters are independently regulated via a software-based PID controller.

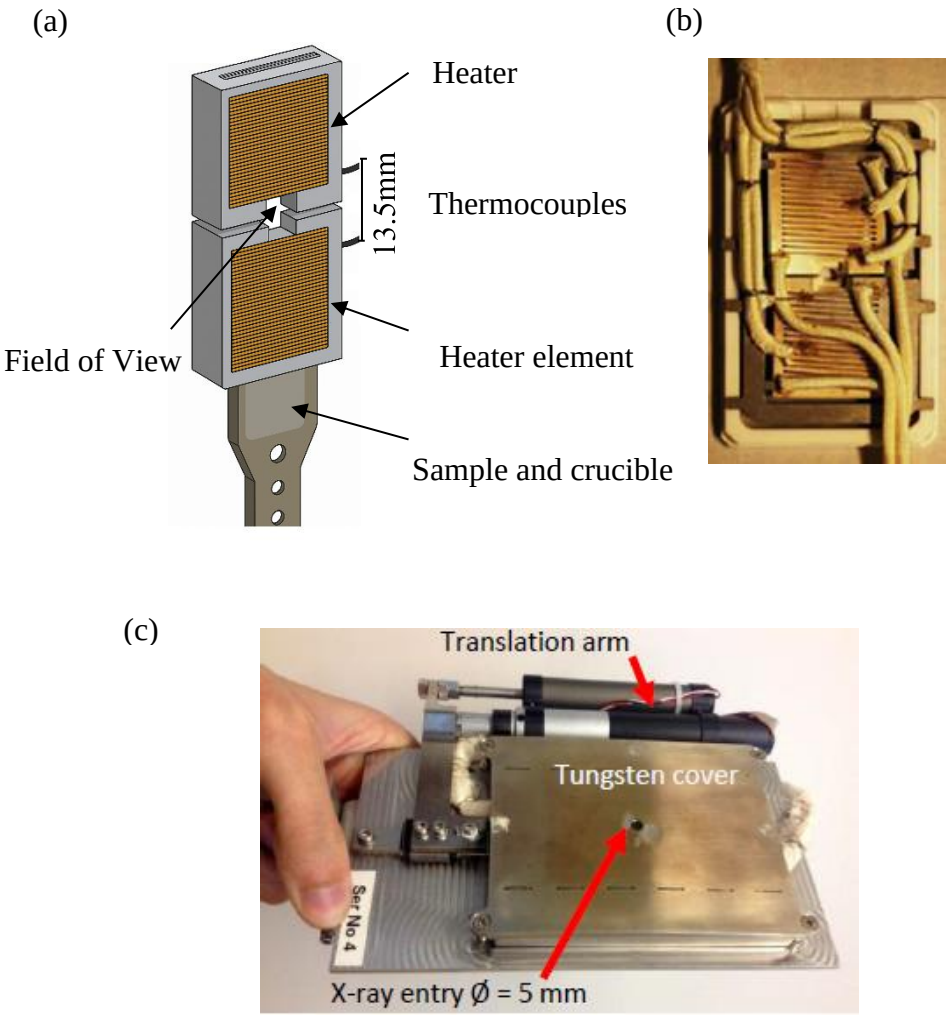

Figure 2.32: (a) Scheme of the furnace with its components and the field of view. (b) Photo of the furnace showing the connection of the thermocouples and the heating elements (c) Furnace inside the tungsten cover.

2.3.1.4 Sample and crucible assembly

In order to ensure adequate X-ray transmission, it is essential to maintain precise control over the thickness of the sample, as previously discussed. In accordance with the conclusions of previous studies [61], the optimal sample thickness is estimated to be approximately 200 µm. Once prepared, the samples, supported by stainless-steel frames with a 150 µm thickness are enclosed between two 150 µm-thick glassy carbon sheets, stitched with 200 µm silica thread to ensure proper positioning and attachment to the furnace translation arm, as shown in Figure 2.33(a). The total thickness of the

assembled structure must not exceed 600 µm, a limitation that corresponds to the dimensions of the furnace aperture.

The complete assembly is subsequently positioned within the furnace, ensuring direct contact with the heaters on both sides. Before solidification, X-ray imaging must be used to verify sample centering in the field of view, Figure 2.33(b). If misalignment is detected, the assembly is dismantled and reassembled to ensure correct positioning.

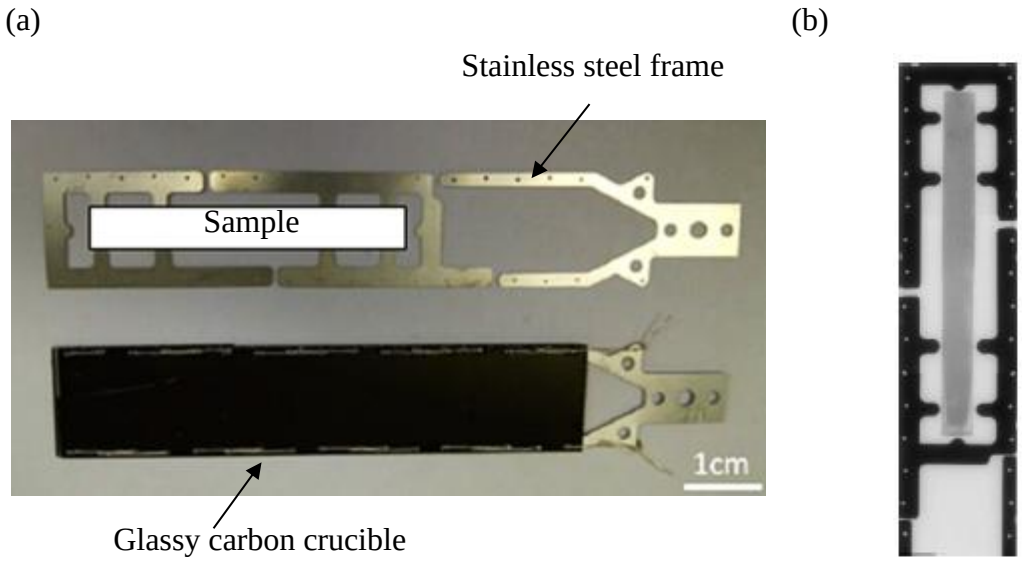

Figure 2.33: (a) Photo of the stainless-steel frame and glassy carbon crucible; (b) radiograph of the sample inside the crucible.

2.3.2 Image processing techniques

The contrast obtained in the X-ray radiography images is related to the relative absorption of X-rays when crossing the different phases. It depends on composition, density, and is also related to the thickness of the material. In addition, certain artefacts inherent to the device make the raw images difficult to read. The artefacts result from various factors, including fluctuations in the temporal and spatial intensities of the X-ray beam or even defects on the detector background. Consequently, a preliminary step to the image analysis includes image processing to ensure data integrity and facilitate the image content comprehension.

Typically, two different image processing techniques were employed in the framework of this PhD for the analysis of the images. In order to understand the

techniques, it is imperative to know that the 16-bit images have a greyscale with pixel values ranging from 0 (black) to 65563 (white). Image processing consist mainly of pixel-wise mathematical operations between images, that can be carried out using the ImageJ software [72].

2.3.2.1 Flat-Field processing

A first and commonly employed image processing technique is the Flat-Field correction, which consist in dividing "pixel by pixel" the raw image recorded at t1, where the dendritic microstructure is not easily visible as shown in Figure 2.34(a), by a reference image recorded at t0 just before the beginning of the solidification, when the region of interest within the Field-of-View is nearly entirely in the liquid state as shown in Figure 2.34(b) [73]. The resulting image in Figure 2.34(c) displays a notable enhancement in readability, with an increased grey level contrast observed between the dendrites (rich in aluminum) and the liquid (enriched in copper and tin because of solute rejection during the phase transformation). Similar image processing can also be achieved by subtracting the reference image from the raw images. However, this operation can give negative pixel values.

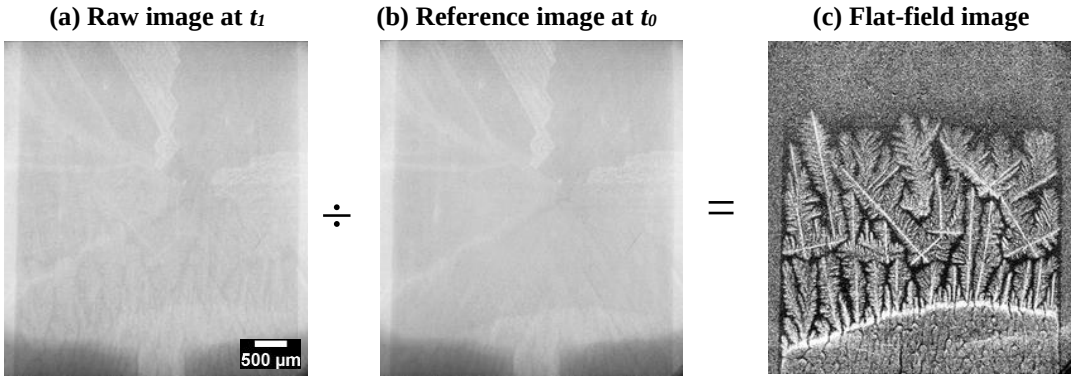

Figure 2.34: Illustration of the Flat-Field image processing procedure used to improve the legibility of the images. (a) raw image recorded at any time t_1. (b) reference image recorded before applying the cooling rate, (c) result of the flat-field correction reveal revealing more clearly the microstructure.

Previous studies conducted in the laboratory have demonstrated that the quality of the flat-field correction can be further enhanced by reducing noise in the reference image recorded just before the solidification beginning. This is achieved by averaging multiple image captured prior to the onset of solidification [61].

2.3.2.2 Frame-differencing processing

The second image processing is called Frame Differencing. This technique is widely used in computer vision to highlight differences between two frames and has been successfully extended to solidification studies. For this purpose, an image of interest recorded at any time t_1, as shown in Figure 2.35(a), is divided by another one recorded a few seconds prior, as shown in Figure 2.35(b). At first glance, these two images are identical but a very detailed visual analysis reveals a few differences between the two microstructures.

The time interval between the two images must be chosen to ensure distinct grey level contrast in the resulting images. In fact, too short interval does not show any or enough change in the microstructure, while a too long interval may lead to a loss of information about microstructure evolution, depending on the time evolution of the solidification microstructure. A value in the range of 5-7 seconds was chosen for most of our experiments and the resulting image emphasizes the changes that occurred during that time interval through variation in color contrast as shown in Figure 2.35(c).

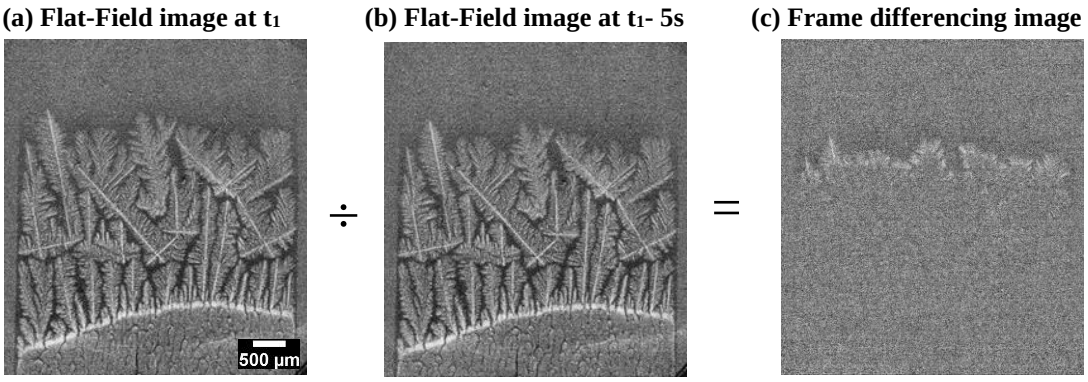

Figure 2.35: Illustration of the Frame differencing image processing procedure used to detect small changes between successive frames. (a) image recorded at any time t1 after flat field correction, (b) Image recorded five seconds before the first image after flat field correction, (c) frame differencing image obtained by dividing the two images, revealing the new solid forms during the five seconds.

By applying the frame differencing image processing to the radiographs, the solid dendritic network that only very slowly evolved during the sample cooling is completely erased and replaced by a uniform gray background, while the light regions indicate the newly solid formed during the 5 seconds separating the two images.

Frame differencing is really useful for detecting reactions that take place in the semi-solid state, when small events occur in the residual liquid within the dendritic network. This method has been used for example to visualize the crossing of the eutectic front [74]. In the framework of this PhD, it will be applied to reveal both the liquid phase separation and the monotectic reaction during the cooling of the sample.

2.3.3 Directional solidification experiments

In-situ and real time observation of the directional solidification process was performed using the SFINX device for all Al-10wt.%Cu-xwt.%Sn alloys under identical thermal conditions and in horizontal orientation, with the main sample surface perpendicular to the gravity vector $\boldsymbol{g}$. This configuration is chosen to damp gravity-related phenomena such as buoyancy and convective flow [68].

First, the alloy was melted by applying a temperature gradient between the two heating elements and increasing the temperature until the sample was partially melted. Keeping part of the sample in a solid/mushy state is important to have a seed that guides the growth of columnar grains at the onset of solidification. Before solidifying, the temperatures were adjusted to position the seed at the bottom of the field of view. The values reached by the heating elements for each experiment are specified in Table 2.1.

Solidification was achieved by applying the same cooling rate to both heating elements (power-down method) whiling maintaining a constant temperature gradient. Previous experiments conducted in the laboratory have demonstrated that the isotherms within the field of view may exhibit a noticeable tilt. While this tilt is negligible under high thermal gradients (G = 11 °C/mm), it becomes significant when the thermal gradient falls below G = 3.7 °C/mm. This phenomenon is likely attributed to the furnace design due to heat losses induced by the field of view aperture and must be considered during results analysis. Based on prior investigations, a temperature gradient of 5.55°C/min and a cooling rate of -0.15°C/s were applied, as this parameters set has been

shown to yields microstructures with features that are clearly distinguishable using the current imaging system.

Table 2.1: SFINX solidification parameters

Alloy	Temp Cold zone (°C)	Temp Hot zone (°C)	Thermal Gradient (°C/mm)	Cooling Rate (°C/s)
Al-10Cu-5Sn	601	677	5.63	-0.15
Al-10Cu-10Sn	595	670	5.55	-0.15
Al-10Cu-20Sn	570	645	5.55	-0.15

The image acquisition time were set to 500ms, resulting in a temporal resolution of two frames per second. Concomitantly, the temperature evolution was recorded on the two thermocouples. This allowed the temperature at the center of the field of view to be estimated by averaging the thermocouple temperature values when the image was captured. This average temperature value is considered a reliable approximation of the actual temperature at the center of the field of view and helps to identify the reactions in relation to the Thermo-Calc and DSC results.

2.4 Results and discussions

2.4.1 Thermodynamic calculation of Al-Sn-Cu solidification paths

2.4.1.1 CALPHAD analysis

Understanding the alloys behavior requires precise knowledge of phase diagrams, which are derived from thermodynamics analysis based on a system's Gibbs free energy. Therefore, thermodynamic calculations have become a fundamental tool for materials science.

Precise thermodynamic modelling is based on the variation in the Gibbs free energy of the mixture, which consists of two terms: the ideal mixing energy (ΔG_{mix}^{ideal}) and the non-ideal, called excess energy (ΔG_{mix}^{Excess}). The ideal term assumes no chemical interaction between the atoms in the solution, making it a convenient starting point, but it does not reflect most real solutions. The excess term, on the other hand, account for

interactions between different elements and reflects the nature of the interaction between them, formalizing the deviation from the ideal case. As this term considers the particularity of the interaction between all elements, may become complex to calculate, especially in multicomponent alloys [75–77]. And so computational thermodynamics becomes necessary.

The CALPHAD (CALculation of PHAse Diagrams) method, which combines experimental data with mathematical models to predict phase equilibrium and thermodynamic properties of multicomponent systems, provides a hierarchical mechanism to build property databases starting from pure elements evolving to binary and ternary systems. With extrapolation, CALPHAD can also predicts the properties of higher-order alloys [75–77]. At the commercial level, there are software packages like Thermo-Calc that use the CALPHAD approach to develop their databases and performs thermodynamic calculations.

The methodology used by the Thermo-Calc software to create its databases consists of five main steps, the first being the collection of available experimental data or in cases of lack of experimental data, estimating model parameters through ab-initio calculations, learning machine tools, empirical relationships and/or practical rules. Next, a critical assessment of the captured data is carried out, and the appropriate model is chosen based on this data. The third step is to optimize the free parameters of the chosen models. The fourth step consists of storing the investigated system in databases in a format readable by Thermo-Calc and the last step is to validate the predictions in relation to the experimental results. From these databases, available in a user-friendly interface, it is possible to find many thermodynamic solutions [78]. Thermodynamic assessments were thus conducted with the Thermo-Calc software, using the TCAL7: Al-Alloys v7.1 version 2024b database [79].

2.4.1.2 Pseudo-binary phase diagram

The solidification paths of both binary Al-Cu and Al-Sn alloys are rather standard with the formation of α-Al as primary phase and then a eutectic reaction from the residual liquid. However, the comprehension of the solidification paths in the ternary alloys Al-Sn-Cu is much more complex, in part due to the occurrence of

multiple transformations during the cooling process [31]. In a first approach, the Al-Sn pseudo-binary phase diagram with a fixed amount of 10 wt.% Cu was calculated. The pseudo-binary phase diagram considers the variation in relation to the temperature of two elements (Al and Sn) while keeping the quantity of a third one (Cu) fixed, being easier to read than a ternary diagram. The pseudo-binary phase diagram of the Al-10 wt% Cu-X wt% Sn system is shown in Figure 2.36 for Sn content varying from 0 wt% up to 25 wt%.

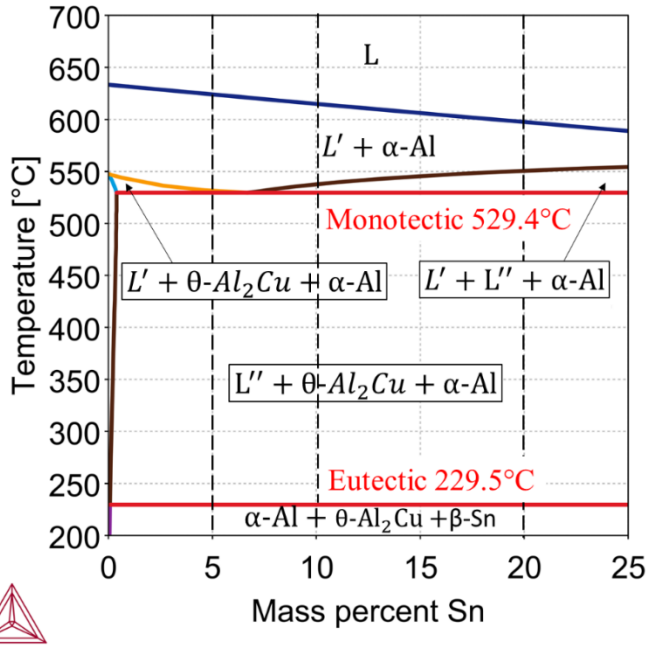

Figure 2.36: Al-10 wt.% Cu- X wt.%Sn pseudo-binary diagram.

The pseudo-binary phase diagram gives a general idea of what could occur during the solidification of the ternary alloy. In this composition range, two reactions are detected, one at 529.4°C, which is the monotectic reaction, and another one at 229.5°C, which is the final eutectic reaction. In addition, a liquid miscibility gap is partially visible when Sn content is greater than 6.6 wt.%.

2.4.1.3 Solidification paths

While the pseudo-binary diagram provides a general idea of the solidification sequence, it is essentially a two-dimensional cross-section of a three-dimensional phase diagram, and hence does not capture all relevant data. For a more complete understanding, the equilibrium solidification paths were calculated for each composition, considering the full variation of all three elements (Al, Sn, Cu). Figure 2.37 shows the calculated solidification paths for the four investigated alloys, represented by the evolution of phase fractions as a function of temperature (from the right side to the left side).

Figure 2.37(a) shows that the binary Al-10wt.%Cu alloy begins solidification with the formation of α-Al dendrites (red curve) at 633°C. As solidification progresses, solute rejection enriches the liquid until eutectic reaction (α-Al + θ-Al_2Cu) at 547.5°C. This binary alloy is widely used as a reference model in solidification studies.

As shown in Figure 2.37(b), the ternary alloy Al-10 wt.% Cu-5 wt.% Sn solidification also begins with α-Al dendrites formation but at a lower temperature of 624°C. Figure 2.37(b) also shows the simultaneous decrease of liquid phase L' proportion and increase of aluminium solid phase during the solidification phase down to 531.5°C. Between the temperatures 531.5 °C and 524.8 °C, the liquid phase L' gives birth to two solid phases (α-Al + θ-Al_2Cu) and is enriched with Cu and Sn. Between 524.8 °C and $T_{eutectic}$ = 229.5 °C, the liquid L' interacts with the solid α-Al to form solid θ-Al_2Cu, which explains the slow decrease from right to left of α-Al (red line) and L' (blue line), simultaneously with an increase of θ-Al_2Cu (purple dash-point line). Finally, the residual liquid L' solidifies through a eutectic reaction at $T_{eutectic}$.

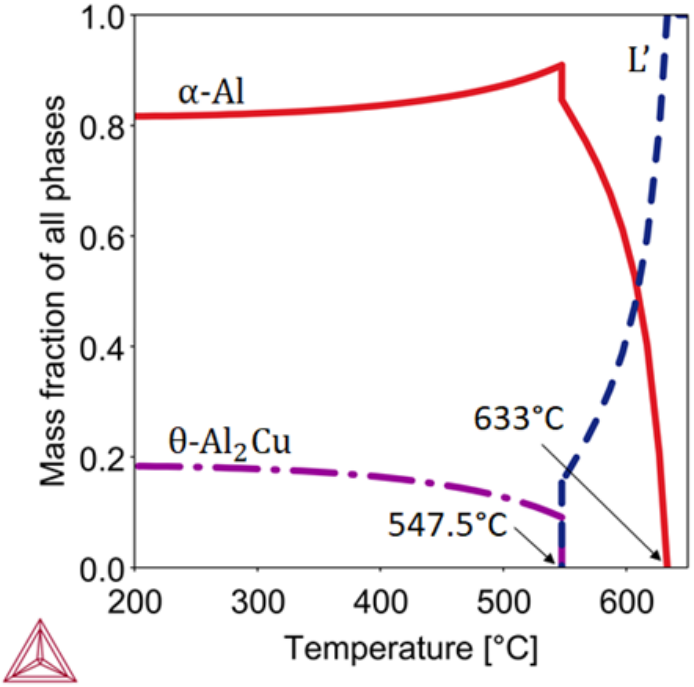

(a) Al-10wt.%Cu

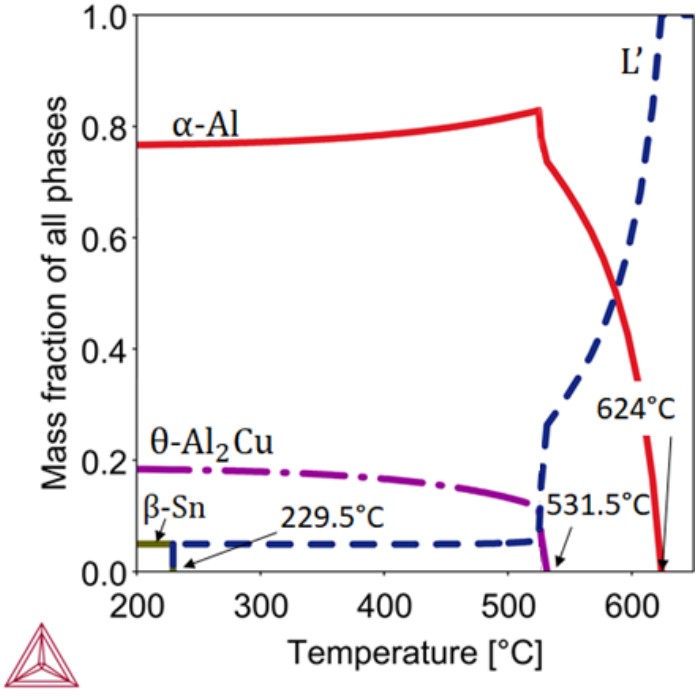

(b) Al-10wt.%Cu-5wt.%Sn

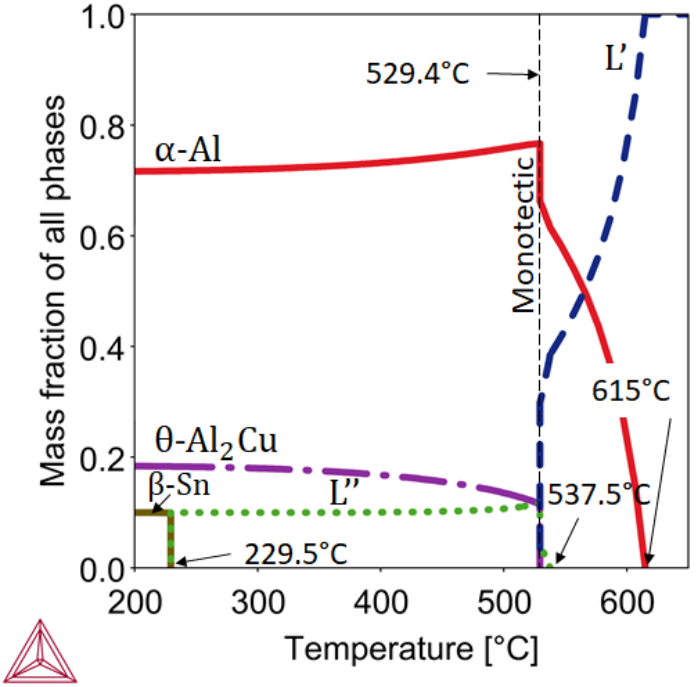

(c) Al-10wt.%Cu-10wt.%Sn

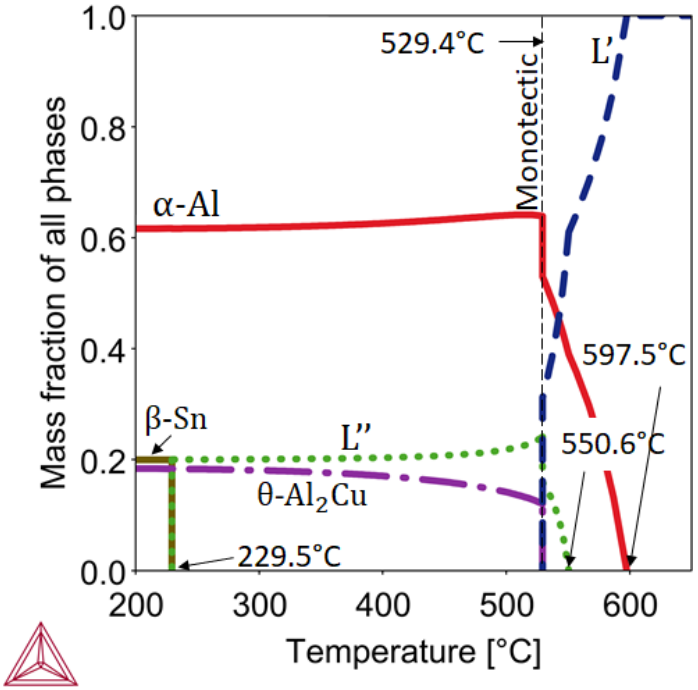

(d) Al-10wt.%Cu-20wt.%Sn

Figure 2.37: Equilibrium solidification paths for the four investigated alloys: a) Al-10 wt% Cu, b) Al-10 wt% Cu-5 wt% Sn, c) Al-10 wt% Cu-10 wt% Sn, d) Al-10 wt% Cu-20 wt% Sn.

For the two alloys with higher Sn compositions (X = 10 wt.% and X = 20 wt.%), solidification paths are similar to each other but more complex than for the low-Sn alloy due to the presence of the miscibility gap in the phase diagram (Figure 2.36). Similarly, to the low Sn-content alloy, solidification begins with α-Al formation but at different temperatures: at 615 °C for the Al-10 wt.% Cu-10 wt.% Sn as visible in Figure 2.37(c) and 597.5°C for the Al-10 wt.% Cu-20 wt.% Sn in Figure 2.37(d).

Figure 2.37(c) and (d) shows the simultaneous decrease of liquid proportion and increase of aluminum solid phase during the early solidification. Once these two compositions cross the liquid miscibility gap, the amount of α-Al continues to increase but a liquid phase separation occurs concomitantly. A dense Sn-rich liquid L'' begins to separate from L', usually in the form of droplets in the experiments, resulting in the formation of two distinct immiscible liquids. The number and size of droplets directly depend on the initial liquid composition [81]. For the 20 wt.% Sn alloy (Figure 2.37(d)), this separation becomes evident at 550.6°C, marked by a change in the slope of the initially monotonous liquid L' line (in blue), concomitantly with a formation of Sn-rich liquid L'' (in green), along with a change in the slope of the α-Al line (in red). The same phenomenon occurs in the 10 wt.%Sn alloy Figure 2.37(c), but for a very narrow range of temperature (from 537.5°C to 529.4°C), making it more difficult to distinguish.

At $T_{monotectic}$ = 529.4°C, a ternary monotectic reaction occurs, forming two solid phases (α-Al and θ-Al_2Cu), concomitantly with the enrichment in Cu and Sn of the residual liquid phase L' due to solute rejection during the liquid to solid phase transformation. Between $T_{monotectic}$ and $T_{eutectic}$ = 229.5°C, the residual liquid interacts with the solid α-Al to form solid θ-Al_2Cu. This slow reaction explains the slow decrease from right to left of α-Al (red line) and L' (blue line), simultaneously with an increase of θ-Al_2Cu (purple dash-point line). The residual liquid finally gives birth to the eutectic phase consisting of β-Sn, α-Al and θ-Al_2Cu at Teutectic = 229.5◦C.

2.4.1.4 Isothermal sections

For a sake of completeness, the isothermal sections of the Al-Sn-Cu alloy system were also calculated by using the Thermo-Calc software for a selection of key

temperatures to ascertain the solidification paths of both high solute content alloy compositions for which a liquid phase separation is expected (Figure 2.38).

- Figure 2.38(a) is the isothermal section calculated at T = 625 °C, which is an arbitrary temperature higher than the *liquidus* temperatures of both alloys (615 °C for Al-10Cu-10Sn and 597.5 °C for Al-10Cu-20Sn). For this temperature, it can be seen that both alloy compositions (dot in red for Al-10Cu-10Sn and dot in blue for Al-10Cu-20Sn) are in the region corresponding to the fully liquid state in the Al rich corner.
- The first solidification step involves the formation of solid α-Al corresponding to the green tie lines, as seen in Figure 2.38(b). This step is expected to start at a temperature slightly lower than the respective *liquidus* temperature of each alloy. Due to the solute rejection during the liquid to solid transformation, the copper and tin interdendritic liquid compositions progressively rise as solidification proceeds.
- The second step takes place when the enriched liquid L' meets the liquid miscibility gap. This occurs at a temperature of 537.5 °C for Al-10Cu-10Sn and 550.6 °C for Al-10Cu-20Sn. Figure 2.38(c) is the isothermal section at T = 540 °C, when the high-Sn content alloy (blue dot) is inside the region of liquid decomposition, whereas the low-Sn content alloy (red dot) is still in the $L' + \alpha - Al$ region.
- In Figure 2.38**(**d), both alloys are inside the region of liquid decomposition for a temperature just higher than the monotectic temperature of 529.4 °C. Within the miscibility gap, concomitant with the growth of α-Al, the interdendritic liquid phase is expected to undergo separation into two immiscible liquids. At this stage, there is a formation of dense Sn-rich liquid L''droplets, which separate from light Al-rich L'.
- According to Thermo-Calc calculations, the liquid phase demixing ends at the invariant ternary monotectic reaction, which takes place at the temperature of 529.4 °C with the simultaneous formation of two Al-rich solid phases (α-Al and θ-Al_2Cu), concomitantly with the Cu/Sn-enrichment of the residual liquid phase L' always due to Cu/Sn rejection during the liquid to solid phase transformation.

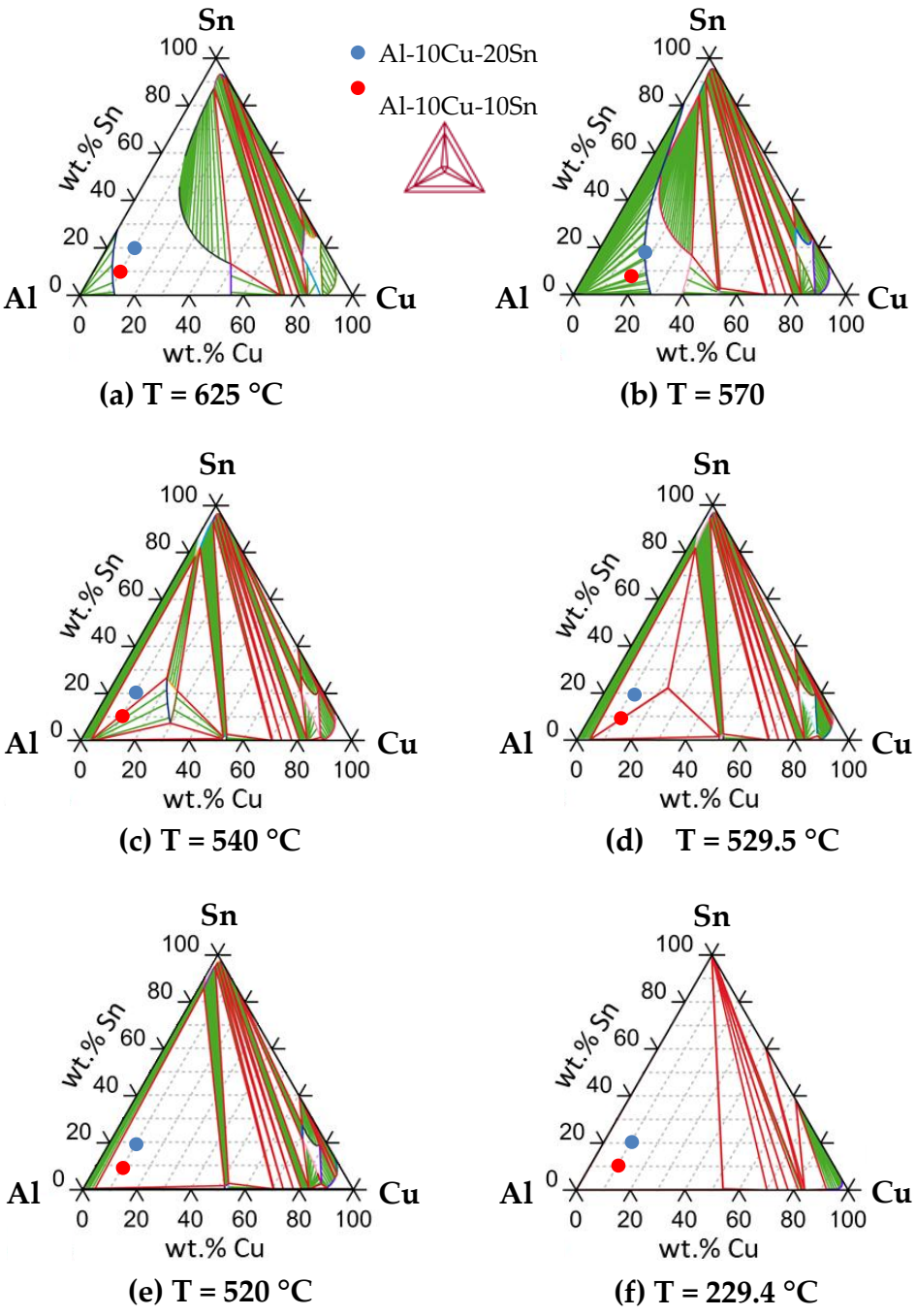

Figure 2.38: Series of isothermal sections of the ternary phase diagram for Al-Cu-Sn alloy, calculated at several temperatures by Thermo-Calc software: a) T = 625 °C; (b) T = 570 °C; (c) T = 540 °C; (d) T = 529.5 °C; (e) T = 520 °C; (f) T = 229.4 °C. The red and blue dots indicate the positions of the Al-10Cu-10Sn and Al-10Cu-20Sn alloy compositions in the isothermal sections.

2.4.2 Solidification paths by Differential Scanning Calorimetry (DSC)

Differential scanning calorimetry (DSC) was employed to investigate the solidification sequence. Measurements were performed by Dr. H. Soltani at School of Mines and Metallurgy Annaba, Algeria, using a NETZCH SAT 449 F3 Jupiter differential scanning calorimeter (Selb, Germany) shown in Figure 2.39. The equipment was calibrated using the melting points and enthalpies of fusion of high purity In, Sn, Bi, Zn, Al, Ag, Au and Ni metals.

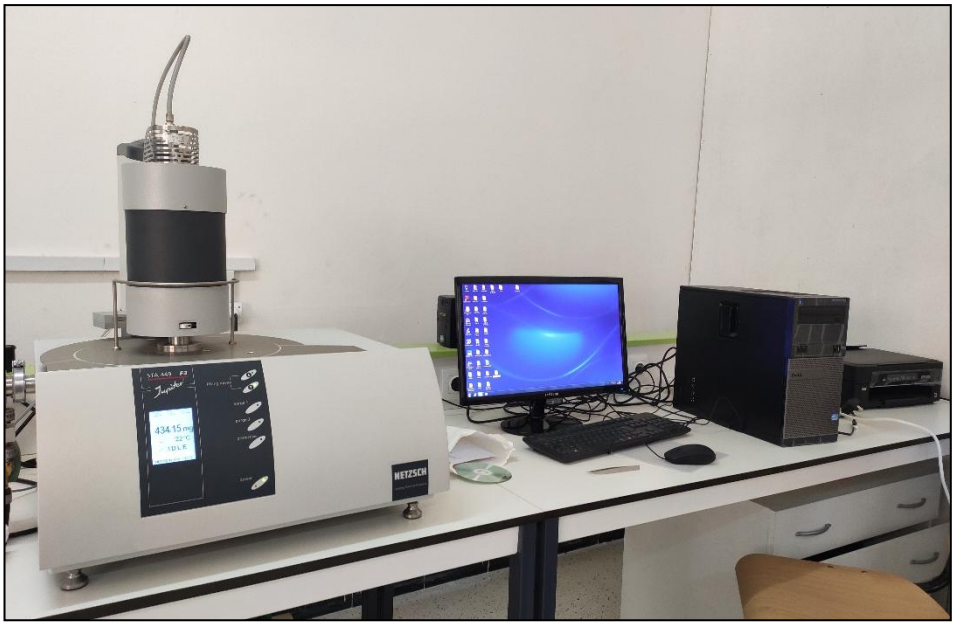

Figure 2.39: NETZCH SAT 449 F3 Jupiter differential scanning calorimeter equipment.

Calorimetric measurements are particularly convenient for monitoring the kinetics of phase transformations such as melting or solidification [82]. Changes in heat content in a solidifying material are directly proportional to the amount of solidification which has taken place and are closely related to the thermodynamic forces driving the solidification process [83].

Samples, approximately 20 mg ± 3 mg in weight, were sealed in alumina crucible while a second empty crucible was used as a reference. Analysis were conducted under nitrogen atmosphere with a flow rate of 20 mL/min. Heating and cooling were carried out at a constant rate of 5 °C/min over a temperature range from

room temperature to 750°C. A 15 minutes isothermal hold at 750°C was applied to ensure thermal homogenization prior to cooling.

2.4.2.1 DSC heating curves

The DSC heating curves (Figure 2.40) for all three alloys exhibit endothermic peaks with different widths and amplitudes. For increasing temperature (from the left side to the right side of each DSC melting curves), the successive key temperatures are:

(i) Eutectic reaction ($T_{eutectic}$): The first endothermic peak corresponds to the melting of ternary eutectic constituent β-Sn + θ-Al_2Cu + α-Al. This peak appears slightly below 230°C and nearly identical for all three compositions, indicating that eutectic reaction is relatively unaffected by Sn content within this composition range. This behavior is consistent with the Thermo-Calc equilibrium diagram, which predicted a stable eutectic reaction near this temperature.

(ii) Monotectic reaction ($T_{monotetic}$): The second peak is marked by a sharp, narrow peak located around 530°C for all compositions. This peak corresponds to the melting involving θ-Al_2Cu and α-Al phases. In the alloys with a high Sn content, this temperature marks the monotectic reaction according to Thermo-calc Figure 2.36.

(iii) Liquid phase separation: In the Al-10 wt% Cu-10 wt % Sn and Al-10 wt% Cu-20 wt% Sn alloy, a very shallow endothermic peak is observed just after the monotectic reaction, at about 549.2°C and 551.7°C, respectably. This subtle feature may be interpreted as the homogenization of the reimaging liquid phase, likely indicating the end of the miscibility gap and transition to a single liquid phase. Such behavior is supported by the Thermo-Calc phase diagrams, which predict a miscibility gap in the liquid phase at high Sn contents.

(iv) Melting of α-Al ($T_{liquidus}$): The latest peak corresponds to the melting of the α-Al dendrites. This peak shifts to lower temperatures with increasing Sn content and are particularly sensitive to composition, decreasing from roughly 617°C to below 585°C, this behavior agrees with the Thermo-Calc predictions.

(a)Al-10 wt. %Cu -5 wt.%Sn

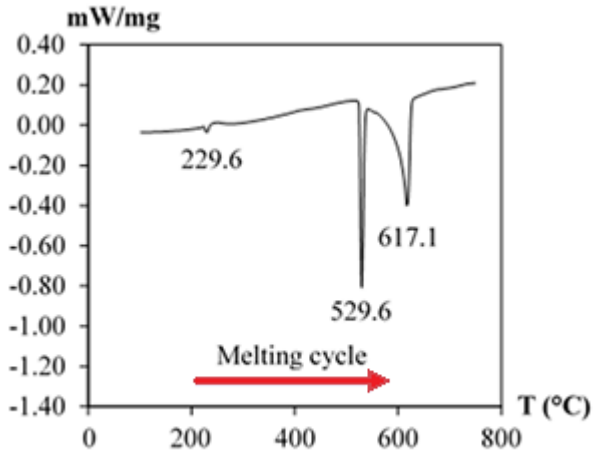

(b)Al-10 wt. %Cu -10 wt.%Sn

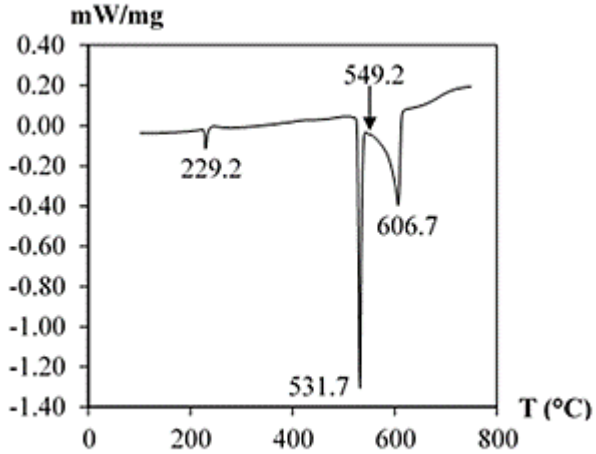

(c) Al-10 wt. %Cu -20 wt.%Sn

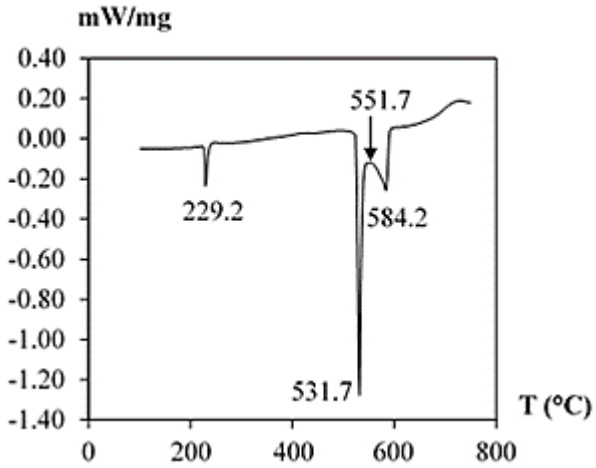

Figure 2.40: Melting DSC curves of the three different alloys recorded during sample heating, showing the endothermic peak of each transformation: (a) Al-10 wt.% Cu-5 wt.% Sn; (b) Al-10 wt.% Cu-10 wt.% Sn and (c) Al-10 wt.% Cu-20 wt.% Sn.

2.4.2.2 DSC cooling curves

The cooling DSC curves (Figure 2.41) exhibits exothermic events related to the solidification sequence. Notably, the number and values of peaks vary between the low Sn content alloys and the high Sn content alloys:

(i) Primary solidification (α-Al): The first exothermic peak corresponds to the nucleation and growth of α-Al dendrites. As Sn content increases from 5wt.% to 20wt.%, the $T_{\alpha\text{-Al}}$ decreases from 610°C to 572°. This trend is consistent with the Thermo-Calc predictions in Figure 2.36.

(ii) Liquid phase separation: A small exothermic peak is visible at 525.5°C for the 10wt.% Sn and at 530.3°C for the 20wt.%Sn alloy. It corresponds to the liquid phase separation, when the homogeneous liquid comes into the miscibility gap. This peak is absent in the 5wt.%Sn alloy, which aligns with the Thermo-Calc diagrams showing no miscibility gap at low Sn concentration of Figure 2.37 (b).

(iii) Monotectic Reaction: The monotectic reaction at $T_{monotectic}$ gives birth to a very narrow and intense peak, with the formation of both θ-Al_2Cu and α-Al phases.

(iv) The last transformation occurs at Teutectic and ends the solidification path with the formation of the eutectic phases β-Sn + θ-Al_2Cu + α-Al.

(a) Al-10 wt. %Cu -5 wt.%Sn

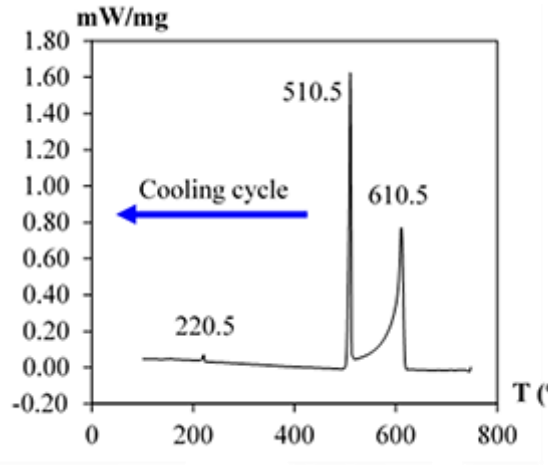

(b)Al-10 wt. %Cu -10 wt.%Sn

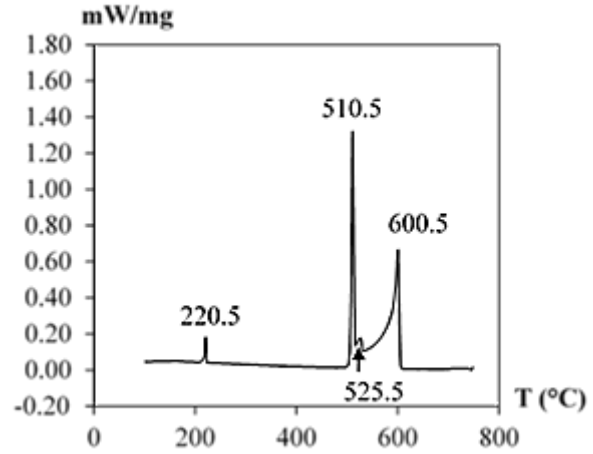

(c)Al-10 wt. %Cu -20 wt.%Sn

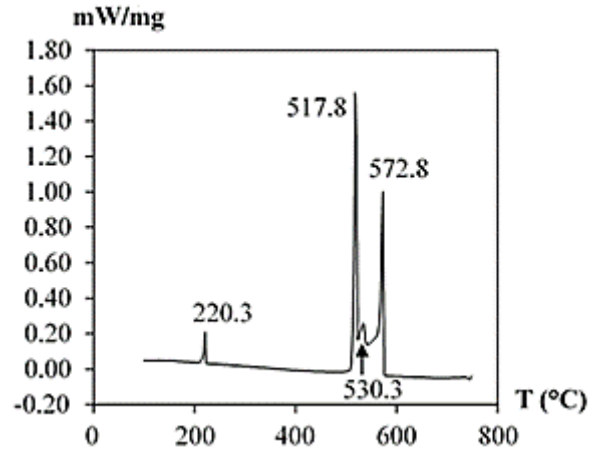

Figure 2.41: Cooling DSC curves of the three different alloys showing the exothermic peak of each transformation: (a) Al-10wt.%Cu-5wt.%Sn; (b) Al-10wt.%Cu-10wt.%Sn and (c) Al-10wt.%Cu-20wt.%Sn.

The main difference between the cooling curves of the high Sn content alloys (10 and 20 wt. %) and the low Sn content (5 wt.%) lies in the presence of an additional peak between the Tα-Al and $T_{monotectic}$. This intermediate peak corresponds to the liquid phase separation associated with the miscibility gap on the system Figure 2.36. The absence of this feature in the 5 wt.% Sn alloy supports the CALPHAD computational data indicating a single liquid phase regime for that composition.

According to the data obtained from the Thermo-Calc mass fraction diagrams, Figure 2.37, and associated spreadsheets, the critical transformations for each alloy composition were identified and compared with the peak temperatures of the DSC cooling cycle. The temperatures from both analyses are summarized in Table 2.2, Table 2.3, and Table 2.4.

Table 2.2: Temperature ranges of the different reactions calculated using Thermo-Calc and deduced from the temperature peaks in the DSC data during the cooling of the Al-10 wt.% Cu-5 wt.% Sn alloy.

Phase reactions	**Temperature range (Thermo-Calc)**	**Temperature range (DSC; Cooling)**
L	Above 624°C	Above 610.5°C
L' → α-Al	From 624 to 531.5 °C	From 610.5 to 510.5 °C
L' → α-Al + θ-Al_2Cu	From 531.5 to 524.8 °C	From 510.5 to 220.5 °C
L' + α-Al → θ-Al_2Cu	From 524.8 to 229.5 °C	
L' → α-Al + θ-Al_2Cu + β-Sn	At 229.5 °C (Eutectic reaction)	At 220.5 °C (Eutectic reaction)

Table 2.3: Temperature ranges of the different reactions calculated using Thermo-Calc and deduced from the temperature peaks in the DSC data during the cooling of the Al-10 wt.% Cu-10 wt.% Sn alloy.

Phase reactions	**Temperature range (Thermo-Calc)**	**Temperature range (DSC; Cooling)**
L	Above 615°C	Above 600.5°C
L' → α-Al	From 615 to 537.5 °C	From 600.5 to 525.5 °C
L' → α-Al + L''	From 537.5 to 529.4°C	From 525.2 to 510.5°C
L' → α-Al + L'' + θ-Al_2Cu	At 529.4 °C (Monotectic reaction)	At 510.5 °C (Monotectic reaction)
L'' + α-Al → θ-Al_2Cu	From 529.4 to 229.5°C	From 510.5 to 220.5°C
L'' → α-Al + θ-Al_2Cu + β-Sn	At 229.5 °C (Eutectic reaction)	At 220.5 °C (Eutectic reaction)

Table 2.4: Temperature ranges of the different reactions calculated using Thermo-Calc and deduced from the temperature peaks in the DSC data during the cooling of the Al-10 wt.% Cu-20 wt.% Sn alloy.

Phase reactions	**Temperature range (Thermo-Calc)**	**Temperature range (DSC; Cooling)**
L	Above 597.5°C	Above 572.8°C
L' → α-Al	From 597.5 to 550.6 °C	From 572.8 to 530.3 °C
L' → α-Al + L''	From 550.6 to 529.4°C	From 530.3 to 517.8°C
L' → α-Al + L'' + θ-Al_2Cu	At 529.4 °C (Monotectic reaction)	At 517.8 °C (Monotectic reaction)
L'' + α-Al → θ-Al_2Cu	From 529.4 to 229.5°C	From 517.8 to 220.3°C
L'' → α-Al + θ-Al_2Cu + β-Sn	At 229.5 °C (Eutectic reaction)	At 220.3 °C (Eutectic reaction)

2.4.3 In-situ observations during directional solidification experiments

2.4.3.1 Dendritic microstructure formation

Sets of X-ray images representing the initial formation of α-Al are presented for each Al-10wt.%Cu-xwt.% Sn in Figure 2.42. The growth of columnar α-Al dendrites from the solid seeds initiated a few seconds after cooling begins for each alloy. These dendrites, which appear as bright white in the radiographs, have this brightness due to their lower X-ray absorption and are surrounded by darker regions, which corresponds to the liquid enriched in Cu and Sn rejected at the solid/liquid interface. The solute rejection induced the formation of an undercooled liquid ahead of the solidification front, leading to the nucleation of new dendritic grains on the sample wall that blocked the progression of the first columnar grains. The new α-Al grains had random crystallographic orientations and developed preferentially in the temperature gradient direction [69,84]. In a same way, a few additional grains nucleated ahead of the elongated grains and were incorporated into the solidification front. After this transient step, the solidification front corresponding to the position of the dendrite tips (outlined by the dashed lines) was quite flat, indicating that there is no significant transverse temperature gradient or convective flow. As cooling progresses, the entire field of view was filled with dendrites that have grown and slowly coarsened.

A careful examination of the dendrite morphology highlighted that the secondary dendrite arms do not develop perpendicular to the primary trunks as usually expected in aluminum alloys, but with a lower angle for Al-10wt.%Cu-10wt.%Sn and for Al-10wt.%Cu-20wt.%Sn as shown in Figure 2.43(a). The growth orientation of the dendrite arms was determined unambiguously for the Al-10wt.%Cu-20wt.%Sn and for the Al-10wt.%Cu-5wt.%Sn by post-mortem analyses using EBSD (Electron Backscatter Diffraction) (Figure 2.43). Orientation maps were collected using a Zeiss Gemini 500 field-emission gun scanning electron microscope (FEG-SEM) equipped with an EDAX Hikari Super acquisition system [85].

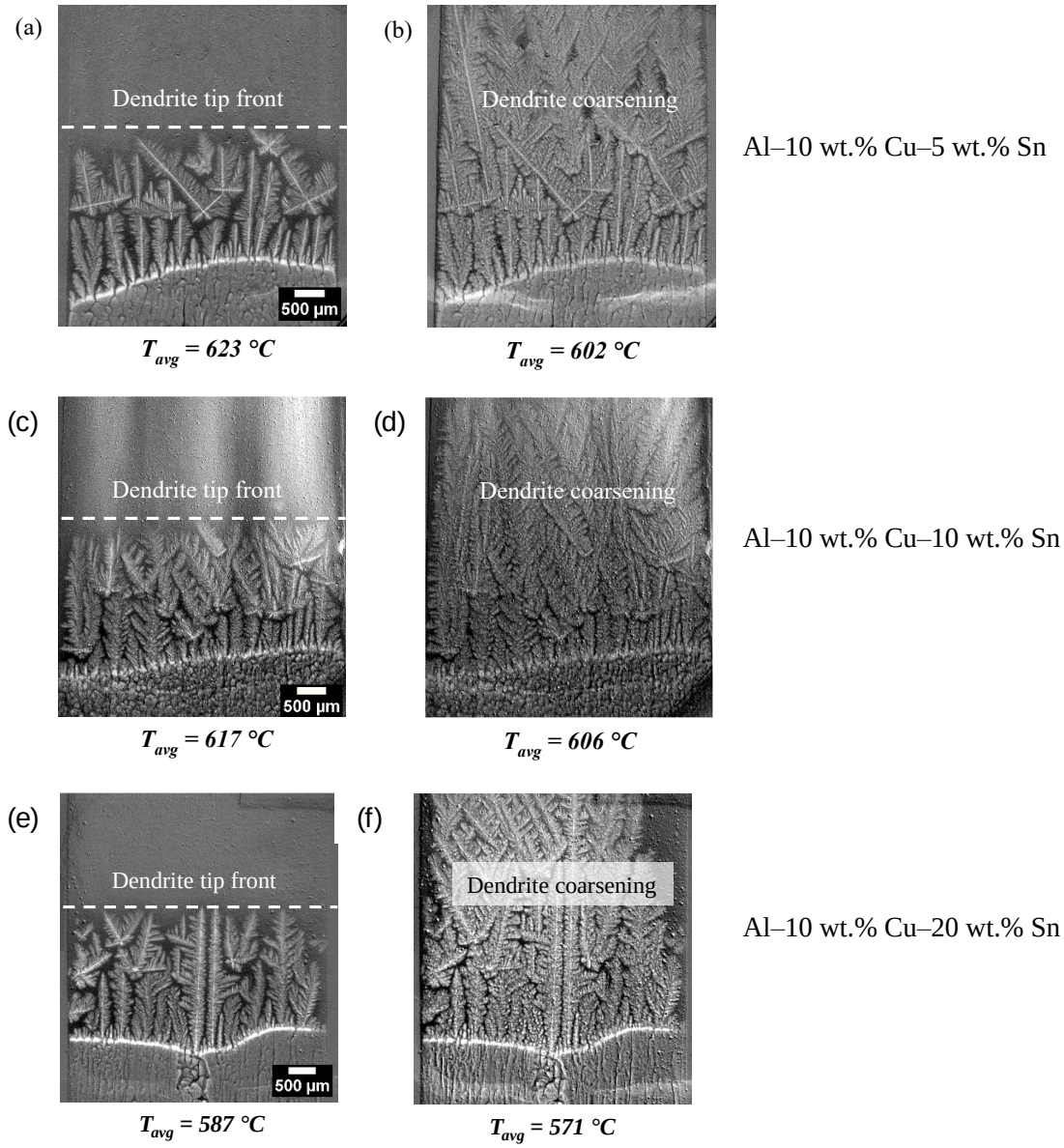

Figure 2.42: Sequence of radiographs recorded during the dendritic growth regime (R = 0.15 °C/s and G_{app} = 5.55 °C/mm).

The comparison between the arm growth directions and the (101) pole figure obtained for a dendritic crystal of Al-10wt.%Cu-20wt.%Sn indicates that the primary trunk and secondary arms have been developing in <110> directions. This deviation from the <100> directions, commonly found in aluminum and aluminum alloys, is characteristic of a Dendrite Orientation Transition (DOT). Such as transition in metallic systems was recently highlighted by Haximali *et al.* [86] for Al-Zn binary alloys and is reported in the literature for several other binary alloys such Al-Ge [87], Al-Sm [88]

and Al-Cu [89]. To date, the occurrence of a DOT in a ternary alloy such as Al-Sn-Cu hasn't been reported. However, a study combining experimental and numerical investigations of the equilibrium shape of droplets for Al-Sn alloys by Napolitano *et al.* [90] hinted at the possibility that <110> may be favored at high Sn content. However, the detailed investigation of the DOT is out-of-the scope of the present PhD

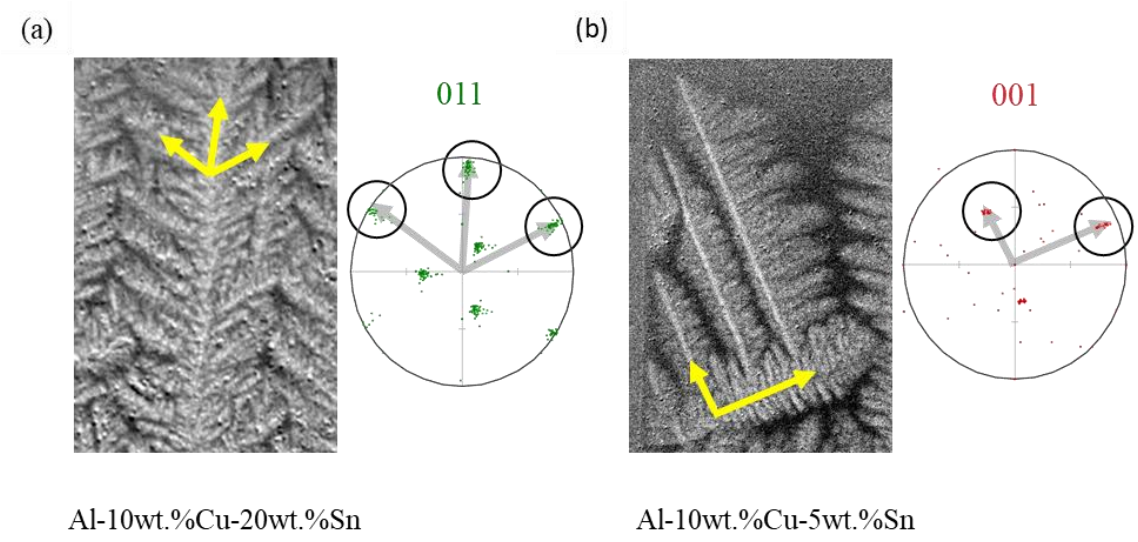

Figure 2.43: Close-ups of radiographs showing an aluminum dendrite and corresponding pole figure obtained by EBSD for (a) Al-10wt.%Cu-20wt.%Sn and (b) Al-10wt.%Cu-5wt.%Sn.

2.4.4 Subsequent solidification of the Al-10wt.%Cu-5wt.%Sn alloy

The observation of the subsequent solidification of the Al-10wt.%Cu-5wt.%Sn alloy is illustrated in Figure 2.44, showing a radiograph recorded at temperature of 537°C and by applying flat-field correction (Figure 2.44(a)) and frame differencing (Figure 2.44(b))

As visible in Figure 2.44(a), the dendritic network has experienced a long coarsening period, and the secondary and ternary arms are now difficult to distinguish. In addition, the half top part of the sample is brighter than the half-bottom part of the sample. This change in grey level is abrupt as indicated by the dashed line, which means that a phase transformation occurred. In Figure 2.44(b), the frame differencing image

reveals the formation of a dark layer above a white layer at this given temperature. Notably, coarsening phenomena are not detectable in the frame-differencing images because of the very weak modification induced by coarsening during the short-time interval between the two raw images. The white layer can be attributed to the formation of α-Al phase, which is less absorbing, and the dark layer can be attributed to the formation of Al_2Cu phase, as it is more absorbing than the initial liquid phase. Accordingly, Al_2Cu formation is probably the cause of the global darkening seen in the lower part of Figure 2.44(a). These findings are consistent with the predicted solidification path for this alloy, as illustrated in Figure 2.37(b) and detailed in Table 2.2.

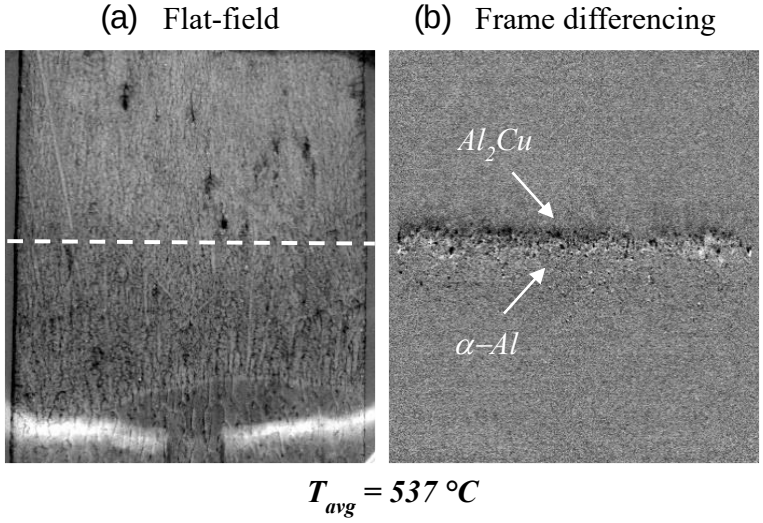

Figure 2.44: Sequence of radiographs of Al-10wt.%Cu-5wt.%Sn solidification (R = 0.15 °C/s and G_{app} = 5.55 K/mm) showing the reaction L'→ α-Al + θ-Al_2Cu. (a) flat-field image and (b) image with frame differencing correction highlighting the formation of Al_2Cu and α-Al.

The solidification process ended with the eutectic transformation, which gives the formation of β-Sn, α-Al and θ-Al_2Cu phases. This transformation induces a very small change in absorption contrast on the radiograph but could nevertheless be detected by using the frame-differencing procedure in all alloys. An estimate of the eutectic

temperature from the in-situ experiments is T_{eut} = 223°C, in good agreement with Thermo-Calc and DSC measurements.

2.4.4.1 Phase separation and monotectic reaction

As expected from the previous thermodynamic calculations and DSC measurements, a liquid phase separation followed by a monotectic reaction was observed in both Al-10wt.% Cu-10wt.%Sn and Al-10wt.%Cu-20wt.% Sn during the experiments using X-ray radiography. However, in-situ observations revealed distinct features in the Sn-richest investigated composition as will be described below.

a) Phase separation and monotectic reaction in the Al-10wt.%Cu-10wt.%Sn

Figure 2.45 exhibits radiographs recorded at a temperature close to 540°C for the Al-10 wt.% Cu-10 wt.% Sn alloy. In the flat-field image of Figure 2.45(a), a sharp contrast separates a brighter upper region from a darker middle section, suggesting the occurrence of a reaction around that specific temperature, but whose features are difficult to distinguish. Fortunately, the frame differencing image Figure 2.45(b) further clarifies this transition. As previously mentioned, the solid dendritic network that evolves only very slowly during the sample cooling is completely erased and replaced by a uniform grey background by applying the frame differencing procedure to the radiographs. As a result, the formation of two distinct layers is significantly highlighted: a top stripe featuring dispersed black dots, followed by a bright white region with smaller black dots. These observations are consistent with the occurrence of liquid phase separation and monotectic reaction, where the black layer corresponds to the formation of a large amount of the Sn-rich liquid L'' during the liquid phase separation. The bright layer underneath occurs due to the formation of a high amount of α-Al, as expected during the monotectic reaction. It is worth mentioning that the black dots in the white layer can be either θ-Al_2Cu or L'' phases that are both absorbing and thus could not be distinguished with the current spatial resolution, but are both related with the darkening of the bottom part of the image in Figure 2.45(a).

From these observations, it can be deduced that the liquid demixing begins in the center of the field of view at a value of roughly 540 °C, while it is predicted to start at

537.5 °C by Thermo-Calc software (Table 2.3). Those values are in good agreement, considering the uncertainties or errors of both methods. For directional solidification experiments, the uncertainty is mainly attributed to the temperature distribution in the FoV, the resolved pixel size (of about 4 µm) and possibly the presence of natural convection, which is not fully eliminated, or buoyancy forces acting on Sn droplets. All these effects prevent obtaining an accurate value for the inception of the liquid separation.

The time evolution of a longitudinal cut of the central region of the FoV was analyzed in detail (Figure 2.45c, d and e) to reveal the dynamics of the liquid phase separation and monotectic reaction. At the bottom of Figure 2.45(c), the inception of the liquid phase separation in between the dendrites is visible; the white dash line indicates the first droplets that are detected, measuring a few tens of microns in diameter. The black areas correspond to the Sn-rich liquid L''zones that have nucleated in the L' liquid during the liquid demixing. These Sn-rich liquid zones are shaped either in the form of round droplets, or as large zones of liquid which could be the result of droplet coalescence. The few white dots are artefacts due to the frame-differencing image processing. As cooling proceeds, it is then possible to see in Figure 2.45(d) and Figure 2.45(e) both the liquid phase demixing and the subsequent monotectic reaction. The impact of the dark and white layers on the vertical average grey level profile along the field-of-view is visible in Figure 2.45(f). The extent of the liquid phase separation appears as a bump toward the left side of the average grey-value, while the monotectic reaction appears as a narrower peak toward the right-hand side. The temperature gap between the liquid phase separation and the monotectic reaction can be estimated from the distance between the inception of the phase separation and the monotectic front and knowing the applied temperature gradient. A temperature difference of about 5 °C is obtained, which is nearly twice as small as the value predicted by Thermo-Calc calculations which is about 8 °C (Table 2.3).

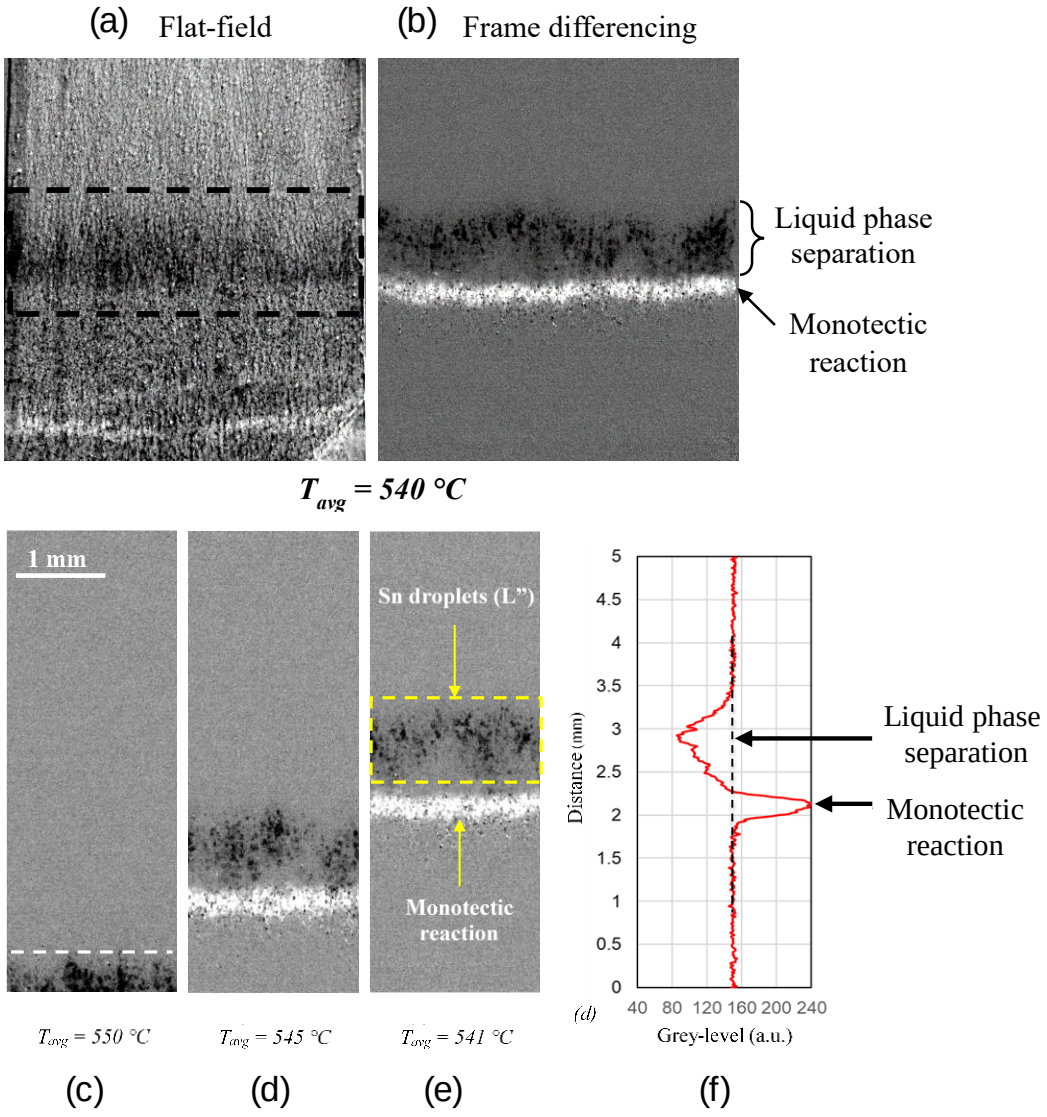

Figure 2.45: Sequence of radiographs of Al-10wt.%Cu-10wt.%Sn solidification (R = 0.15 °C/s and G_{app} = 5.55 °C/mm) showing the liquid phase separation and monotectic reaction. (a) flat-field image with the separation of the liquid phase highlighted in the frame. (b) image with frame differencing correction, highlighting the liquid phase separation (L'+L") and the monotectic reaction. (c), (d) and (e), sequence of three radiographs after the frame differencing processing revealing the propagation of the liquid phase separation front followed by the monotectic reaction front. T_{avg} is the temperature at the center of the field of view, (f) Vertical average grey level profile along the field-of-view is in arbitrary unit (a.u.).

b) Phase separation and monotectic reaction in the Al-10wt.%Cu-20wt.%Sn

Figure 2.46 shows observations made at a temperature of 543°C by applying flat-field correction (Figure 2.46(a)) and frame differencing (Figure 2.46(b)) to the same radiograph. This time, three regions with different contrasts indicated by dashed lines can be distinguished in Figure 2.46(a): the top part and bottom parts of the image are brighter than the middle part. Figure 2.46(b) (frame differencing image) reveals, from top to bottom, a light grey layer containing small black dots above a dark layer, and a white region also containing small black dots.

The light grey layer in the top of the field of view can be attributed to the depletion in Sn of the L' liquid due to the formation of the Sn-rich L'' liquid, appearing as small black droplets. The black layer below corresponds to the sudden formation of a large amount of the Sn-rich liquid L'' during the liquid phase separation and is the cause of the darkening seen in the middle part of Figure 2.46(a). Finally, the white region agrees with the formation of a high amount of α-Al as expected during the monotectic reaction and is the cause of the brightening seen in the bottom part of Figure 2.46(b). As previously mentioned, the black dots in the white layer can be either Al_2Cu or L'' phases that are both absorbing and thus could not be distinguished with the current spatial resolution.

This time, the sequence of phase formation is only partly in line with the theoretical solidification path (Figure 2.37 and Table 2.4), as the phase separation leading to the formation of the Sn-rich liquid L'' did not occur with a linear increase of the mass fraction of L'' but in two steps: firstly, the progressive formation of small droplets and secondly the sudden occurrence of a large amount of L'' as indicated in Figure 2.46(b). These results suggest that although the overall sequence of phase formation remains consistent across both 10wt.%Sn and 20wt.%Sn compositions, the kinetics of liquid phase separation are strongly influenced by the Sn content.

For a sake of completeness, Figure 2.46(c) to Figure 2.46(f) display three images illustrating the liquid phase separation during the solidification experiment of the Al-10wt.%Cu-20wt.%Sn alloy, as well as the vertical average grey level profile along the field-of-view. It is worth reminding that the three radiographs are processed by using frame differencing to enlighten the liquid phase decomposition. In the lower third of

Figure 2.46(a), the early stages of the liquid phase separation in between the dendrites are visible. Below the dash line, the first step of the liquid demixing is clearly visible, with the nucleation of small spherical black Sn droplets (L''), measuring a few tens of microns in diameter, in a light grey layer (L'). The light grey layer that is visible in Figure 2.46(c) and then visible on the top of the yellow rectangle in Figure 2.46(d) and Figure 2.46(e) can be ascribed to the Sn depletion of the remaining liquid L'. In Figure 2.46(f), the light grey layer causes a small bump towards the right-hand side to appear on the top of the vertical average grey level profile.

As cooling proceeds, it is then possible to see in Figure 2.46(d) the second step of the liquid phase demixing and the subsequent monotectic reaction. The second step of liquid phase demixing starts with a sudden increase of L''amount, which leads to the formation of a blurred dark region with the presence of a few droplets, roughly one millimeter below the beginning of the first step of liquid phase demixing. This darkening causes the bump toward the left side seen in the vertical average grey level in Figure 2.46(f). At a lower temperature, the monotectic reaction creates a very white layer due to the formation of a large amount of α-Al and θ-Al_2Cu.

The temperature difference between the liquid phase separation and the monotectic reaction can be estimated in the same way than for the l0wt.%Sn-content alloy. A temperature gap of about 11 °C is measured, which is nearly half the value predicted by Thermo-Calc calculations which is about 21 °C according to Table 2.4. This temperature interval between liquid demixing and the onset of the monotectic reaction is wider than in the 10 wt% Sn alloy and the light grey layer wasn't detected in the 10wt.%Sn alloy. This is most probably because the phase separation and the monotectic reaction occurred at closer temperatures in the 10wt.%Sn alloy and the change in composition of L' was lower.

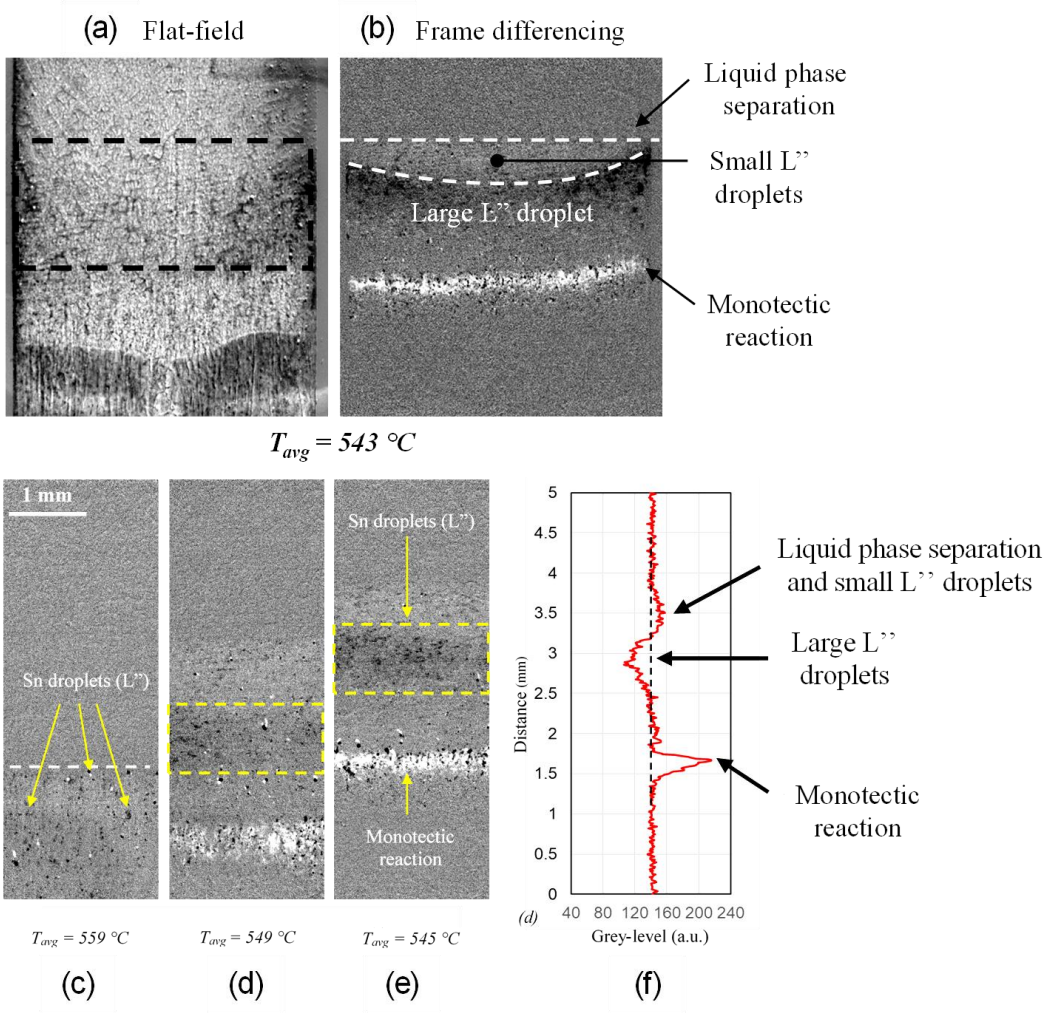

Figure 2.46: Sequence of radiographs of Al-10wt.%Cu-20wt.%Sn solidification (R = 0.15 °C/s and G_{app} = 5.55 °C/mm) showing the liquid phase separation and monotectic reaction. (a) flat-field image with the separation of the liquid phase highlighted in the frame. (b) image with frame differencing correction, highlighting the liquid phase separation (L'+L") and the monotectic reaction. (c), (d) and (e), sequence of three radiographs after the frame differencing processing revealing the propagation of the liquid phase separation front followed by the monotectic reaction front. T_{avg} is the temperature at the center of the field of view, (f) Vertical average grey level profile along the field-of-view is in arbitrary unit (a.u.).

2.4.4.2 Discussion on the liquid phase separation dynamic

The two-step liquid phase separation observed during the solidification of the Sn-richer alloy can be interpreted through two hypotheses, both supported by prior

literature. Due to the limited spatial resolution of the in-situ radiographic images, the explanations proposed here remain speculative and are intended to offer a plausible framework for understanding the observed phenomena.

One potential explanation may be a transition of the liquid from the immiscible domain to a miscible domain as suggested by [66] for Al-6wt.%Bi-8wt.%Zn. Like for Al-10Cu-20Sn, the liquid phase demixing in their ternary alloy is followed very closely by the monotectic reaction. With synchrotron in-situ X-ray radioscopy, Schaffer *et al*. [66] found that, as the monotectic front approaches the Bi droplets, they dissolve and form diffuse clouds as can be seen in Figure 2.47, reproduced from reference [66].

A similar mechanism may be active in the Al-10wt.%Cu-20wt.%Sn alloy. During the monotectic reaction, which occurs at a lower temperature than the liquid phase separates, significant rejection of Sn into the remaining melt crates a Sn-rich boundary layer by diffusion ahead of the advancing front. This local composition shift may reduce the surface tension of the L'' droplets, leading to a transition from the immiscible domain to a miscible domain, which causes the droplets to break up into clouds. This change in droplets behavior may likely explain the 'fuzzy' black color in larger quantities in Figure 2.46(e).

A second alternative interpretation is grounded in the thermodynamical of liquids phase separation, particularly the transition from the binodal region to the spinodal region of the miscibility gap, which occurs as a result of changes in composition and temperature as described by [29]. Indeed, in certain cases, the miscibility gap may comprise two regions (Figure 2.48):

- In the region between the binodal and the spinodal curves, the uniform liquid is assumed to be metastable. Therefore, the formation of Sn droplets requires a certain amount of energy, which can be greatly reduced by the help of inhomogeneities or impurities in the system (heterogenous nucleation). In our experiments, owing to the thickness of the sample, the internal oxide layer of the sample could provide some active sites, like for the nucleation and growth of equiaxed grains [14,68]. Nevertheless, the nucleation and growth of Sn droplets remains rare.

- For liquid compositions within the spinodal dome, the homogeneous solution is unstable against microscopic fluctuations in density or composition. Therefore, the liquid demixing will take place immediately, with no thermodynamic barrier to the growth of a new phase and the phase transformation is solely diffusion controlled. In that case, the Sn-rich liquid may appear in the form of clouds and in large quantity.

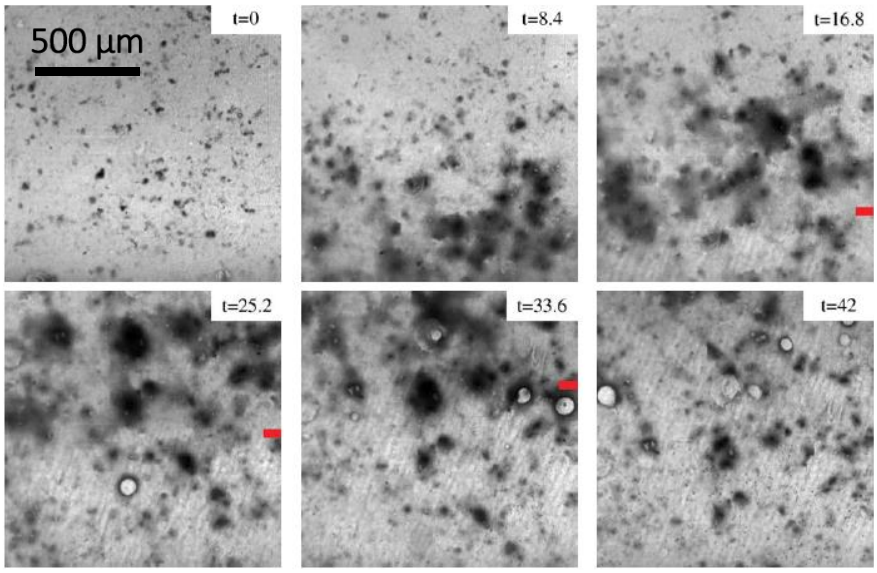

Figure 2.47: (Reproduced from [66]) Al - 6wt.%Bi-8wt.%Zn alloy solidified in a thermal gradient of 60 K/mm and at a velocity of 17.5 µm/s. The transition from immiscible to miscible liquids when the Zn-rich boundary layer approaches can be seen from t = 0 to 16.8s. As the diffuse Bi domains move closer to the monotectic front Zn concentration reduces and immiscibility re-establishes leading to secondary nucleation of Zn droplets (t = 25.2 to 42s). Image size corresponds to 1.3 × 1.3 mm^2.

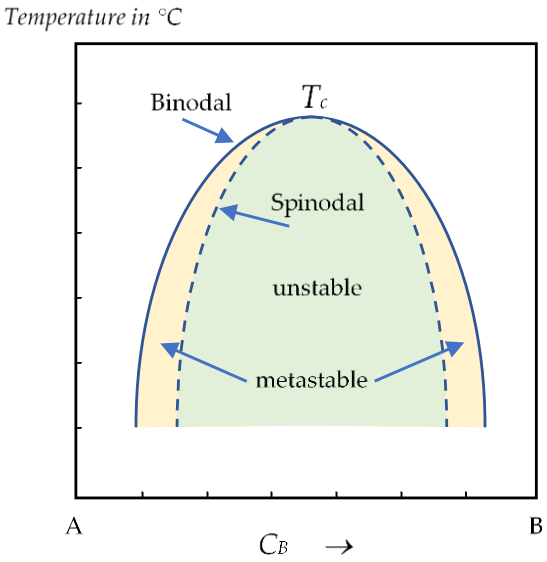

Figure 2.48: Typical Temperature x Composition graph for a binary alloy, showing the miscibility gap and spinodal line in a regular solution system. Uniform liquid within the spinodal curve is unstable and can decompose without overcoming an energy activation barrier. Uniform liquid between the binodal and spinodal curves are metastable and decomposition must proceed by a process of nucleation and growth.

Accordingly, in our experiments with Al-10Cu-20Sn alloy, the two-step liquid phase separation that has been observed by in-situ X-ray radiography may be explained by the fact that, to reach the spinodal region of the phase diagram, a transition must take the material through the binodal region, so that liquid phase separation will start by a first step of nucleation and growth of some rare Sn droplets, followed by the spinodal decomposition with the formation of a huge quantity of Sn liquid.

Using phase field simulation, Oliveira *et al.* [38] also observed variations in the size and shape of liquid domains during their evolution in the miscibility gap region of the Bi-Zn system. Morphological analysis as function of temperatures for a certain composition revealed that, as the temperature decreased, the precipitated liquid evolved from spherical shapes to thicker, interconnected domains.

2.5 Conclusions

Determination of reliable solidification paths for ternary alloys is difficult. In the literature, several different approaches are used, which sometime present divergent results and are subject to large uncertainties. In this work the solidification paths of Al-10 wt% Cu-X wt% Sn (with X = 5; 10 and 20) alloys were successfully investigated by using three different and complementary approaches, namely Thermo-Calc calculations, thermal analysis and solidification experiments with *in-situ* X-ray radiography monitoring. The results provided a comparison between those methods, both qualitatively (nature of the successive phase transformations) and quantitatively (temperature at which each phase transformation occurs).

Evaluation of the temperature at which each phase transformation occurs has been also carried out by the different methods. A wide dispersion has been found, up to 10°C for some phase transformations. Thermo-Calc calculations and thermodynamic measurements have intrinsic limitations. For solidification experiment, the main weakness is the accurate knowledge of the temperature distribution in the Field-of-View. Further improvements of the current apparatus are required to achieve the necessary temperature resolution.

The main qualitative conclusion is that all these methods describe correctly the successive phase transformations, from the initial α-Al dendrite growth to the final eutectic transformation of the residual liquid. However, it has been found that, depending on the alloy composition, the liquid-phase separation processes were dramatically different. For the low-Sn-content sample, the liquid-phase separation takes place gradually until the monotectic reaction occurs. For the high-Sn-content sample, liquid-phase separation is performed in two steps, which cannot be predicted by Thermo-Calc calculations. The origin of this two-step liquid separation is unclear and two plausible explanations are proposed. Further analyses and complementary experiments are required to improve our knowledge about this topic. Nevertheless, the high sensitivity of liquid-phase separation behavior depending on alloy composition, and the resulting different microstructures, show the importance of this type of study from both fundamental and industrial points of view.

CHAPTER 3 – AL-20SN-1CU SELF-LUBRICATING ALLOY: MICROSTRUCTURE, MECHANICAL PERFORMANCE, AND WEAR BEHAVIOR

3.1 Introduction

Aluminum alloys are extensively used in engineering applications, particularly in the aerospace and automotive sector, owing to their favorable combination of high specific strength, low density, corrosion resistance, and recyclability. In practice, however, the superior performance of these alloys is not solely defined by their chemical composition, but to a great extent by the microstructure that develops during solidification. Consequently, a thorough understanding of solidification phenomena is essential for controlling microstructural features and, ultimately, material performance.

Chapter 2 addressed the fundamental aspects of solidification, including key concepts such as non-faceted and faceted solid/liquid interfaces, morphological instabilities due to constitutional undercooling, and the formation mechanisms of cell and dendrites. Building on this foundation, the present chapter shifts from model alloys solidified under controlled cooling rate and thermal gradient to an industrial alloy solidified under transient heat extraction. Such conditions are typical of manufacturing processes such as permanent mold casting, die casting, and rapid solidification, in which heat flow varies both spatially and temporally. As a result, non-uniform thermal gradients and fluctuations in the solidification front velocity are inherently produced.

Within this context, this chapter provides an overview of the physical phenomena governing transient solidification. It begins with an analysis of the heat transfer during solidification, which enables the estimation of solidification times and the evaluation of thermal gradients across the component thickness. This is followed by an analysis of the influence of thermal solidification parameters, such as cooling rate, thermal gradient, and solidification front velocity, highlighting how these dynamic factors shape the microstructure. Special attention is given to dendritic growth prediction models applied to aluminum alloys, which are essential tools for linking processing conditions to microstructural scale.

The discussion then narrows to a specific and advanced material class: self-lubricating aluminum alloys. Through selected case studies, the influence of varying

cooling rates, in combination with specific solute elements, is assessed. These investigations highlight the impact of solidification kinetics on the microstructure formation, offering insights into the design and processing of advanced aluminum-based materials.

Self-lubricating Al alloys are composite materials consisting of hard and soft phases, each with distinct functional roles. The hard phase is responsible for load-bearing, while the soft phase acts as a solid lubricant, reducing friction at the contact interface. Typical soft phases include Sn, In, Pb, and Bi, which are characterized by low melting points and low shear strength. Under sliding conditions, these elements may form lubricating films due to frictional heating, thereby improving wear resistance.

The performance of these alloys is strongly governed by their microstructure, particularly by the morphology, size, and distribution of the soft phases. These features significantly influence both mechanical properties and wear behaviour. To better understand these effects, different types of wear, referred to as adhesive, abrasive, oxidative, and fatigue wear, as well as their underlying mechanisms must be discussed.

In this framework, the present chapter reports a comprehensive study of the Al-20wt%Sn-1wt%Cu alloy, focusing on the relationship between its solidification microstructure, mechanical properties, and wear behavior. For this purpose, a directional solidification ingot was produced under heat transient conditions, covering the entire process from material preparation to directional solidification.

3.2 Literature review

3.2.1 Generalities of solidification under transient heat flow conditions

3.2.1.1 Unsteady-state directional solidification

Considering solidification under equilibrium, there is complete solute redistribution ahead of the solid/liquid interface. In which case, the microstructure tends to be uniform with nominal composition, well-defined phase fraction, following the equilibrium phase diagram [1]. In contrast, during non-equilibrium solidification, typical of most industrial casting processes, the high heat extraction rate, combined with the limited diffusion length of the solute in the solid, hinders solute redistribution, and consequently prevents compositional homogenization. This leads to microstructural features that deviate from equilibrium predictions, including solute segregation [16,34], refinement [50,91] non-uniforms phase distribution, and the development of complex grain morphologies [92]. Consequently, such features can significantly affect the mechanical performance of the final material [20,93]. Therefore, understanding microstructural evolution under non-equilibrium conditions is essential for predicting and controlling the properties of cast alloys.

Among the experimental techniques used to investigate solidification, directional experiments has been widely applied [94] and the studies can be divided into two main regimes: those solidification processes conducted under steady-state heat flow conditions, and those performed under unsteady-state, or transient, heat flow conditions. Each contributing in parallel to the advancement of the metallic alloys solidification's field.

In the steady-state regime, the thermal gradient (G) and the solidification front velocity (V) can be controlled independently and maintained constant throughout the experiment, with the Bridgman and Stockbarger methods being two approaches used for this purpose. Both involve heating and cooling a sample within a furnace that imposes a fixed temperature gradient between hot and cold zones. In the Bridgman method, whose generic device is shown in Figure 3.1, the sample is translated at a desired pull rate (V) in a constant thermal gradient (G). In the Stockbarger method, the sample remains stationary, and the thermal gradient is displaced by applying a controlled cooling rate (R) to the furnace zones [15]. Steady-state conditions are valuable not only for the

production of single crystals [1], but also for investigating solidification kinetics, as they allow the independent control of each variable and its effects on microstructure [8,62,95].

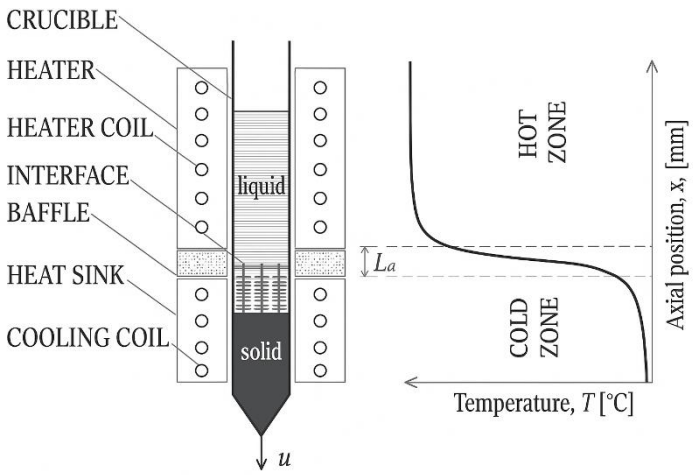

Figure 3.1: Schematic of a typical Bridgman furnace and temperature profile [96].

Imposing specific solidification conditions is also a major advantage of stationary methods. For example, the observation of cell-dendritic transition at minimal cooling rates, such as 0.005°C/s in the Al-3wt%Mg-1wt%Si alloy, was facilitated by the meticulous regulation of thermal conditions in the Bridgman furnace. This level of precision was not attained by the authors in the transient regime experiment, where the minimum cooling rate achieved was 0.2 °C/s [97]. In a similar manner, the impact of solidification velocity on the formation of intermetallic in Al-Fe alloys was examined by precisely regulating the thermal parameters within a Bridgman-type furnace. At low velocity, ranging from 50 to 300 μm/s, the plate-like Al_3Fe intermetallic phase was predominant. However, at higher speeds, obtained in the transient regime, the same alloy exhibited a predominance of rod-like Al_6Fe formation [98]. This is an interesting result, considering that the properties of Al-Fe alloys are significantly influenced by the morphology of the intermetallic compound. For example, when present as thin plates, these compounds can act as stress concentrators, thereby weakening the alloy.

Soltani *et al* [14], also using a Bridgman-type furnace, controlled the thermal gradient and the cooling rate to emphasize the effects of gravity on the growth and orientation of refined Al-Cu grains. The results showed that gravity influences grain

size distribution, grain elongation, and growth direction, mainly through buoyancy and solute flow. The part of this PhD developed in France and presented in Chapter 2 involved steady state directional solidification in a Bridgman-type furnace, which allowed reproduce identical thermal conditions in all experiments when investigating the solidification path of Al-Cu-Sn model alloys.

In contrast to steady-state condition, transient directional solidification is characterized by a dynamic evolution of heat flow. In this regime, key thermal parameters as cooling rate (*R*), thermal gradient (*G*) and the solidification front velocity (*V*) vary significantly over time and/or position within the solidified bulk. Understanding solidification under transient heat flow is essential, as it encompasses some industrial casting techniques, such as chill casting, sand casting, die casting, continuous casting, and ingot casting [99].

In the field of aluminum alloys, forced water cooling studies employing devices similar to those depicted in Figure 3.2 are a common practice [3,16,34,52,100]. These studies enable the detailed mapping of microstructural evolution under variable thermal conditions within a single experiment. This facilitates the correlation of the cooling rate, thermal gradient, and solidification front velocity with the microstructural cellular/dendritic scale [3,22,52], macrosegregation [16,34,101], and phase distribution [100,101].

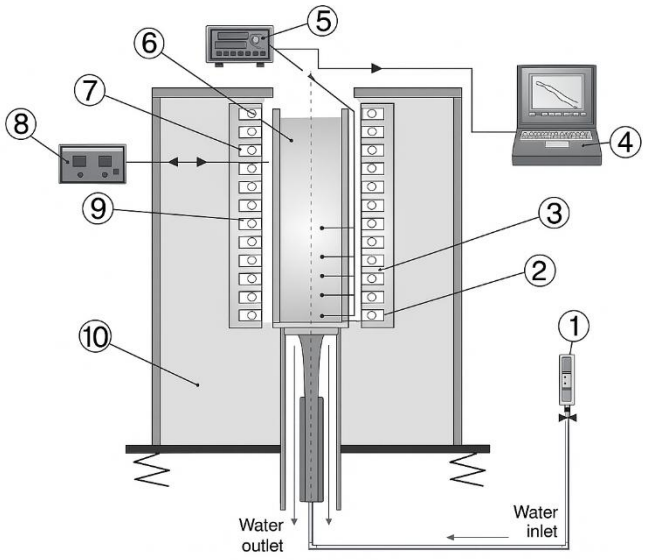

Figure 3.2: Schematic representation of typical unsteady-state solidification setup: (1) rotameter; (2) heat- extracting bottom; (3) thermocouples; (4) computer and data

acquisition software; (5) data logger; (6) casting; (7) mold; (8) temperature controller; (9)) electric heaters; and (10) insulating ceramic shielding [34].

Figure 3.3 highlights the microstructural variety at macroscopic and microscopic scales obtained in a single unidirectional solidification experiment under transient heat extraction conditions by Souza *et al* [102] They performed the solidification of the Al-7wt%Si-3wt%Cu-0.3wt%Fe alloy in a horizontally oriented water-cooled device, and successfully find out an association between secondary dendritic arm spacing, cooling rate, solidification velocity, and mechanical properties.

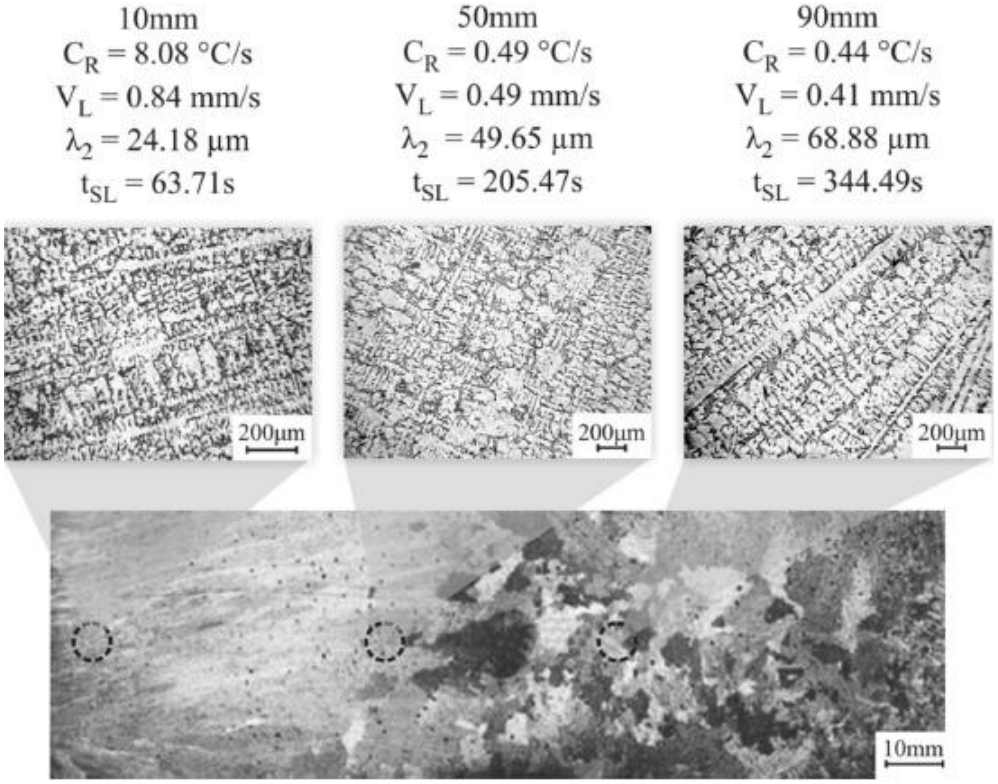

Figure 3.3: Typical solidification structures at the macrostructural and microstructural scales resulting from the horizontal solidification of Al-Si-Cu-Fe alloys at three positions relative to the cooled surface: 10, 50, and 90 mm. Where C_R is the cooling rate, V_L is the solidification interface velocity, λ_2 is the secondary dendritic spacing, and t_{SL} is the solidification time [102].

Transient directional solidification technique also helps to clarify unusual microstructures, such as feathery grains. Rappaz *et al*. [92] reported that in Al-Mg-Cu alloys solidified under upward cooling, feathery grains were predominant in the lower part of the ingot but decreased toward the upper regions. This indicates that feathery grains nucleated near the bottom of the mold, where the thermal gradient and cooling rate were highest, suggesting an influence of these factors on the formation of such grains.

The doctoral work carried out in Brazil, presented in this Chapter, focused on the study of the transient directional solidification of an industrial Al-20wt%Sn-1wt%Cu alloy, with the objective of characterizes its microstructural evolution under conditions more related with industrial casting practice.

3.2.1.2 Heat and mass transfer in solidification

During solidification, a substantial amount of thermal energy must be transferred from the liquid phase into the surrounding environment to enable nucleation and growth of the solid phase. Initially, energy removal occurs in the form of sensible heat, cooling the liquid until it reaches the equilibrium solidification temperature and then, energy is extracted as latent heat, driving the phase change from liquid to solid.

The general temperature variation in a casting can be schematically represented in Figure 3.4, with each region imposing a specific resistance to heat flow: the liquid, the solidified metal, the metal/mold interface, the mold body, and the surroundings [103]. These resistances are governed by three fundamental modes of energy transport; conduction, convection, and radiation; all of which are active during casting solidification. Conduction and convection occur within the casting and at the metal/mold interface, conduction within the mold, while radiation transfers energy from the mold surface to its surroundings, typically air [99].

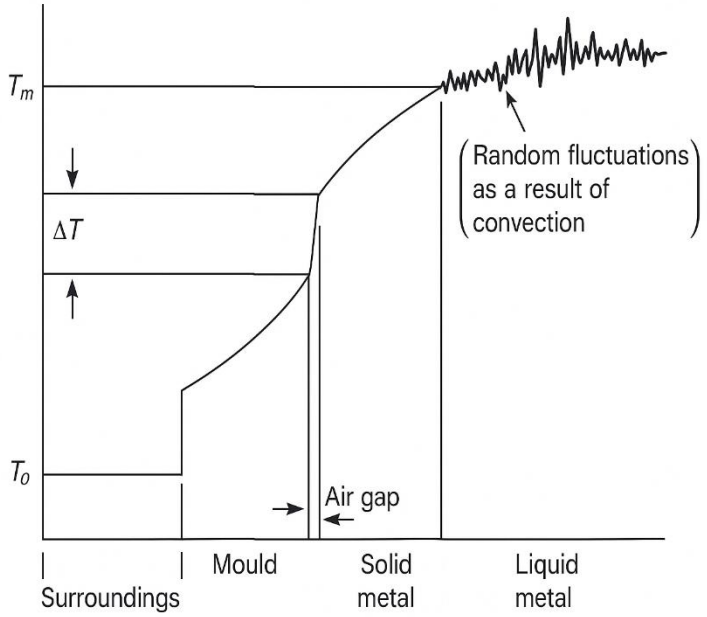

Figure 3.4: Temperature profile across a casting freezing in a mold, showing the effect of the addition of thermal resistances that control the rate of loss heat. Where T_m is the melting point, T_o is the surrounding temperature, and ΔT is the temperature variation as a function of the resistance at the metal/mold interface [103].

Conduction is the transfer of thermal energy through direct particle interaction and can occur in solids, liquids, or gases [104]. The conduction flux (q_c, in W/m^2), depends on material's thickness (x, in m) and thermal diffusivity (α, in m^2/s). It is described by Fourier's law, *Equation 3.1* [99].

$$q_c = -\alpha \frac{\partial(\rho . C_p . T)}{\partial x} \qquad \textbf{\textit{Equation 3.1}}$$

Where ρ is the density (kg/m^3), and C_p the heat capacity (J/K), at constant pressure. Convection is the heat transfer mode between a solid surface and an adjacent moving fluid, involving both conduction and bulk fluid motion. In the absence of fluid motion, heat transfer occurs purely by conduction. When fluid motion arises from density differences, the process is termed natural convection, while externally driven motion corresponds to forced convection. The convective heat transfer flux (q_h, in W/m^2) is proportional to the convective heat transfer coefficient (h, W/m^2.K) and the

temperature difference [104]. It is conveniently expressed by Newton's law of cooling, *Equation 3.2* [99].

$$q_h = h.(T_s(t) - T(0)) \qquad \textbf{Equation 3.2}$$

Where Ts is the surface temperature and T_0 is the temperature of the fluid ahead. Radiation transfers heat via electromagnetic waves and, unlike conduction and convection, does not require a material medium. The radiative heat flux is described by the Stefan-Boltzmann law, [104], described by *Equation 3.3* [99], where σ is the Stefan-Boltzmann constant, and ε is the emissivity factor . Although often negligible for aluminum due to its relatively low melting point, radiation may still contribute under certain conditions such as in processes like continuous casting, in stages where the ingot no longer has contact with the mold [1].

$$q_r = \varepsilon.\sigma(T_s^4 - T_0^4) \qquad \textbf{Equation 3.3}$$

In general, the mean resistances to heat flow from a casting are associated with the mold, the metal-mold interface, and the solidified metal. Among these, heat transfer at the metal-mold interface is particularly complex, as it involves all modes of heat transfer and often constitutes a significantly thermal resistance, especially when both the metal and mold exhibit reasonably high thermal conductivities [103].

This thermal resistance in the metal/mold interface arises from several factors, including the low physic-chemical affinity between the mold material and the molten metal, the roughness of the mold's inner surface caused by machining, the application of release agents or lubricants that further reduce contact by forming an interfacial film, among others. These factors result in incomplete contact with the mold wall. Furthermore, the thermal expansion and contraction of the mold and metal during solidification result in an air gap at the interface. This air gap has been shown to significantly effect heat flow [1].

Hu and Pehlke [99,103] conducted a detailed analysis of the interfacial heat transfer coefficient in the metal-mold interface, focusing on the air-gap formation process. They demonstrated that the total heat transfer across the interface can be

estimated by superimposing the contributions from gas conduction and radiation within the gap. Their analysis considered three distinct stages during solidification:

- Stage I - Initial Contact: At the onset of solidification, thermal contact is high, and heat transfer occurs predominantly via conduction from the liquid metal to the mold wall. While the casting surface conforms to the mold, solid-solid conduction dominates. This conduction can be enhanced by increasing contact pressure, as in squeeze casting.
- Stage II - Gap Formation: As cooling proceeds and the metal approaches its *liquidus* temperature, it contracts. Simultaneously, the mold heats and may expand away from the casting, producing a partial air gap. Heat transfer in this stage occurs through conduction at the remaining contact points at the interface between metal and mold, supplemented by gas conduction and radiation across the gap.
- Stage III - Complete Separation: At the final stage, the casting fully separates from the mold, and heat transfer occurs entirely through the gap. Under these conditions, gas conduction is the primary mechanism, with radiation playing a secondary role.

The overall interfacial heat transfer coefficient in the metal-mold interface (h_i) can thus be expressed accordingly *Equation 3.4*:

$$h_i = h_{mc} + h_{gc} + h_{gr} \qquad \textbf{\textit{Equation 3.4}}$$

Where h_{mc} represents metal-mold conduction, h_{gc} conduction through the air gap, and h_{gr} radiation through the gap.

It is important to note that h_i is not constant but evolves throughout solidification, transitioning from efficient conduction in Stage I, to mixed conduction, gas conduction, and radiation in Stage II, and finally to gas conduction with minor radiation in Stage III.

With regard to mold resistance, the characteristics of the mold itself play a decisive role in heat transfer. The material composition, geometry, and cooling method

influence the rate and uniformity of heat extraction. Semi-infinite molds, in which it is assumed that the material is so thick that diffusion occurs in only one direction and that the temperature at the surface is kept constant, can be designed to absorb all the heat transferred until the end of solidification or to only raise their external temperature in the final moments of the process, minimizing heat loss to the environment. In contrast, water-cooled molds maintain a constant external temperature through continuous circulation of the coolant, thus accelerating heat removal. As for the material, sand molds, with their low thermal conductivity, substantially reduce the overall heat transfer rate, slowing the growth of solid metal, as illustrated in Figure 3.5, where the solidification speed is significantly lower for sand molds compared to cast iron mold [1].

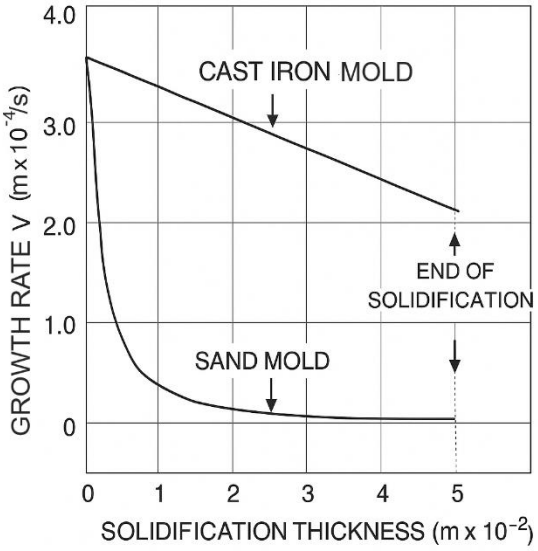

Figure 3.5: Solidification growth rate profiles of an aluminum plate solidified in sand and cast-iron molds. Adapted from [1].

In addition to heat transfer, mass transport plays a critical role in the dynamics of solidification. Mass transport occurs through two primary mechanisms: diffusion, driven by compositional gradients, and convection within the liquid metal. Both mechanisms can promote segregation, defined as any deviation from a uniform distribution of alloying elements.

At the microscopic scale, solute segregation ahead of the solidification front is a key driving force for interface instabilities It also leads to microsegregation, which

occurs between dendrite arms and within grains. Because the diffusion distances involved are relatively small, typically in the range of 10-100 μm, microsegregation can often be significantly reduced through homogenization heat treatments. In contrast, macrosegregation, which occurs over distances from 1 cm to 1 m, cannot be removed by heat treatment and remains a permanent feature of the casting [103].

Convection in the liquid phase can be driven by thermal gradients, where hotter liquid expands, becomes less dense, and rises, while cooler liquid contracts, becomes denser, and sinks or it can arise from solute gradients: heavy solutes increase density, causing the liquid to sink, while lighter solutes decrease density, promoting flotation [103].

To investigate the influence of such convective motion, some studies perform directional solidification both, with and against the direction of gravity [105]. When unidirectional solidification progresses against gravity, the ingot's own weight enhances thermal contact with the cooled base and if the interdendritic liquid is denser, no convective currents occur, neither due to temperature nor to density differences. In contrast, when solidification is oriented in the same direction as gravity, it is inevitable the presence of some degree of convective motion. In this case, the liquid temperature profile increases toward the cold zone, which ensures at least thermally driven convection. Moreover, if solute rejection leads to an interdendritic liquid denser than the nominal melt, solute driven convection will also be present [94].

3.2.1.3 Unidirectional solidification – Thermal variables

The variation of thermal parameters in the transient regime (cooling rate and thermal gradient) is not only an inherent characteristic of the process but also represents a mechanism for understanding the microstructure and, consequently, controlling the material properties. For instance, the direct correlation between cooling rate and microstructural refinement [34,52], associated with the inverse relationship between dendritic spacing and tensile properties [93,106], or the association between homogeneous microstructure and better wear behavior [107], indicate how a precise control of cooling is a fundamental lever for modulating material performance [34,51,94]. Thus, the complexity of transient variation can be transformed into a powerful engineering tool for material optimization. In directional solidification studies,

thermocouples record temperature variations at different positions in the molten material to generate experimental cooling curves, which reveal the thermal parameters of solidification. The main thermal variables under study in directional solidification with transient heat extraction flow are:

- Local Solidification Time (t_S): Defined as the time difference between the passage of the *solidus* and *liquidus* temperature at a given location within the ingot [52]. This parameter influences dendritic coarsening.
- *Liquidus* temperature passage times (t): Along the ingot, the cooling curves are intersected by the *liquidus* temperature (T_L) at distinct times, as shown in Figure 3.6(a). These data allow the construction of graph that relates the position in the ingot to the corresponding time (t_L) at which the *liquidus* temperature is reached. This correlation establishes a graph according to P=f(t), as shown in Figure 3.6(b).

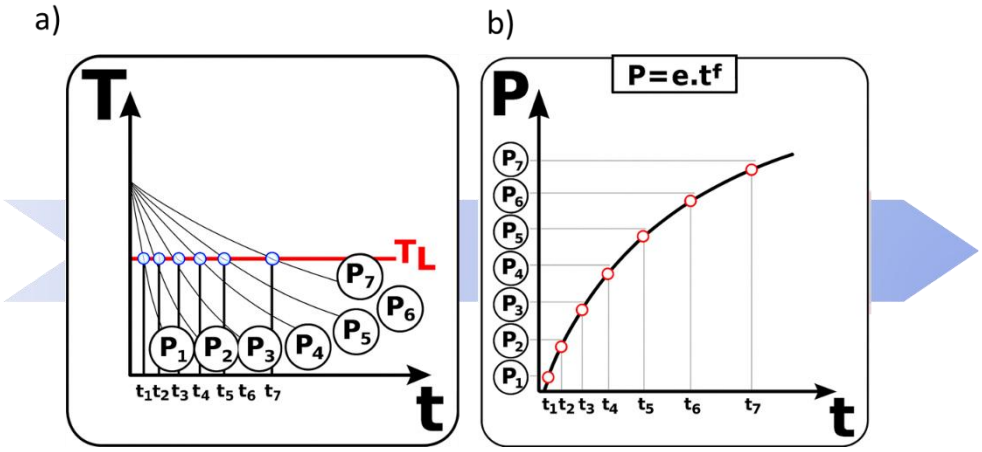

Figure 3.6: a) Cooling curves at different positions along the ingot (P) intersected by the liquidus temperature (T_L) at each position P, and (b) The P = f(t_L) graph. Adapted from [108]**.**

- Solidification front velocity (*V*): The growth rate refers to the velocity at which the *liquidus* temperature advances, which can be regarded as the dendrite tip velocity. The solidification front velocity is found by taking the derivative of the function P=f(t_L) with respect to time. This is expressed

mathematically in *Equation 3.5* and represented schematically in Figure 3.7 [52,109,110].

- $$V = \frac{dP}{dt_L} \qquad \textbf{\textit{Equation 3.5}}$$

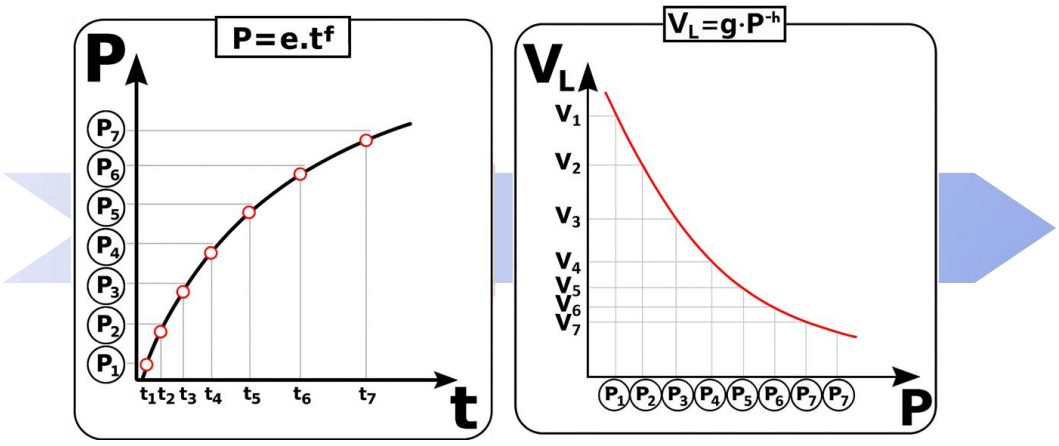

Figure 3.7: Sequence of steps for obtaining the solidification front velocity from the P=f(t_L) graph. Adapted from [108]**.**

- Cooling Rate (*R*): Defined as the temperature variation as a function of time at the moment when the temperature passes through the *liquidus*. Experimentally, the cooling rate is determined from the cooling curves. In practice, polynomial functions are fitted to the temperature-time data in the vicinity of the *liquidus*, and the time derivative of these functions provides the local cooling rate, [111,112]. This procedure can be better visualized by applying *Equation 3.6*. Figure 3.8 shows a schematic representation of this procedure.

$$R = \frac{dT}{dt} \qquad \textbf{\textit{Equation 3.6}}$$

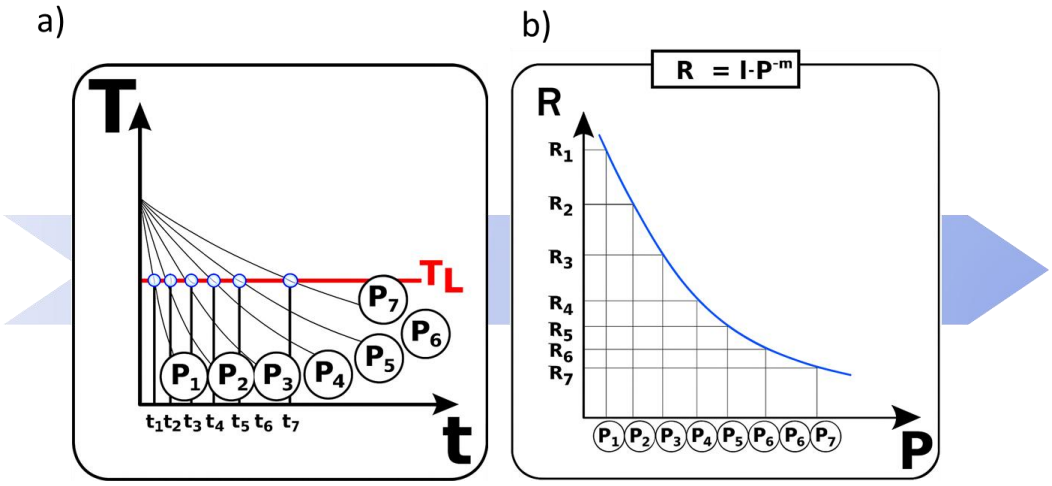

Figure 3.8: (a) Cooling curves showing temperature-time data at each position P, and (b) Schematic diagram showing the experimental correlation between cooling rate and position relative to the mold plate [108]**.**

- Thermal Gradient (*G*): This is the temperature variation per unit distance ahead of the solid/liquid interface. It plays a decisive role in determining the growth mode of the interface. They are obtained by dividing the experimental cooling rates (*R*) by the experimental solidification front velocity (*V*), as expressed by *Equation 3.7*.

$$G = \frac{R}{V} \qquad \textbf{\textit{Equation 3.7}}$$

There are theoretical models that seek to describe how variations in these parameters influence dendritic spacing, thus providing predictive tools for microstructural control. These issues will be addressed in the subsequent topic.

3.2.1.4 General models for dendritic growth

Theoretical models for dendritic growth aim to establish quantitative correlations between solidification parameters, such as the thermal gradient (*G*) and solidification front velocity (*V*) with the dendritic spacings $\lambda_{1,2}$. Under steady-state heat flow

conditions, *G* and *V* can be controlled independently and kept constant. In such cases, dendritic growth models generally express the spacing of primary and secondary arms as functions of these two independent variables. In contrast, when solidification occurs under transient heat flow regime, *G* and *V* vary freely and the dendritic spacings are often correlated with the cooling rate, which can be calculated by $R = G \times V$ [113].

The dimensioning of steady-state analytical models is less complex, since it does not consider time-dependent factors [113]. Consequently, these models have been the focus of extensive research, providing a solid theoretical base for estimating microstructural spacing and for subsequent studies considering solidification in transient conditions. In general, when considering solidification in a steady state regime, the primary dendritic spacing varies with G and V according to a generic expression described by *Equation 3.8* [1]:

$$\lambda_1 = K.G^{-a}.V^{-b} \qquad \textbf{\textit{Equation 3.8}}$$

Here, the constant *K* is associated with solute concentration, while the exponential factors a and b are more directly related to the growth mechanism [1]. This relationship is described by authors such as Hunt [114] and Kurz and Fisher [115], who have defined the values of exponent as -1/2 and -1/4, as shown in *Equation 3.9*.

$$\lambda_1 = K.G^{-1/2}.V^{1/4} \qquad \textbf{\textit{Equation 3.9}}$$

K encompass the Gibbs-Thomson coefficient, the equilibrium solidification interval range, the solute partition coefficient, and solute diffusivity in the liquid phase. It is calculated differently for each model [114,115].

Despite the simplification adopted here to describe the Hunt [114] and Kurz-Fisher [115] models, this relationship reveals that primary dendrite arm spacing is not equally influenced by *G* and *V*. It is inversely proportional to the square root of the thermal gradient and to the fourth root of the growth velocity, indicating that spacing is significantly more sensitive to variations in *G* than in *V*. It should be emphasized that these models were developed for steady-state conditions and for binary alloys.

Secondary dendrite arm spacing (SDAS or λ_2) has also been extensively investigated, mainly due to its strong influence on mechanical properties [93,106] and subsequent homogenization treatments. According to Kurz and Fisher [4], during the development of secondary arms, the ripening process is very important, in which the initially highly branched arms evolve over time into coarser, less branched, and more widely spaced structures, making SDAS strongly dependent on the local solidification time, as illustrated in Figure 3.9. Note that there was little variation in primary dendritic spacing, unlike secondary dendritic spacing for the same period.

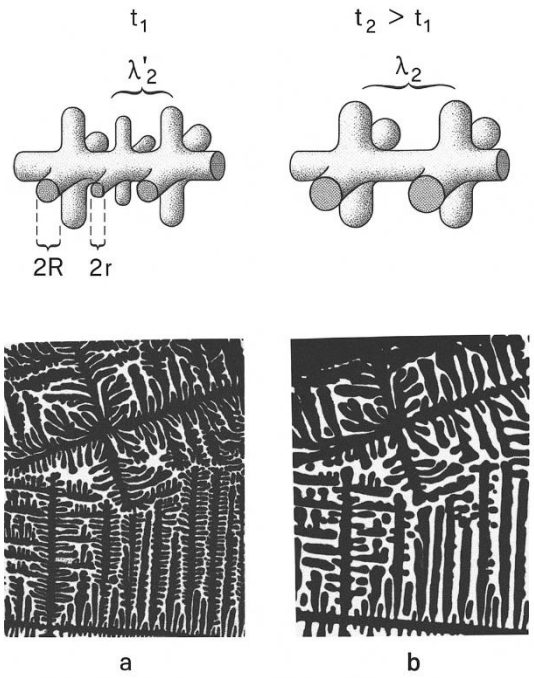

Figure 3.9: Variation in secondary dendrite arm spacing (SDAS) over time, where t is time and R/r are the radius of secondary branching [4].

Rappaz and Boetting [116] expanded the predictive framework of binary alloys to multicomponent systems to calculate SDAS, incorporating the variation in liquid composition during solidification and the temperature dependence of diffusion coefficients. The researchers found a relationship between secondary dendritic spacing and time, as shown in *Equation 3.10*.

$$\lambda_2 = (M.t_f)^{1/3} \qquad \textbf{\textit{Equation 3.10}}$$

Where t_f is the solidification time, and M accounts for the multicomponent nature of the alloy described in *Equation 3.11*:

$$M = \frac{-\Gamma}{\sum_{j=1}^{n} m_j(1-k_j)(c_{b,j}-c_{0,j})/D_j} ln\left[\frac{\sum_{j=1}^{n} m_j(1-k_j)c_{b,j}/D_j}{\sum_{j=1}^{n} m_j(1-k_j)c_{0,j}/D_j}\right] \qquad \textbf{\textit{Equation 3.11}}$$

Here, c_b is the final composition of the liquid at the dendrite base, m is the slopes of the *liquidus*, k is the partition coefficients, D is the solute diffusion coefficients in the liquid, Γ is the Gibbs-Thomson coefficient, and n is the number of elements. For binary alloys, the equation simplifies to n = 1.

In pursuit of models that better reflect real solidification conditions, estimates of dendritic spacing were developed considering the transient heat extraction regime. In this context, the theoretical models of Bouchard and Kirkaldy [113] for unsteady-state conditions show that the exponential relationship between primary dendrite arm spacing and cooling rate ($G \times V$) is best represented by a relationship described by *Equation 3.12*, where K relates to solute concentration, and an exponent of -1/2 is the best fit. This relationship has been extensively compared with experimental work [52,94,109].

$$\lambda_1, \lambda_2 = K(G.V)^{-1/2} \qquad \textbf{\textit{Equation 3.12}}$$

For secondary dendrite arm spacing, the authors found that an exponent of -1/3 with respect to cooling rate satisfactorily describes the dependence on the controlling parameter under steady and unsteady heat flow conditions [113].

3.2.2 Microstructural coarsening in self-lubricating alloys

3.2.2.1 Growth laws in self-lubricating Al-based alloys

Despite their usefulness, analytical models do not fully reflect experimental observations for transient solidification, underestimating or overestimating predictions, often depending on the adjustment of the K constant. Consequently, experimental work has being done to complete the understanding of the characteristics of specific alloys.

A literature review focusing on self-lubricating Al-based alloys, such as Al-In, Al-Pb, Al-Sn, and Al-Bi, reveals experimental equations relating dendritic spacing to cooling rate (*R*) or interface velocity (*V*) during upward directional solidification experiments. These equations are summarized in Table 3.1.

Table 3.1: Experimental relationships between microstructural coarsening and cooling rate or velocity of several self-lubricating Al-based alloys during directional solidification. Empty cells in the table indicate equations not determined. *V* and *R* are, respectively, the experimental solidification velocity and the cooling rate. λ is the microstructural spacing.

Alloy (wt%)	**Dependence on *R***	**Dependence on *V***	**Ref**
Al-5.5%In		$\lambda_{In} = 46.V^{-1/2}$ Droplets	[112]
Al-1.2%Pb		$\lambda_{Pb} = 25.V^{-1/2}$ Droplets $\lambda_{Pb} = 23.V^{-2.2}$ Fibers	[110]
Al-2.1%Pb		$\lambda_{Pb} = 46.V^{-2.2}$ Fibers	[110]
Al-2.6%Sn Al-7.5%Sn Al-10%Sn	$\lambda_C, \lambda_1 = 70.R^{-0.55}$		[111]
Al-9%Sn	$\lambda_C, \lambda_1 = 70.R^{-0.55}$		[111]
Al-9%Sn-1%Pb	$\lambda_C, \lambda_1 = 80.R^{-0.55}$		[111]
Al-15%Sn Al-20%Sn	$\lambda_1 = 70.T^{-0.55}$		[34]
Al-20%Sn Al-30%Sn Al-40%Sn	$\lambda_1 = 70.T^{-0.55}$ $\lambda_2 = 30.T^{-0.55}$	$\lambda_1 = 50.V^{-2/3}$ $\lambda_2 = 22.V^{-2/3}$	[52]
Al-10%Sn-10%Cu	$\lambda_1 = 145.T^{-0.55}$	$\lambda_1 = 84.V^{-1.1}$	[16]
Al-20%Sn-10%Cu	$\lambda_1 = 194.T^{-0.55}$	$\lambda_1 = 73.V^{-1.1}$	[16]
Al-15%Sn-5%Si	$\lambda_1 = 123.T^{-0.55}$	$\lambda_1 = 80.V^{-1.1}$	[16]
Al-25%Sn-5%Si	$\lambda_1 = 204.T^{-0.55}$	$\lambda_1 = 125.V^{-1}$	[16]

Al-2%Bi	$\lambda_C = 72.R^{-0.55}$	$\lambda_c = 35.V^{-1.1}$	[105]
Al-3.2%Bi		$\lambda_{Bi} = 41.V^{-1/2}$	[117]
Al-5%Bi		$\lambda_{Bi} = 20.V^{-1.1}$	[91]
Al-7%Bi		$\lambda_{Bi} = 46.V^{-1.1}$	[91]
Al-3.2%Bi-3%Cu	$\lambda_{Bi} = 44.5\ R^{-0.35}$	$\lambda_{Bi} = 41.V^{-1/2}$	[22]
Al-3.2%Bi-3%Zn	$\lambda_{Bi} = 54.4\ \ R^{-0.5}$	$\lambda_{Bi} = 41.V^{-1.6}$	[101]
Al-3.2%Bi-1%Pb	$\lambda_{Bi} = 62.R^{-0.5}$		[107]
Al-3.2%Bi-3%Pb	$\lambda_{Bi} = 83.R^{-0.5}$		[107]
Al-3.2%Bi-1%Sn	$\lambda_C = 70.R^{-0.55}$	$\lambda_{Bi} = 23.V^{-1.1}$	[118]
Al-2%Bi-1%Sn	$\lambda_C = 60.R^{-0.55}$	$\lambda_{Bi} = 19.V^{-1.1}$	[118]
Al-7%Bi-1%Sn	$\lambda_C = 35.R^{-0.55}$	$\lambda_{Bi} = 15.V^{-1.1}$	[118]

The alloys listed in Table 3.1 are characterized by secondary phases consisting of elements with very low solubility in the aluminum matrix, which consequently form discrete, dispersed particles. In the case of In, Pb, and Bi, these phases predominantly manifest as isolated droplets distributed throughout the matrix, as illustrated in Figure 3.10(a). Although variations in the thermal gradient and solidification velocity can induce morphological changes in such phases, where the transitions will be from isolated droplets to strings of pearls or fibrous structures [110,117]. For these alloys, the characteristic microstructural parameter quantified corresponds to the interphase spacing, designated as λ_{In}, λ_{Pb}, and λ_{Bi}, respectively. Conversely, in Al-Sn alloys, the Sn phase forms a continuous network within the interdendritic regions, as shown in Figure 3.10(b). In this case, the relevant length scale is defined by the primary or secondary dendrite arm spacing, denoted as λ_1 and λ_2, respectively.

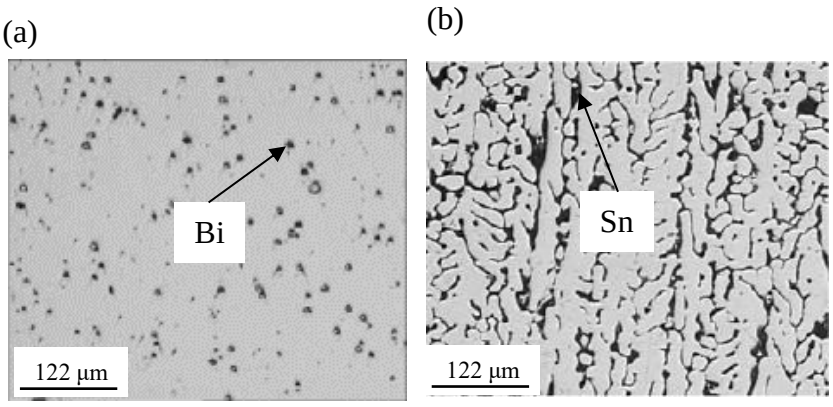

Figure 3.10: Bi droplets in the Al-7%Bi alloy, longitudinal section, V=1.5mm/s [117], (b) Sn phase distributed in the interdendritic region, longitudinal section of the Al-30%Sn alloy, V=1.2mm/s and R = 1.9 °C/s [52].

The spacings between most droplet-shaped phases and between secondary dendrite arms have been quantified along the longitudinal section of the castings by averaging the horizontal distance between particles, taking the center of each droplet or dendrite arm as the reference point. In the case of primary dendrite arm spacing in Al-Sn alloys and interphase spacing in Al-Bi ternary alloys, measurements were conducted on transverse sections using the triangle method [119] to determine the characteristic spacing.

A synthesis of the experimental equations presented in Table 3.1 allows for several conclusions to be drawn regarding the microstructural growth laws as a function of the solidification thermal parameters in the self-lubricating alloys analyzed:

- The relationship between the primary dendritic spacing λ and the cooling rate (*R*) for both binary and ternary alloys, fits well with the model proposed by Bouchard and Kirkaldy [113], yielding an exponent close to −1/2, with the exception of the Al-3.2%Bi-3%Cu alloy.
- In addition to correlating the interphase spacing with the cooling rate, some authors have also analysed its dependence on the growth rate (*V*) obtaining a relationship of the form $\lambda = K.V^{-1/2}$, where K is a system-dependent constant. Interestingly, this correlation is typically associated with eutectic growth [120], suggesting an analogy between the prediction of droplet growth

in monotectic systems such as Al-In, Al-Pb, and Al-Bi (within certain compositions) and the growth behaviour of the eutectic microconstituent.

- For the majority of the alloys investigated, the interphase spacing was correlated with the growth rate (V) through a relationship $\lambda = K.V^{-1.1}$, indicating that the spacing is practically inversely proportional to the velocity, with K being a characteristic constant specific to each composition.

3.2.2.2 Cooling rate effects in self-lubricating alloys

As shown in Table 3.1, alloy composition significantly influences microstructural coarsening in addition to thermal variables. For instance, in Al-Sn alloys with Sn contents up to 40 wt%, composition was found to have little effect on λ_1, with a single power-law expression adequately describing the variation of spacing with the cooling rate for all binary alloys. However, the addition of alloying elements modifies the constant K in the growth laws, where such additions tend to promote microstructural coarsening. According to Bertelli *et al.* [16], the growth law of ternary alloys can be expressed as a relationship between the growth laws of their constituent binary systems; specifically, the higher the Sn concentration in Al-Sn-Cu and Al-Sn-Si alloys, the closer the ternary alloy behavior approaches that of the Al-Cu and Al-Si binary alloys, respectively.

A similar effect of microstructural coarsening due to the addition of alloying elements in Al-Sn based alloy was reported by Oliveira *et. al*. [111]. When comparing the binary Al-9%Sn with the ternary Al-9%Sn-1%Pb alloy, the authors further suggest that the addition of Pb appears to destabilize the high-cooling-rate cells observed in the binary alloy and promotes the formation of dendrites at higher cooling rates. This behavior was attributed to the formation of a ternary eutectic mixture at the cell/dendrite boundaries, instead of a binary eutectic as in the binary alloy. In contrast, Bi-containing alloys, both binary and ternary, appear to be strongly influenced by composition with respect to their interphase spacing.

Finally, when comparing the growth laws presented in Table 3.1 for Al-Bi and Al-Sn based alloys, for which spacing was evaluated using relationships of the form $\lambda = K(R)^{-1/2}$, it seems that, for the same cooling rate, Bi-containing alloys exhibit a

finer microstructure in terms of secondary phase distribution. It is noteworthy that, although the measurement methods and phase morphologies differ between Al-Sn- and Al-Bi-based alloys, the spacings reported by the authors aim to capture the same phenomenon: understanding how the cooling rate influences phase distribution and, consequently, the resulting microstructure.

Understanding how alloying elements influence microstructural coarsening is particularly relevant, as it strongly affects material properties. According to studies in which Al-Pb [44] and Al-In [121] alloys were subjected to wear test, coarser droplets of the lubricating phase were associated with improved wear resistance in both systems. A similar trend has been observed in Al-Sn-based alloys, where reduced wear was correlated with an increase in dendrite arm spacing. In contrast, the wear volume has been reported to increase with larger microstructural spacing in Al-Bi alloys [22], and the same experimental tendency was confirmed when Bi was associated with Sn [100]. These findings indicate that the design of self-lubricating bearings using Al-based alloys must consider the control of the solidification cooling rate (R) during casting. Specifically, higher cooling rates for Al-Bi alloys and lower values for Al-Pb, Al-In, and Al-Sn alloys are necessary to obtain microstructural patterns that promote optimal wear performance [111].

3.2.3 Generalities on wear in metal alloys

3.2.3.1 Technological importance

Tribology, the science of friction, wear, and lubrication, is a field of immense economic and environmental importance. The relevance of this area was first highlighted in a significant way in the 1960s with the Peter Jost Report, that revealed the enormous financial losses the United Kingdom was suffering due to a lack of attention to the relative movement between surfaces. The research showed that wear in industries such as steel manufacturing generated annual losses equivalent to about 1% of the country's GDP at the time. The majority of this loss, approximately two-thirds of the total, was caused by breakdowns and unscheduled maintenance [122].

Since the Jost Report, the understanding of tribology's impact has only grown. A global study conducted over the last decade revealed that approximately 23% of the

world's total energy consumption is directly linked to tribological contacts. This energy loss is divided into two main parts: 20% is spent to overcome friction, and 3% is consumed in remanufacturing worn parts and producing replacement equipment [123]. Tribology integrates the study of friction, wear, and lubrication. From bearings in cars to sliding components in precision instruments, the ability to control frictional forces and mitigate material loss by wear is directly linked to energy conservation, productivity, and maintenance costs [124]. Within this framework, friction represents the resistance to motion, wear denotes the progressive removal of material at the interface, and lubrication acts as a mediator aimed at reducing both [125]. Among these, wear will be the main subject in the framework of this PhD thesis.

Within this context, one of the most studied components is sliding bearings, which are essential for the operation of machinery like internal combustion engines. With over 10^9 units produced annually, these bearings are not a niche product but a vital engineering element [126,127]. They consist of a cylindrical steel shell with a thin inner surface, commonly lined with a soft bearing material such as lead or tin babbitt, bearing bronze, or a plastic [124]. The importance of studying them lies in the fact that friction and wear in the contact area between the shaft and the bearing can lead to catastrophic failures, in poor working conditions or after a long service time, compromising the reliability of the entire system [127].

The function of sliding bearings depends directly on their multi-layered structure. The two common configurations are bimetallic and trimetallic bearings. Illustrated in Figure 3.11.

- Trimetallic Bearings: Formed by four layers. The topmost thinner layer is composed of Sn and Pb, acting as a protectant against corrosion and dirt when not in use. This layer flashes off when a bearing is running. The second layer, made of Ni, serves as a barrier to prevent the diffusion of Sn into the main layer. The third layer is the primary functional part, made of lead bronze, which offers excellent anti-seizing properties. Finally, the steel back provides the solid base and support for all the layers, ensuring the component's integrity [128].

- Bimetallic Bearings: This type of bearing is composed of two main layers. The first layer is the bearing alloy, typically made of Al and Sn, which is the main load-bearing element and works to reduce friction. Below it is an aluminum bonding layer, whose function is to ensure a strong bond between the bearing alloy and the steel back, the final layer that provides the shape and structural support to the bearing [128].

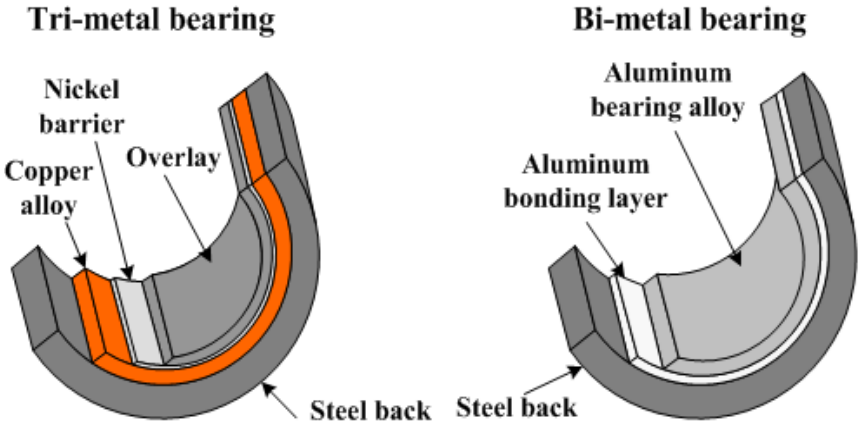

Figure 3.11: Engineering bearing structures. Adapted from [128]**.**

3.2.3.2 Surface contact and wear

A fundamental step in understanding wear, lies in examining how two surfaces interact. Even when polished, surfaces are not perfectly smooth but consist of microscopic irregularities, known as asperities. Contact therefore occurs only at discrete points and the mechanics of these asperity contacts dictate whether a surface deforms elastically or plastically, and consequently, how material loss develops. Thus, modeling asperity behavior provides the necessary bridge between surface roughness and macroscopic wear performance [125].

To capture these interactions, tribological analysis often begins with the model of deformation of single-asperity. By replacing the complex ensemble of asperities with a single spherical protuberance that is pressed by a loaded sphere. When observed more closely, this contact is considered as a flat surface against the tip of the asperity, as illustrated in Figure 3.12. The elastic contact between the asperity of radius β and a

plane under normal load *W*, gives rise to a circular patch of radius *a*, calculated according to *Equation 3.1*3. The *E* is defined as the equivalent elastic modulus of the materials under contact [124,125].

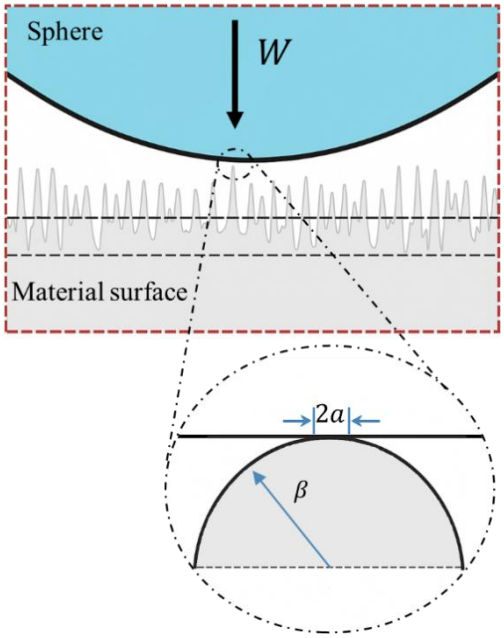

Figure 3.12: Deformation of Single Asperity - Highlighting a single asperity of radius β in contact with the loaded sphere and the contact surface between them. Adapted from [124]**.**

$$a = \left(\frac{3.W.\beta}{4.E}\right)^{\frac{1}{3}} \qquad \textit{Equation 3.13}$$

When extended to real surfaces composed of multiple asperities, the model assumes that each asperity deforms independently and supports a fraction of the normal load. Therefore, the total contact area can be expressed as the sum of all contact areas of the individual roughness. As the load increases, the softer material eventually yields, leading to plastic deformation, and the actual contact area of the roughness then increases. From that point onwards, under a constant applied load, the total contact area (*A*) becomes inversely proportional to the mean yield pressure (P), or to the hardness (H), as described in the *Equation 3.*, since at fully plastic condition the mean pressure is, in fact, the hardness of the softer material [125]:

$$W = H.\ A = \ H.\sum \pi a^2 \qquad \textbf{Equation 3.14}$$

Plastic deformation predominates in most practical conditions. Consequently, continuous sliding promotes the repetitive formation and destruction of asperity contacts. Wear is therefore characterized by the detachment of material fragments originating from these asperities. The volume of each detached fragment is proportional to the cube of the contact dimension (*a)*. For simplicity, if the worn volume is considered to be that of a half sphere, the volume in each roughness can be determined by *Equation 3.* [125] :

$$\delta V = \frac{2.\pi.a^3}{3} \qquad \textbf{Equation 3.15}$$

However, only a fraction of asperity contacts generates actual wear particles. This proportionality is given by η [125]. Thus, the rate of wear (*Q*) as a function of sliding distance, considering the total contact area and the proportion of particles actually worn, is given by *Equation 3.*:

$$Q = \frac{\eta.\delta V}{2a} = \frac{\eta}{3}.\sum \pi a^2 \qquad \textbf{Equation 3.16}$$

The interrelation between *Equation 3.* and *Equation 3.* gives rise to Archad's equation for sliding wear, according to *Equation 3. 17*:

$$Q = \frac{K.W}{H} \qquad \textbf{Equation 3. 17}$$

Where Q is the wear volume per unit sliding distance in [mm^3/m], *W* is the applied normal load [N], H is the hardness of the softer material, and K is the dimensionless wear coefficient, interpreted as the probability of a roughness contact leading to a wear particle, incorporating η, described in *Equation 3.*.

In summary, the tribological framework starting from the single-asperity contact model and culminating in Archard’s equation provides a powerful basis for interpreting

wear processes as it highlights the essential variables that control the severity of wear. In practical applications, the ratio between the dimensionless wear coefficient and the hardness K/H is adopted for simplification. This generates the dimensional wear coefficient k, usually given in $mm^3/N.m$ [124,125].

It is worth noting that the coefficient of friction is not considered in Archard's equation, due to the fact that wear coefficients can vary by up to five orders of magnitude (10^{-2} to 10^{-7}), while the friction coefficients for most engineering materials under environmental conditions tend to remain within a much narrower range (typically 0.1 - 1) [125]. However, the effect of friction should not be disregarded when analyzing wear behavior, as it can influence both the type of wear and the change from one mechanism to another.

3.2.3.3 Wear regimes

Wear inevitably occurs whenever two surfaces are in sliding contact. The most common types are adhesive and abrasive wear, although fatigue and corrosion-related wear also frequently occur. Each mechanism is governed by distinct driving forces and microstructural processes, yet in practice, transitions between different wear modes often occur over time.

a) Adhesive wear

Adhesive wear is the most prevalent form of wear in sliding contacts. It arises when asperity junctions form and subsequently break during relative motion, like shown in Figure 3.13. Under load, strong “cold welds” may develop at asperity junctions; upon shearing, these junctions may fracture either along the interface or within one of the asperities, typically that of the softer material. The resulting wear fragments may either adhere to the counter-surface or be released as free debris particles. Material transfer generally occurs from the softer body to the harder one, although detachment of harder fragments has also been reported [124]. For instance, in ball-crater wear tests, traces of Fe [100,101,121], and other elements characteristic of the steel ball have been found on the worn surface, confirming that fragments from the harder counterpart can also be released.

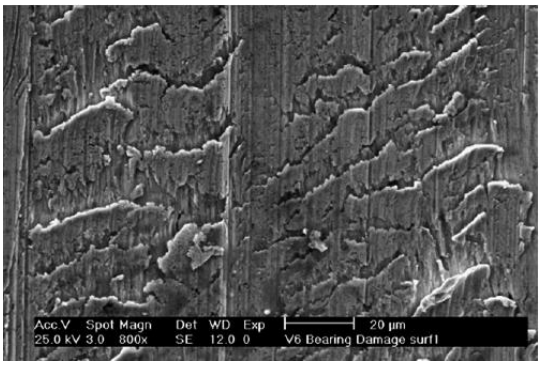

Figure 3.13: Surface of a severely overloaded bearing, showing adhesive wear of the SAE 49P (Cu-Pb) surface which was exposed after removal of the coating [126]**.**

The Archard equation provides a useful framework for predicting adhesive wear behavior. However, it is important to note that even under identical loading and sliding conditions, different wear rates may be observed depending on material properties and lubrication regimes. This variability is reflected in the wear coefficient K, which typically assumes higher values under dry sliding conditions [124].

The relationship between friction and material compatibility was extensively studied by Rabinowicz [129], who demonstrated that metallurgically compatible materials, those with high mutual solubility, exhibit stronger adhesion at asperity junctions. This enhances the likelihood of adhesive wear, particularly when both surfaces are composed of the same material. Rabinowicz termed such pairs as tribologically incompatible, since adhesion is detrimental to tribological behavior. Conversely, dissimilar metals with low mutual solubility display reduced adhesive tendencies due to weaker junction formation, resulting in lower wear coefficients. The table in Figure 3.14 summarizes this trend. When comparing the wear coefficient of different pairs of materials, identical or metallurgically compatible pairs (empty circle and circle with a dot in the center) tend to have a higher K value. In contrast, pairs of different materials (half-filled circle) and, especially, those with low solubility (solid circle) have a lower K value. In both cases, lubrication affects the severity of wear, with dry contact being the worst condition.

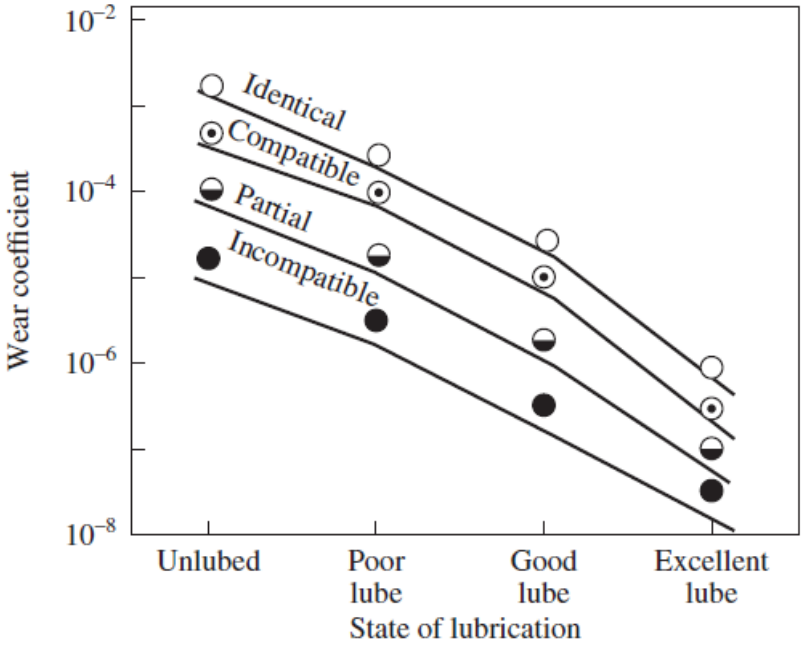

Figure 3.14: Typical wear coefficients for adhesive and abrasive wear [124]**.**

Several studies also highlight the interplay between adhesive wear and fatigue. When asperity junctions are subjected to cyclic stresses, cracks may nucleate within the softer body if rupture does not occur immediately. Over repeated cycles, fatigue-induced cracks propagate, eventually detaching as loose wear fragments. This mechanism is well recognized as the dominant failure mode in rolling-element bearings [124].

Another phenomenon observed under adhesive wear conditions is delamination wear. This process is explained by subsurface plastic deformation in the softer material, leading to the nucleation of voids and cracks propagating parallel to the surface. Once these cracks reach a critical length, they deflect upward, releasing thin, sheet-like wear particles. These laminated fragments often span distances one to two orders of magnitude greater than the original asperity contact diameter. The delamination theory also accounts for the development of subsurface strain gradients: while near-surface dislocations emerge and rupture oxide layers, deeper dislocations accumulate, causing strain hardening. This subsurface stress distribution facilitates crack nucleation and subsequent detachment of wear lamellae [124]. Delamination is often observed on worn surfaces of Al-based alloys under sliding conditions. [101,107,130].

b) Abrasive wear

Abrasive wear occurs when harder asperities or particles scratch the surface of a softer material. In many cases, it originates from a transition of adhesive wear over time, as wear debris particles evolve into a third body that moves freely between the sliding surfaces [51]. Indeed, experimental studies frequently report a time-dependent transition from adhesive to abrasive wear [100,101,107,131]. Alternatively, abrasive wear may also result from the ingress of external hard particles into the contact. These particles can cause abrasion to both members of the contact pair, leaving behind characteristic grooves. Two main modes are recognized: two-body abrasion, in which wear occurs between two surfaces, such as a shaft and a bearing, for example, and three-body abrasion, in which external particles or debris roll freely [124].

An effective mitigation strategy in abrasive environments is the use of highly elastic bearing materials, which accommodate debris through embeddability [126].

Comparative analyses indicate that abrasive wear rates are higher than those of adhesive wear, as illustrated in Figure 3.15. Besides, wear coefficients for two-body abrasion are higher, typically range from 6×10^{-2} to 3×10^{-3}, whereas three-body abrasion produces rates approximately one order of magnitude lower, since particles spend most of the time rolling (~90%) rather than sliding (~10%) [124].

The main wear types of the bearing were abrasive wear under stable working conditions and adhesive wear, abrasive wear, and fatigue wear under start-up and stop conditions [127].

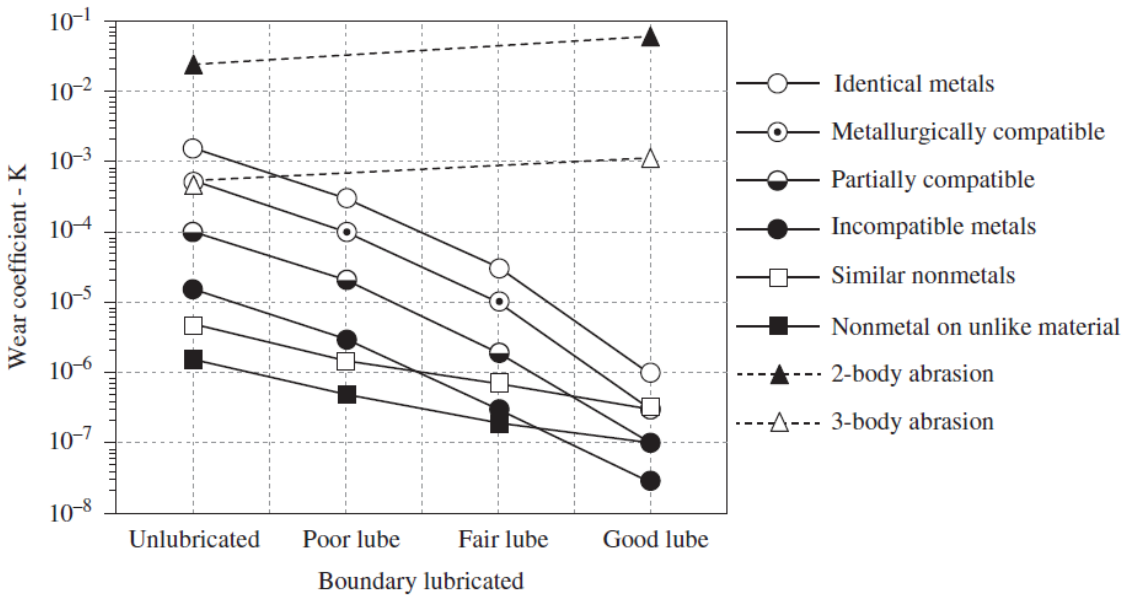

Figure 3.15: 2-body and 3-body abrasion wear coefficient compare to sliding wear [124]**.**

c) Oxidative wear

Oxidative wear arises from the formation and disruption of oxide films on sliding surfaces. Its severity strongly depends on operating conditions such as load, speed, and environmental humidity. Important to note that, frictional heating elevates contact temperatures, accelerating oxidation rates. In mild oxidative wear, protective oxide films form rapidly enough to prevent direct metallic contact. These films reduce both friction and wear. However, under severe conditions, such as high loads or sliding velocities, the rate of fresh surface exposure surpasses the rate of oxide film formation. This results in insufficient protection, leading to increased friction and higher wear rates [124]. The formation of oxide in the worn layer plays a complex role in wear behavior, as it can form a protective layer [132,133], which can be altered depending on the test conditions, causing higher wear rates, especially if the oxide layer is harder and more brittle than the substrate, it may break off entirely, further accelerating material loss [22,100,131,133,134].

3.2.3.4 The ball-cratering test applied to the study of wear

Traditional techniques such as the pin-on-disc or reciprocating sliding wear tests have been successfully employed to analyze wear behavior in metallic materials [127,135]. However, several other approaches are available. In general, wear test devices are based on the relative motion between two surfaces, typically the sample and a harder counter-body, with the purpose of quantifying the wear imposed on the sample under defined conditions of load, sliding distance, speed, and lubrication. Depending on the equipment, both the wear volume or depth and the frictional response can be evaluated.

At the laboratory scale, the ball-cratering test has gained increased attention. Originally designed for the study of micro-abrasion and thin protective coatings [136], it has also demonstrated significant applicability in dry sliding studies [22,34,107,121]. The principle of the method consists of rotating a ball against the surface of a specimen, thereby generating a spherical crater. The technique was derived from two earlier methods: dimpling, which is employed to prepare samples for transmission electron microscopy, and cap-grinding, which is used to measure coating thickness. Both of these techniques produce spherical indentations [136]. The broader advantages of the ball-cratering test include its simplicity, low cost, and the ability to evaluate small specimens and thin coatings [135,136].

Two main types of machines are commonly employed for this test. In free-ball machines, the ball is driven by friction with a motor shaft, and the load is applied by the ball's own weight combined with the inclination of the sample. Although mechanically simple, this configuration is considered less rigid [137,138]. In contrast, fixed-ball machines constrain the ball between rotating shafts, which directly drive its motion, while the load is independently applied through a separate system, such as weights. This configuration allows for higher loads than the ball weight itself, enhances mechanical rigidity, and eliminates relative motion between the shaft and the ball. For these reasons, the fixed-ball configuration is the most widely adopted [136–139].

Although the ball-cratering test is not yet fully standardized, efforts toward international standardization are underway, both through ASTM in the United States and CEN in Europe [136].

In the framework of this PhD thesis, a fixed-ball wear testing machine was employed in the M2PS laboratory at UFSCar, as in Figure 3.16. The setup consists of a hardened AISI 52100 steel ball, with a diameter of 25.4 mm and hardness of 818 HV, mounted on a rotating shaft. The specimen is secured in a holder attached to a pivoting arm, and the rotating ball is pressed against the specimen surface by applying test loads through dead weights. Prior to testing, equilibrium contact between the ball and the specimen is achieved by balancing the mass of the specimen-holder assembly with a counterweight on the pivoting arm, ensuring minimal initial contact. Only then are the additional dead weights applied to establish the desired normal load. The ball's rotational speed is controlled by an electric motor, which allows speed adjustments monitored by a digital tachometer (MINIPA – T-2238A).

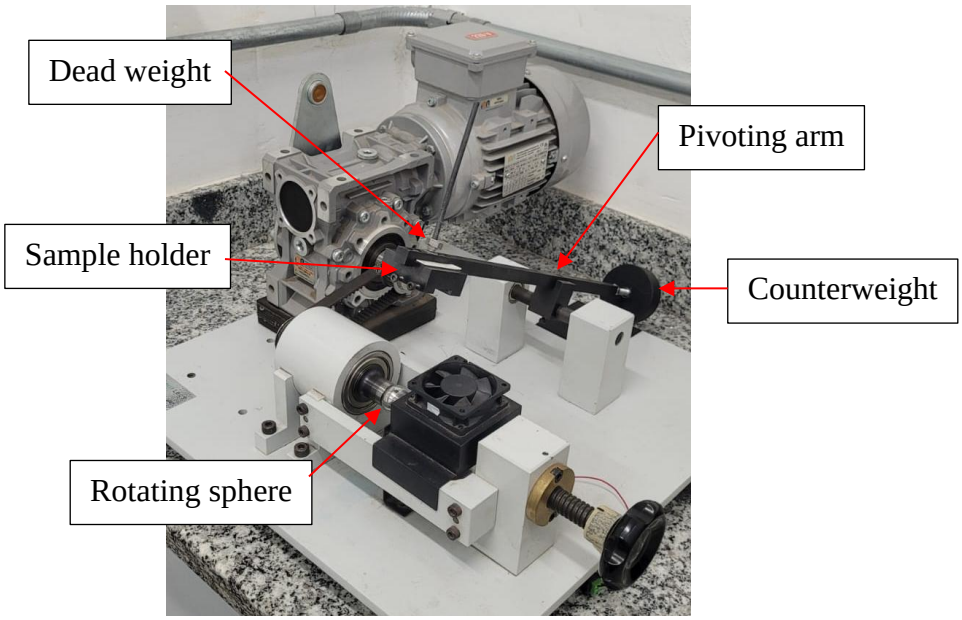

Figure 3.16: Ball cratering device at M2PS laboratory

During the test, material is removed from the sample surface, producing a spherical crater. The crater diameter is measured four times, and the average value is used to calculate the worn volume according to *Equation 3.*:

$$V_w = \frac{\pi . d^4}{64 . R} \qquad \textbf{\textit{Equation 3.18}}$$

Where V_w is the wear volume, R is the radius of the ball, and d is the mean crater diameter.

Gee *et al.* [135] demonstrated the reproducibility of the ball-cratering test using standard wear-resistant coatings, reporting a high consistency of wear depth measurements with a standard deviation of less than 5%. Similarly, promising reproducibility results were reported by Macedo *et al.* [138], who observed a standard deviation below 10% for wear volume measurements in micro-abrasion tests using the ball-cratering device.

3.2.4 A specific case: Self-lubricating alloys

3.2.4.1 Defining wear behavior in self-lubricating alloys

In tribology, several distinct regimes are commonly used to describe the fundamental mechanisms of friction and wear. These regimes range from fluid film lubricating, which completely separates moving surfaces, to dry sliding, where direct contact occurs between asperities of the opposing surfaces [124]. Under dry sliding conditions, friction and wear are governed by the interactions of these asperities, where adhesive junctions form at the contact points. To shear these bonds and allow relative motion, energy is required, and shear stress acts at the interface to break them.

Friction can be significantly reduced by introducing a thin film of material with low shear strength (τ_i) between the contacting surfaces. This principle underlies the operation of conventional lubricants. By supplying a layer of material that possesses much lower shear resistance than the bulk surfaces, lubricants decrease the coefficient of friction and consequently mitigate wear [125]. In this context, there is a class of materials able to supply a lubricating film by itself, the self-lubricating alloys.

Self-lubricating, soft or tribo-alloys, represent a class of multiphase composite materials which combine mechanical strength with intrinsic tribological functionality. They are typically composed of a hard metallic matrix, commonly based on aluminum, copper, or nickel, and dispersed inclusions of soft, low-melting-point phases such as Sn, Pb, Bi, or In [121,126,130,140–142]. The fundamental concept behind their design is to integrate a lubricating phase within the alloy itself, enabling the material to generate a protective film during sliding without the need for external lubricants.

These alloys are often applied in sliding bearings [126,142,143], as shown in Figure 3.11. In such systems, their self-lubricating capability becomes particularly critical under boundary or mixed lubrication regimes, where liquid lubricants alone are insufficient to prevent direct metallic contact. Under operating loads and frictional heating, the soft secondary phases within the alloy are gradually extruded to the surface, forming a thin film that reduces friction and protects the harder matrix and the counter face from severe damage mechanisms such as seizure, scoring, and scuffing [31,45,142].

Figure 3.17 shows the deformation of the dendritic matrix on the surface of an Al-20wt.% Sn alloy sample during ball cratering wear testing. The dark regions correspond to the aluminum matrix, while the light gray regions indicate the Sn-rich phase. On the right side of the micrograph, worn after only three minutes of testing, the soft phase shows clear deformation. This behavior is consistent with the initial formation of a lubricating film, which typically arises from the spreading of the soft phase over the worn area [144]. It should be noted that the formation of the lubricating film depends on the wear conditions and alloy composition.

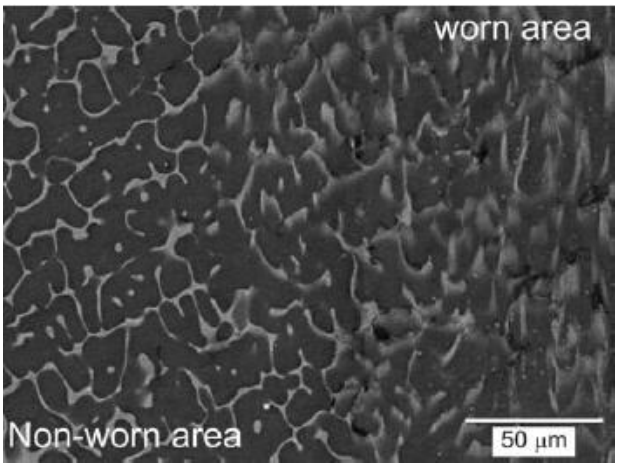

Figure 3.17: Scanning electron micrograph of the worn surface produced in an Al-20wt.%Sn alloy after a wear test [34]**.**

Bushe *et al.* [31] studied how the resistance of the phases of a self-lubricating alloy influences on lubricant film formation, considering an aluminum matrix and a second soft phase such as Sn or Pb. The study revealed that if the external load imposed on the material is high and the yield stress of the matrix is not very high, the matrix

undergoes plastic deformation. In this region, the soft inclusions are completely squeezed to the surface, forming the lubricating film. On the other hand, at lower loads or with a high-strength matrix, the deformation of the matrix is predominantly elastic. In this case, the amount of soft phase expelled is defined by the plastic deformation of the inclusions themselves. Pathak and Mohan [145] interpreted in their studies with self-lubricating alloys that the lower the modulus of elasticity of the soft phase, the more effective the wear protection.

In addition to lubricant film formation, to perform effectively in bearing applications, the self-lubricating alloys must meet a delicate balance of mechanical requirements. Since they are often employed as the innermost lining in contact with the rotating shaft, they must be softer than the crankshaft material to accommodate operational imperfections such as misalignment, machining tolerances, or contamination [142]. At the same time, they must have high strength to withstand pressure peaks in the lubricant and peak loads from the engine. However, their hardness needs to be low enough to prevent damage to the crankshaft, and fatigue resistance is also desirable to withstand cyclic stresses [30]. Thus, a successful self-lubricating alloy must exhibit adequate mechanical strength and hardness, to support service loads without damaging the shaft, fatigue resistance, enabling long-term operation under cyclic loading and ductility, which allows conformability to geometric imperfections and prevents brittle fracture, often all provided by the hard matrix.

Traditionally, wear behavior is described by Archard's law, which predicts that wear rate decreases as hardness increases. This relationship is confirmed for some conventional alloys, such as Al-Si and Al-Mg-Zn systems [34,127,146]. However, for cast self-lubricating alloys, hardness alone cannot predict wear resistance. In fact, several studies report an inverse or non-monotonic correlation between hardness and wear resistance [51,121,147], emphasizing that wear protection emerges not only from mechanical strength but also from the efficiency of film formation. Thus, the balance between load-bearing capacity and tribological performance is more complex than conventional models suggest. The volume fraction, morphology, and distribution of soft phases are central to this balance [31,34,36,45,107].

Bushe *et al.* [31] showed that, for alloys with low-strength matrices, the thickness of the lubricating film increases significantly with higher soft-phase

concentrations. In contrast, alloys with high-strength matrices display a non-linear response, reaching a maximum value for a given soft phase concentration. Similar findings were reported by Oliveira *et al.* [107], who observed that Al-3%Bi alloys with higher Pb contents exhibited superior wear resistance despite having similar hardness values. Moura *et al.* [144] also demonstrated that Al-3%Cu-Bi alloys with higher Bi content resisted wear more effectively. Even without varying the chemical composition, some studies reveal that regions richer in soft phase, whether due to macrosegregation or microstructural spacing, also exhibit better wear behavior [34,51].

The nature of the added elements brings more complexity to the wear behavior of self-lubricating alloys. For example, increasing the Bi content in Al-Sn-Bi alloys can increase the brittleness of the alloy. This, in turn, can lead to a decrease in self-lubricating properties, as brittleness can result in the formation of Bi fragments during friction. Research shows that the coefficient of friction of Al-20Sn-xBi alloys (where x = 0, 1, 2, 3% by weight) first decreases to 0.23 and then increases to 0.32 as the Bi content increases from 0% by weight to 3% [45].

The dispersion of phases also plays a critical role in the wear behavior of aluminum alloys. However, their distribution is generally evaluated only through two-dimensional microstructural observations. Bushe *et al*. [31] proposed that the amount of lubricant released increases as the average spacing between inclusions decreases, provided the overall concentration remains constant. The effect of dispersion, however, strongly depends on the nature of the minority phases and does not follow a straightforward relationship, as is often the case with bulk mechanical properties. In alloys with higher Bi content, where Bi is harder than Sn, Pb, and In, wear resistance improves with more refined microstructures, characterized by smaller and more uniformly distributed particles (i.e., shorter interparticle spacing). Such refinement promotes the formation of a more effective lubricating layer, which shields the aluminum matrix from damage and reduces both wear volume and wear rate [44,100,107,144]. In contrast, alloys containing softer elements such as Sn, Pb, or In exhibit the opposite trend: their wear resistance improves with coarser microstructures, where larger and more widely spaced particles facilitate the development of a thicker and more continuous lubricating film. This film provides more effective protection during sliding, leading to improved wear performance [34,44,51,147].

Importantly, microstructural spacing and dispersion can be tailored through solidification parameters. By controlling microstructural refinement, it becomes possible to design alloys that simultaneously provide adequate load-bearing capability and enhanced self-lubricating performance.

3.2.4.2 Al-Sn-Cu self-lubricating alloys

Aluminium-based alloys are widely used for bearing components, particularly those traditionally alloyed with Pb. These alloys exhibit favourable tribological properties when in contact with steel shafts, and they formed the basis of the renowned Babbitt alloys [124]. However, increasing environmental concerns have renewed interest in replacing lead, and Sn has emerged as an excellent alternative due to its self-lubricating properties. However, although binary alloys composed of soft, self-lubricating elements offer adequate wear resistance, the incorporation of additional elements has been shown to increase their load-bearing capacity. Consequently, there has been interest in incorporating reinforcing elements into the matrix, such as Cu [16,51]. And the study of Al-Sn-Cu systems for tribological applications.

The combination of these elements is strategic, with each one playing a complementary role in the alloy's performance. The soft Sn phase, with its low melting point of approximately 232 °C and low strength, approximately 19 MPa at room temperature [148], acts as a solid lubricant, reducing the coefficient of friction and wear. The aluminum matrix, known for its ductility and light weight, can be reinforced by adding Cu. Copper, in turns, significantly enhances the alloy's mechanical properties, such as hardness and fatigue strength, either through solid solution strengthening or the precipitation of Al_2Cu intermetallic [53]. This additional strength is crucial for compensating for the low load-bearing capacity and inherent softness of high-tin content Al alloys [16].

The addition of Cu to the Al-Sn system, however, introduces significant complexity to microstructural control. At a certain point, Cu promotes a stable liquid miscibility gap, which can lead to monotectic reactions and the separation of the alloy into two distinct liquid phases during cooling [149]. For example, studies have shown that in Al-20wt.%Sn alloy, liquid demixing occurs when the Cu content exceeds 3 wt.%

[53]. This phenomenon, known as phase segregation, makes microstructural control during solidification more challenging.

Controlling phase segregation requires precise control of thermal variables. The cooling rate is a critical factor. For example, Figure 3.18(a) shows the microstructure of an Al-20wt.%Sn-1wt.%Cu alloy produced by the Belt Casting (BC) technique. It presents a cellular/dendritic morphology with large α-Al grains (dark contrast) and β-Sn (bright contrast) segregated in the interdendritic regions, a typical feature of solidification under low cooling rates [149]. In contrast, Figure 3.18(b) shows the same alloy produced by melt-spinning. Although the magnifications differ, the microstructural features are clear. Due to the extremely high cooling rate (~4.7×10^5 K/s), the alloy solidified by melt-spinning follows a metastable monotectic solidification route: the homogeneous liquid separates into Al-rich (L_1) and Sn-rich (L_2) liquids. During rapid cooling, fine droplets of the minor L_2 phase are trapped in the solidifying L_1, producing a refined microstructure of small, rounded β-Sn particles homogeneously distributed within a much finer α-Al matrix. This contrasts with the coarse segregation observed in the BC sample (Figure 3.18(b)) [149] . Similar refinement and uniform phase dispersion have also been reported for intensive melt shearing [41].

These results highlight that non-conventional processing routes can effectively reduce segregation in Al-Sn-Cu alloys. However, it is important to note that the conventional production of these alloys for sliding bearings is still based on standard casting. Therefore, understanding solidification under such conditions, as well as its relationship with microstructure, mechanical properties, and wear behaviour, remains essential.

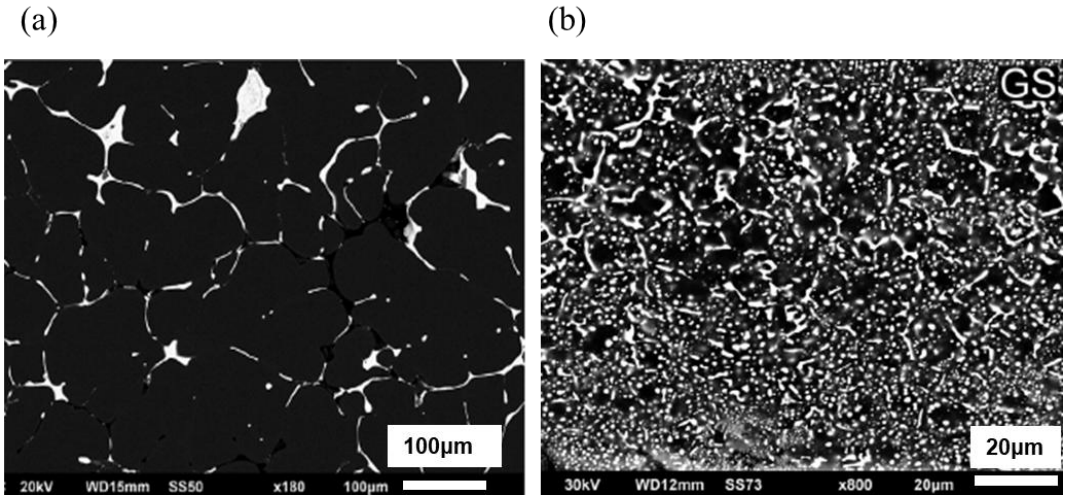

Figure 3.18: SEM micrographs of Al-20wt.%Sn-1wt.%Cu samples solidified by (a) belt casting method and (b) melt-spinning. Adapted from [149]**.**

The commercial SAE 783 (Al-20wt.%Sn-1%Cu) alloy is a practical example of a bearing material optimized for performance. Its composition is designed to provide excellent wear resistance without the need for an additional overlay. This alloy offers high fatigue strength, excellent corrosion resistance, high thermal conductivity, and a low cost, making it ideal for sliding bearings [124]. The manufacturing process for bearings using SAE 783 alloys can involve conventional casting with graphite profile die, as illustrated in Figure 3.19. After solidification, the alloy undergoes hot rolling followed by bonding with a layer of commercially pure Al, which is then clad with a 1008 low-carbon steel, forming bi-metallic bearing structure, as shown in Figure 3.11. This layer of pure Al will act as a compatibility interface between the Al alloy and the steel, promoting adhesion in the cladding process that occurs next. The final step involves heat treatment for stress relief and microstructure stabilization. The process delineated herein is founded upon a technical visit to the MAHLE Metal Leve S.A. factory in São Bernardo do Campo, São Paulo, Brazil.

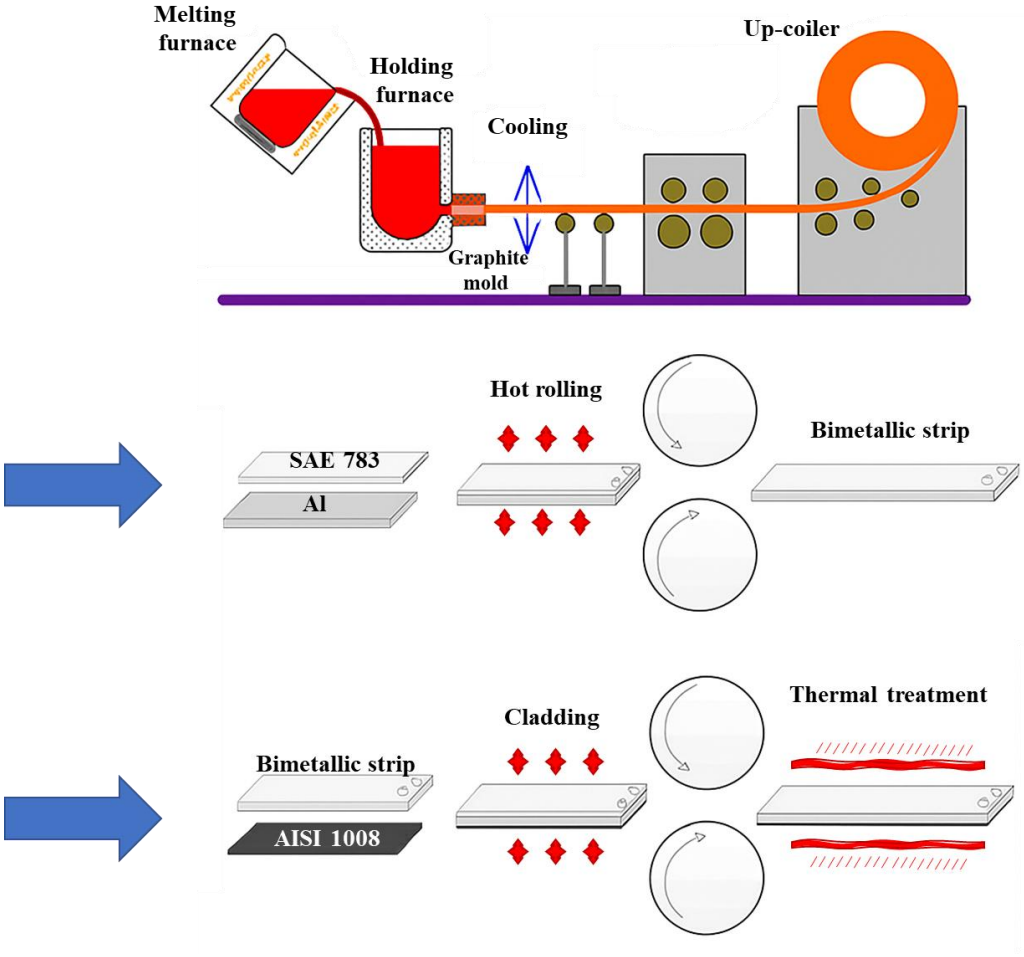

Figure 3.19: Production plant for bi-metallic strip SAE 783 alloy for the production of sliding bearings. Adapted from [150] and [151] using artificial intelligence tools.

At the end of this process, the profile of the alloy produced resembles that shown in Figure 3.20,in which three distinct sections are discernible. The SAE 783 alloy (Al-20wt.%Sn-1wt.%Cu), with a dark gray aluminum matrix and a light-colored Sn-rich phase dispersed throughout, the light gray steel back, and the layer of pure aluminum bonded to the other two.

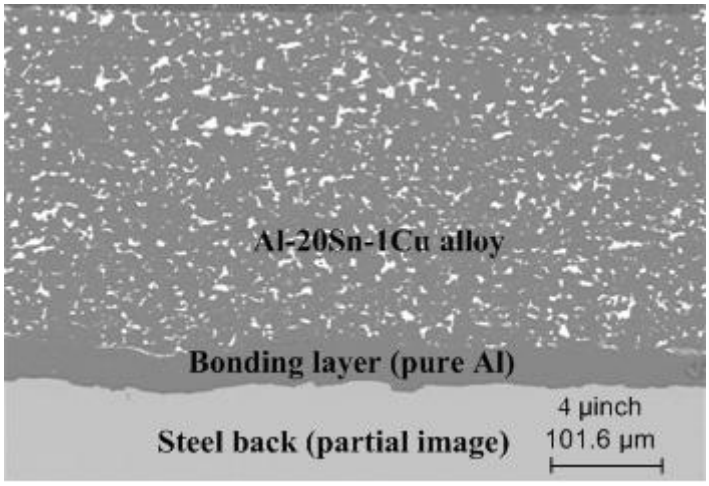

Figure 3.20: Bi-metal Al-Sn-Cu bearing (microstructure) [152]**.**

3.3 Experimental procedures and results

3.3.1 Al-20wt.%Sn-1wt.%Cu solidification under transient regime

3.3.1.1 Solidification path Thermodynamical calculations

The solidification path of the Al-20wt.%Sn-1wt.%Cu alloy was first calculated using the Scheil model, which assumes complete solute mixing in the liquid and negligible diffusion in the solid [1]. This approach closely reflects the experimental conditions, as solidification occurred under non-equilibrium and Sn exhibits very limited solubility in Al. The Scheil model is therefore especially useful for comparison with the non-steady directional solidification experiment.

For reference, the solidification path was also calculated under equilibrium conditions, in which the mass fraction of each phase evolves with temperature. Unlike the Scheil model, this approach provides a clearer insight into the thermodynamic stability of phases and the sequence of transformations expected under slow cooling. All thermodynamic calculations were performed with Thermo-Calc software, using the TCAL7: Al-Alloys v7.1 database (version 2024b) [79].

Figure 3.21 presents the Scheil solidification path for the Al-20wt.%Sn-1wt.%Cu alloy, expressed as the variation of solid fraction with temperature (from the left side to the right side). Solidification begins at 630.2 °C with the nucleation of α-Al dendrites (red dashed-line). Between 529.1 °C and 229.4 °C (green dashed-dotted line),

the θ-Al_2Cu phase nucleates and grows in equilibrium with both the liquid and the α-Al phase. As the process advances, solute rejection progressively enriches the remaining liquid until the (α-Al + θ-Al_2Cu+ β-Sn) eutectic reaction takes place at 229.4 °C.

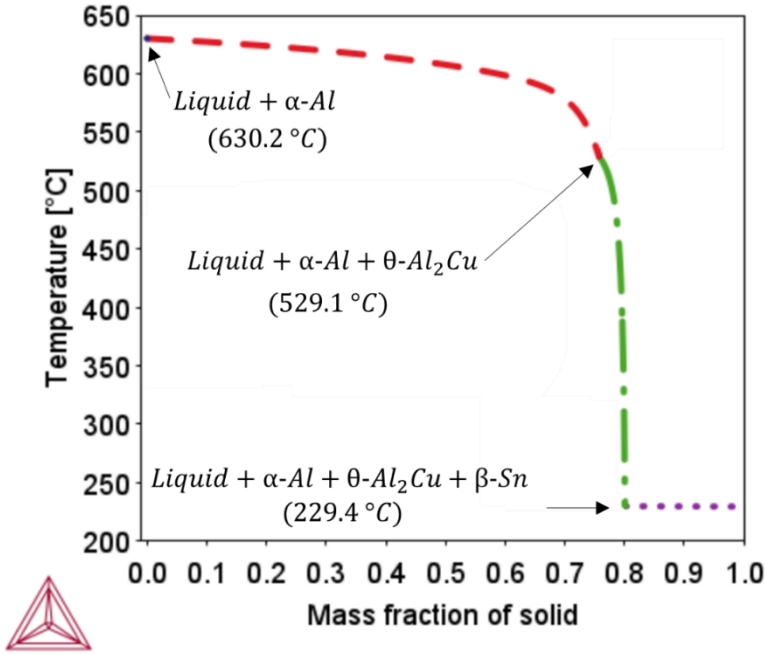

Figure 3.21: Solidification path of the Al-20%Sn-1%Cu alloy provided by Scheil's model.

The equilibrium solidification path, shown in Figure 3.22, from the right side to the left side, begins with α-Al formation at 630 °C, marked by a simultaneous decrease of the liquid phase mass fraction (blue solid-line) and an increase of the solid aluminium phase (red dashed-line), continuing until 382.5 °C. Below 382.5 °C and down to the eutectic temperature (229.5 °C), the liquid phase reacts with the solid α-Al to form θ-Al_2Cu intermetallic (green dashed-dotted line). This explains the very slight decrease of both α-Al and liquid fractions in the graph, concomitantly with an increase in θ-Al_2Cu phase fraction. Finally, the remaining solute-enriched liquid solidifies via a eutectic reaction, forming the α-Al/β-Sn/θ-Al_2Cu solid at 229.5 °C. Because Sn solubility in Al is extremely low, the β-Sn phase remains nearly pure tin, accounting for ~20 wt.% of the alloy, while θ-Al_2Cu and α-Al correspond to ~2 wt.% and ~78 wt.% of the solid, respectively, at 150 °C.

Comparison of Figure 3.21 and Figure 3.22 shows that both equilibrium and non-equilibrium conditions predict the same sequence of phases and similarly long solidification intervals of nearly 400 °C, which emphasizes the strong influence of the microstructural scale of α-Al on β-Sn distribution. The main difference is the earlier appearance of θ-Al_2Cu under Scheil conditions, which results from faster solidification that promotes localized Cu enrichment at the solid-liquid interface. Notably, the addition of 1 wt.% Cu is insufficient to induce a monotectic reaction or liquid phase separation, consistent with previous reports [53].

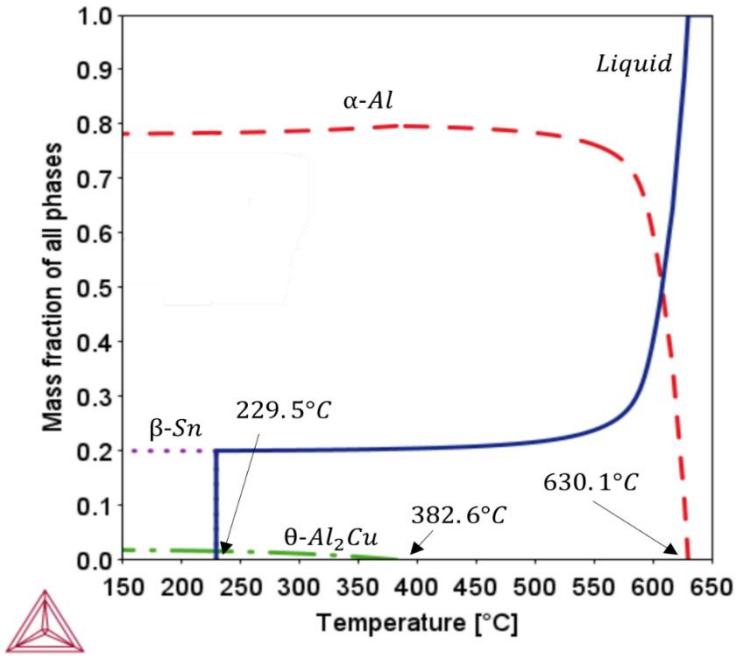

Figure 3.22: Solidification path of the Al-20%Sn-1%Cu alloy at equilibrium.

3.3.1.2 Upwards solidification apparatus

A schematic representation of the experimental setup used for the transient unidirectional solidification of the Al-20wt.%Sn-1wt.%Cu alloy is shown in Figure 3.23. The apparatus was specifically designed so that heat extraction occurs exclusively through a water-cooled base, thereby promoting upward directional solidification and minimizing natural convection. This configuration enables the production of ingots under a wide range of cooling rates, which gradually decrease with increasing distance from the chilled surface. Consequently, a gradient of microstructures is generated along

the longitudinal axis of the ingot. This variation allows for direct correlation between solidification thermal parameters and microstructural features within a single ingot.

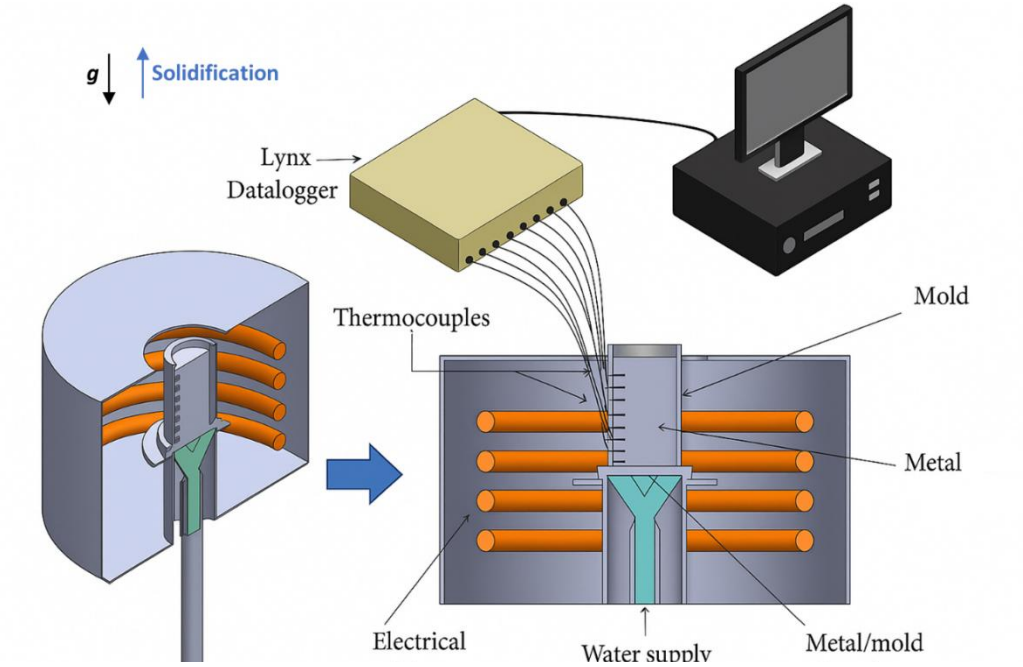

Figure 3.23: Upward directional solidification furnace, where ***g*** is the gravity vector. Image generated by artificial intelligence.

The heating system in the furnace consists of electrical resistances embedded in a cylindrical refractory block, thermally insulated from the environment by a layer of refractory cement. The temperature is controlled by adjusting the electric current supplied to the resistances and a thermocouple located inside the heating system provides feedback to a power controller, ensuring precise temperature regulation. The melt temperature is recorded by type K thermocouples positioned on the mold wall, and data acquisition is performed by a Lynx ADS-1800 data logger, which allows the use of 8 acquisition channels at a rate of 5 measurements per second on each channel, transforming the records into real-time digital data using the manufacturer's software. Figure 3.24 presents a photograph of the directional solidification setup used in this study, installed at the Department of Materials Engineering at UFSCar.

The mold assembly, in which the directionally solidified ingot was produced, was a split mold made of AISI 310 stainless steel. When assembled, it has an inner diameter

of 60 mm, a height of 160 mm, and a wall thickness of 5 mm. Eight holes along its sides allow for thermocouple placement. Attached to the base of the mold is a 3 mm-thick steel plate made of AISI 1020, which serves as the heat-extracting surface during solidification. The contact surface of this plate, crucial for efficient heat transfer, was polished up to #1200 grit finish. To minimize radial heat loss, seal the mold, and facilitate ingot removal, the inner sidewalls were coated with a ~1.5 mm layer of silico-aluminous ceramic fiber cement (QF-180, Unifrax). Figure 3.25 shows the split mold with its refractory coating, the thermocouple insertion positions and the base.

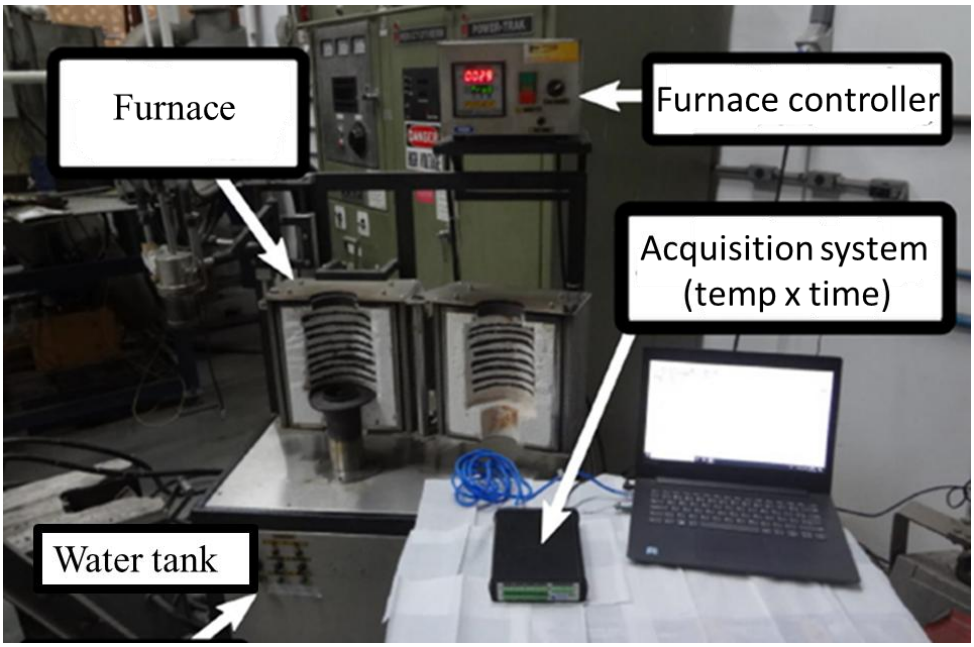

Figure 3.24: Directional solidification equipment belonging to the M2PS laboratory at UFSCar.

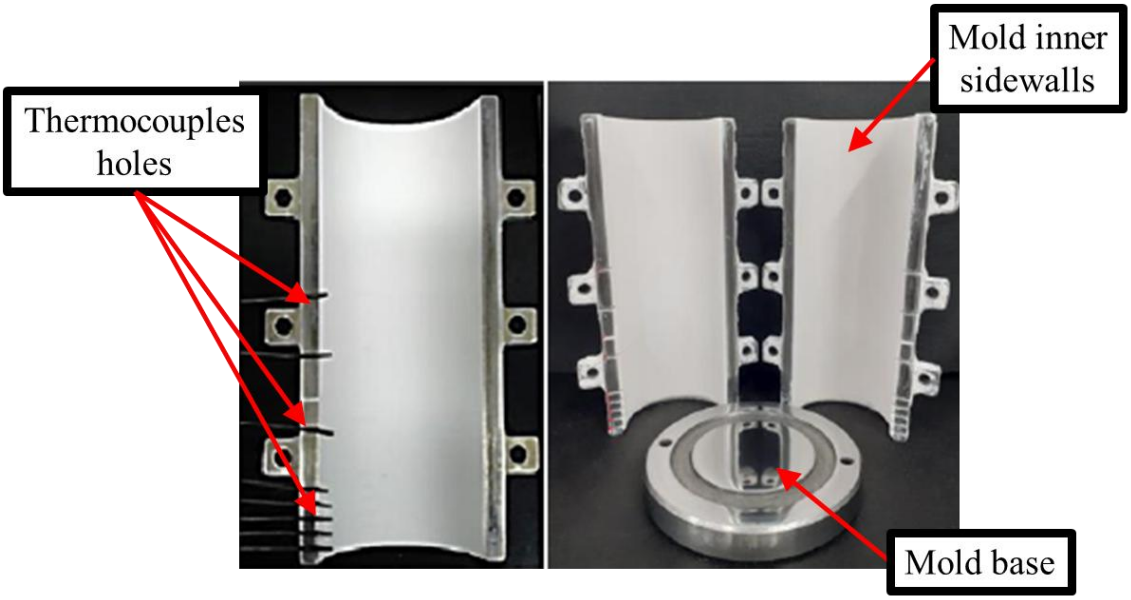

Figure 3.25: AISI 310 stainless steel split mold used in directional solidification and 1020 carbon steel mold base, with detail, in the photo on the left, of the thermocouples positioned in the mold wall.

3.3.1.3 Upwards directional solidification experiment

The experimental study on the Al-20wt.%Sn-1wt.%Cu alloy comprised both the preparation of the alloy and its subsequent directional solidification. The alloy was produced by melting commercially pure metals, carefully weighed to match the nominal stoichiometric composition. Melting was performed in a silicon carbide crucible (Carbosil, model AS 6) placed inside an induction furnace (Inductotherm VIP, Power-Trak 50-30 R).

Once the alloy was produced in the induction furnace, it was necessary to determine the experimental *liquidus* temperature for comparison with thermodynamic calculations and the determination of the superheating temperature before solidification. The *liquidus* temperature (T_L) is conventionally identified as the point at which the first major deviation from the linearity of a slow cooling curve occurs, resulting from the release of latent heat during nucleation. In practice, T_L is found by recording cooling curves at rates slow enough to ensure a perceptible change in slope. Experimentally, the procedure was performed by monitoring the cooling curve of a small amount of alloy, approximately 300 g, placed in a silicon carbide crucible insulated with a thermal

blanket. The test was performed inside the induction furnace, which had been turned off but remained hot to reduce heat flow.

The experimentally determined *liquidus* and eutectic temperatures are presented in Figure 3.26. The *liquidus* was found to be 627.4 °C and the eutectic 227.5 °C. These values are in excellent agreement with thermodynamic predictions obtained with Thermo-Calc (Figure 3.22), as the differences between experimental and calculated values are within 3 °C, well inside the instrumental error of the thermocouple.

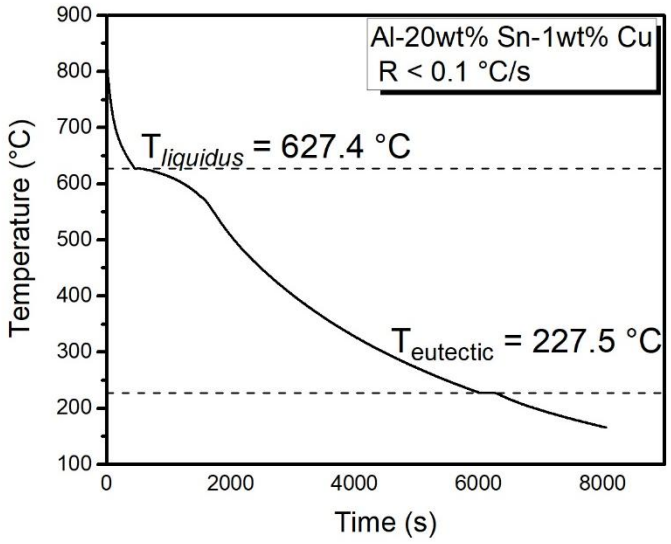

Figure 3.26: Experimental liquidus and eutectic temperature found for the Al-20%Sn-1%Cu alloy. Cooling rate (R) lower than 0.1 °C/s.

After determining the experimental *liquidus* temperature, upward directional solidification experiments were performed under transient heat extraction conditions. During these experiments, while the alloy was re-melted in the induction furnace previously described, the mold assembly was preheated within the directional solidification device. Preheating was controlled such that the thermocouple located closest to the mold base indicated a temperature nearly 10% above the experimentally determined *liquidus* temperature.

Once this preheating stage was completed, and after degassing and slag removal of the molten alloy, the melt was poured into the mold. The electrical resistance heaters surrounding the mold maintained the alloy in the liquid state for a few minutes. This

holding period was necessary to minimize liquid motion generated during pouring, ensuring that the experiments started from a stationary condition of the molten metal.

Subsequently, the resistive heating system was switched off, allowing the melt to cool down until the thermocouple nearest to the mold base again reached a temperature 10% above the *liquidus*. At this point, water flow through the bottom chill plate was activated, initiating directional solidification. The cooling curves were recorded using thermocouples inserted at distances of 5.2, 9.2, 14.3, 19.1, 24.0, 44.4, 69.2, and 89.3 mm from the base of the ingot.

3.3.1.4 Solidification variables: cooling rate, thermal gradient, solidification velocity

The cooling curves recorded by the eight thermocouples are shown in Figure 3.27, where each curve corresponds to a thermocouple whose position is indicated in the legend. Figure 3.27 shows the time delay required for the isotherms to propagate from the cooled base of the ingot, both for the experimental *liquidus* (T_L = 627.4 ◦C) and the eutectic temperatures (T_{eut} = 227.5 ◦C), confirming the unidirectional heat flow. The set of cooling curves recorded at different positions along the ingot provides the necessary data for determining the solidification thermal parameters, according to the procedures described in topic 3.2.1.3.

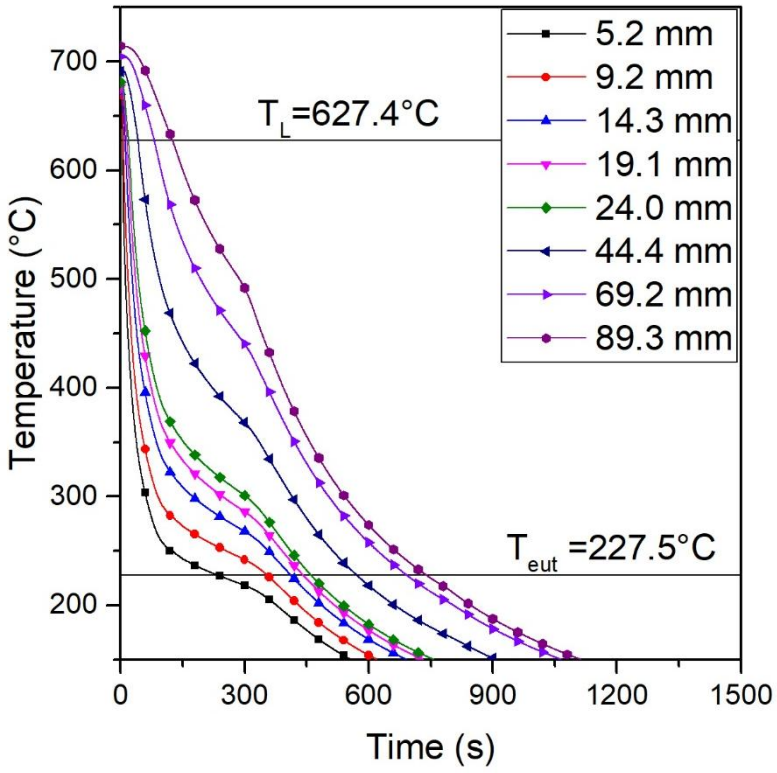

Figure 3.27: Experimental cooling curves from upward directional experiment with the Al-20wt.%Sn-1wt.%Cu alloy.

The first parameter analyzed was the time taken for the *liquidus* temperature to pass through the ingot. This was determined by identifying the time at the *liquidus* temperature intersected each cooling curve (Figure 3.27), generating position x time pairs as plotted in Figure 3.28. A power law fit function, $P = 2.55 \times t^{0.74}$, was applied to these data. Subsequently, from the derivative of this fitted function, values of the solidification front velocity were obtained.

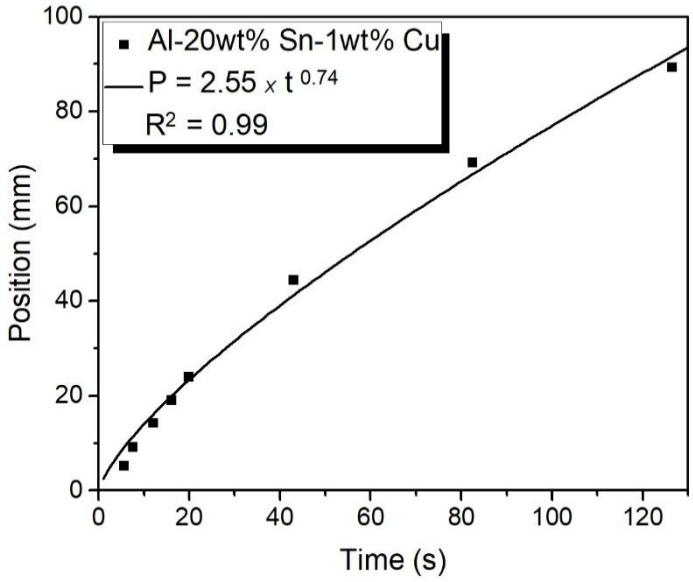

Figure 3.28: Position from the metal/mold interface as a function of the liquidus temperature passage time in the Al-20wt.%Sn-1wt.%Cu alloy. R^2 is a statistical measure that indicates the proximity of the experimental data to the adjusted regression line.

The front velocity according to position is presented in Figure 3.29, where the experimental data were also fitted by a power-law curve, $V = 2.4 \times P^{-0.33}$.

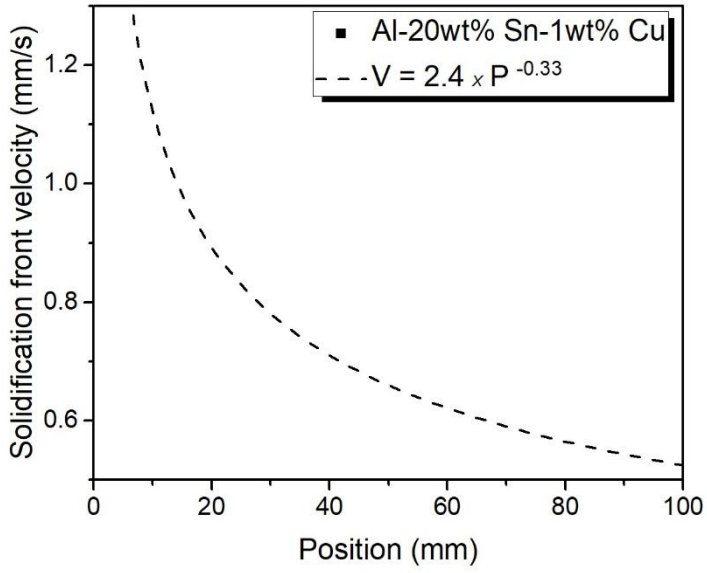

Figure 3.29: Graph of the solidification front velocity as a function position from the metal/mold interface in the Al-20wt.%Sn-1wt.%Cu alloy.

The local cooling rate was determined from the first derivative of a polynomial function in the vicinity of the *liquidus* temperature. The resulting cooling rate x position pairs were then fitted by a power curve, $R = 174.5 \times P^{-1.1}$, as shown in Figure 3.30.

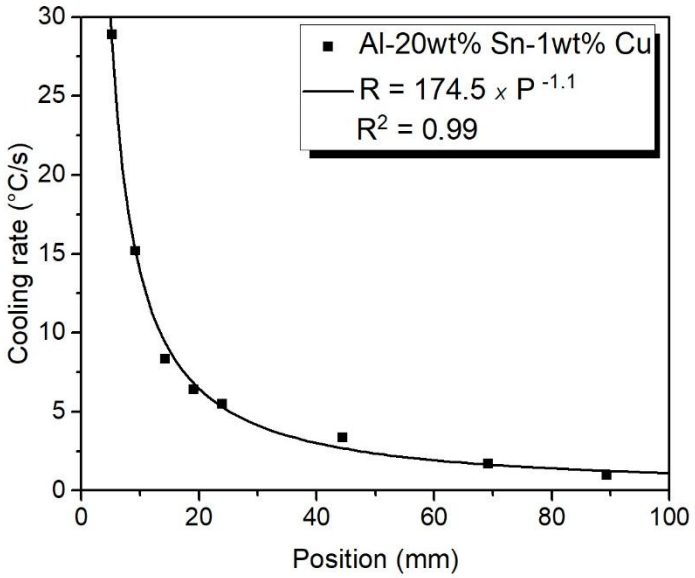

Figure 3.30: Cooling rate as a function position from the metal/mold interface in the Al-20wt.%Sn-1wt.%Cu alloy. R^2 is a statistical measure that indicates the proximity of the experimental data to the adjusted regression line.

Finally, the relationship between cooling rate and front velocity enabled the calculation of the thermal gradient for each monitored position. The resulting thermal gradient x position pairs were then fitted by a power curve, $G = 104.8 \times P^{-0.9}$, as shown in Figure 3.31.

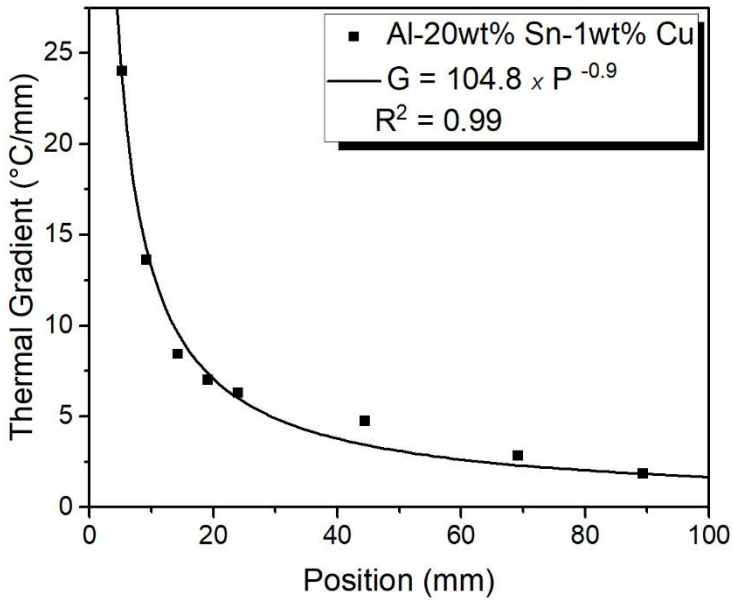

Figure 3.31: Thermal gradient as a function position from the metal/mold interface in the Al-20wt.%Sn-1wt.%Cu alloy. R^2 is a statistical measure that indicates the proximity of the experimental data to the adjusted regression line.

In summary, the velocity varies from 1.2 to 0.5 mm/s, the cooling rate varies from 28.9 to 1.0 °C/s, and the thermal gradient varies from 24.0 to 1.8 °C/mm, with the highest values occurring near the cooled surface, followed by a gradual reduction along the length of the ingot. The results clearly demonstrate that forced cooling at the mold base imposes a decreasing profile for the thermal parameters. This behavior arises from the increasing thermal resistance of the growing solidified layer with distance from the chilled surface. Such variation directly correlates with the experimental measurements of dendritic spacings as well as phase size, which will be discussed in the following.

3.3.2 Macro and microstructure characterization

3.3.2.1 Macrographic analysis

Macrographic analysis was performed to identify the nature of the grains induced by the imposed solidification conditions. For this purpose, the directionally solidified cylindrical ingot was longitudinally sectioned along its axis, providing full access to the interior of the ingot. The exposed surface was sequentially ground using abrasive papers of decreasing grit size (#80, #120, #320, #400, and #600). To reveal the

macrostructure, the prepared surface was etched by swabbing the Poulton's solution (12 ml HCl + 6 ml HNO_3 + 1 ml HF + 1 ml H_2O).

Figure 3.32 shows the macrostructure along the ingot, for which three zones can be identified. From the bottom to the top, zone I, which covers the highest cooling rates, from 28.9 to 5.5 ◦C/s, is characterized by a high density of very small chilled grains. Some of these grains grew oriented to the growth direction coinciding with the heat flow. Then, a mixed zone with the coexistence of fine columnar grains and few equiaxed grains is observed [147,153], i.e., zone II, which covers the positions cooled between 3.4 and 1 °C/s. Zone III represents the blockage of columnar grains by equiaxial grains caused by a transition between growth modes, the columnar-to-equiaxial transition [64,154]. The analysis of zone III is outside the scope of this study.

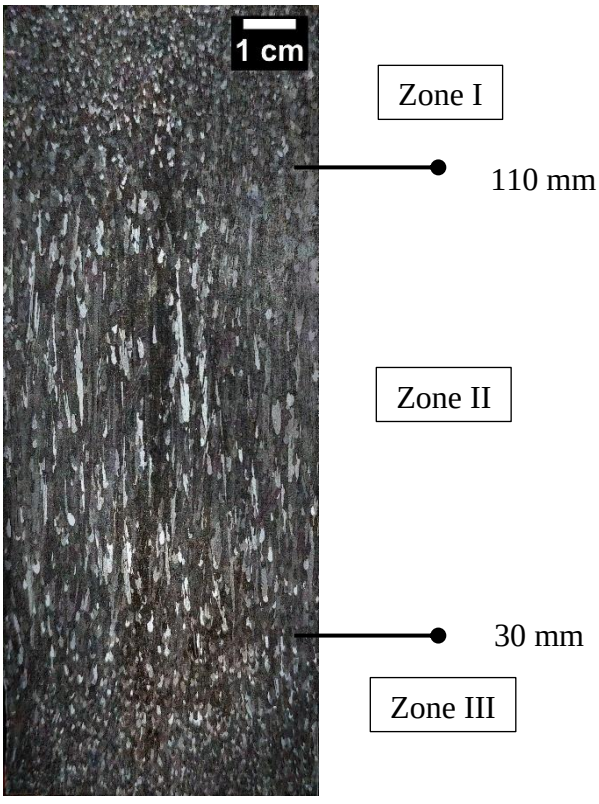

Figure 3.32: Macrostructure at the center surface of the ingot, highlighting zone I (cooled between 28.9 and 5.5 °C/s), zone II (cooled between 3.4 and 1.0 °C/s) and zone III, located at the top of the ingot in the Al-20wt.%Sn-1wt.%Cu alloy.

3.3.2.2 α-Al spacing

To investigate the microstructural evolution along the cooling direction, eight cross-sectional samples were extracted from the ingot at positions corresponding to the thermocouple locations. The metallographic preparation of the samples consisted of cold mounting, followed by grinding with SiC papers of #320, #400, #600, #1200, and #1500 grit, and polishing with a 1 μm diamond suspension, in accordance with ASTM E3-11 [155]. The samples were then etched by immersion for 10 s in Keller's reagent (2 mL HF, 3 mL HCl, 5 mL HNO_3, and 75 mL H_2O) to reveal the dendritic structure. Optical microscopy (OM) was performed using an Olympus BX41M-LED (Tokyo, Japan), and dendritic spacing was quantified with the ImageJ software package [72,156].

The conventional triangle method for primary dendrite arm spacing (λ_1) [119] could not be used due to the complexity of the dendritic morphology. Therefore, a technique adapted from the Heyn linear intercept method [157] was developed and applied, in which the average dendritic arm spacing (λ_A) was automatically determined by calculating the ratio between the number of dendritic arms intersected and the length of a reference line.

In order to automatically quantify the dendritic arm spacing, the micrographs were segmented into two regions of interest: the dendritic and the interdendritic areas. For this purpose, the "Trainable Weka Segmentation" (TWS) plug-in of ImageJ [158,159] was employed, which provides an advanced tool for supervised image segmentation. In this approach, representative examples of each region of interest (ROI) are supplied so that the algorithm can learn their distinguishing features and then apply this knowledge to segment new images. The training process requires the manual selection of characteristic areas of both dendritic and interdendritic regions, enabling the algorithm to differentiate between them based on shape, color, and pixel intensity. Once trained, the model is capable of automatically classifying similar images, assigning pixel labels according to the learned classes. Figure 3.33(a) and Figure 3.33(b) illustrate the original and the segmented images, respectively, where the green color represents the interdendritic region and the red color corresponds to the dendritic region. Figure 3.33(c) shows the overlap of the two, confirming that the segmentation procedure was successful in isolating the regions of interest, with a strong agreement between the

expected features and the segmented areas. This demonstrates the reliability and accuracy of the method in distinguishing the dendritic morphology.

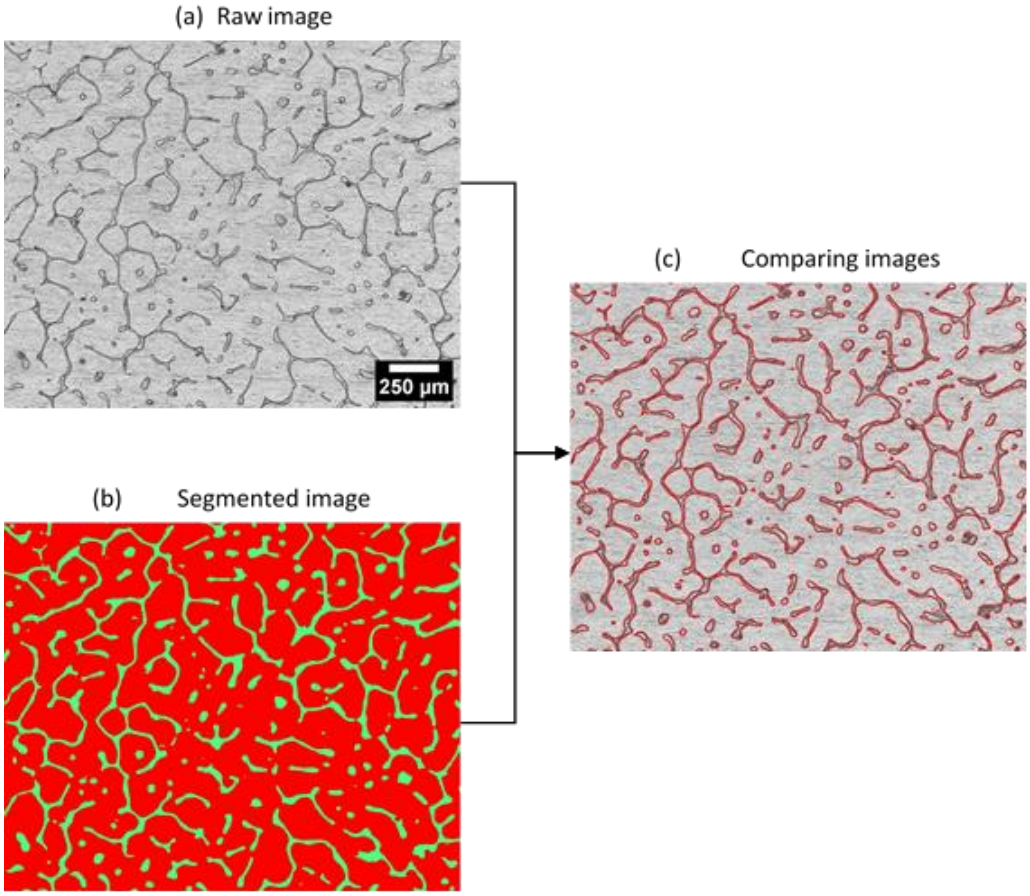

Figure 3.33: Segmentation of the micrograph of the Al-20wt.%Sn-1wt.%Cu alloy using the WTS tool: a) the original image, b) the image segmented into two regions, the dendritic region in red and the interdendritic region in green, c) the comparison between the original image and the segmented image with the interdendritic regions delimited in red.

After segmentation, the average dendritic spacing can be accurately calculated by binarizing the image using thresholding. Binarization transforms the image into two classes of pixels: one class representing the dendrites (white) and the other representing the interdendritic region (black), as shown in Figure 3.34.

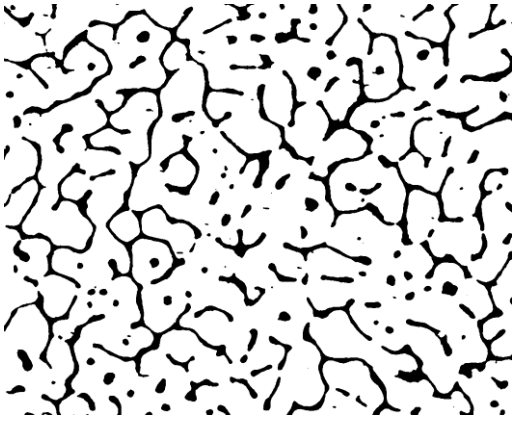

Figure 3.34: Binarized figure. In white, the dendritic region and, in black, the interdendritic region.

The average dendritic arm spacing was then measured using a macro created in ImageJ software. This script automatically draws 100 lines of known length at different orientations across the image, counts the number of intersections with the dendritic region, and normalizes the result by the line length. The analysis was performed in pixel units and subsequently converted to micrometers using the original image scale. The repeatability of the method was verified, showing uniformity in the mean value and standard deviation, as confirmed by Figure 3.35.

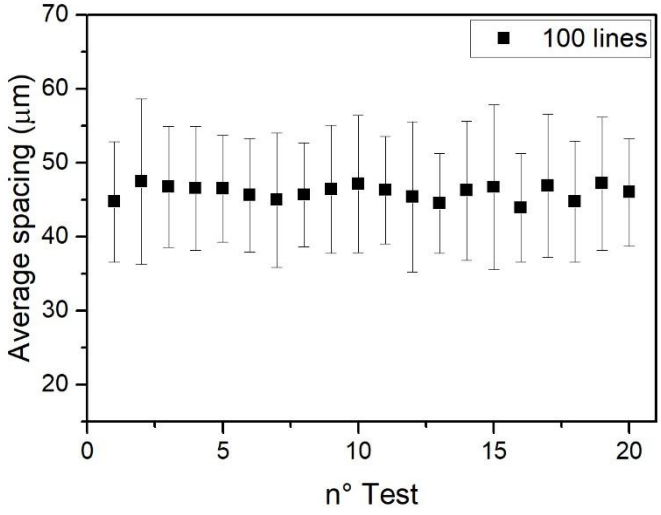

Figure 3.35: Repeatability of measurement in average dendritic spacing of the Al-20wt.%Sn-1wt.%Cu alloy using the automated method.

Figure 3.36 presents representative micrographs obtained at the eight positions along the ingot cross-section, correlated with the solidification thermal parameters and the average dendritic spacing determined using the described method. The images emphasize the coarsening in dendrites as the samples are taken at positions distant from the cooled base of the ingot, resulting in a reduction in velocity, gradient, and cooling rate.

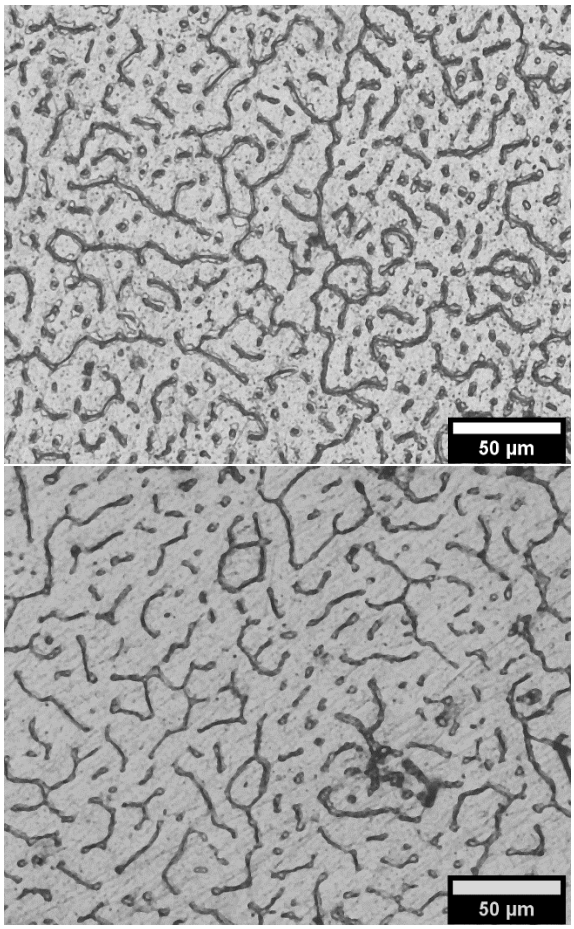

P = 5.2mm

V = 1.2 mm/s

G = 24 °C/mm

R = 28.9 °C/s

λ_A = 15.7 ± 2.2 µm

P = 9.2 mm

V = 1.1 mm/s

G = 13.6 °C/mm

R = 15.2 °C/s

λ_A = 19.8 ± 3.3 µm

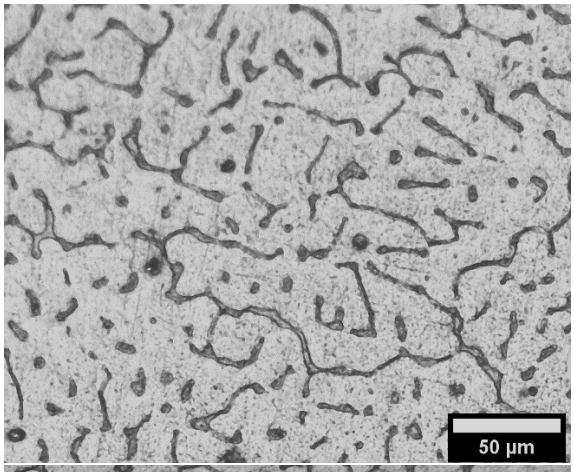

P = 14.3 mm

V = 1.0 mm/s

G = 8.4 °C/mm

R = 8.3 °C/s

λ_A = 22.2 ± 4.6 µm

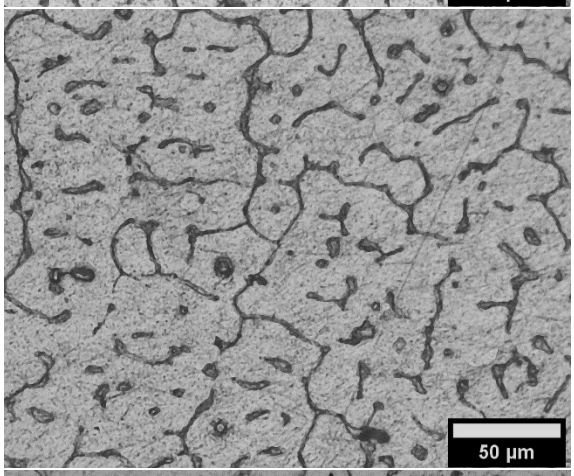

P = 19.1 mm

V = 0.9 mm/s

G = 7.0 °C/mm

R = 6.4 °C/s

λ_A = 25.5 ± 4.6 µm

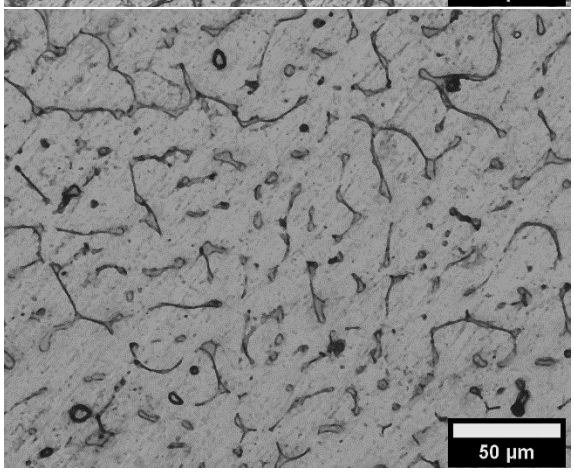

P = 24.0 mm

V = 0.9 mm/s

G = 6.3 °C/mm

R = 5.5 °C/s

λ_A = 28.2 ± 6.8 µm

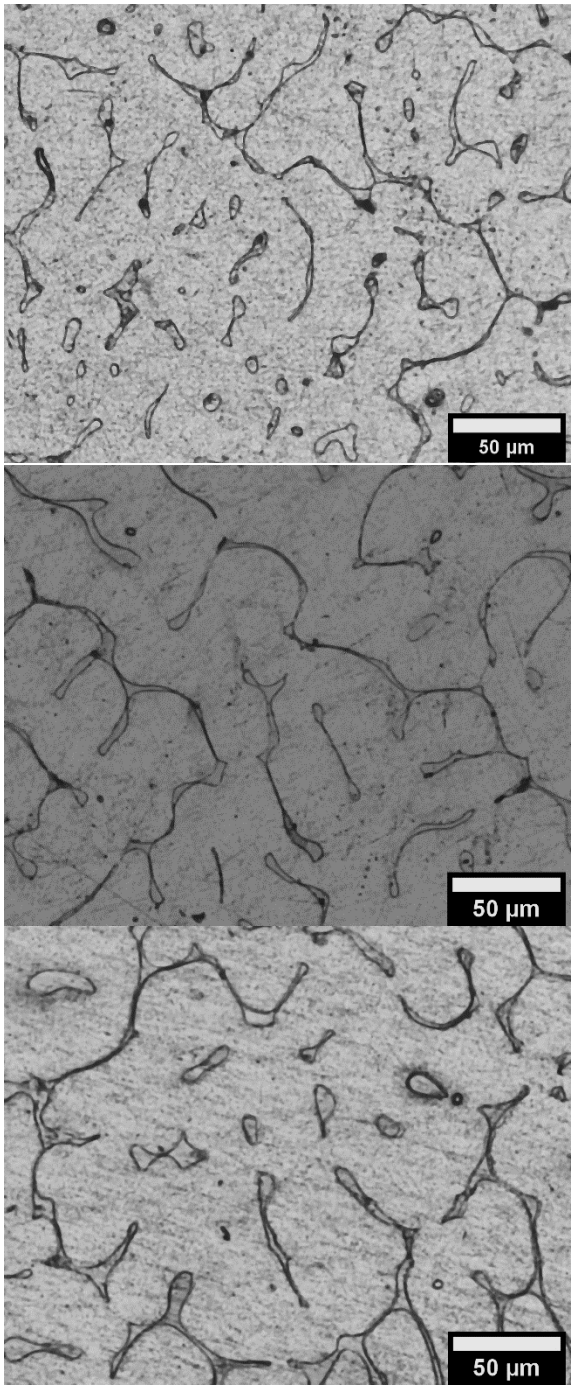

P = 44.4 mm
V = 0.7 mm/s
G = 4.8 °C/mm
R = 3.4 °C/s
λ_A = 34.7 ± 5.6 µm

P = 69.2 mm
V = 0.6 mm/s
G = 2.8 °C/mm
R = 1.7 °C/s
λ_A = 45.0 ± 8.7 µm

P = 89.3 mm
V = 0.5 mm/s
G = 1.9 °C/mm
R = 1.0 °C/s
λ_A = 49.8 ± 7.9 µm

Figure 3.36: Representative micrographs along the Al-20wt.%Sn-1wt.%Cu ingot, associated with the corresponding positions (P), counting from the cooled base, the velocity (V), the thermal gradient (G), the cooling rate (R), and the average dendritic spacing (λ_A).

Further image analyses were performed to assess the effect of cooling rate on β-Sn morphology. Three conditions were examined, corresponding to samples solidified

at 28.9, 5.5, and 1.0 °C/s, representing fast, intermediate, and slow solidification. Figure 3.37 presents BSE micrographs of these samples, where owing to the chemical contrast of this technique, the β-Sn morphology within the Al matrix is clearly highlighted. The β-Sn phase was quantified in terms of particle area and aspect ratio (AR), the latter defined as the ratio between the width and height of the best-fit ellipse for each particle [156]. An AR of 1 corresponds to an approximately circular shape, whereas higher values indicate increasing elongation. Between 700 and 1300 particles were analyzed for each condition. Figure 3.37(d) shows the distribution of particle areas in three categories: smaller than 50 μm², between 50 and 500 μm², and larger than 500 μm². Figure 3.37(e) depicts the distribution of aspect ratios, restricted to the representative range between 1 and 3.5.

Comparing the quantitative results from the graphs in Figure 3.37 reveals a clear trend: the average β-Sn particle size increases as the cooling rate decreases. Faster cooling (28.9 °C/s) produces a higher proportion of fine particles (<50 μm², red bars), whereas slower cooling (1.0 °C/s) leads to a greater fraction of coarse particles (>500 μm², blue bars). As expected, the intermediate condition (5.5 °C/s) shows values between these two extremes (Figure 3.37(d)). The aspect ratio further clarifies the morphological evolution. As shown in Figure 3.37(e), particles formed under slower cooling rates (blue and green bars) are predominantly circular or slightly elliptical (AR < 2), whereas the higher cooling rate condition (red bars) produces a greater fraction of elongated particles.

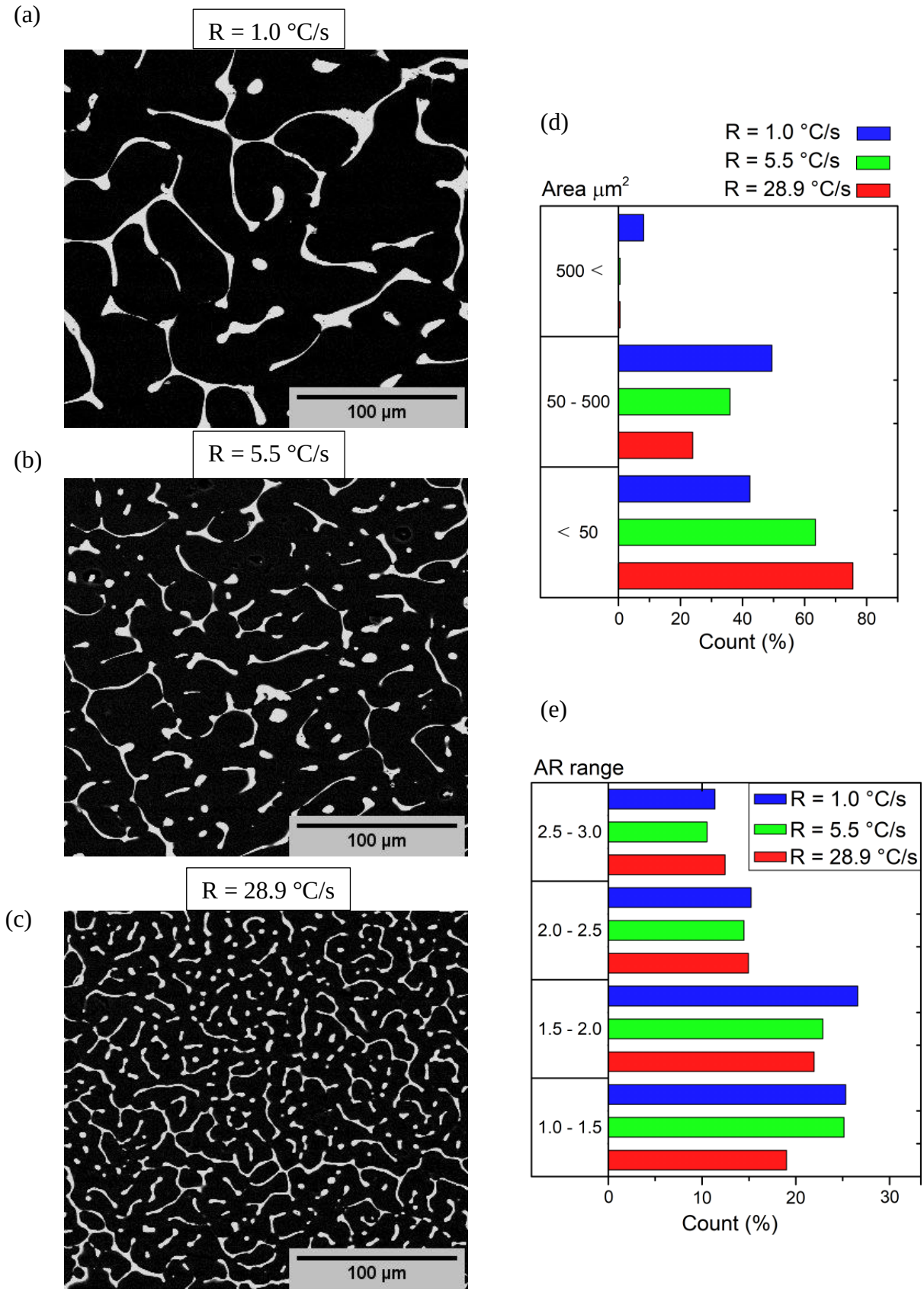

Figure 3.37: BSE micrographs of the Al-20wt.%Sn-1wt.%Cu alloy samples solidified at (a) 1.0°C/s, (b) 5.5 C/s and (c) 28.9°C/s, along with the distribution of the morphology of the β-Sn in terms of (d) area expressed in µm2, and (c) aspect ratio (AR).

3.3.2.3 Chemical analyses

To investigate macrosegregation along the length of the ingot, chemical analyses were carried out by Inductively Coupled Plasma Optical Emission Spectroscopy (ICP-OES) on two samples of approximately 10g each at the Chemical Characterization Laboratory of the University of Campinas. The samples were collected from the bottom and the top of the ingot, samples cooled at 28.9°C/s and 1.0°C/s, respective. The ICP-OES results revealed a Sn concentration of 25 wt.% at the bottom and 20 wt.% at the top. This distribution indicates the occurrence of inverse macrosegregation, i.e., Sn enrichment at the base of the ingot. Such behavior is consistent with previous reports [16] and is attributed to the large density difference between Al (2.7 g/cm³) and Sn (7.2 g/cm³). The Cu concentration, in contrast, remained essentially constant throughout the ingot at ~0.3 wt.%.

The solidification microstructure was further analyzed by Scanning Electron Microscopy (SEM) coupled with Energy Dispersive Spectroscopy (EDS). Figure 3.38 depicts a representative SEM micrograph and its respective chemical mapping. The elements subjected to analysis were Al, Cu, Sn and Fe. The latter was measured as impurity in the commercially pure Al used for the alloy production.

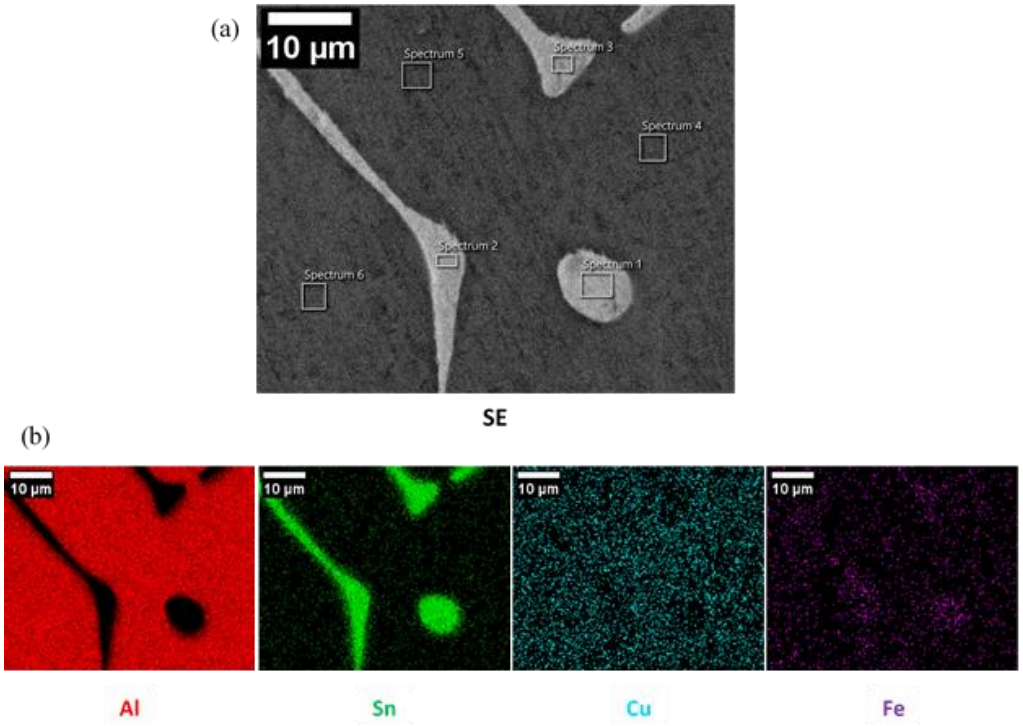

Figure 3.38: (a) SEM image and (b) EDS chemical mappings of a typical sample in the Al-20wt.%Sn-1wt.%Cu alloy – cooling rate 5.5 °C/s.

The chemical mapping in Figure 3.38(b) illustrates the low solubility of Sn in Al, showing an Al rich matrix and an interdendritic region composed of Sn. Meanwhile Cu is homogeneously distributed, especially throughout the α-Al matrix. The wt. % compositions of the phases were also determined. Table 3.2 presents the average results for Al, Sn, Cu and Fe from the selected EDS area analysis carried out on samples solidified at 28.9, 5.5, and 1 °C/s. Figure 3.38(a) shows typical regions analyzed, namely matrix (dark grey regions) and interdendritic region (light grey regions).

Table 3.2: Spot EDS chemical analyses in the interdendritic and α-Al matrix regions of the Al-20wt.%Sn-1wt.%Cu alloy (in wt.%).

Bottom of ingot – 28.9 °C/s		
Element	Matrix	Interdendritic region
Al	**99.2 ± 0.1**	4.1 ± 2.7
Fe	0.0 ± 0.0	0.1 ± 0.1
Cu	0.4 ± 0.1	0.4 ± 0.2
Sn	0.4 ± 0.2	**95.5 ± 2.7**
Middle of ingot – 5.5 °C/s		
Element	Matrix	Interdendritic region
Al	**99.5 ± 0.3**	2.5 ± 0.1
Fe	0.1 ± 0.1	0.1 ± 0.2
Cu	0.1 ± 0.1	0.7 ± 0.1
Sn	0.3 ± 0.2	**96.6 ± 0.2**
Top of ingot – 1.0 °C/s		
Element	Matrix	Interdendritic region
Al	**99.4 ± 0.1**	0.8 ± 0.1
Fe	0.0 ± 0.0	0.1 ± 0.0
Cu	0.4 ± 0.1	0.1 ± 0.2
Sn	0.1 ± 0.0	**99.0 ± 0.3**

Phase identification was complemented by X-ray diffraction (XRD) analyses of samples extracted from analogous positions along the ingot from the EDS analysis. The specimens were carefully ground and polished to ensure flat surfaces. The diffractograms were obtained using a Bruker D8 Advance diffractometer with Cu-Kα radiation (λ = 0.15406 nm), scanned in the 5-90° 2θ range with a step size of 0.02°. Phase identification was performed by comparing the observed diffraction peaks with those of known phases, according to the thermodynamical calculation (Figure 3.22), i.e α-Al [160], β-Sn [161], and θ-Al_2Cu [162].

Figure 3.39 shows the diffractograms for the specimens cooled at 28.9, 5.5 and 1.0 ◦C/s. The main crystalline constituents identified were the α-Al phase (red triangle

symbols) and the β-Sn (blue squares). The characterization of the θ-Al_2Cu phase was inconclusive, both by EDS and by XRD. This can likely be attributed to two reasons: (1) the small volume fraction of Al_2Cu that forms due to the limited Cu content, as identify by ICP and EDS, and (2) the possibility that the amount of this phase is below the XRD detection threshold, typically around 1–2 vol% [163].

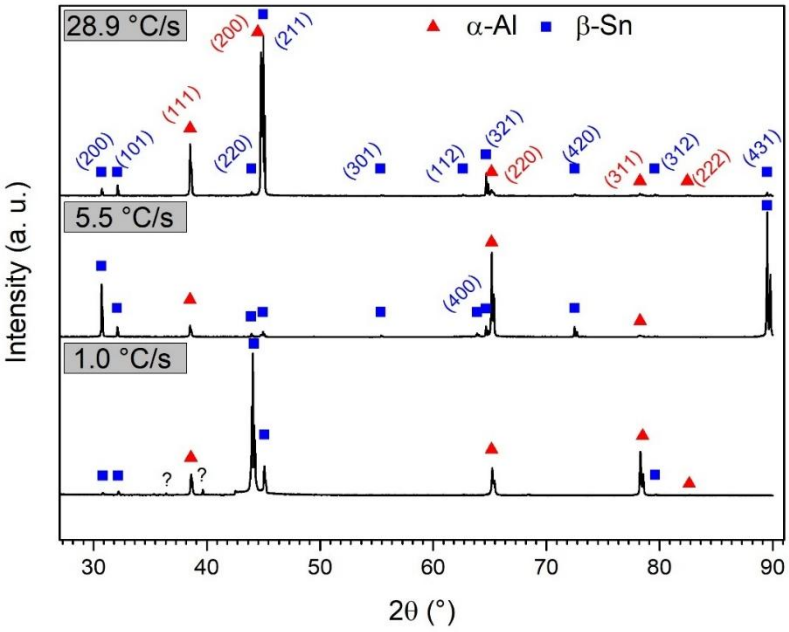

Figure 3.39: X-ray diffraction (XRD) spectra analysis of the samples cooled at 28.9, 5.5 and 1.0 °C/s in the Al-20wt.%Sn-1wt.%Cu alloy.

3.3.2.4 X-ray microtomography analysis

The X-ray computed tomography (XCT) technique was applied to study the morphology of the β-Sn phase, providing a 3D reconstruction of the samples and therefore more detail on the microstructure compared to a 2D micrograph (Figure 3.40(a1-c1)). These analyses were carried out on samples at three conditions, similar to the chemical and 2D morphological analysis: 28.9, 5.5, and 1.0 °C/s cooling rate, representing fast, intermediate, and slow solidification. The images were taken with a Synchrotron light source at a high-brightness of 22 keV (Mahogany line at SIRIUS-CNPEM, Campinas-Brazil). For each 3D image, the reconstruction was carried out using an algorithmic projection filter, processing 2048 projections. The voxel size was 546 nm. Considering 5 voxels are required to reliably define the morphology, therefore,

the resolution of the analysis was estimated to be 2.5 μm. The result was analyzed using the Avizo (2022.1) software (Thermo Fisher Scientific, Waltham-USA).

After obtaining the 3D tomography data, non-local means and unsharp masking filters were applied to reduce noise and enhance contrast. The variation in gray intensity caused by the difference in X-ray absorption of the Al and Sn was used to segment the interdendritic β-Sn phase using a grayscale threshold. The individually segmented β-Sn phase was filtered to sharp the boundaries between phases and exclude small spots of artifacts from the radiographs. Finally, the segmentation results allowed for measurements of volume fraction, surface area and average trunk radius of the interdendritic phase. The volumetric reconstructions of the Sn phase are shown in Figure 3.40(a2), Figure 3.40(b2), and Figure 3.40(c2), revealing a distinct network structure.

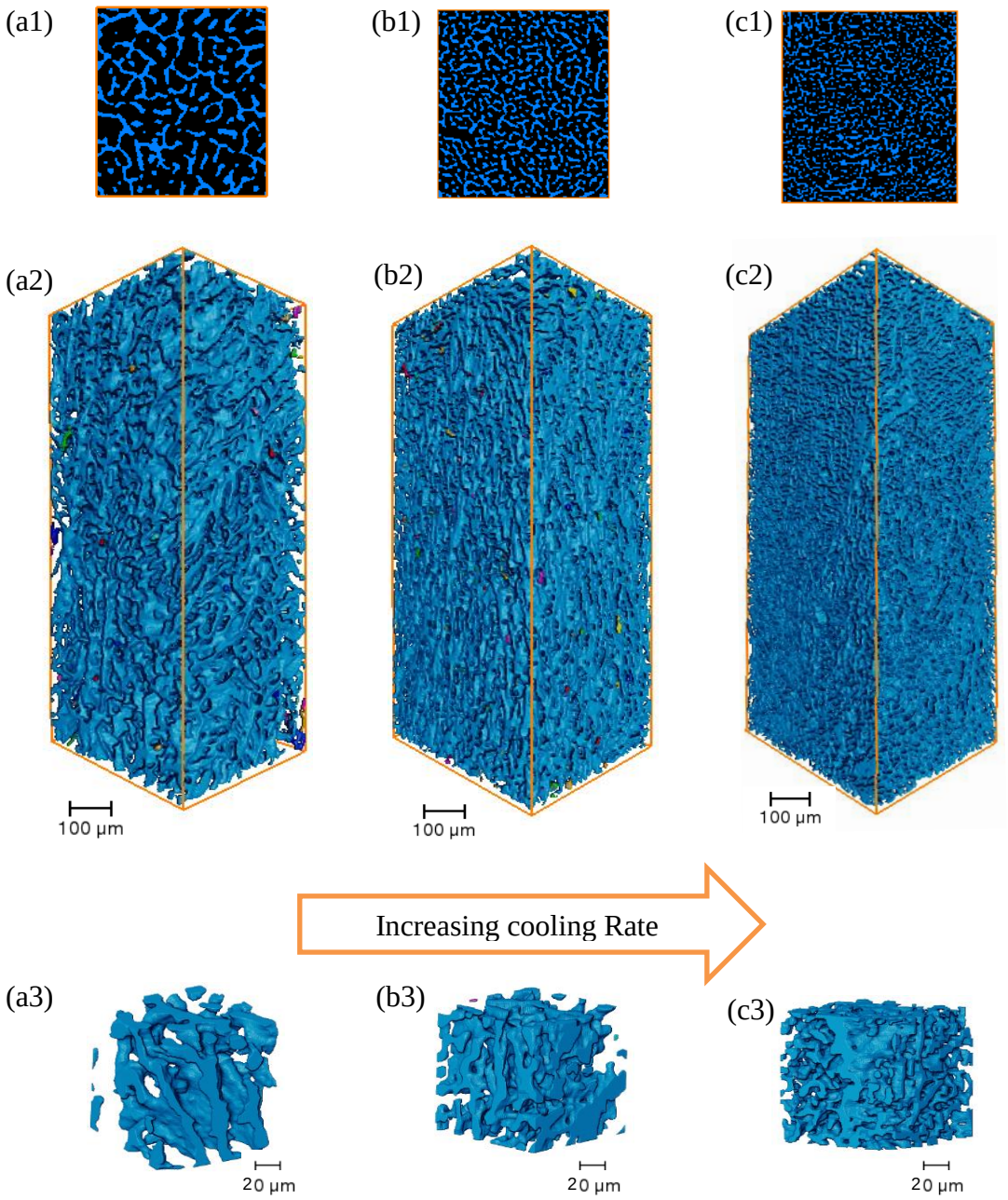

Figure 3.40: Cross-sectional views from above, XCT rendering of the β-Sn phase separated at the boundaries of the α-Al dendrites and details of the morphology in the Al-20wt.%Sn-1wt.%Cu alloy samples solidified at (a) 1.0°C/s, (b) 5.5°C/s and (c) 28.9 °C/s after exclusion of the Al-rich phase.

Because of the extremely low solubility of Sn in Al, β-Sn solidifies as the last, as predicted in Figure 3.21 and Figure 3.22, Consequently, it segregates to the interdendritic regions, where it forms a continuous β-Sn network, clearly visible in Figure 3.40, as the main blue network. During segmentation, this network was distinguished from smaller isolated particles, which were assigned distinct colors but excluded from the analysis to ensure consistency, since their size and volume were negligible in comparison with the blue network. The 3D segmentation and reconstruction further highlighted the foam-like, interconnected morphology of the β-Sn phase across the interdendritic regions, which was then quantified in terms of volumetric fraction, surface area, and average branch radius, as summarized in Table 3.3. The comparison of volumetric fraction indicates a slight enrichment of solute at the base of the ingot. Notably, the finer sample (base of the ingot) has the most complex and densely interconnected β-Sn phase network, since it has a surface area (3.9E+07 μm^2) more than twice that of the slowly cooled sample (1.6E+07 μm^2) for a similar volume fraction. As can be seen in Figure 3.40(a3-c3).

Table 3.3: Quantitative XCT results of volumetric fraction, surface area and average branch radius of the β Sn phase of the Al-20wt.%Sn-1wt.%Cu samples solidified at 1.0 °C/s, 5.5 °C/s and 28.9 °C/s.

Sample	**β-Sn Vol. fraction (%)**	**β-Sn Surface area (μm^2)**	**β-Sn Mean radius (μm)**
1.0 °C/s	24.8	1.6 E+07	3.9
5.5 °C/s	27.7	2.5 E+07	2.8
28.9° C/s	26.2	3.9E+07	1.6

3.3.3 Mechanical properties

3.3.3.1 Hardness

The microhardness profile along the solidification direction of each Al-20 wt.%Sn-1wt.%Cu ingot was determined as the average of 20 measurements per position, using a Shimadzu HMV-G20ST equipment. The tests were conducted under a load of 0.500 kgf for 10 s, employing a 40× magnification lens. Vickers microhardness

measurements were performed on transverse sections of the metallographic samples, ensuring consistent evaluation across the ingot. It is worth noting that, during the hardness analyses, the indentations had a diagonal of approximately 180 µm, which included both the dendrites and the interdendritic regions, thus reflecting a combined behavior of both phases.

Figure 3.41 shows the correlation of micro-hardness and average dendritic spacing, revealing that it remained almost constant at around 25 HV for all specimens, regardless of microstructural coarsening.

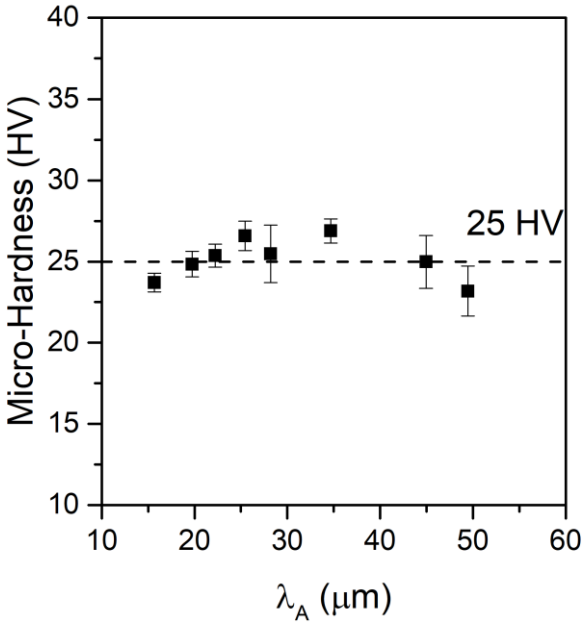

Figure 3.41: Vickers microhardness (HV) as a function of the average dendritic arm spacing in the Al-20wt.%Sn-1wt.%Cu alloy.

3.3.3.2 Tensile properties

The tensile test specimens were prepared from transverse sections of the directionally solidified ingots in order to ensure greater microstructural uniformity. This procedure enables consistent correlations between structural and thermal parameters and the resulting mechanical properties. The specimens were machined with their longitudinal axis oriented perpendicular to the ingot's solidification direction, while the transverse axis was kept parallel to it.

Figure 3.42 schematically illustrates the orientation and positions of the tensile specimens along the ingot. The ingots were sectioned in a way to allow the production of at least four specimens per position, centered at 6 mm, 20 mm, 34 mm, 48 mm, 62 mm, 76 mm, and 90 mm, respectively.

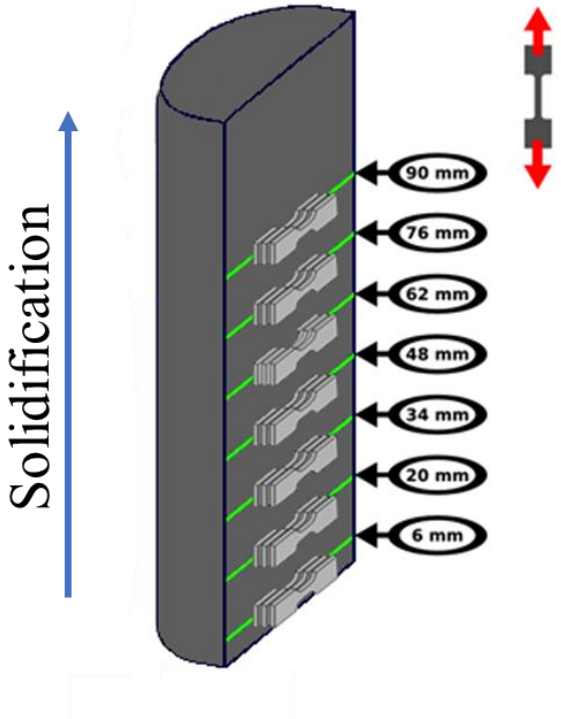

Figure 3.42: Schematic diagram of specimen extraction for tensile testing, highlighting the central position of the specimens.

Figure 3.43 presents the geometry of the tensile specimens used in the mechanical tests. Their dimensions were scaled proportionally to those standardized by ASTM E8/E8M-21 [164]. The tensile test results obtained under these conditions were therefore considered directly comparable to standardized data, as also reported in previous studies [19].

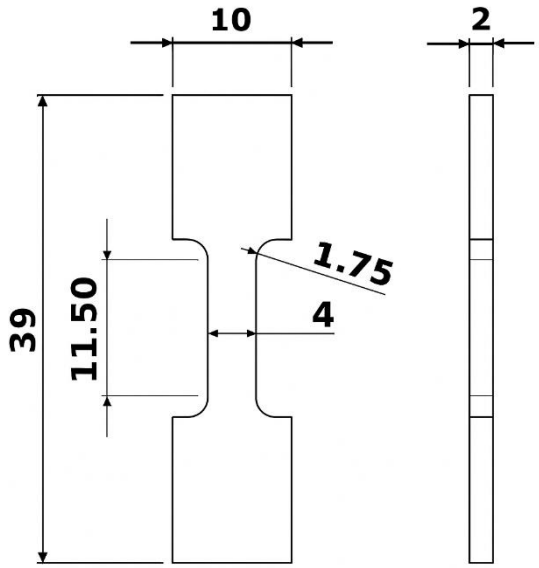

Figure 3.43: Dimensions of test specimens for tensile testing, in mm [108].

Tensile tests were performed at a strain rate of 3.0×10^{-3} s^{-1} using a Universal Instron 5500R machine (Instron, Massachusetts, USA) with a 250 KN load cell. An optical extensometer assisted in measuring the displacement of the samples during the tests.

All discussions of tensile properties are based on the true stress and strain values calculated from the strain and force values provided in the test. To convert engineering values, subscript "E", to true values, subscript "R", *Equation 3.1*9 and ***Equation 3.2***0 were used. The exception was toughness, that was calculated using the engineering stress-strain curve, based on an empirical approximation according *Equation 3.21* [165].

$$\varepsilon_R = \ln(\varepsilon_e + 1) \qquad \textbf{\textit{Equation 3.19}}$$

$$\sigma_R = \sigma_e(\varepsilon_e + 1) \qquad \textbf{\textit{Equation 3.20}}$$

$$\sigma_T = \frac{\sigma_Y + \sigma_{UTS}}{2} \times \varepsilon_U \qquad \textbf{\textit{Equation 3.21}}$$

Where σ_Y is the yield tensile strength, σ_{UTS} is the ultimate tensile strength, and ε_e uniform elongation at fracture experimentally measured.

Considering that strain localization is the critical event during the wear of ductile tribological alloys, Bravo *et al.* [30] suggested that the yield strength and the strain hardening exponent (*n*) are the main quantitative parameters for the evaluation of sliding bearing alloys. Thus, the strain hardening exponent (*n*) was calculated from the Hollomon equation [166] according to *Equation 3.*. Only plastic deformation was considered for the calculation of *n*.

$$\sigma_R = Q.\varepsilon_R^n \qquad \textbf{\textit{Equation 3.22}}$$

Where σ_R and ε_R are the true stress and strain, Q is the strength coefficient and n is the strain-hardening exponent.

The typical true stress-strain curves corresponding to each analyzed position are shown in Figure 3.44.

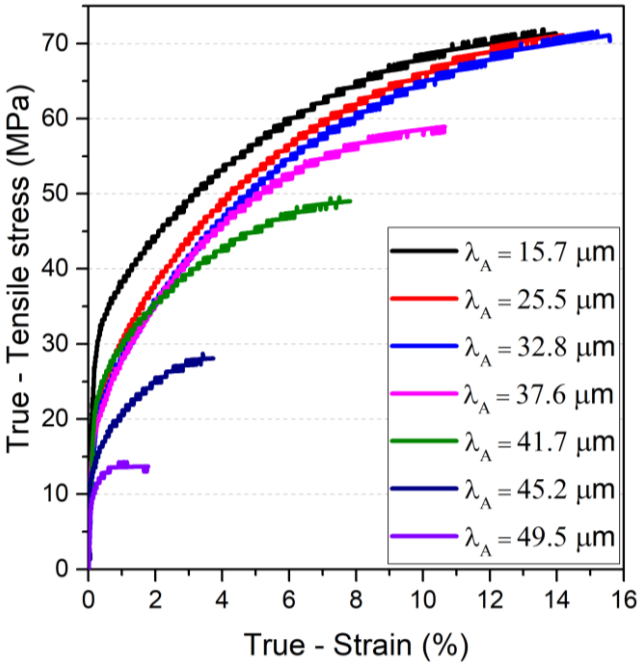

Figure 3.44: Typical true stress-strain curves representative of each of the ingot positions and their respective average dendritic arm spacing (λ_A) in the Al-20wt.%Sn-1wt.%Cu alloy.

The association of the λ_A with the mechanical properties is shown in Figure 3.45. Where yield strength, σ_Y -0.2% proof stress, and tensile strength σ_U values are

plotted on the left axis, while elongation-to-fracture ε_U is plotted on the right. The properties are plotted as a function of the λ_A, which reflects the cooling rate. The tensile properties, in addition to the strain hardening coefficient "*n*" from the Hollomon equation (***Equation 3.***), are summarized in Table 3.4.

Table 3.4: Experimental tensile properties of the Al-20wt.%Sn-1wt.%Cu alloy. λ_A Average dendritic spacing; σ_Y: Yield tensile strength; σ_U Ultimate tensile strength; ε_u: Elongation-to-fracture; σ_T: Toughness; n: Strain hardening exponent; Q: Strength coefficient.

λ_A (µm)	σ_Y (MPa)	σ_U (MPa)	ε_U (%)	σ_T (MPa)	n	Q (MPa)
15.7	32.8	72.4	14.1	7.2	0.28	129.8
26.5	27.4	67.4	13.3	6.8	0.31	133.3
32.8	25.2	68.1	13.5	7.9	0.28	127.4
37.6	24.1	58.6	10.1	4.2	0.33	133.5
41.7	22.8	42.5	5.7	3.2	0.28	97.8
45.2	19.0	26.4	2.9	0.8	0.19	54.6
49.5	13.9	15.4	2.1	0.2	0.10	23.2

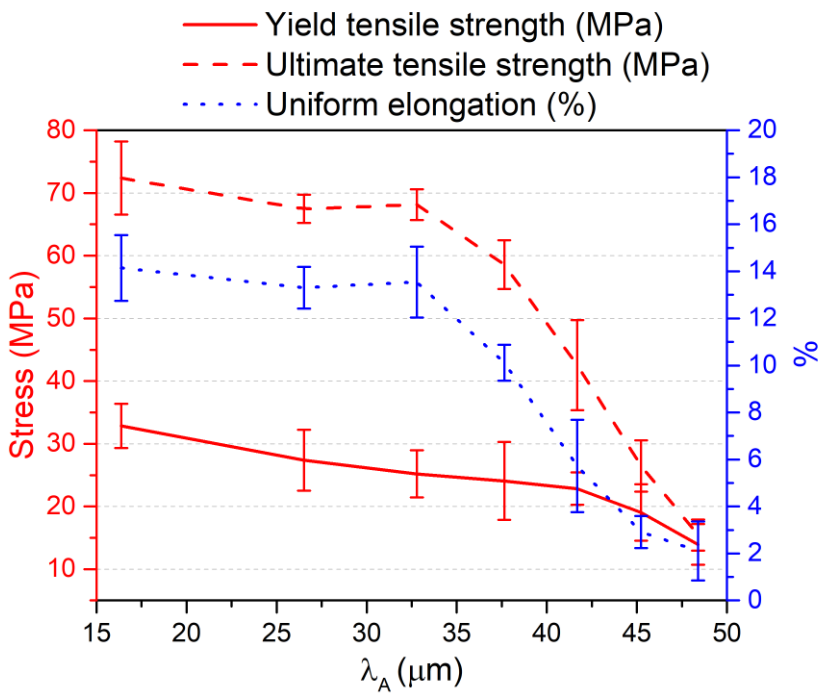

Figure 3.45: Experimental correlations of the true tensile properties and average dendritic arm spacing (λ_A) of the Al-20wt.%Sn-1wt.%Cu alloy: yield tensile strength, ultimate tensile strength and elongation-to-fracture.

According to Figure 3.44, as the λ_A decreases, the fracture is more ductile, while a brittle fracture occurs with very little deformation before rupture as the microstructure becomes coarser. This is in line with the n-exponents, which ranged from 0.28 to 0.10 and showed a marked decrease with coarser microstructures in Table 3.4.

As can be observed in Figure 3.45 and Table 3.4, there is a continuous increase in yield tensile strength as the microstructure becomes refined. For example, it can be noted that for λ_A = 15.7 μm, the average yield strength is 32.8 MPa. For coarser microstructures, such as λ_A = 49.5 μm, the yield strength is only 13.9 MPa. Additionally, when observing the data related to tensile strength and ductility an unexpected trend is noted, as there is a simultaneous increase in strength and ductility. It is noteworthy that a change in the behavior of tensile strength and elongation-to-fracture at λ_A = 32.8 μm is observed, with a sharper drop from that point onwards.

Generally, increasing the mechanical strength of an alloy is accompanied by a reduction in ductility and toughness [167,168]. However, for the Al-20wt.%Sn-

1wt.%Cu alloy, considering the solidification conditions adopted in this investigation, it is observed that microstructure refinement is beneficial for both strength and ductility. For instance, in the case of the microstructure with λ_A = 15.7 μm, the finest condition studied, an ultimate tensile strength of 72 MPa and a ductility of 14% were achieved. At the opposite, in the coarsest microstructural condition, a tensile strength of 16 MPa and a significantly reduced ductility of around 2% were obtained, highlighting the detrimental effects of inadequate cooling rates and dendritic coarsening.

Fractographies of the finer (λ_A = 15.7 μm) and coarser (λ_A = 49.5 μm) specimens, after tensile tests, are shown in Figure 3.46(a-b) and Figure 3.46(c-d), respectively, in order to illustrate the most extreme conditions of mechanical behavior and microstructure. There are significant differences between the two fracture surfaces that clarify the fracture mechanism. In the more refined microstructure, there is higher adhesion between the α-Al matrix and the β-Sn phase besides more homogenization of the β-Sn regions (black points). This phenomenon was observed over almost the entire fracture surface, and a representative image is shown in Figure 3.46(a). Details of this fractography show small dimples in the β-Sn phase on the contour between the dendrites, Figure 3.46(b) (indicated by black arrows).

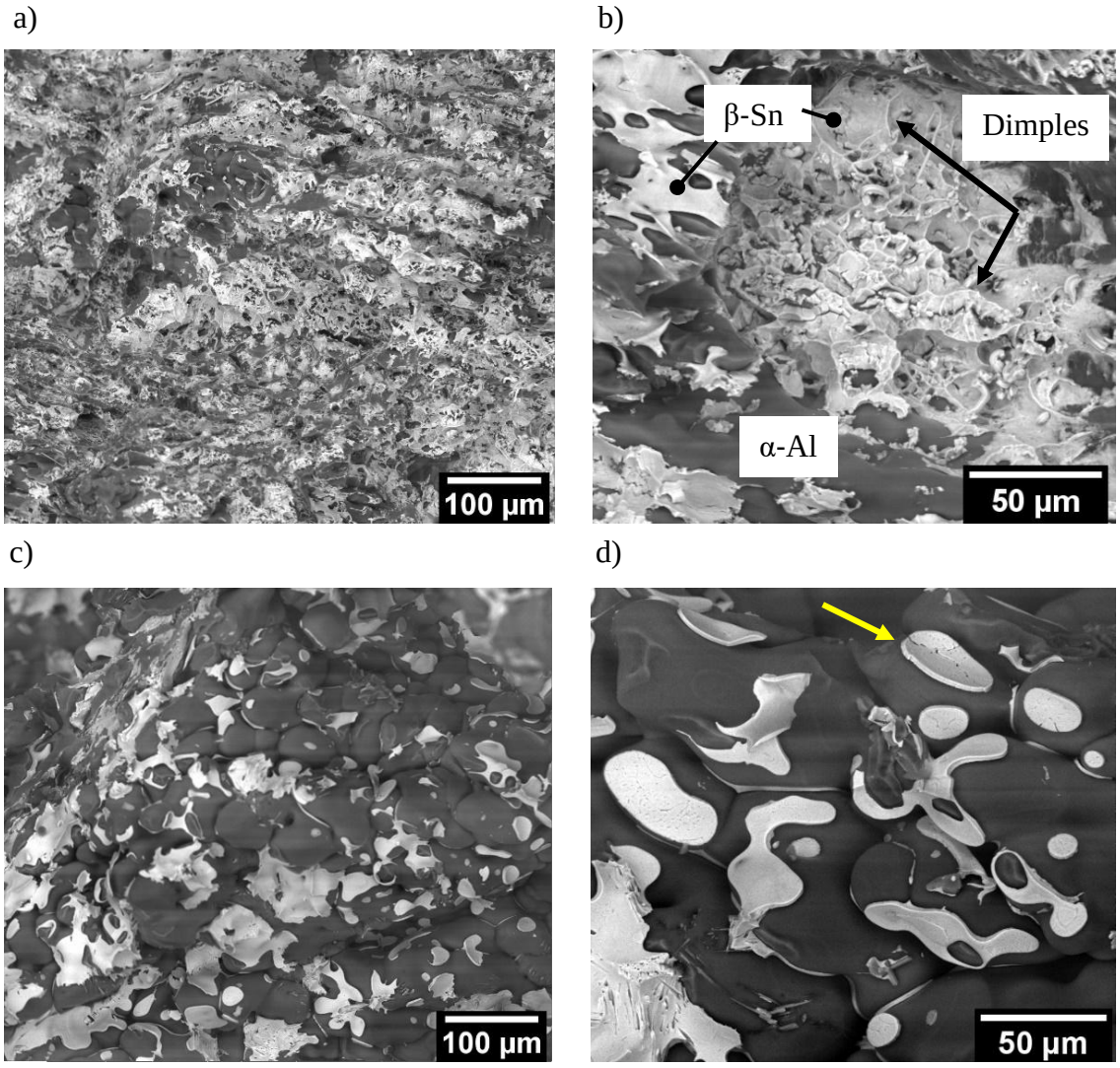

Figure 3.46: Fracture surfaces of the finer sample (a-b) and the coarser samples (c-d) of the Al-20wt.%Sn-1wt.%Cu alloy after the tensile tests. β Sn in white and α Al in dark gray.

On the other hand, Figure 3.46(c), referring to the coarser microstructure, shows less adhesion between α-Al matrix and β-Sn, a more dispersed distribution of the interdendritic phase and the preservation of the dendritic microstructure, characteristic of decohesive and, brittle rupture. In addition, there is embrittlement of the β-Sn phase, shown in detail in Figure 3.46(d) (yellow arrow).

3.3.4 Wear behavior

3.3.4.1 Dimensional wear coefficient

The wear test samples were extracted perpendicularly along the length of the ingot. The tests were carried out using a ball-cratering device shown in Figure 3.16 Spheres of AISI 52100,with hardness of 818 HV, and 25.4 mm diameter were rolled against the samples, forming a wear crater [22,144]. The ball sliding speed was 260 rpm, and a normal contact load of 0.6 N was applied, following [34]. These tests were performed on samples taken from the positions of the bottom and the top of the ingot to encompass a wider range of solidification conditions, solidified at 28.9 and 1.0°C/s, respectively.

The tests lasted between 20 and 200 minutes, with measurements taken at 20-minute intervals. Table 3.5 shows the time intervals and the corresponding sliding distances. To ensure that only the microstructure influenced the results, the tests were performed without the use of any lubricants or abrasive particles. Environmental conditions remained on average at 22°C and 46% humidity. Figure 3.47 shows the boundary of a worn crater, showing the spreading of the β-Sn phase to form the lubricating film.

Table 3.5: The time intervals and the corresponding sliding distances of wear test.

Time (min)	20	40	60	80	100	120	140	160	180	200
Sliding distance (m)	417	835	1252	1669	2087	2504	2922	3339	3756	4174

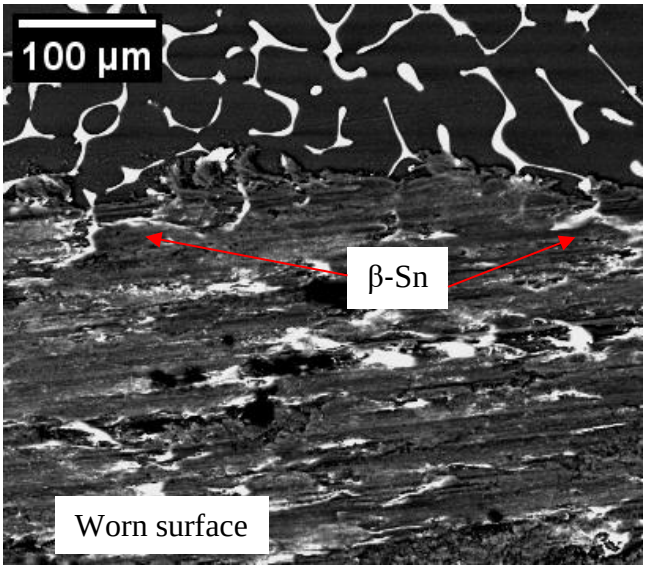

Figure 3.47: Edge of the worn cap. Al-20wt.%Sn-1wt.%Cu sample cooled at 1°C/s. Details showing the spreading of the β Sn phase to form the lubricating film.

Quantitatively, the wear behavior was analyzed using the dimensional wear coefficient *k*, in units of mm^3/N.m, which represents the volume of material removed by wear per unit of sliding distance per unit of normal load on the contact. *k* was calculated in this work using *Equation 3.23* [125]:

$$k = \frac{V_W}{m.N} \qquad \textbf{\textit{Equation 3.23}}$$

Where V_W is the worn volume, obtained by *Equation 3.*, *m* is the sliding distance, and *N* is the test load.

Figure 3.48 presents the dimensional wear coefficient as a function of sliding distance for the two samples analyzed, corresponding to the extreme conditions of cooling rate and dendritic spacing, i.e., solidification at 1.0 °C/s and 28.9 °C/s, which correspond to λ_A = 49.5µm and λ_A = 15.7 µm, respectively.

Although performed with the addition of a micro abrasive, Silva *et al.*[139] , using equipment similar to the ball-cratering apparatus employed in the present study, reported that a Steady-State Wear Regime (SSWR) is established when the wear volume exhibits a linear increase with sliding distance. This condition is important

because it improves the statistical reliability of tribological measurements. In the work by Silva *et al.*[139], the steady-state regime was reached after only 100 m of sliding distance, a value much shorter than that demonstrade in this present work (Table 3.5).

Indeed, as shown in Figure 3.48, a linear increase is observed between the wear coefficient, k, and the sliding distance, until approximately 2000 m, when the dimensional wear coefficient reaches a plateau, indicating stability in the material removal rate at 5.3×10^{-4} $mm^3/N.m$ for the most refined sample (λ_A = 15.7 μm) and at 4.5×10^{-4} $mm^3/N.m$ for the coarsest sample (λ_A = 49.5 μm).

Although the experimental points are relatively close to each other, those corresponding to finer microstructures tend to have higher k values. The observation that the volume loss of the materials increases continuously with increasing sliding distance is consistent with Archard's Law and is corroborated by other studies on wear in Al alloys [100,147,169]. However, the indication of a stabilization of volume loss over prolonged testing periods is of particular interest.

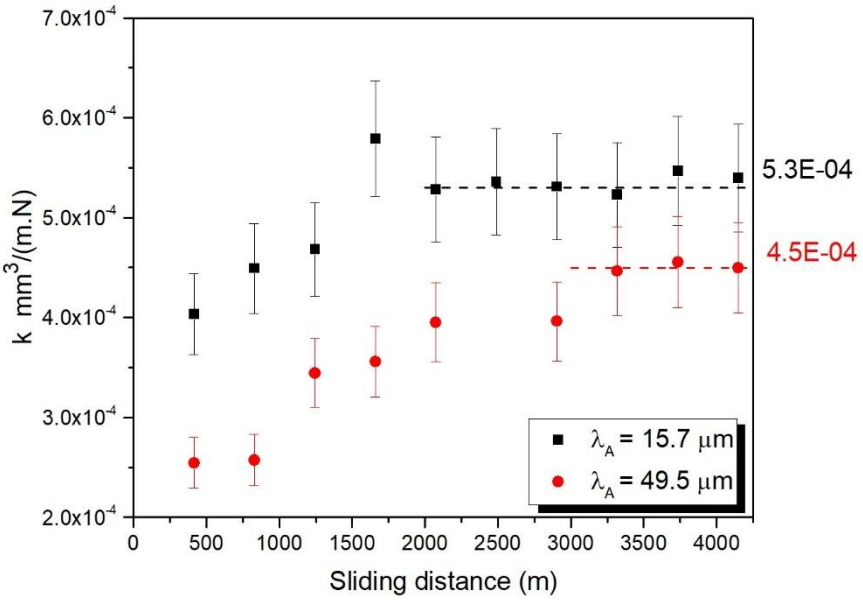

Figure 3.48: Dimensional wear coefficient as a function of sliding distance evaluated on the finest (λ_A=15.7 μm) and coarsest (λ_A=49.5 μm) samples of the Al-20wt.%Sn-1wt.%Cu alloy. 10% error considered based on [138].

3.3.4.2 Worn surface

Complementing the quantitative analysis of wear behavior, Figure 3.49 shows the worn surfaces of the two wear-tested samples. The deformed white areas, which correspond to the β-Sn phase and are indicated as the lubricating film in Figure 3.49, illustrate the self-lubricating mechanism, whose anti-friction effect arises from the extrusion of the soft phase, to form a protective film that shields the friction surfaces from seizure and scoring [30,31,45]. However, the effectiveness of this film is influenced by the microstructure, as demonstrated by comparing the two samples in Figure 3.48 and Figure 3.49.

It is noticeable that the lubricating film regions are smaller and more widely spaced in the more refined sample, Figure 3.49(a), as well as the presence of rough surface regions, resulting from a higher proportion of material detachment (delamination). In contrast, the coarser microstructure sample exhibits larger pockets of lubricating film, more widely spaced, along with fine, shallow grooves aligned with the sliding direction, as illustrated in Figure 3.49(b).

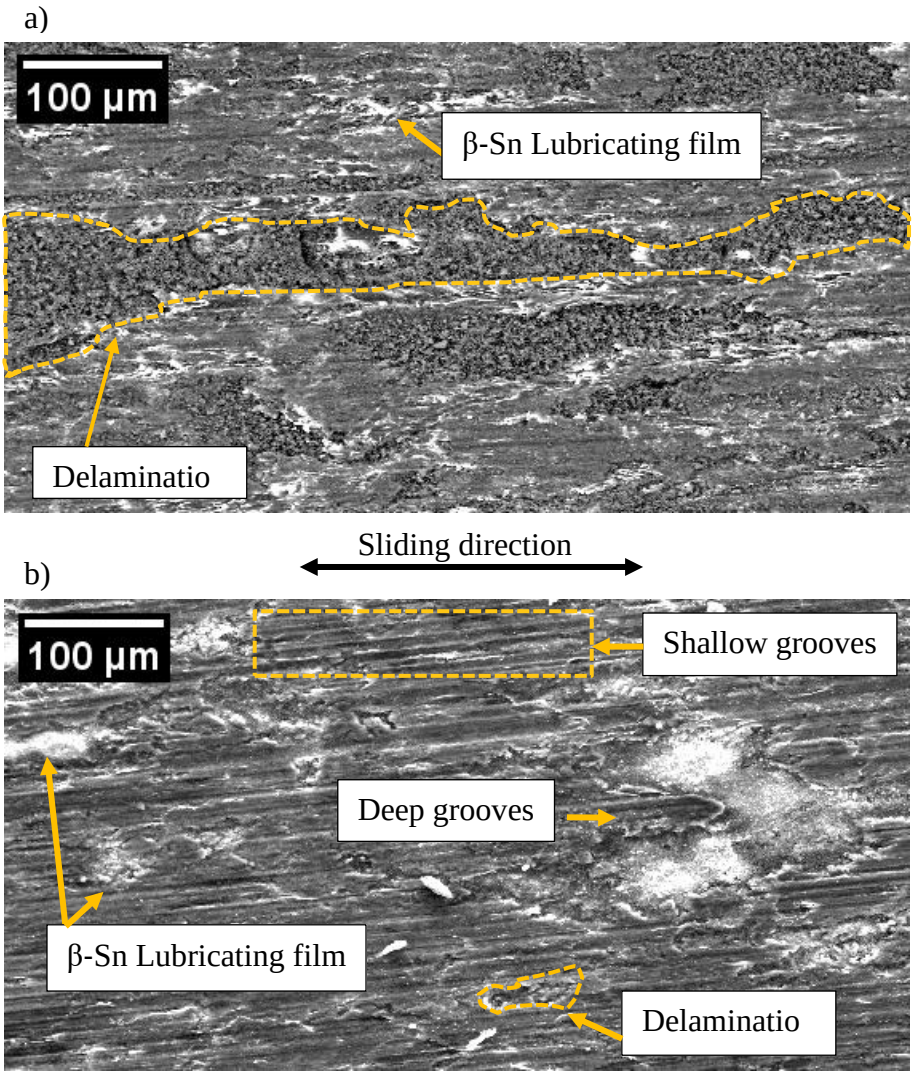

Figure 3.49: SEM micrographs of the worn surfaces showing the different surface morphologies after 4,000 m of sliding distance and distinct microstructures: (a) λ_A = 15.7 µm and (b, d) λ_A = 49.5 µm.

The results of the energy-dispersive spectroscopy (EDS) analysis of the worn surfaces of both samples are presented in Figure 3.50. Al, O, Sn, Fe and Cu were the elements analyzed. A significant amount of oxygen (O) can be seen in both samples, as well as a higher amount of iron (Fe). The quantity of Sn was also calculated, yielding slightly higher values in the refined sample (Figure 3.50), which is consistent with the other results presented thus far, though each sample exhibited distinct morphologies. In the refined sample, Sn appears to be more rigid with well-defined particles, while in the coarse sample, Sn appears crumpled. The SE figure of the chemical mapping demonstrates delamination in association with the O presence, for both samples.

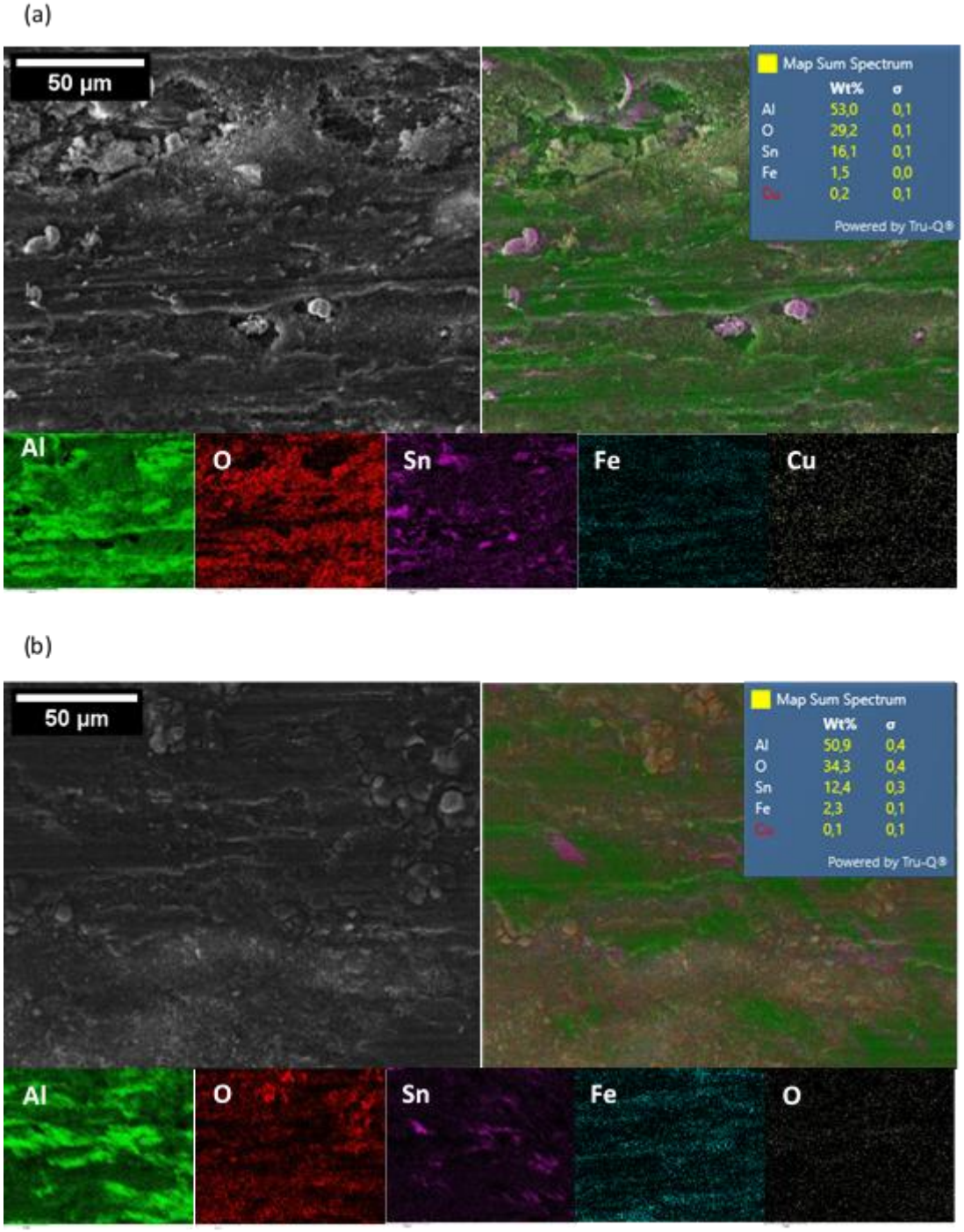

Figure 3.50: SEM micrographs and EDS elemental maps of worn surfaces. The left panels show the secondary electron images; the right panels display the superimposed elemental distribution maps of Al, O, Sn, Fe, and Cu. Individual elemental maps are shown below each corresponding image. (a) λ_A = 15.7 µm and (b) λ_A = 49.5 µm.

3.4 Discussions

3.4.1 Correlation of thermal variables with coarsening and phase distribution

The relationship between the average dendritic arm spacing (λ_A) and the cooling rate (R) was experimentally established and fitted by the power-law equation: $\lambda_A = 47.70 \times R^{-0.33}$, as can be seen in Figure 3.51. This correlation confirms that higher cooling rates promote the formation of finer dendritic structures, highlighting the critical role of this parameter in controlling the as-cast microstructure and, consequently, the final properties of the alloy.

Interestingly, the obtained power-law exponent (-0.33) does not follow the model proposed by Bouchard and Kirkaldy [113], which predicts an exponent close to -1/2. Instead, a more moderate exponent of -0.33 was observed. Similar values have been reported for multicomponent Al-based alloys solidified under unsteady-state conditions [93,147,170], although those studies focused on secondary dendritic spacings, which are also determined using the intercept method, comparable to the approach adopted in this work. This observation suggests that the methodology employed to measure the average dendritic spacing may capture contributions not only from primary but also from secondary and even tertiary spacings, thus explaining the deviation of the exponent toward values typically associated with secondary dendritic spacing behavior.

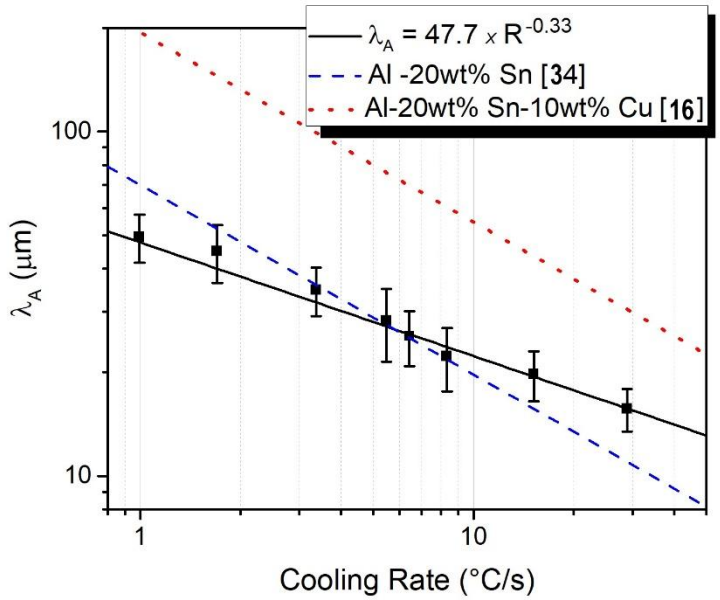

Figure 3.51: Average dendritic spacing as a function of cooling rate for Al-20wt.%Sn-1wt.%Cu alloys. R^2 is a statistical measure that indicates the proximity of the experimental data to the adjusted regression line.

The average dendritic spacing relationship obtained in this work was compared with the power-law correlations experimentally established for the binary Al-20 wt.% Sn [34] alloy and for the ternary alloy with high Cu content, Al-20 wt.% Sn-10 wt.% Cu [16], both determined for primary dendritic spacing, identified as dashed lines in Figure 3.51. The comparison confirms, as discussed in topic 3.2.2.1 that the addition of alloying elements to the binary system promotes coarsening of the dendritic structure. Furthermore, it shows that the effect of cooling rate on the average dendritic spacing is less pronounced than on the primary dendritic spacing, since a smaller exponent characterizes the average growth.

Figure 3.52 presents the average dendritic spacings as a function of the solidification front velocity, where a power-law correlation of type $\lambda_A = 21.5 \times V^{-1.5}$ was obtained. In comparison with the alloys summarized in Table 3.1, the relationship found here does not follow the commonly reported exponent of -1.1 for self-lubricating Al-based alloys. This deviation is likely due to the fact that the spacing measured in this study corresponds to the average dendritic spacing, which inherently encompasses not

only the primary spacing but also contributions from secondary and possibly tertiary dendritic arms.

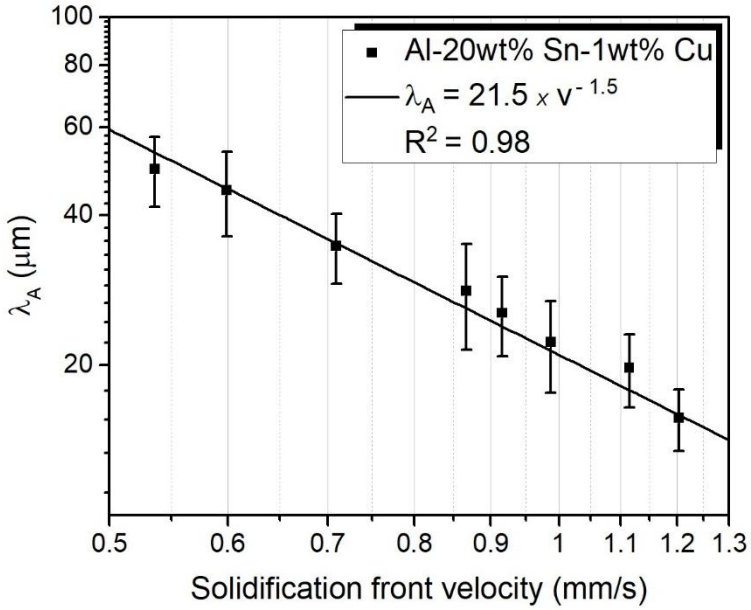

Figure 3.52: Average dendritic spacing as function of the solidification front velocity for Al-20wt.%Sn-1wt.%Cu alloys. R^2 is a statistical measure that indicates the proximity of the experimental data to the adjusted regression line.

This complexity in the dendritic arms feature is most likely associated with deviations in arm orientation. In a dendritic structure, the crystallographic direction plays a key role in determining the growth directions of the arms. In Al alloys, the preferred growth direction typically belongs to the <100> family [4], which forms six perpendicular branches [119]. However, as shown in previous studies with Al-Ge [87] and Al-Zn [171] alloys, dendrites oriented along the <110> direction can also grow in solute-rich Al-Sn alloys [85,90]. Consequently, those dendrites have a greater number of branches and angles other than 90° between them, resulting in a more complex geometry, as similarly observed in studies dealing with the Al-20 wt% Sn alloy [52,147].

It is worth noting that, given the long solidification intervals characterizing Al-Sn alloys, cooling rates have a huge influence on the microstructure, not only on the

microstructural coarsening as shown in Figure 3.51, but also on the morphology of the β-Sn phase as shown in XCT microtomography analysis Figure 3.40.

As the α-Al phase grows in isolation over a temperature range of approximately 250 °C, the Sn-rich liquid tends to sediment within the melt, under the influence of gravity. This motion is smoothed out and the coalescence of this liquid is reduced thanks to the α-Al dendritic arms. However, the more refined the microstructure, the more branched the dendritic arms become, increasing the complexity of the β-Sn phase network.

As observed in the microtomography results, although the variation in volume fraction between the most distinct samples is relatively small (<5%), the difference in surface area is significantly more pronounced. At faster cooling, the surface area of the β-Sn phase more than doubles when compared to the slower cooled sample. This represents a substantially greater packing of the secondary phase associated with high cooling rates. Complementing the 2D morphological analysis of the β-phase (Figure 3.37), which associated higher cooling rates with elongated β-Sn shapes, while lower cooling rates were associated with thicker dendrites and larger particles with more circular shapes.

3.4.2 Effect of microstructure morphology on the mechanical properties

In as-cast alloys strength improvement is achieved by the refinement of the dendritic microstructure, which ensures a weak microsegregation and a uniform distribution of second phases and other barriers to dislocation movement during slip [172]. However, in terms of microhardness, the Al-20wt.%Sn-1wt.%Cu alloy investigated in this study exhibited nearly constant values of about 25 HV, regardless of the microstructural scale (Figure 3.41). Although the dendritic spacing almost tripled, the microhardness varied by only ~4 HV between the maximum and minimum values. This behavior indicates that both microstructural refinement and Sn macrosegregation contribute to the overall hardness response. On one hand, finer microstructures tend to increase hardness; on the other hand, regions enriched in Sn, a soft metal with a very low hardness of ~7 HV, as measured here, counteract this effect. As a result, the

opposing influences of microstructural scale and Sn segregation balance each other, leading to the nearly invariant microhardness observed.

Similar to the present work, Bertelli *et al.* [16] observed macro-segregation in Al-20wt.%Sn-10wt.%Cu ingot solidified upward and noted an anomalous hardness behavior, as described here. This confirms that Sn content above 20% by weight affects hardness as much as the dendritic microstructural scale due to intense macro-segregation.

In a study of directionally solidified Al-20wt.%Sn alloy [34], macro-segregation levels comparable to those reported by Bertelli *et al.* [16] were also observed, but the authors did not verify the influence of macro-segregation on tensile strength as they did on microhardness, which was also noted in the present work. Figure 3.45 and Table 3.4 show that there was an increase in strength as the dendritic spacing decreased, culminating in higher strengths at the smaller average spacings, despite the accumulation of Sn in these samples. As noted by Campbell [103], finer dendritic arm spacing results in reducing microsegregation and enhancing stress and pore distribution, leading to better properties.

Surprisingly, both yield strength and elongation increased together. Thus, in addition to the dendritic spacing, another fundamental aspect to tensile properties understanding are the interfaces, even more between dendrite and phases. This issue was demonstrated by Ghassemali *et al.* [106] on as-cast Al-Si alloys, where most cracks were initiated at the dendrite/eutectic boundary, regardless of the grain boundary location. The authors found out the higher elemental segregation at the dendrite/eutectic boundaries compared to grain boundaries in cast alloys can introduce stress concentration at the dendritic boundaries interfering in the strain hardening and fracture mechanism.

There is a strengthening mechanism known as hetero-deformation-induced hardening (HDI), which occurs in heterostructured (HS) materials, characterized by having zones with distinct mechanical properties. These heterogeneous zones can be created through processing, such as lamination or gradient deformation, or they can exist due to the alloy phases. The critical requirement is the coexistence of a soft and hard region, since the different flow stresses between these two regions during straining creates strain gradients at the interface [173].

To preserve the integrity of the boundaries between regions during strain, many geometrically necessary dislocations (GNDs) accumulate near the interfaces of the soft zone. This generates high back stress, which, in turn induces forward stress in the adjacent hard zone. As a result, internal stresses are formed at the interface, referred to as HDI stress. Importantly, as the deformation strain increases, so does the HDI stress. Thus, during plastic deformation, the interfaces between the hard and soft phases act as barriers against dislocation movement and therefore a dislocation transformation (e.g. slip) must take place at these boundaries to continue strain [173].

This mechanism has been successfully verified in laminated CuCrZr alloys, with alternating hard CuCrZr layers and soft Cu layers [174]; bi-phase medium-entropy alloy consisting of a hard Cu-rich phase and a soft Fe-rich phase [175], and in a gradient-structured Cu-Al alloys, in which the surface region with ultrafine grains exhibited much higher hardness compared to the coarse-grained interior [176]. Across these studies, a general consensus is that it is necessary to have a significant strength disparity between zones and a well-bonded interfaces to anchor the dislocations and sustain HDI hardening [173].

Based on this, the increase in strength in parallel with the increase in ductility in the Al-20wt.%Sn-1wt.%Cu alloy analyzed in this PhD Thesis can be attributed to HDI hardening. Chemical analyses by EDS (Figure 3.38 and Table 3.2) revealed that the dendritic matrix and the interdendritic region consist of almost pure materials, Al and Sn, respectively. Due to the significant differences in their mechanical behavior, the alloy can be classified as a heterostructured material. In addition, microtomography analysis mapped the α-Al matrix/β-Sn particle interface and its variation as a function of cooling rate, as seen in Figure 3.40 and Table 3.3. It was observed that a larger interface area between the Al matrix and Sn particles occurs in samples with a more refined structure, as they have a larger surface area of the β-Sn phase and, therefore, greater adhesion, which would contribute to HDI hardening and justify the finer samples being more resistant and more ductile.

This explanation can be confirmed by analyzing the fractographs shown in Figure 3.46. When comparing the more refined sample and the coarser sample, it appears that there is a higher adhesion between the β-Sn particles and the α-Al dendritic matrix in the more refined sample (Figure 3.46(a)), as there is no clear separation

between the phases and there are signs of deformation throughout the fractography, including the presence of dimples (Figure 3.46(b)).

Under these conditions occurred a ductile fracture, which culminates in an improved strength and greater ductility (Figure 3.44, Figure 3.45, and Table 3.4). Strain hardening exponent values also reinforces the argument of strain hardening by HDI, where higher values were estimated in the more refined microstructures. There is a sharp decrease in the *n* value as the average dendritic spacing increases, concomitantly with the reduction in the surface area of β-Sn and, therefore, in the adhesion of the α-Al and β-Sn phases. The fractography in Figure 3.46(c) and (d)), as well as the typical stress-strain curves shown in Figure 3.44 and the tensile properties shown in Figure 3.45 suggest that a decohesive brittle fracture in the interdendritic region is associated with the coarser microstructures (Figure 3.46(c) and (d)).

When the volumetric fraction of the β-Sn soft phase is too high to be fully constrained by the hard phase, it will undergo plastic deformation under lower applied stress, resulting in reduced yield strength and rupture at the interface as seen in Figure 3.46c). As a variation occurs in the morphology and, consequently, in the adhesion of β-Sn to the α-Al matrix, the variation in the tensile strength and ductility curves observed in Figure 3.44 can be seen.

3.4.3 Influence of microstructure morphological on the wear behavior

Considering the microhardness data shown in Figure 3.41, it can be observed that the two samples associated with the microstructural conditions subjected to wear test (that is, finer sample λ_A= 15.7 μm and coarser sample λ_A= 49.5 μm) exhibit very similar hardness values, i.e., ~25 HV, which explains the difference in the wear results solely by the β-Sn phase morphology and distribution. Thus, the Archard equation, which implies volume loss decreases as hardness and strength increase [124], does not fully capture the wear behavior of the Al-20wt.%Sn-1wt.%Cu alloy analyzed, which makes the dimensional wear coefficient a more suitable parameter for understanding the wear alloy behavior. This conclusion is supported by the dimensional wear coefficient as a function of sliding distance graph, as shown in Figure 3.48, with clearly different

trend lines for each sample, within the same order of magnitude, with the coarser sample having the best wear resistance.

The volume of material worn from both samples initially increased sharply until reaching a state of relative equilibrium (Figure 3.48). This phenomenon can be attributed to the tribological behavior of aluminium-based alloys under dry sliding contact, as observed in literature [100,147,169]. This phenomenon can be justified by the fact that during the initial contact between the rolling ball and the flat sample, adhesive wear occurs, characterized by a high wear rate and intense surface damage. As the experiment progresses, the interaction between the removed material and the existing phases prompts a transition in the wear mechanism, potentially resulting in a reduction in the rate of volume removed, eventually stabilizing at a lower and more consistent value.

Indeed, the topography of the worn surface and the EDS chemical map (Figure 3.49 and Figure 3.50) indicate the presence of multiple wear mechanisms in both alloys. As indicated by [22,100,121,147], the progression of wear mechanisms in the context of soft alloys unfolds as depicted below: At the initial point of contact, the soft phase is pulled towards the surface. These particles then cover the worn surface, forming a solid lubricant film. However, failure or inefficiency of this film may lead to direct contact between the worn surface and the rotating element, causing adhesive wear, and removing a large volume of material. As sliding continues, material removed during the adhesive wear stage adheres to the ball, creating abrasive particles that contribute to abrasive wear, other wear mechanisms are also possible as sliding progress.

In self-lubricating alloys, the wear behavior is largely attributed to the soft phase, its quantity and distribution. By comparing the chemical map and SE images of the worn surfaces of the two samples tested (Figure 3.50), it was identified that only in the coarser sample the β-Sn phase have a ground appearance, consistent with what is expected to form a protective film. In the more refined sample, β-Sn was present in greater quantities, but with a rigid and preserved morphology. According to the microtomography results (Figure 3.40 and Table 3.3), the refined sample presents a higher Sn surface area, which should favor the formation of the lubricating layer, however the wear results suggest the opposite. Perhaps the complexity of the refined network, where the β-Sn phase is well adhered to the α-Al matrix, makes it difficult to

knead it towards the worn surface. Considering adhesive wear as the initial stage and the one responsible for removing large volumes of material, the low efficiency in the formation of the protective film of the more refined sample reflects its higher dimensional wear coefficient, corroborated by the intense delamination marks shown in the SEM images (Figure 3.49 and Figure 3.50).

Fragments from the steel ball, identified by the presence of Fe on Figure 3.50 suggest wear by adhesion through material transfer or abrasion when the detachment of harder particles begins to act as a third-body abrasive. Additionally, EDS dot mapping revealed a high presence of oxygen in both worn surfaces (~ 30% in wt.%). The heat generated by friction combined with the reaction between atmospheric oxygen and the contact region, led to the formation of an oxide layer [147], most likely aluminum oxide (Al_2O_3). The oxide formation was mainly concentrated in the delaminated regions, which were torn off due to the inefficiency of the β-Sn solid lubricant layer coverage, as seen in the SE image (Figure 3.50). The existence of an oxide layer on the worn surface can have detrimental or beneficial effects on wear, depending on the alloy system and the wear conditions. The oxide layer formed on the worn surface can compete with the solid lubricant layers, potentially reducing the effectiveness of the lubrication. In addition, the oxide layer can become brittle and promote the detachment of hard particles that can act as third wear bodies [22,100,146,147,177]. However, in certain cases, a stable oxide layer can have positive effects, as observed in the studies by [133] and [178] with Al2024 alloys reinforced with B4C composites and Al-Si reinforced with Si/Cp, respectively.

In this present Thesis, it was not possible to determine whether oxidation is affected by microstructure, since the O values of both surfaces were similar. However, it was possible to conclude that the samples exhibited multiple wear mechanisms: adhesive, abrasive and oxidation.

Although the finer dendritic microstructure is not as effective in wear as it is in properties like ductility and tensile strength, this behavior has been observed in other self-lubricating Al alloys with soft second phases such as Sn [16,34,147], In [121], and Pb [44], since these elements have extremely low hardness and similar wear mechanisms.

The measure of wear provided by *k* is particularly useful for comparing wear rates in different materials, allowing comparisons with the literature. To compare the wear behavior of the alloy studied in this work with that of other alloys reported in the literature, the dimensional wear coefficient was calculated using previously published data. For consistency, only studies employing ball-cratering devices under dry wear conditions were considered. Based on experimental relationships between worn volume, time, and microstructural spacing, the corresponding worn volumes were determined. From these, dimensional wear coefficients were calculated under equivalent load conditions and comparable microstructural spacings, and subsequently compared [22,34,44,121]. Figure 3.53 presents this comparison for an average soft-phase spacing of 15.7 µm, which corresponds to the least favorable condition observed in the present study (Figure 3.48).

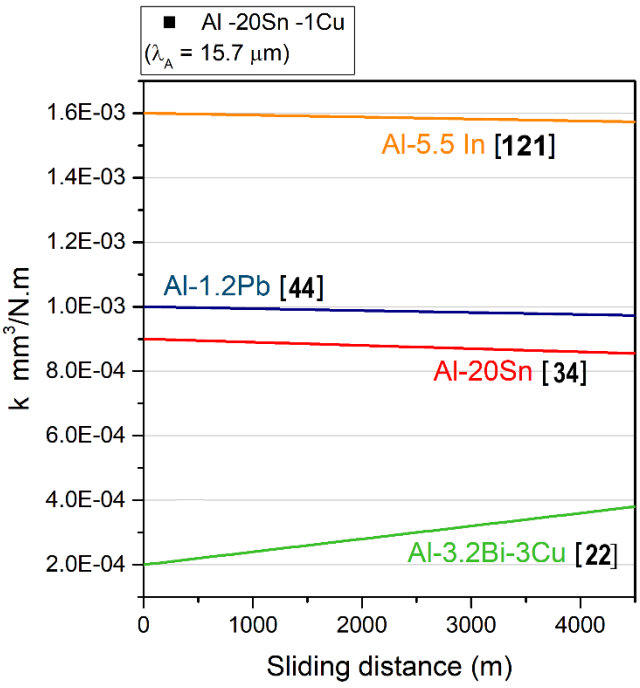

Figure 3.53: Comparison between the dimensional wear coefficient as a function of the sliding distance of the more refined sample (λ_A=15.7 µm) produced with the Al-20wt.%Sn-1wt.%Cu alloy in this study and other studies in the literature.

The comparison of wear coefficient data in Figure 3.53 with other self-lubricating alloys from the literature is, to some extent, encouraging, since it exhibited a

lower wear coefficient compared to many other tested alloys, which indicates that finer scale demonstrates competitive wear behavior for bearing alloys, in addition to having good strength. Furthermore, after a certain distance of approximately 2,000 meters of wear, the Al-20wt.%Sn-1wt.%Cu alloy exhibited stabilization in its wear behavior, which is most likely due to the formation of a stable tribological layer.

3.5 Conclusions

The present study successfully demonstrated effect of solidification conditions on the Al-20wt.%Sn-1wt.%Cu alloy. The use of an upward directional solidification setup allowed for precise measurement of cooling rates, enabling the production of a wide range of dendritic microstructures and the study of their influence on mechanical and wear properties The main findings can be summarized as follows:

- The solidification of the Al-20wt.%Sn-1wt.%Cu alloy is characterized by inverse macrosegregation of Sn and the formation of a continuous, interconnected β-Sn network within the interdendritic regions.
- A finer dendritic microstructure, achieved at higher cooling rates, significantly improves both the ultimate tensile strength and ductility of the alloy. This is attributed to the hetero-deformation-induced (HDI) hardening mechanism, where the large surface area of the refined Sn network enhances strain hardening.
- A coarser microstructure provides better wear resistance. The larger, more widely spaced Sn regions in a coarse structure are more effective at forming a stable, solid lubricating film on the worn surface, which reduces the wear coefficient. The Al-20wt.%Sn-1wt.%Cu alloy shows a competitive wear resistance compared to other self-lubricating alloys, and its wear behaviour stabilizes after a certain sliding distance, indicating the formation of a durable tribological layer.

CHAPTER 4 – GENERAL CONCLUSIONS

This doctoral research addressed the solidification of Al-Sn-Cu alloys through a dual investigation. Immiscible alloys in France and the industrial alloy SAE 783 Al-20wt.%Sn-1wt.%Cu in Brazil.

The study of immiscible Al-10%Cu-X%Sn alloys, using complementary methodologies such as thermodynamic calculations (CALPHAD), thermal analysis (DSC), and directional solidification monitored by *in situ* radiography, allowed for a comprehensive description of the solidification trajectories and revealed the complexity of liquid phase separation during solidification. Although all methods consistently identified the sequence of phase transformations from the onset of α-Al dendritic growth to the final eutectic reaction, X-ray radiography exposed distinct liquid phase separation behaviors: gradual separation in alloys with low Sn content and a two-step mechanism in alloys with high Sn content. These characteristics, not predicted by thermodynamic calculations, highlight the limitations of purely computational approaches and the need for experimental validation. The sensitivity of liquid phase separation to alloy composition underscores the relevance of this research for both scientific knowledge and industrial alloy design.

The investigation of SAE 783 under transient directional solidification provided valuable information on the correlation between thermal conditions, microstructural development, and final performance. The results confirmed that microstructural refinement, promoted by higher cooling rates, increases tensile strength and ductility through hetero-deformation-induced hardening mechanisms. On the other hand, coarser microstructures exhibited superior wear resistance due to the ability of large, well-distributed β-Sn regions to form stable lubricating films during sliding. These findings demonstrate that the optimization of industrial alloys cannot depend on a single microstructural objective: instead, it is necessary to balance strength and wear performance according to the intended application.

In conclusion, this work contributes to the advancement of the field of solidification metallurgy by:

- Demonstrating the critical role of alloy composition in controlling liquid phase separation and monotectic behavior in immiscible Al-Sn-Cu alloys.

- Validating and comparing different methodologies (thermodynamic modeling, calorimetry, and X-ray radiography) to determine solidification path.
- Establishing correlations between thermal parameters, microstructural characteristics, and mechanical/tribological performance in the SAE 783 alloy.
- Highlighting the importance of morphology and adhesion between the α-Al and β-Sn phases to balance conflicting property trends, strength and ductility versus wear resistance.

PERSPECTIVES

As a general remark, this thesis has also addressed several problematics opening the way for further investigations. Future works can expand from our study in the following directions:

- Throughout the study, both in the analysis of model alloys with high Sn content (10 and 20wt.%) and in the SAE 783 alloy (Al-20wt.%Sn-1wt.%Cu), variations in dendritic arm growth orientation were observed, which are indicative of the dendritic orientation transition (DOT) phenomenon. Preliminary analyses using EBSD (Electron Backscatter Diffraction) and microtomography on model alloy samples revealed the growth of secondary dendrite arms on orientation other than the <100> family. However, these results were not deeply explored, and broader investigations are required.
- The initial project of this thesis included the addition of bismuth to the SAE 783 alloy (Al-20wt.%Sn-1wt.%Cu). The aim was twofold: (i) to introduce an additional self-lubricating phase [45] and (ii) to modify the morphology of the β-Sn phase by breaking its branching structure [36], thereby enhancing the alloy's tribological properties. However, numerous difficulties arose during attempts to produce ingots with Bi additions. For instance, three attempts were made to produce directionally solidified ingots, but in all cases feathering grains developed along the ingot, which hindered the correlation between thermal variables and microstructure, since dendrite morphology is altered in such grains. In addition, two attempts were made to produce samples using a laboratory-scale centrifuge, both unsuccessful. As demonstrated in this work, when the β-Sn phase morphology was circular or nearly circular, the associated wear dimensional coefficient was lower. Therefore, future studies should explore the morphological changes induced by Bi addition, as well as the implications of this element on wear behavior and tensile properties. This is particularly relevant considering that, unlike the findings of the present work, binary Al-Bi alloys exhibit a dendritic spacing inversely proportional to wear performance [22].

- A preliminary attempt was made to study the modified SAE 783 alloy (Al-20wt.%Sn-1wt.%Cu) with Bi addition using the SFINX device for *in-situ* and real time solidification observation. The presence of Bi in this alloy induces liquid phase separation; however, surface tension between the elements caused Bi and Sn to leak along the sample walls, posing a risk of damaging the device. Consequently, the experiment had to be interrupted at an early stage. Nevertheless, investigating the solidification kinetics of this alloy remains a promising direction. Future studies could focus on applying a suitable coating to the sample, capable of retaining the elements within the boundaries and enabling safe and complete analysis
- From a tribological perspective, it would also be valuable to correlate wear with the coefficient of friction. This was not possible in the present work due to limitations of the equipment available during the course of the thesis.

REFERENCES

[1] A. Garcia, Solidificação: Fundamentos e Aplicações, 2°, Editora Unicamp, 2007.

[2] S. Kim, W.F. Flanagan, B.D. Lichter, R.N. Grugel, Electrical conductivity in directionally solidified lead-9 and -20 wt pct copper alloys, Metall. Trans. A. 24 (1993) 975–979. https://doi.org/10.1007/BF02656519.

[3] M. V. Canté, J.E. Spinelli, N. Cheung, A. Garcia, The Correlation Between Dendritic Microstructure and Mechanical Properties of Directionally Solidified Hypoeutectic Al-Ni Alloys, Met. Mater. Int. 16 (2010) 39–49. https://doi.org/10.1007/S12540-010-0039-2.

[4] W. Kurz, D.J. Fisher, Fundamentals of Solidification, Third, Trans Tech Publications, Netherlands, 1992.

[5] W. Zhai, L. Hu, D.L. Geng, B. Wei, Thermodynamic properties and microstructure evolution of ternary Al-10%Cu-x%Sn immiscible alloys, J. Alloys Compd. 627 (2015) 402–409. https://doi.org/10.1016/j.jallcom.2014.11.191.

[6] H. Nguyen-Thi, Y. Dabo, B. Drevet, M.D. Dupouy, D. Camel, B. Billia, J.D. Hunt, A. Chilton, Directional solidification of Al-1.5 wt% Ni alloys under diffusion transport in space and fluid-flow localisation on earth, J. Cryst. Growth. 281 (2005) 654–668. https://doi.org/10.1016/j.jcrysgro.2005.04.061.

[7] M. Charpentier, D. Daloz, A. Hazotte, E. Gautier, G. Lesoult, M. Grange, Study of microstructure and solute partitioning in a cast Ti-48Al-2Cr-2Nb alloy by quenching during directional solidification technique, Metall. Mater. Trans. A Phys. Metall. Mater. Sci. 34 A (2003) 2139–2148. https://doi.org/10.1007/s11661-003-0278-7.

[8] P.L. Schaffer, R.H. Mathiesen, L. Arnberg, In-situ investigation of liquid-liquid phase separation in hypermonotectic alloys, Mater. Sci. Forum. 649 (2010) 149–158. https://doi.org/10.4028/www.scientific.net/MSF.649.149.

[9] J.Z. Zhao, T. Ahmed, H.X. Jiang, J. He, Q. Sun, Solidification of immiscible alloys: A review, Acta Metall. Sin. (English Lett. 30 (2017) 1–28. https://doi.org/10.1007/s40195-016-0523-x.

[10] H. Nguyen-Thi, A. Bogno, G. Reinhart, B. Billia, R.H. Mathiesen, G. Zimmermann, Y. Houltz, K. Löth, D. Voss, A. Verga, F. De Pascale, XRMON-

GF experimental set-up devoted to X-Ray radiographic observation of directional solidification under microgravity on MASER 12 sounding rocket mission, Eur. Sp. Agency, (Special Publ. ESA SP. 700 SP (2011) 479–486.

[11] H. Nguyen Thi, G. Reinhart, A. Buffet, T. Schenk, N. Mangelinck-Noël, H. Jung, N. Bergeon, B. Billia, J. Härtwig, J. Baruchel, In situ and real-time analysis of TGZM phenomena by synchrotron X-ray radiography, J. Cryst. Growth. 310 (2008) 2906–2914. https://doi.org/10.1016/j.jcrysgro.2008.01.041.

[12] H. Nguyen Thi, H. Jamgotchian, J. Gastaldi, J. Härtwig, T. Schenk, H. Klein, B. Billia, J. Baruchel, Y. Dabo, Preliminary in situ and real-time study of directional solidification of metallic alloys by x-ray imaging techniques, J. Phys. D. Appl. Phys. 36 (2003). https://doi.org/10.1088/0022-3727/36/10a/317.

[13] C. Rakete, C. Baumbach, A. Goldschmidt, D. Samberg, C.G. Schroer, F. Breede, C. Stenzel, G. Zimmermann, C. Pickmann, Y. Houltz, C. Lockowandt, O. Svenonius, P. Wiklund, R.H. Mathiesen, Compact x-ray microradiograph for in situ imaging of solidification processes: Bringing in situ x-ray micro-imaging from the synchrotron to the laboratory, Rev. Sci. Instrum. 82 (2011). https://doi.org/10.1063/1.3650468.

[14] H. Soltani, F. Ngomesse, G. Reinhart, M.C. Benoudia, M. Zahzouh, H. Nguyen-Thi, Impact of gravity on directional solidification of refined Al-20wt.%Cu alloy investigated by in situ X-radiography, J. Alloys Compd. 862 (2021) 158028. https://doi.org/10.1016/j.jallcom.2020.158028.

[15] L. Abou-Khalil, Study of the influence of external fields on solidification microstructures formation by X-ray radiography, Univeristé D'Aix-Marseille, 2017. https://www.theses.fr/2017AIXM0005.

[16] F. Bertelli, C. Brito, I.L. Ferreira, G. Reinhart, H. Nguyen-Thi, N. Mangelinck-Noël, N. Cheung, A. Garcia, Cooling thermal parameters, microstructure, segregation and hardness in directionally solidified Al-Sn-(Si;Cu) alloys, Mater. Des. 72 (2015) 31–42. https://doi.org/10.1016/j.matdes.2015.02.006.

[17] D.A. Porter, K.E. Easterling, M.Y. Sherif, Phase Transformation in Metals and Alloys, 3rd ed., 2009.

[18] K.A. Jackson, Constitutional supercooling surface roughening, J. Cryst. Growth. 264 (2004) 519–529. https://doi.org/10.1016/j.jcrysgro.2003.12.074.

[19] S.M. de Albuquerque Sousa, G.L. de Gouveia, J.E. Spinelli, Evaluating grain size, dendritic scale, and tensile properties of a NbB-inoculated 6201 alloy using solidification rate, Mater. Sci. Eng. A. 835 (2022) 142680. https://doi.org/10.1016/J.MSEA.2022.142680.

[20] J.E. Spinelli, B.L. Silva, A. Garcia, Assessment of tertiary dendritic growth and its effects on mechanical properties of directionally solidified Sn-0.7Cu-xAg solder alloys, J. Electron. Mater. 43 (2014) 1347–1361. https://doi.org/10.1007/s11664-014-3087-4.

[21] G.L. de Gouveia, A. Garcia, J.E. Spinelli, Tailoring microstructure and tensile properties of Mg-Si alloys varying solidification cooling rate and Si content, Mater. Sci. Eng. A. 825 (2021). https://doi.org/10.1016/j.msea.2021.141905.

[22] R. V. Reyes, V.E. Pinotti, C.R.M. Afonso, L.C. Casteletti, A. Garcia, J.E. Spinelli, Processing, As-Cast Microstructure and Wear Characteristics of a Monotectic Al-Bi-Cu Alloy, J. Mater. Eng. Perform. 28 (2019) 1201–1212. https://doi.org/10.1007/s11665-018-3851-3.

[23] W.R. Osório, A. Garcia, Modeling dendritic structure and mechanical properties of Zn-Al alloys as a function of solidification conditions, Mater. Sci. Eng. A. 325 (2002) 103–111. https://doi.org/10.1016/S0921-5093(01)01455-1.

[24] D.M. Rosa, J.E. Spinelli, I.L. Ferreira, A. Garcia, Cellular/Dendritic Transition and Microstructure Evolution During Transient Directional Solidification of Pb-Sb Alloys, Metall. Mater. Trans. A Phys. Metall. Mater. Sci. 39 (2008) 2161–2174. https://doi.org/10.1007/S11661-008-9542-1.

[25] C. Brito, G. Reinhart, H. Nguyen-Thi, N. Mangelinck-Noël, N. Cheung, J.E. Spinelli, A. Garcia, High Cooling Rate Cells, Dendrites, Microstructural Spacings and Microhardness in a Directionally Solidified Al–Mg–Si Alloy, J. Alloys Compd. 636 (2015) 145–149. https://doi.org/10.1016/J.JALLCOM.2015.02.140.

[26] S. Akamatsu, H. Nguyen-Thi, In situ observation of solidification patterns in diffusive conditions, Acta Mater. 108 (2016) 325–346. https://doi.org/10.1016/j.actamat.2016.01.024.

[27] H.W. Kerr, W. Kurz, Solidification of peritectic alloys, Int. Mater. Rev. 41 (1996) 129–164. https://doi.org/10.1179/imr.1996.41.4.129.

[28] F.C . Campbell, ed., Phase Diagrams—Understanding the Basics, ASM International, 2012.

[29] L. Ratke, S. Diefenbach, Liquid immiscible alloys, Mater. Sci. Eng. R. 15 (1995) 263–347. https://doi.org/10.1016/0927-796X(95)00180-8.

[30] A.E. Bravo, H.A. Durán, V.H. Jacobo, A. Ortiz, R. Schouwenaars, Towards new formulations for journal bearing alloys, Wear. 302 (2013) 1528–1535. https://doi.org/10.1016/j.wear.2013.01.040.

[31] N.A. Bushe, I.G. Goryacheva, Y.Y. Makhovskaya, Effect of aluminum-alloy composition on self-lubrication of frictional surfaces, Wear. 254 (2003) 1276–1280. https://doi.org/10.1016/S0043-1648(03)00110-8.

[32] I. Kaban, M. Köhler, L. Ratke, R. Nowak, N. Sobczak, N. Mattern, J. Eckert, A.L. Greer, S.W. Sohn, D.H. Kim, Phase separation in monotectic alloys as a route for liquid state fabrication of composite materials, J. Mater. Sci. 47 (2012) 8360–8366. https://doi.org/10.1007/s10853-012-6660-3.

[33] G.A. Chadwick, Monotectic solidification, Br. J. Appl. Phys. 16 (1965) 1095–1097. https://doi.org/10.1088/0508-3443/16/8/306.

[34] K.S. Cruz, E.S. Meza, F.A.P. Fernandes, J.M.V. Quaresma, L.C. Casteletti, A. Garcia, Dendritic Arm Spacing Affecting Mechanical Properties and Wear Behavior of Al-Sn and Al-Si Alloys Directionally Solidified under Unsteady-State Conditions, Metall. Mater. Trans. A. 41 (2010) 972–984. https://doi.org/10.1007/S11661-009-0161-2.

[35] L. Ratke, A. Müller, M. Seifert, G. Kapserovich, Monotectic alloys and their growth morphologies, Mater. Sci. Forum. 649 (2010) 137–142. https://doi.org/10.4028/www.scientific.net/MSF.649.137.

[36] Z.M. Wang, Q. Yang, Z.P. Sun, B.R. Zhang, W. Zhao, W.F. Rao, The effects of Bi and Pb on the soft phase in Al82Sn15Si2.2Cu0.8 sliding bearing alloy, Mater. Charact. 170 (2020) 110684. https://doi.org/10.1016/j.matchar.2020.110684.

[37] O. Akinlade, A.O. Boyo, B.R. Ijaduola, Demixing tendencies in some Sn-based liquid alloys, J. Alloys Compd. 290 (1999) 191–196. https://doi.org/10.1016/S0925-8388(99)00232-7.

[38] J.C.R.E. Oliveira, M.H. Braga, R.D.M. Travasso, Simulation of the spinodal phase separation dynamics of the Bi-Zn system, J. Non. Cryst. Solids. 354 (2008)

5340–5342. https://doi.org/10.1016/j.jnoncrysol.2008.07.043.

[39] K. Kadirvel, S.R. Koneru, Y. Wang, Exploration of spinodal decomposition in multi-principal element alloys (MPEAs) using CALPHAD modeling, Scr. Mater. 214 (2022) 114657. https://doi.org/10.1016/j.scriptamat.2022.114657.

[40] J. Zhao, H. Sun, L. Zhang, H. Jiang, L. Yang, J. He, In-situ composite microstructure formation of immiscible alloy solidified in space, Natl. Sci. Rev. 10 (2023) 2022–2024. https://doi.org/10.1093/nsr/nwac261.

[41] H.R. Kotadia, E. Doernberg, J.B. Patel, Z. Fan, R. Schmid-Fetzer, Solidification of Al-Sn-Cu based immiscible alloys under intense shearing, Metall. Mater. Trans. A Phys. Metall. Mater. Sci. 40 (2009) 2202–2211. https://doi.org/10.1007/s11661-009-9918-x.

[42] J.Z. Zhao, L. Ratke, A model describing the microstructure evolution during a cooling of immiscible alloys in the miscibility gap, Scr. Mater. 50 (2004) 543–546. https://doi.org/10.1016/j.scriptamat.2003.10.024.

[43] D. Mirković, J. Gröbner, R. Schmid-Fetzer, Liquid demixing and microstructure formation in ternary Al-Sn-Cu alloys, Mater. Sci. Eng. A. 487 (2008) 456–467. https://doi.org/10.1016/j.msea.2007.10.043.

[44] E.S. Freitas, A.P. Silva, J.E. Spinelli, L.C. Casteletti, A. Garcia, Inter-relation of microstructural features and dry sliding wear behavior of monotectic al-bi and al-pb alloys, Tribol. Lett. 55 (2014) 111–120. https://doi.org/10.1007/s11249-014-0338-8.

[45] B. Dong, Z. Wu, P. Wang, C. Ke, S. Liu, J. Jie, CALPHAD-guided alloy design of Bi-modified Al–Sn bearing alloy with multiphase composite structure and optimal self-lubricating property, J. Alloys Compd. 874 (2021). https://doi.org/10.1016/j.jallcom.2021.159756.

[46] B. Nestler, A.A. Wheeler, L. Ratke, C. Stöcker, Phase-field model for solidification of a monotectic alloy with convection, Phys. D Nonlinear Phenom. 141 (2000) 133–154. https://doi.org/10.1016/S0167-2789(00)00035-X.

[47] F. Wang, A. Choudhury, B. Nestler, Solidification morphologies in monotectic alloys, IOP Conf. Ser. Mater. Sci. Eng. 27 (2011). https://doi.org/10.1088/1757-899X/27/1/012027.

[48] S. De Albuquerque, V. Leme, R. V Reyes, G. Reinhart, D.C.C. Magalhães, J.E.

Spinelli, H. Nguyen-thi, Al – 20Sn – 1Cu self-lubricating alloy : Correlations between microstructure coarsening, mechanical, and application properties, 36 (2025) 7284–7303. https://doi.org/10.1016/j.jmrt.2025.04.250.

[49] R. Schouwenaars, J.A. Torres, V.H. Jacobo, A. Ortiz, Tailoring the Mechanical Properties of Al-Sn-Alloys for Tribological Applications, Mater. Sci. Forum. 539–543 (2007) 317–322. https://doi.org/10.4028/www.scientific.net/msf.539-543.317.

[50] S. Huang, B. Zhu, Y. Zhang, H. Liu, S. Wu, H. Xie, Microstructure Comparison for AlSn20Cu Antifriction Alloys Prepared by Semi-Continuous Casting, Semi-Solid Die Casting, and Spray Forming, Metals (Basel). 12 (2022). https://doi.org/10.3390/met12101552.

[51] F. Bertelli, E.S. Freitas, N. Cheung, M.A. Arenas, A. Conde, J. de Damborenea, A. Garcia, Microstructure, tensile properties and wear resistance correlations on directionally solidified Al-Sn-(Cu; Si) alloys, J. Alloys Compd. 695 (2017) 3621–3631. https://doi.org/10.1016/j.jallcom.2016.11.399.

[52] K.S. Cruz, J.E. Spinelli, I.L. Ferreira, N. Cheung, A. Garcia, Microstructural development in Al-Sn alloys directionally solidified under transient heat flow conditions, Mater. Chem. Phys. 109 (2008) 87–98. https://doi.org/10.1016/j.matchemphys.2007.10.037.

[53] N.A. Belov, T.K. Akopyan, I.S. Gershman, O.O. Stolyarova, A.O. Yakovleva, Effect of Si and Cu additions on the phase composition, microstructure and properties of Al-Sn alloys, J. Alloys Compd. 695 (2017) 2730–2739. https://doi.org/10.1016/j.jallcom.2016.11.193.

[54] D. Mirković, J. Gröbner, R. Schmid-Fetzer, Solidification paths of multicomponent monotectic aluminum alloys, Acta Mater. 56 (2008) 5214–5222. https://doi.org/10.1016/j.actamat.2008.07.001.

[55] K.A. Jackson, J.D. Hunt, Transparent compounds that freeze like metals, Acta Metall. 13 (1965) 1212–1215. https://doi.org/10.1016/0001-6160(65)90061-1.

[56] R.H. Mathiesen, L. Arnberg, H. Nguyen-Thi, B. Billia, In situ x-ray video microscopy as a tool in solidification science, Jom. 64 (2012) 76–82. https://doi.org/10.1007/s11837-011-0213-0.

[57] J. Forsten, H.. Miekkoj, Radiographic Observations of the Solidification of

Metals, J. Inst. Met. 95 (1967) 143–145.

[58] E.W.J. Miller, J. Beech, In-situ radiographic observations of alloy solidification, Metallography. 5 (1972) 298–300. https://doi.org/10.1016/0026-0800(72)90009-2.

[59] W.F. Kaukler, F. Rosenberger, X-ray microscopic observations of metal solidification dynamics, Metall. Mater. Trans. A. 25 (1994) 1775–1777. https://doi.org/10.1007/BF02668541.

[60] P.D. Lee, J.D. Hunt, Hydrogen porosity in directional solidified aluminium-copper alloys: In situ observation, Acta Mater. 45 (1997) 4155–4169. https://doi.org/10.1016/S1359-6454(97)00081-5.

[61] F.A. Ngomesse Mbiandou, Application of X-radiography to the study of the solidification microstructures formation on Earth and in microgravity, Univeristé D'Aix-Marseille, 2022.

[62] G. Reinhart, N. Mangelinck-Noël, H. Nguyen-Thi, T. Schenk, J. Gastaldi, B. Billia, P. Pino, J. Härtwig, J. Baruchel, Investigation of columnar-equiaxed transition and equiaxed growth of aluminium based alloys by X-ray radiography, Mater. Sci. Eng. A. 413–414 (2005) 384–388. https://doi.org/10.1016/j.msea.2005.08.197.

[63] A. Bogno, H. Nguyen-Thi, G. Reinhart, B. Billia, J. Baruchel, Growth and interaction of dendritic equiaxed grains: In situ characterization by synchrotron X-ray radiography, Acta Mater. 61 (2013) 1303–1315. https://doi.org/10.1016/j.actamat.2012.11.008.

[64] L. Abou-Khalil, K.S. da Cruz, G. Reinhart, N. Mangelinck-Noël, H. Nguyen-Thi, Influence of growth velocity on fragmentation during directional solidification of Al – 14 wt.% Sn alloy studied by in-situ synchrotron X-radiography, Acta Mater. 241 (2022) 118370. https://doi.org/10.1016/j.actamat.2022.118370.

[65] W.Q. Lu, S.G. Zhang, J.G. Li, Observation of Bi coarsening and dissolution behaviors in melting Al-Bi immiscible alloy, Acta Metall. Sin. (English Lett. 29 (2016) 800–803. https://doi.org/10.1007/s40195-016-0453-7.

[66] P.L. Schaffer, R.H. Mathiesen, L. Arnberg, M. Di Sabatino, A. Snigirev, In situ investigation of spinodal decomposition in hypermonotectic Al-Bi and Al-Bi-Zn alloys, New J. Phys. 10 (2008). https://doi.org/10.1088/1367-2630/10/5/053001.

[67] P.L. Schaffer, R.H. Mathiesen, L. Arnberg, L2 droplet interaction with α-Al during solidification of hypermonotectic Al-8 wt.% Bi alloys, Acta Mater. 57 (2009) 2887–2895. https://doi.org/10.1016/j.actamat.2009.02.041.

[68] H. Soltani, G. Reinhart, M.C. Benoudia, M. Zahzouh, H. Nguyen-Thi, Impact of gravity-related phenomena on the grain structure formation: Comparative study between horizontal and vertical solidification of a refined Al-20wt.%Cu alloy, IOP Conf. Ser. Mater. Sci. Eng. 529 (2019). https://doi.org/10.1088/1757-899X/529/1/012019.

[69] H. Soltani, G. Reinhart, M.C. Benoudia, F. Ngomesse, M. Zahzouh, H. Nguyen-Thi, Equiaxed grain structure formation during directional solidification of a refined Al-20wt.%Cu alloy: In situ analysis of temperature gradient effects, J. Cryst. Growth. 587 (2022) 126645. https://doi.org/10.1016/j.jcrysgro.2022.126645.

[70] D.J. Browne, F. Garcia-Moreno, H. Nguyen-Thi, G. Zimmermann, F. Kargl, R.H. Mathiesen, A. Griesche, O. Minster, Overview of In Situ X-Ray Studies of Light Alloy Solidification in Microgravity In: Solanki, K., Orlov, D., Singh, A., Neelameggham, N. (eds) Magnesium Technology 2017, in: Springer Int. Publ. Ag, Cham, 2017: pp. 581-590. https://doi.org/10.1007/978-3-319-52392-7.

[71] M.G.C. Xavier, R.A.V. Reyes, L.F. Gomes, J.E. Spinelli, N. Mangelinck-Noël, H. Nguyen-Thi, G. Reinhart, Combined growth of α-Al and Bi in a Al-Bi-Cu monotectic alloy analyzed by in situ X-ray radiography, J. Cryst. Growth. 536 (2020) 125592. https://doi.org/10.1016/j.jcrysgro.2020.125592.

[72] C.A. Schneider, W.S. Rasband, K.W. Eliceiri, NIH Image to ImageJ: 25 years of image analysis, Nat. Methods. 9 (2012) 671–675. https://doi.org/10.1038/nmeth.2089.

[73] G. Reinhart, D. Grange, L. Abou-Khalil, N. Mangelinck-Noël, N.T. Niane, V. Maguin, G. Guillemot, C.A. Gandin, H. Nguyen-Thi, Impact of solute flow during directional solidification of a Ni-based alloy: In-situ and real-time X-radiography, Acta Mater. 194 (2020) 68–79. https://doi.org/10.1016/j.actamat.2020.04.003.

[74] H. Soltani, Analyse in situ par radiographie X du développement de grains dendritiques dans un gradient de température, Université BADJI-Mokhtar, Aix-

Marseille Université, 2020.

[75] R.A. Swalin, Thermodynamics of Solid, second, Wiley-Interscience, Minneapolis, Minessota, 1972.

[76] Z.K. Liu, First-principles calculations and CALPHAD modeling of thermodynamics, J. Phase Equilibria Diffus. 30 (2009) 517–534. https://doi.org/10.1007/s11669-009-9570-6.

[77] P.J. Spencer, A brief history of CALPHAD, Calphad Comput. Coupling Phase Diagrams Thermochem. 32 (2008) 1–8. https://doi.org/10.1016/j.calphad.2007.10.001.

[78] Thermo-Calc Software: CALPHAD Methodology, (n.d.). https://thermocalc.com/about-us/methodology/the-calphad-methodology/ (accessed April 29, 2024).

[79] J.. Andersson, T. Helander, L. Höglund, P.. Shi, B. Sundman, Thermo-Calc and DICTRA, Computational tools for materials science., Calphad. 26 (2002) 273–312.

[80] H.R. Kotadia, A. Das, E. Doernberg, R. Schmid-Fetzer, A comparative study of ternary Al-Sn-Cu immiscible alloys prepared by conventional casting and casting under high-intensity ultrasonic irradiation, Mater. Chem. Phys. 131 (2011) 241–249. https://doi.org/10.1016/j.matchemphys.2011.09.020.

[81] U. Hecht, L. Gránásy, T. Pusztai, B. Böttger, M. Apel, V. Witusiewicz, L. Ratke, J. De Wilde, L. Froyen, D. Camel, B. Drevet, G. Faivre, S.G. Fries, B. Legendre, S. Rex, Multiphase solidification in multicomponent alloys, Mater. Sci. Eng. R Reports. 46 (2004) 1–49. https://doi.org/10.1016/j.mser.2004.07.002.

[82] W.J. Boettinger, U.R. Kattner, K.-W. Moon, J.H. Perepezko, DTA and Heat-flux DSC Measurements of Alloy Melting and Freezing, National Institute of Standards and Technology, 2006.

[83] S. Curiotto, L. Battezzati, E. Johnson, N. Pryds, Thermodynamics and mechanism of demixing in undercooled Cu–Co–Ni alloys, Acta Mater. 55 (2007) 6642–6650.

[84] H. Soltani, G. Reinhart, M.C. Benoudia, F. Ngomesse, M. Zahzouh, H. Nguyen-Thi, Impact of growth velocity on grain structure formation during directional solidification of a refined Al-20 wt.%Cu alloy, J. Cryst. Growth. 548 (2020)

125819. https://doi.org/10.1016/j.jcrysgro.2020.125819.

[85] G. Reinhart, F. Ngomesse, F. Bertelli, P. Benigni, A. Campos, H. Nguyen-Thi, Investigation of Al-20Sn-10Cu alloy directional solidification by laboratory X-radiography, IOP Conf. Ser. Mater. Sci. Eng. 1274 (2023) 012054. https://doi.org/10.1088/1757-899x/1274/1/012054.

[86] T. Haxhimali, A. Karma, F. Gonzales, M. Rappaz, Orientation selection in dendritic evolution, Nat. Mater. 5 (2006) 660–664. https://doi.org/10.1038/nmat1693.

[87] M. Becker, J.A. Dantzig, M. Kolbe, S.T. Wiese, F. Kargl, Dendrite orientation transition in Al–Ge alloys, Acta Mater. 165 (2019) 666–677. https://doi.org/10.1016/j.actamat.2018.12.001.

[88] L. Wang, J.J. Hoyt, N. Wang, N. Provatas, C.W. Sinclair, Controlling solid-liquid interfacial energy anisotropy through the isotropic liquid, Nat. Commun. 11 (2020) 1–7. https://doi.org/10.1038/s41467-020-14530-7.

[89] M. Bedel, G. Reinhart, A.A. Bogno, C.A. Gandin, S. Jacomet, E. Boller, H. Nguyen-Thi, H. Henein, Characterization of dendrite morphologies in rapidly solidified Al-4.5 wt.%Cu droplets, Acta Mater. 89 (2015) 234–246. https://doi.org/10.1016/j.actamat.2015.02.007.

[90] R.E. Napolitano, S. Liu, Three-dimensional crystal-melt Wulff-shape and interfacial stiffness in the Al-Sn binary system, Phys. Rev. B - Condens. Matter Mater. Phys. 70 (2004) 1–11. https://doi.org/10.1103/PhysRevB.70.214103.

[91] A.P. Silva, J.E. Spinelli, N. Mangelinck-Noël, A. Garcia, Microstructural Development During Transient Directional Solidification of Hypermonotectic Al–Bi Alloys, Mater. Des. 31 (2010) 4584–4591. https://doi.org/10.1016/J.MATDES.2010.05.046.

[92] S. Henry, T. Minghetti, M. Rappaz, Dendrite growth morphologies in aluminium alloys, Acta Mater. 46 (1998) 6431–6443. https://doi.org/10.1016/S1359-6454(98)00308-5.

[93] C. Brito, T.A. Costa, T.A. Vida, F. Bertelli, N. Cheung, J.E. Spinelli, A. Garcia, Characterization of Dendritic Microstructure, Intermetallic Phases, and Hardness of Directionally Solidified Al-Mg and Al-Mg-Si Alloys, Metall. Mater. Trans. A Phys. Metall. Mater. Sci. 46 (2015) 3342–3355. https://doi.org/10.1007/s11661-

015-2967-4.

[94] A. Garcia, Influência das variáveis térmicas de solidificação na forma da macroestrutura e da microestrutura e correlação com propiedades decorrentes, Projeções. 23 (2005) 13–32.

[95] F. Ngomesse, G. Reinhart, H. Soltani, G. Zimmermann, D.J. Browne, W. Sillekens, H. Nguyen-Thi, In situ investigation of the Columnar-to-Equiaxed Transition during directional solidification of Al–20 wt.%Cu alloys on Earth and in microgravity, Acta Mater. 221 (2021) 117401. https://doi.org/10.1016/j.actamat.2021.117401.

[96] R.P. Mooney, S. McFadden, Z. Gabalcová, J. Lapin, An experimental-numerical method for estimating heat transfer in a Bridgman furnace, Appl. Therm. Eng. 67 (2014) 61–71. https://doi.org/10.1016/j.applthermaleng.2014.02.048.

[97] C. Brito, H. Nguyen-Thi, N. Mangelinck-Noël, N. Cheung, J.E. Spinelli, A. Garcia, Cellular-to-Dendritic and Dendritic-to-Cellular Morphological Transitions in a Ternary Al-Mg-Si Alloy, IOP Conf. Ser. Mater. Sci. Eng. 529 (2019). https://doi.org/10.1088/1757-899X/529/1/012018.

[98] P.R. Goulart, J.E. Spinelli, N. Cheung, N. Mangelinck-Nöel, A. Garcia, Al-Fe hypoeutectic alloys directionally solidified under steady-state and unsteady-state conditions, J. Alloys Compd. 504 (2010) 205–210. https://doi.org/10.1016/j.jallcom.2010.05.089.

[99] D.M. Stefanescu, Science and Engineering of Casting Solidification, Third, Springer, 2015. https://doi.org/10.1007/978-3-319-15693-4.

[100] T.A. Costa, M. Dias, E.S. Freitas, L.C. Casteletti, A. Garcia, The effect of microstructure length scale on dry sliding wear behaviour of monotectic Al-Bi-Sn alloys, J. Alloys Compd. 689 (2016) 767–776. https://doi.org/10.1016/j.jallcom.2016.08.051.

[101] R. V. Reyes, L.C. Casteletti, A. Garcia, J.E. Spinelli, Characterization of microstructure and wear resistance of a monotectic Al-Bi-Zn alloy, J. Phys. Chem. Solids. 147 (2020). https://doi.org/10.1016/j.jpcs.2020.109631.

[102] F.A. Souza, I.A. Magno, M.O. Costa, A.S. Barros, J.M. Nascimento, D.B. Carvalho, O.L. Rocha, Unsteady-State Horizontal Solidification of an Al–Si–Cu–Fe Alloy: Relationship Between Thermal Parameters and Microstructure with

Mechanical Properties/Fracture Feature, Met. Mater. Int. 25 (2019) 18–33. https://doi.org/10.1007/s12540-018-0174-8.

[103] J. Campbell, Casting, Butterworth-Heinemann, 2003.

[104] Y.A. Çengel, A.J. Ghajar, Transferência de Calor e Massa: Uma Abordagem Prática, Quarta, Ltda, AMGH Editora; Mc GrawHill, 2012.

[105] A.P. Silva, J.E. Spinelli, A. Garcia, Microstructural evolution during upward and downward transient directional solidification of hypomonotectic and monotectic Al-Bi alloys, J. Alloys Compd. 480 (2009) 485–493. https://doi.org/10.1016/j.jallcom.2009.01.105.

[106] E. Ghassemali, M. Riestra, T. Bogdanoff, B.S. Kumar, S. Seifeddine, Hall-Petch equation in a hypoeutectic Al-Si cast alloy: Grain size vs. secondary dendrite arm spacing, Procedia Eng. 207 (2017) 19–24. https://doi.org/10.1016/j.proeng.2017.10.731.

[107] M.Â.O. de Alfaia, R. Oliveira, T.S. Lima, F.E. Mariani, L.C. Casteletti, N. Cheung, A. Garcia, Effects of cooling rate and microstructure scale on wear resistance of unidirectionally solidified Al-3.2wt.%Bi-(1; 3) wt.%Pb alloys, Mater. Today Commun. 25 (2020). https://doi.org/10.1016/j.mtcomm.2020.101659.

[108] G.L. de Gouveia, Análise da microestrutura, parâmetros térmicos e de propriedades mecânicas na solidificação de ligas com alto teor de cobre Al-(x)%Cu-7%Si, Universidade Federal de São Carlos, 2019.

[109] J.E. Spinelli, N. Cheung, A. Garcia, On array models theoretical predictions versus measurements for the growth of cells and dendrites in the transient solidification of binary alloys, Philos. Mag. 91 (2011) 1705–1723. https://doi.org/10.1080/14786435.2010.545779.

[110] A.P. Silva, A. Garcia, J.E. Spinelli, Microstructural morphologies and experimental growth laws during solidification of monotectic and hypermonotectic Al-Pb alloys, J. Mater. Sci. Technol. 30 (2014) 401–407. https://doi.org/10.1016/j.jmst.2013.10.027.

[111] R. Oliveira, T.A. Costa, M. Dias, C. Konno, N. Cheung, A. Garcia, Transition from high cooling rate cells to dendrites in directionally solidified Al-Sn-(Pb) alloys, Mater. Today Commun. 25 (2020).

https://doi.org/10.1016/j.mtcomm.2020.101490.

[112] A.P. Silva, P.R. Goulart, A. Garcia, J.E. Spinelli, Microstructural development during transient directional solidification of a hypomonotectic Al-In alloy, Philos. Mag. Lett. 92 (2012) 442–450. https://doi.org/10.1080/09500839.2012.685962.

[113] D. Bouchard, J.S. Kirkaldy, Prediction of dendrite arm spacings in unsteady- and steady-state heat flow of unidirectionally solidified binary alloys, Metall. Mater. Trans. B Process Metall. Mater. Process. Sci. 28 (1997) 651–663. https://doi.org/10.1007/s11663-997-0039-x.

[114] J.D. Hunt, Keynote Address: Cellular and primary dendrite spacings, in: Int. Conf. Solidif. Cast. Met., Metals Society, London, 1979: pp. 3–9.

[115] W. Kurz, D.J. Fisher, Dendrite growth at the limit of stability: tip radius and spacing, Acta Metall. 29 (1981) 11–20. https://doi.org/10.1016/0001-6160(81)90082-1.

[116] M. Rappaz, W.J. Boettinger, On dendritic solidification of multicomponent alloys with unequal liquid diffusion coefficients, Acta Mater. 47 (1999) 3205–3219. https://doi.org/10.1016/S1359-6454(99)00188-3.

[117] A.P. Silva, J.E. Spinelli, A. Garcia, Thermal parameters and microstructure during transient directional solidification of a monotectic Al-Bi alloy, J. Alloys Compd. 475 (2009) 347–351. https://doi.org/10.1016/j.jallcom.2008.07.021.

[118] T.A. Costa, E.S. Freitas, M. Dias, C. Brito, N. Cheung, A. Garcia, Monotectic Al-Bi-Sn alloys directionally solidified: Effects of Bi content, growth rate and cooling rate on the microstructural evolution and hardness, J. Alloys Compd. 653 (2015) 243–254. https://doi.org/10.1016/j.jallcom.2015.09.009.

[119] M. Gündüz, E. Çadirli, Directional Solidification of Aluminium–Copper Alloys, Mater. Sci. Eng. A. 327 (2002) 167–185. https://doi.org/10.1016/S0921-5093(01)01649-5.

[120] K.A. Jackson, J.D. Hunt, Lamellar and Rod Eutectic Growth, Dyn. Curved Front. 236 (1988) 363–376. https://doi.org/10.1016/b978-0-08-092523-3.50040-x.

[121] E.S. Freitas, J.E. Spinelli, L.C. Casteletti, A. Garcia, Microstructure-wear behavior correlation on a directionally solidified Al-In monotectic alloy, Tribol. Int. 66 (2013) 182–186. https://doi.org/10.1016/j.triboint.2013.05.009.

[122] J. Williams, The Invention of Tribology: Peter Jost's Contribution, Lubricants.

12 (2024). https://doi.org/10.3390/lubricants12030065.

[123] K. Holmberg, A. Erdemir, Influence of tribology on global energy consumption, costs and emissions, Friction. 5 (2017) 263–284. https://doi.org/10.1007/s40544-017-0183-5.

[124] M.M. Khonsari, E.R. Booser, Applied Tribology: Bearing Design and Lubrication, 3rd Editio, John Wiley & Sons, Ltd, 2017.

[125] I.M. Hutchings, Tribology — Friction and wear of engineering materials, 1992. https://doi.org/10.1016/0301-679x(92)90040-t.

[126] R. Schouwenaars, V.H. Jacobo, A. Ortiz, Microstructural aspects of wear in soft tribological alloys, Wear. 263 (2007) 727–735. https://doi.org/10.1016/j.wear.2006.12.037.

[127] F. Du, D. Li, X. Sa, C. Li, Y. Yu, C. Li, J. Wang, W. Wang, Overview of Friction and Wear Performance of Sliding Bearings, Coatings. 12 (2022). https://doi.org/10.3390/coatings12091303.

[128] Mohit, Types of Main Bearings of Marine Engines and their Properties, Main Engine. (2019). https://www.marineinsight.com/main-engine/types-of-main-bearings-of-marine-engines-and-their-properties/ (accessed August 21, 2025).

[129] E. Rabinowicz, The determination of the compatibility of metals through static friction tests, ASLE Trans. 14 (1971) 198–205. https://doi.org/10.1080/05698197108983243.

[130] R.A.V. Reyes, A. Garcia, J.E. Spinelli, Evaluating microstructure, wear resistance and tensile properties of Al-Bi(-Cu,-Zn) alloys for lightweight sliding bearings, Metals (Basel). 11 (2021) 1–16. https://doi.org/10.3390/met11010153.

[131] T.M. Botelho, H.M. Azevedo, G.H. Machado, C.R. Barbosa, F.S. Rocha, T.A. Costa, O.L. Rocha, Effect of solidification process parameters on dry sliding wear behavior of AlNiBi alloy, Trans. Nonferrous Met. Soc. China (English Ed. 30 (2020) 582–594. https://doi.org/10.1016/S1003-6326(20)65237-2.

[132] Z.C. Lu, M.Q. Zeng, Y. Gao, M. Zhu, Minimizing tribolayer damage by strength-ductility matching in dual-scale structured Al-Sn alloys: A mechanism for improving wear performance, Wear. 304 (2013) 162–172. https://doi.org/10.1016/j.wear.2013.05.001.

[133] M. Beder, The effect of high B4C ratio on the improvement of mechanical

properties and wear resistance of Al2024/B4C composites fabricated by mechanical milling-assisted hot pressing, Ceram. Int. 51 (2025) 9528–9547. https://doi.org/10.1016/j.ceramint.2025.01.287.

[134] R. Mittal, A. Tomar, D. Singh, Wear behavior of disk shape spray formed Al-Si-Pb alloys, J. Mater. Eng. Perform. 23 (2014) 975–981. https://doi.org/10.1007/s11665-013-0802-x.

[135] M.G. Gee, A. Gant, I. Hutchings, R. Bethke, K. Schiffmann, V. Acker, S. Poulat, Y. Gachon, J. Von Stebut, Ball Cratering or Micro-Abrasion Wear Testing of Coatings, (2002) 64. https://eprintspublications.npl.co.uk/2545/1/mgpg57.pdf.

[136] M.G. Gee, A. Gant, I. Hutchings, R. Bethke, K. Schiffman, K. Van Acker, S. Poulat, Y. Gachon, J. von Stebut, Progress towards standardisation of ball cratering, Wear. 255 (2003) 1–13. https://doi.org/10.1016/S0043-1648(03)00091-7.

[137] D.N. Allsopp, R.I. Trezona, I.M. Hutchings, The effects of ball surface condition in the micro-scale abrasive wear test, Tribol. Lett. 5 (1998) 259–264. https://doi.org/10.1023/A:1019178716408.

[138] M. de M. Macedo, J.H. de A. Lima, C.M. de Alcântara, W. da S. Labiapari, R.C. Cozza, Projeto, construção e validação de um tribômetro ball-cratering de configuração mecânica esfera-fixa, Tecnol. Em Metal. Mater. e Mineração. 20 (2023) e2096. https://doi.org/10.4322/2176-1523.20222096.

[139] F. Carneiro Da Silva, M. De Matos Macedo, J.M. Costa Miscione, L.C. Fontana, J.C. Sagás, R. Câmara Cozza, C.G. Schön, Use of ball-cratering wear test and nanoscratching test to compare the wear resistance of homogeneous and functionally graded titanium nitride thin films, J. Mater. Res. Technol. 22 (2023) 54–65. https://doi.org/10.1016/j.jmrt.2022.11.049.

[140] K. Fan, Z. Hua, L. Zhang, P. Yang, J. He, Monotectic four-phase reaction and self-lubricating performance of directionally solidified Ni-Nb-Cu ternary immiscible alloys, J. Alloys Compd. 1021 (2025) 179668. https://doi.org/10.1016/j.jallcom.2025.179668.

[141] J. Xiao, Y. Wu, W. Zhang, J. Chen, C. Zhang, Friction of metal-matrix self-lubricating composites: Rrelationships among lubricant content, lubricating film coverage, and friction coefficient, Friction. 8 (2020) 517–530.

https://doi.org/10.1007/s40544-019-0270-x.

[142] R. Schouwenaars, V.H. Jacobo, A. Ortiz, Quantitative comparison of the microstructural quality of two classes of commercial soft triboalloys, Mater. Charact. 59 (2008) 312–320. https://doi.org/10.1016/j.matchar.2007.01.018.

[143] L. Zhao, J. Li, Q. Yang, Y. Wang, X. Zhang, H. Li, Z. Yang, D. Xu, J. Liu, Study on Friction and Wear Properties of New Self-Lubricating Bearing Materials, Crystals. 12 (2022). https://doi.org/10.3390/cryst12060834.

[144] D.A. de Moura, L.F. Gomes, C.A. Siqueira, A. Garcia, J.E. Spinelli, Understanding solidification and wear behaviour of Al-3Cu-Bi alloys, Mater. Sci. Technol. 39 (2022) 694–704. https://doi.org/10.1080/02670836.2022.2132733.

[145] J.P. Pathak, S. Mohan, Tribological behaviour of conventional Al-Sn and equivalent Al-Pb alloys under lubrication, Bull. Mater. Sci. 26 (2003) 315–320. https://doi.org/10.1007/BF02707453.

[146] B.P. Reis, M.M. Lopes, A. Garcia, C.A. dos Santos, The correlation of microstructure features, dry sliding wear behavior, hardness and tensile properties of Al-2wt%Mg-Zn alloys, J. Alloys Compd. 764 (2018) 267–278. https://doi.org/10.1016/j.jallcom.2018.06.075.

[147] A. Barros, C. Cruz, T. Botelho, A. Silva, L. Casteletti, A. Garcia, N. Cheung, Dry Sliding Wear Features of an Al-20Sn-5Zn Alloy Affected by Microstructural Length Scales, Lubricants. 10 (2022). https://doi.org/10.3390/lubricants10120352.

[148] P. Adeva, G. Caruana, O.. Ruano, M. Torralba, Microstructure and high temperature mechanical properties of tin, Mater. Sci. Eng. A1. 194 (1995) 17–23. https://doi.org/10.1016/j.jmrt.2023.03.065.

[149] M.C. Lucchetta, F. Saporiti, F. Audebert, Improvement of surface properties of an Al–Sn–Cu plain bearing alloy produced by rapid solidification, J. Alloys Compd. 805 (2019) 709–717. https://doi.org/10.1016/j.jallcom.2019.07.082.

[150] P. WANG, Z. CHEN, H. HUANG, J. LIN, B. LI, Q. LIU, Fabrication of Ti/Al/Mg laminated composites by hot roll bonding and their microstructures and mechanical properties, Chinese J. Aeronaut. 34 (2021) 192–201. https://doi.org/10.1016/j.cja.2020.08.044.

[151] Dr. Dmitri Kopeliovich, Horizontal continuous casting in graphite mold, (n.d.).

https://www.substech.com/dokuwiki/doku.php?id=horizontal_continuous_casting_in_graphite_mold (accessed August 22, 2025).

[152] Bi-metal AlSnCu bearing (microstructure), (n.d.). https://www.substech.com/dokuwiki/lib/exe/detail.php?id=aluminum_based_bearing_materials&cache=cache&media=bi-metal_alsncu_bearing.png (accessed August 22, 2025).

[153] H. Jung, N. Mangelinck-Noël, H. Nguyen-Thi, B. Billia, Columnar to equiaxed transition during directional solidification in refined Al-based alloys, J. Alloys Compd. 484 (2009) 739–746. https://doi.org/10.1016/j.jallcom.2009.05.029.

[154] C.A. Gandin, Experimental study of the transition from constrained to unconstrained growth during directional solidification, ISIJ Int. 40 (2000) 971–979. https://doi.org/10.2355/isijinternational.40.971.

[155] ASTM E3-11 Standard Huide for Preparation of Metallographic Specimens, in: ASTM Int., West Conshohocken, 2017: p. 12.

[156] T. Ferreira, W. Rasband, ImageJ User Guide IJ 1.46r, Image J User Guid. (2012). https://doi.org/10.1038/nmeth.2019.

[157] ASTM International ASTM E112-13, ASTM E112-13 Standard Test Methods for Determining Average Grain Size, (2014).

[158] I. Arganda-Carreras, V. Kaynig, C. Rueden, K.W. Eliceiri, J. Schindelin, A. Cardona, H.S. Seung, Trainable Weka Segmentation: A machine learning tool for microscopy pixel classification, Bioinformatics. 33 (2017) 2424–2426. https://doi.org/10.1093/bioinformatics/btx180.

[159] Trainable Weka Segmentation, (n.d.). https://imagej.net/plugins/tws/ (accessed January 29, 2025).

[160] A. S. Cooper, Precise lattice constants of germanium, aluminum, gallium arsenide, uranium, sulphur, quartz and sapphire, Acta Cryst. 15 (1962) 578–582.

[161] H.F. Swanson, E. Tatge, Standard X-Ray Diffraction Powder Patterns, Natl. Bur. Stand. Circ. 539. 1 (1953).

[162] S.. Meetsma, A.; de Boer, J.L.; van Smaalen, Refinement of the crystal structure of tetragonal Al2 Cu, J. Solid State Chem. (1989) 370–372.

[163] K. Niu, R. Bao, Y. Su, Y. Wang, X.C. Liu, Y. Dai, Effects of hot rolling and heat treatment on the microstructure, mechanical and corrosion properties of Al-xCu-

0.5Mg-0.7Si alloy, Int. J. Electrochem. Sci. . 20 (2025). https://doi.org/10.1016/j.ijoes.2025.101054.

[164] ASTM International, ASTM E8 / E8M - 21 Standard Test Methods for Tension Testing of Metallic Materials, (2021). https://doi.org/10.1520/E0008_E0008M-21.

[165] A. Garcia, J.A. Spim, C.A. dos Santos, Ensaios dos Materiais, 2nd ed., LTC, 2012.

[166] S.K. Kang, Y.C. Kim, K.H. Kim, D. Kwon, J.Y. Kim, Constitutive equations optimized for determining strengths of metallic alloys, Mech. Mater. 73 (2014) 51–57. https://doi.org/10.1016/j.mechmat.2014.01.010.

[167] R.O. Ritchie, The conflicts between strength and toughness, Nat. Mater. 10 (2011) 817–822. https://doi.org/10.1038/nmat3115.

[168] M. Gensamer, Strength and Ductility, Metallogr. Microstruct. Anal. 6 (2017) 171–185. https://doi.org/10.1007/s13632-017-0341-1.

[169] X. Liu, M.Q. Zeng, Y. Ma, M. Zhu, Wear behavior of Al-Sn alloys with different distribution of Sn dispersoids manipulated by mechanical alloying and sintering, Wear. 265 (2008) 1857–1863. https://doi.org/10.1016/j.wear.2008.04.050.

[170] R. Kakitani, C. Konno, A. Garcia, N. Cheung, The Effects of Solidification Cooling and Growth Rates on Microstructure and Hardness of Supersaturated Al-7%Si-x%Zn Alloys, J. Mater. Eng. Perform. 31 (2022) 1956–1970. https://doi.org/10.1007/s11665-021-06341-8.

[171] J. Friedli, J.L. Fife, P. Di Napoli, M. Rappaz, Dendritic growth morphologies in Al-Zn alloys - Part I: X-ray tomographic microscopy, Metall. Mater. Trans. A Phys. Metall. Mater. Sci. 44 (2013) 5522–5531. https://doi.org/10.1007/s11661-013-1912-7.

[172] J.A. Dantzig, M. Rappaz, Solidification - Revised & Expanded, 2th editio, EPFL Press English Imprint, 2016.

[173] X. Dong, B. Gao, L. Xiao, J. Hu, M. Xu, Z. Li, J. Meng, X. Han, H. Zhou, Y. Zhu, Heterostructured Metallic Structural Materials: Research Methods, Properties, and Future Perspectives, Adv. Funct. Mater. 2410521 (2024) 1–34. https://doi.org/10.1002/adfm.202410521.

[174] F. Han, Y. Jiang, F. Cao, L. Cai, S. Liang, A hard/soft layered micro-structured

CuCrZr alloy with strength, ductility and electrical conductivity synergy, Mater. Charact. 199 (2023) 112836. https://doi.org/10.1016/j.matchar.2023.112836.

[175] J. Moon, J.M. Park, J.W. Bae, N. Kang, J. Oh, H. Shin, H.S. Kim, Hetero-deformation-induced strengthening by twin-mediated martensitic transformation in an immiscible medium-entropy alloy, Scr. Mater. 186 (2020) 24–28. https://doi.org/10.1016/j.scriptamat.2020.04.044.

[176] X. Li, M. Nakatani, J. Yang, J. Zhang, B. Sharma, H. Pan, K. Ameyama, J. Fang, X. Zhu, Investigation of mechanical properties and microstructural evolution in Cu─Al alloys with gradient structure, J. Alloys Compd. 890 (2022) 161835. https://doi.org/10.1016/j.jallcom.2021.161835.

[177] M. Beder, T. Varol, S.B. Akçay, Impact of high Al2O3 content on the microstructure, mechanical properties, and wear behavior Al–Cu–Mg/Al2O3 composites prepared by mechanical milling, Ceram. Int. 50 (2024) 38610–38631. https://doi.org/10.1016/j.ceramint.2024.07.230.

[178] X.Y. Li, K.N. Tandon, Microstructural characterization of mechanically mixed layer and wear debris in sliding wear of an Al alloy and an Al based composite, Wear. 245 (2000) 148–161. https://doi.org/10.1016/S0043-1648(00)00475-0.